Convective and Segregative Mechanisms in Vibrofluidised Granular Systems

C. R. K. Windows-Yule

June 9, 2015

UNIVERSITY OF
BIRMINGHAM

University of Birmingham Research Archive

e-theses repository

This unpublished thesis/dissertation is copyright of the author and/or third parties. The intellectual property rights of the author or third parties in respect of this work are as defined by The Copyright Designs and Patents Act 1988 or as modified by any successor legislation.

Any use made of information contained in this thesis/dissertation must be in accordance with that legislation and must be properly acknowledged. Further distribution or reproduction in any format is prohibited without the permission of the copyright holder.

Contents

1 Introduction **2**

1.1 Granular Materials - An Introduction 2

1.2 Vibrated Granular Systems 6

2 Overvew of Previous Work **12**

2.1 Granular Convection 12

2.1.1 Buoyancy-Driven Convection 13

2.1.2 Frictionally-Driven Convection 15

2.2 Granular Segregation 19

2.2.1 Size Segregation 20

2.2.2 Density Segregation 24

2.2.3 Inelasticity-Induced Segregation 30

2.2.4 Geometrically-Induced (Shape) Segregation 32

3 Methodology **37**

3.1 Experimental Setup 37

3.2 Positron Emission Particle Tracking (PEPT) 39

3.2.1 The Physics of PEPT and its Application to Granular Systems 39

3.2.2 Extracting Whole-Field Data from PEPT 46

3.3 Simulations - the MercuryDPM Code 58

4 Convective Flow, and its Influence on the Dynamical and Segregative Behaviours of Granular Systems 65

4.1 Thermal Convection in Monodisperse Systems – The Rôle of Sidewall Dissipation . . . 65

4.2 Thermal Convection in Binary Systems – The Interrelation of Convection and Segregation . . . 76

4.3 Thermal Convection in Binary Systems – Energy Non-Equipartition . . . 89

4.4 Frictionally Driven Convection and Segregation in Unary, Binary and Ternary Systems . . . 98

4.5 Summary . . . 106

5 Density-Driven and Inelasticity-Induced Segregation in Non-Convective, Monosized Granulates 107

5.1 Density-Driven and Inelasticity-Induced Segregation – The Influence of Packing Density and System Geometry . . . 108

5.2 Exploiting Hysteresis to Accelerate Segregation . . . 130

5.3 Suppressing Inelasticity-Induced Segregation . . . 155

5.4 Segregation and Energy Transfer in Systems of Non-Spherical Particles . 171

6 Conclusions 196

List of Figures

1.1 Visualisation of a simple, quasi-two-dimensional, vibrated system based on results acquired using the MercuryDPM discrete particle method simulation software (see section 3.3). The images show the system in a weakly-excited, solid-like state (left), a moderately-excited, liquid-like state (centre) and a strongly excited, gaseous state (right). Although the systems discussed throughout this thesis are typically more complex than those represented here in terms of their size and dimensionality, the simplified systems shown nonetheless provide a useful, visual representation of the three major states achievable by a vibrated granulate. 7

1.2 Exemplary experimental packing density profile for a single monolayer of 6mm glass particles driven with base acceleration $\Gamma = \frac{4\pi^2 f^2 A}{g} = 17$ (where f and A are, respectively, the frequency and amplitude of vibration), producing a dilute, highly fluidised granular bed plotted on (a) linear and (b) semi-logarithmic axes. The exponential nature of the profile's decay is emphasised in panel (b) through the inclusion of a dotted line representing a 'true' exponential. The images shown correspond to currently unpublished data. 9

3.1 The modified dual-headed positron camera used to acquire PEPT data. 40

3.2 Schematic diagram illustrating the triangulation of a tracer particle's spatial position (not to scale). For clarity, the tracer particle is here highlighted in red, although in reality the tracers used are both visually and physically identical to all others in the system. Since the trajectories taken by γ rays produced via electron-positron annihilation events are known to be effectively collinear, if a pair of γ photons are detected by the camera's opposing detectors within a predefined 'resolving time', the path between the two detection events can be recreated. The point of intersection of multiple such γ-ray paths can, as illustrated, be used to determine the spatial position of the tracer particle. 42

3.3 Schematic diagram providing a visual illustration of commonly encountered false coincidence events (the system shown is not to scale). Image (a) shows a *random* coincidence, whereby two entirely unassociated γ rays happen to be detected within the resolving time, τ_r. Panel (b), meanwhile, shows a false coincidence whereby one of the two emitted photons becomes scattered, causing it to deviate from its initial, collinear path. 44

3.4 (a) Two-dimensional particle concentration distribution for the (light) polyurethane component of a binary mixture of equally sized (heavy) steel and polyurethane particles. The volume fraction of polyurethane particles in a given region of two-dimensional space can be determined using the colour key provided in the image. (b) One-dimensional packing profile for both light (red circles) and heavy (black squares) components of the system shown in (a). 48

3.5 Mean squared displacement, $M(t)$, as a function of time for vibrofluidised granular beds housed in containers of horizontal extent (a) 120 mm and (b) 25 mm. 51

3.6 Examples of velocity distributions acquired from PEPT data. Data is shown for two highly excited granular systems, one of which exhibits a near-Gaussian velocity distribution (blue squares), as would be expected of a similar *molecular* system, while the second demonstrates the augmented high energy 'tails' typical of granular systems (orange circles). A dashed line corresponding to a true Gaussian is included as a guide to the eye. For the interested reader, the context and significance of this image may be found in our reference [1]. 52

3.7 Two-dimensional, depth-averaged velocity field showing the steady-state particle flow for a vertically vibrated system in which strong convective flow is present. 53

3.8 Plot showing a typical, convective velocity field for a dense, narrow granular system (centre) and its influence on the distribution of differently massive particles in binary (left) and ternary (right) systems. Data is taken from our reference [2], which is discussed in detail in section 4.4. . 56

3.9 Vertical packing density profiles for both components of a binary bed comprising nylon (circles) and steel (squares) spheres driven with a dimensionless acceleration $\Gamma = 14$. Data is shown for a full data set of length $t_r = 4800$ s (red) as well as for a series of individual 'segments' of this data set, each of length $\frac{t_r}{10}$ (blue, green, orange and black) corresponding to various points chosen to span the entirety of t_r. 58

3.10 Experimental (a) and simulational (b) packing density profiles for a vertically vibrated bed of 3 mm diameter stainless steel particles. The bed has a dimensionless depth of $N_L = 6$ particle layers, and is driven at a fixed dimensionless energy input $S = \frac{4\pi^2 f^2 A^2}{gd} = 5.44$ produced using various combinations of A and f, as specified in the legend provided in the image. The strong agreement shown here provides a powerful example of the advantage of directly modelling the vibrational motion of the base of a system as opposed to simply approximating the base's energy input using a static '*thermal wall*', an assumption often used in other simulation models [3–6]; were such an approximation used here, the simulated profiles would all be identical! 64

4.1 Convective flow rate, J, in ms^{-1} as a function of effective sidewall inelasticity, ε_w for the case $N = 863$. Figure taken from our reference [7]. . . . 68

4.2 Convective flow rate as a function of particle number, N, for steel (blue circles), copper (green crosses) and perspex (red squares) sidewalls. Figure taken from our reference [7]. 70

4.3 Velocity vector plots in the x-z plane for $N = 321$ particles in two equally-sized, identically-driven systems differing only in the material of the sidewalls used to constrain the system laterally. Images are shown for (a) mild steel ($\varepsilon_w = 0.70$) and (b) tufnol ($\varepsilon_w = 0.39$) sidewalls. Velocity values are averaged over the z-dimension. 71

4.4 Vertical temperature profiles for the case N = 963, normalised in each case by the average temperature of a particle taken over all data points. Profiles are shown for systems with sidewalls composed of mild steel (blue circles), lead (orange triangles) and perspex (red squares). Aside from this variation in sidewall material, all systems shown are identical in terms of their driving, size and indeed all other major variables. Inset: theoretical temperature profiles for cases equivalent to steel (ε_w = 0.7 – dashed curve) and perspex (ε_w = 0.33 – solid curve). 73

4.5 Variation of the ratio of vertical to horizontal temperature components (T_z/T_h) for systems with varying particle number, N, and sidewall elasticity, ε_w. Data is shown for beds of size N = 321 (orange triangles), N = 428 (blue squares), N = 642 (red diamonds) and N = 856 (black circles). Figure taken from our reference [7]. 74

4.6 Velocity probability density function (vPDF) for the extremal values of particle elasticity explored in experiment, shown alongside a corresponding Gaussian distribution (black dashed line). Data is shown for systems with sidewalls composed of mild steel (solid orange line) and lead (blue dotted line). In all cases, a particle number N = 856 is used. Figure taken from our reference [7]. 77

4.7 Double-logarithmic plot of the high-$|v|$ region of the vPDFs for the case N = 642. Data is shown for lead- (orange triangles), tufnol- (red squares) and steel-walled (blue diamonds) systems, with a Gaussian distribution represented by a dashed line. Figure taken from our reference [7]. 77

4.8 Variation of convective flow rate, J, with sidewall elasticity, ε_w, for (a) monodisperse systems of glass (L) and steel (H) spheres and (b) a bidisperse mixture of these materials. In all cases the particle number N = 1000, with $N_H = N_L = \frac{N}{2}$ in the binary case. Figure taken from our reference [8]. 78

4.9 Segregation intensity, I_s, (as defined in section 3.2.2) as a function of the system's average convective flow rate for a 50:50 by volume binary mixture of glass and steel particles. In this image, I_s remains unnormalised, such that a value $I_s = 0.5$ represents complete segregation, while $I_s = 0$, as usual, indicates perfect mixing between species. Figure taken from our reference [8]. 80

4.10 Segregation intensity, I_s, as a function of (a) the convection rate ratio, $\frac{J_L}{J_H}$, and (b) thel diffusivity ratio (i.e. the ratio of self diffusion coefficients, $\frac{D_L}{D_H}$). Data is shown for the case in which convective and diffusive motion is varied through alteration of the system's driving parameters (diamonds) as well as for the situation in which the system's dynamics are altered through a variation in sidewall material (circles). Figure taken from our reference [8]. 82

4.11 One-dimensional packing profiles providing a visual illustration of the vertical segregation observed for binary systems of glass and steel particles with horizontal boundaries constructed of (a) steel ($\varepsilon_w = 0.70$), (b) perspex ($\varepsilon_w = 0.33$) and (c) brass ($\varepsilon_w = 0.58$). All other system parameters are held constant for all images shown. Figure taken from our reference [8]. 84

4.12 Simulated data showing the relationship between segregation intensity, I_s, and the ratio of convective flow rates, $\frac{J_L}{J_H}$, for various particle combinations and system widths (Note: in the published paper from which this image originally appeared, the width of the system was denoted 'W' as opposed to '$L_{x,y}$' as is the case in the current work). Figure taken from our reference [8]. 86

4.13 Local granular temperature, $T(z)$ (measured in Joules), plotted as a function of z, the height from the system's base. Data is shown for each of the individual components of a glass/steel binary mixture for systems bounded by both brass ($\varepsilon_w = 0.52$) and perspex ($\varepsilon_w = 0.33$) sidewalls, as indicated in the Figure – in each case, the legend provides this information as *[wall material] ([particle material])*. Figure taken from our reference [9]. 91

4.14 Variation with height, z, of the granular temperature ratio, $\gamma = \frac{T_H}{T_L}$, for the data shown in Figure 4.13. Here, blue circles represent the ratio for a perspex-walled system and orange circles that of a brass-walled system. It is interesting to note from this Figure that the temperature ratio within the bulk of the material ($z \lesssim 30$ mm) remains relatively constant, as expected from previous studies [10], yet varies significantly for large z. This is likely due to the fact that the upper regions of the system exist in the dilute Knudsen regime where the system's dynamics are governed by differing processes [11,12]. 92

4.15 Temperature ratio, $\gamma = \frac{T_H}{T_L}$, as a function of segregation intensity, I_s. Data is shown for the case in which I_s is altered due to a variation in sidewall dissipation (circles), as well as that in which the degree of segregation is altered through a change in the system's driving parameters (squares). In both cases, all other system parameters are held constant. Figure taken from our reference [9]. 93

4.16 Experimentally acquired packing profiles for the steel and glass components (blue solid and dashed lines, respectively) of a binary bed shown alongside the corresponding temperature ratio, $\gamma = \frac{T_H}{T_L}$, between the two species (orange dotted lines). The upper image shows data for a perspex-walled system ($\varepsilon = 0.33$), while the lower image corresponds to an otherwise identical system bounded instead by copper walls ($\varepsilon = 0.58$). Figure taken from our reference [9]. 95

4.17 Temporally and spatially averaged *total* temperature ($T_H + T_L$) for both components of a glass/steel binary system as a function of the system's total flow rate ($J_H + J_L$). Here, data is shown only for the case of varied ε_w, as opposed to varied driving strength, as the latter will additionally influence the energy input to the system, hence obscuring the J-dependence with which this image is concerned. Figure taken from our reference [9]. 98

4.18 Two dimensional particle concentration plots showing the spatial distribution of light (L) polyurethane particles (image (a)) and heavy (H) steel particles (image (b)) within a system comprising a 50 : 50 mixture of these two species. The system shown here is driven with a fixed dimensionless acceleration $\Gamma = 11$. In each image shown, the local fractional concentration, ϕ, of the relevant species can be determined from the colour key provided. Figure taken from our reference [2]. 99

4.19 *Top:* Two-dimensional particle concentration plots showing the spatial distributions of steel (H) particles (image (a)), glass (M) particles (image (b)) and polyurethane (L) particles (image (c)) for a $\frac{1}{3}:\frac{1}{3}:\frac{1}{3}$ mixture of these species. The system is driven with an acceleration $\Gamma = 11$. In each image shown, the local fractional concentration, ϕ, of the relevant species can be determined from the colour key provided. *Bottom:*Image (d) shows one-dimensional projections of the data presented in panels (a)-(c), with blue squares corresponding to H particles, yellow triangles representing M particles and red circles denoting the local packing fractions of the L species. The positions of the time-averaged vertical mass centres of each species are marked by solid, dotted and dashed lines for the H, M and L species respectively. Figure taken from our reference [2]. 101

4.20 Experimentally acquired depth-averaged velocity vector fields shown for the system's x-z plane (note that the image refers to the vertical dimension as 'y' due to the differently defined coordinate system used in the original publication from which this image is taken). Data is shown for monodisperse (M), binary (MH) and ternary (LMH) systems in panels (a), (b) and (c) respectively. In all cases, the system is driven with a fixed dimensionless acceleration $\Gamma = 11$, the total particle number N is held constant and – for the binary and ternary systems – the volume fractions of all particle species are held equal to one another (i.e. $N_M = N_H = 3000$ for image (b), $N_L = N_M = N_H = 2000$ in image (c)). Figure taken from our reference [2]. 103

4.21 Experimentally acquired one-dimensional vertical temperature profile for a ternary system driven with an acceleration $\Gamma = 14$; the T values shown represent the average across all three particle species for each region of the experimental system. The form of the profile shown is typical of that exhibited by all systems studied, with a relatively large temperature at small and large heights, z, with a near-constant, lower-T region throughout the main bulk of the bed. Figure taken from our reference [2]. 104

5.1 Variation of the system's bulk packing fraction with the dimensionless resting bed height, N_L. Data is shown for monodisperse systems comprising glass (circles and dashed line) and brass (triangles and solid line) spheres, as well as a binary mixture of brass and glass particles (squares and dotted line). In each case, discrete points represent experimental data, while continuous lines correspond to simulational data. Data is also shown (crosses) for simulations in which particles possess the density of glass particles but the restitution coefficient of brass particles, demonstrating a seeming mass-independence which will be further evidenced and discussed in greater detail in section 5.4. Figure taken from our reference [13]. 109

5.2 Power spectra corresponding to the vertical centre of mass motion of a bed with dimensionless height $N_L = 6$ driven with a fixed dimensionless peak energy $S = 1.83$. Results are shown for systems in which the desired S value is achieved using various differing combinations of driving frequency, f, and peak amplitude, A. Specifically, we show here the cases $f = 9.55$ Hz, $A = 5$ mm (black), $f = 11.9$ Hz, $A = 4$ mm (blue) and $f = 19.9$ Hz, $A = 2.4$ mm (red). In all cases, the power spectra themselves are represented by continuous, solid lines while vertical dashed lines are used to demarcate the position on the horizontal axis pertaining to the relevant driving frequency of each given system. All data presented is acquired from experiment. Figure taken from our reference [14]. 111

5.3 Segregation intensity as a function of the density ratio, $\frac{\rho_H}{\rho_L}$, between heavy (H) and light (L) particle species for a system of resting depth $N_L = 2.5$. Experimental data (open triangles) and simulational results (open squares) are shown for various binary combinations of the materials shown in table 5.1; the specific pairings of particle species are demarcated using the abbreviations provided in the table. Results are also shown (solid circles) for simulations in which the experimental *density* values are maintained, but the *effective elasticities* of particles are held constant at a value $\varepsilon_{\alpha\alpha} = \varepsilon_{\beta\beta} = 0.91$, thus demonstrating the case of *purely density-driven* segregation, and its distinction from the situation in which elasticity-induced segregative effects are also present. Additional results (open circles) are included for simulations in which, as before, $\varepsilon_{\alpha\alpha} = \varepsilon_{\beta\beta} = 0.91$, but the density ratio is instead varied by holding the density of the lighter component constant at 2500 kgm^{-3} whilst varying ρ_H to produce the desired density ratios. In this image, I_s is not normalised, and a value $I_s = 0.5$ corresponds to a fully segregated system. Figure taken from our reference [13]. 113

5.4 Segregation intensity, I_s, (red triangles) and average void fraction for the *lower half* of the system (black circles) as a function of ε_H, the effective elasticity of the system's heavier component. In this instance, the bed height is once more equal to 2.5 particle diameters, while the density ratio $r = \frac{\rho_H}{\rho_L}$ is now held constant at $r = 4$. As with the previous image, an I_s value of 0.5 corresponds to a fully-segregated system. All data shown is derived from DPM simulations. Figure taken from our reference [13]. 115

5.5 I_s as a function of packing fraction, η, for the case in which segregation is due solely to inelasticity effects (i.e. $r = 1$; specifically, $\rho_A = \rho_B =$ 2500 kgm^{-3}), illustrating the considerable variation in the strength of inelasticity-induced segregation for systems of differing system density. Data is shown for systems in which the elasticity of the different system components varies by a factor of 1.5 (blue diamonds), a factor of 2 (black circles) and a factor of 4 (orange triangles); in all instances, the effective elasticity of the less-dissipative component is held constant at a value $\varepsilon = 0.95$. For both images, $I_s^{max} = 0.5$. Figure taken from our reference [13]. 116

5.6 Segregation intensity, I_s, as a function of the density ration $r = \frac{\rho_H}{\rho_L}$ for the case of a bed with resting height $N_L = 10$. All symbols used are as defined in Figure 5.3. Figure taken from our reference [13]. 117

5.7 Log-linear plot of the time required for a simulated system to reach its steady segregated state (red triangles) shown alongside the time required for a single, light particle in an experimental system to rise from the base to the free upper surface of a vibrated bed comprising purely heavy particles (black circles). Figure taken from our reference [13]. 118

5.8 Variation with aspect ratio, $\mathcal{A} = \frac{N_L}{L_x/d}$, of the degree of segregation, I_s, exhibited by a given binary system of $N = 1000$ particles, driven with a constant frequency $f = 70$ Hz and amplitude $A = 1.06$ mm. Data is shown for three different combinations of particles: glass and steel (blue squares), glass and brass (red triangles) and aluminium and steel (black circles). A 50:50 ratio of the relevant species is utilised in all cases. Figure taken from our reference [15]. 119

5.9 Two dimensional spatial packing density distributions for two otherwise identical glass/steel systems with aspect ratios (a) $\mathcal{A} = 1.95$ ($N_L = 15.6$) and (b) $\mathcal{A} = 8$ ($N_L = 40$). Darker shades are representative of regions of comparatively higher packing. In both images, the container's base (not visualised by PEPT) coincides with a vertical position of 284 mm. It is important to note that in the research paper from which this image is taken, the vertical coordinate was denoted 'y' as opposed to 'z' as is the case for the majority of this thesis. Figure taken from our reference [15]. 121

5.10 Vertical position of a single, glass tracer particle within a binary bed of (a) glass and steel and (b) glass and brass with, in both cases, an aspect ratio $\mathcal{A} = 1.95$, shown as a function of time. The vertical position is here shown as a dimensionless quantity, $z^* = \frac{z}{d}$, with d the particle diameter. Figure taken from our reference [15]. 123

5.11 Time evolution of the vertical position of a single *brass* tracer in a binary glass/brass system with aspect ratio $\mathcal{A} = 1.95$. 124

5.12 Evolution with time of the horizontal (x) position of a single *brass* tracer particle in a bed of glass and brass spheres of aspect ratio $\mathcal{A} = 1.95$. The horizontal position is normalised by the particle diameter, d, to give the dimensionless variable $x^*(t)$. Figure taken from our reference [15]. . . . 125

5.13 Two dimensional packing density distributions for a system of aspect ratio $\mathcal{A} = 1.13$ comprising a $50 : 50$ mixture of 6 mm glass and brass particles. Panels (a), (b) and (c) correspond to data acquired from a single experimental run for different intervals in time, as described in the main text. In the images, darker regions represent areas of increased particle density while lighter shading represents more dilute regions. Figure taken from our reference [15]. 127

5.14 Two dimensional packing density distributions for a system of aspect ratio $\mathcal{A} = 1.13$ comprising a 50 : 50 mixture of 6 mm glass and *steel* particles. Each image shown corresponds to a different, non-overlapping 500 s period of a single data set. In this image, red corresponds ti regions of high packing and blue to regions of low particle density. 128

5.15 Vertical position vs. time for a single glass particle in a glass/brass system of aspect ratio $\mathcal{A} = 1.95$. Data is shown over a period of time corresponding to a single downward transit through the system. 129

5.16 Variation of the steady-state segregation intensity, I_s, achieved by a binary mixture (black circles) and the time required (red triangles) for a given system to reach this equilibrium distribution with the bulk packing density, η, of the granular bed under investigation. The data shown here pertain to the case in which segregation is purely density-driven , i.e. $R = \frac{\varepsilon_H}{\varepsilon_L} = 1$. The density ratio, r, between species is equal to 5, ensuring that all systems are capable of achieving complete segregation if other system parameters allow. Figure taken from our reference [13]. 131

5.17 Comparison of the time-evolution of the centre of mass ratio for light and heavy particles, $\frac{Z_L}{Z_H}$, for two otherwise identical systems exposed to initially strong driving, ISD, (black line) and continuous driving, CD, (red line), the definitions of which are provided in the main text. For both ISD and CD systems, $N_L = 24.4$, Γ_0, the steady-state peak acceleration, is equal to 17 times the strength of gravity and the density ratio $r = 5$. Clearly, a larger ratio $\frac{Z_L}{Z_H}$ represents more complete segregation. Figure taken from our reference [13]. 133

5.18 Experimentally acquired velocity autocorrelation functions, $C_v(t)$, for a bed of height $N_L = 7$ driven with a constant peak acceleration $\Gamma_0 = 14.5$ (solid red line) and $\Gamma_0 = 15$ (solid black line). Figure taken from our reference [16]. 135

5.19 Comparison of experimental mean squared displacements, $M(t)$, for continuously driven (CD) and initially strongly driven (ISD) systems of resting height $N_L = 7$ driven with dimensionless acceleration $\Gamma_0 = 14.5$ (panel (a)) and $\Gamma_0 = 15$ (panel (b)). The ISD systems are initially driven with peak acceleration $\Gamma_i = \frac{3}{2}\Gamma_0$ for a period of two seconds. Figure taken from our reference [16]. 137

5.20 Experimentally acquired mean squared displacement, $M(t)$, as a function of time for a monodisperse bed of steel particles bed with a resting depth of $N_L = 7$ particle diameters which is excited with a steady state dimensionless acceleration $\Gamma_0 = 13$. Data is shown for equivalent continuously driven (black circles) and initially strongly driven (red triangles) systems. In the ISD case, the system is initially excited for a period of two seconds at a peak acceleration $\Gamma_i = \frac{3}{2}\Gamma_0 = 19.5$. The inset of the image shows the same data presented on a linear, as opposed to log-linear, scale, emphasising the increased mobility for the ISD case. Figure taken from our reference [16]. 139

5.21 A typical example of the evolution with time of the (horizontal) x-position of a single tracer particle within the continuously driven (black line) and initially strongly driven (red line) systems detailed in Figure 5.20 above. Figure taken from our reference [16]. 140

5.22 Experimentally obtained vertical packing density profiles for the same systems as discussed in Figures 5.20 and 5.21. Figure taken from our reference [16]. 140

5.23 Mean squared displacement behaviour corresponding to a pair of experimental granular systems identical in terms of their steady-state driving ($\Gamma_0 = 13$), resting bed height ($N_L = 12$) and other relevant properties, differing only in the manner of their original excitation – one bed, represented by red triangles, is initially vibrated at an increased acceleration $\Gamma_i = 19.5$ for a two second period while the other, represented by black circles, is driven continually at Γ_0. Figure taken from our reference [16]. 141

5.24 Experimental results showing (a) the variation with time of the mean squared displacement, $M(t)$, for particles within a pair of corresponding initially strongly driven and continuously driven systems and (b) the evolution with time of the relevant tracer particle's horizontal position in the x-direction for the same CD-ISD dyad. For both ISD and CD systems, $N_L = 12$ and $\Gamma_0 = 14.5$, with an initial driving acceleration $\Gamma_i = 21.75$ in the ISD case. Figure taken from our reference [16]. 143

5.25 (a) Radial distribution function, $g(r/d)$, for an ISD-CD dyad with $\Gamma_0 = 14$ ($\Gamma_i = 21$ for the ISD system) and $N_L = 10$. (b) Coordination number distributions for the case $\Gamma_0 = 13$ ($\Gamma_i = 19.5$), $N_L = 8$. In both images, results pertaining to the CD system are represented by a solid black line, while those corresponding to the ISD system are depicted as dashed red lines. The marked variations in the two quantities shown between the equivalent CD and ISD systems provide a clear illustration of the differing degrees of crystalline order within the differently driven systems. All data shown correspond to DPM simulations. Figure taken from our reference [16]. 147

5.26 Two-dimensional spatial packing density distribution for an experimental continuously driven (CD) system of depth $N_L = 14$ excited with a peak dimensionless acceleration $\Gamma_0 = 14$. Regions of the bed for which the local solids fraction exceeds the random close-packed value $\eta = 0.63$ are highlighted in yellow, while areas in which the packing density falls below this value are shown in blue. The presence of multiple, localised regions for which $\eta > \eta_{rcp}$ provides a strong indication of the presence of crystalline structure within the system. Figure taken from our reference [16]. 148

5.27 Simulated one-dimensional vertical packing profiles for the heavy (solid black line) and light (dashed blue line) components of a binary system of depth $N_L = 7.4$ whose components vary in density by a ratio $\frac{\rho_H}{\rho_L} = 8$. The system is driven with a peak dimensionless acceleration $\Gamma = 3.5$ and a peak driving velocity $v = 0.14$ ms^{-1}. 150

5.28 Experimental data plotting the variation with time of the vertical (z) position of a single glass ($\rho = 2500$ kgm^{-3}) sphere as it rises upward through a bed of equally-sized steel ($\rho = 7900$ kgm^{-3}) spheres. In each case, data is shown for both continuously driven (black lines) and initially strongly driven (red lines) systems with otherwise identical parameters. In panel (a), we see the behaviour of a bed of height $N_L = 7$, while the data shown in panel (b) corresponds to a bed with $N_L = 12$. In both cases, the steady-state driving acceleration, Γ_0, is equal to 13, with an initial driving $\Gamma_i = \frac{3}{2} \cdot \Gamma_0 = 19.5$ for the ISD systems in each of the two panels. Figure taken from our reference [16]. 151

5.29 The centre of mass ratio, $\frac{Z_L}{Z_H}$ – an indicator of segregation – shown as a function of time for simulated ISD and CD systems with driving parameters and bed depths identical to those in Figure 5.28. Figure taken from our reference [16]. 153

5.30 A visual illustration of the extent to which initial strong driving is found, on average, to accelerate the separation of particle species in a vibrated binary system for a range of steady-state driving strengths, Γ_0, and hence differing packing fractions, η. Shown here is experimental data, in the form of a ratio between the time taken for a single (light) glass particle to rise from the base to the free surface of a bed of (heavy) steel spheres for equivalent CD and ISD systems, and simulational data, presented as a ratio of the necessary times for complete (steady-state) segregation to be achieved by the two members of a CD-ISD pair. Figure taken from our reference [16]. 154

5.31 One-dimensional vertical packing distributions for both heavy (H) and light (L) components of a binary granular bed the case $N_L = 5.4$, $\varepsilon_H = \varepsilon_L = 0.83$ and $r = \frac{\rho_H}{\rho_L} = 4$. Data is shown for dimensionless driving accelerations $\Gamma = 3.5$ (panel (a)) and $\Gamma = 11$ (panel (b)). In each panel, particle distributions are shown for systems in which the *average* particle density varies from $\bar{\rho} = 1250$ kgm^{-3} ($\rho_L = 500$ kgm^{-3}, $\rho_H = 2000$ kgm^{-3}) to $\bar{\rho} = 10000$ kgm^{-3} ($\rho_L = 4000$ kgm^{-3}, $\rho_H = 16000$ kgm^{-3}). Figure taken from our reference [17]. 159

5.32 Plot showing the relationship connecting the average packing density, η, of a simulated, monodisperse granular system and the effective elasticity, ε, of the particles forming the bed. Data is shown for a range of driving parameters and bed heights, whose values span the ranges used in experiment. The η values are normalised by a factor $N_L^{\frac{1}{2}}(\omega A/\sqrt{dg})^{-\frac{1}{4}}$, whose significance is explained in the main text. Figure taken from our reference [18]. 160

5.33 Plot of the critical ratio, r_c, of particle densities above which segregative effects due to differences in particle elasticity may be neglected as a function of the average packing density, η, of a binary granular bed. Open circles represent data from simulations while the (theoretical) solid line corresponds to the situation for which the inequality in equation (5.8) becomes balanced, i.e. the boundary dividing regions for which inelasticity effects may and may not be ignored. Figure taken from our reference [18]. 164

5.34 Variation with packing fraction, η, of the typical lifespan (red triangles) of the localised regions of high density or '*cold droplets*', the existence of which is believed [19, 20] to facilitate inelasticity-induced segregation within vibrofluidised systems such as ours, and the local packing density of these droplets as compared to the system's average η value (black circles). The data shown corresponds to the situation $N_L = 2.5$, $\rho_A = \rho_B = 2500$ kgm^{-3} and $\varepsilon_A = 3 \cdot \varepsilon_B = 0.9$. Figure taken from our reference [13]. 165

5.35 Phase diagram showing, for various combinations of the key dissipative control parameter χ and key excitation control parameter V the minimal necessary ratio, r_c, for which inelasticity effects on segregation are fully suppressed. Panel (a) shows data acquired from DPM simulations, while panel (b) presents the relevant theoretical predictions based on the framework presented above. Figure taken from our reference [18]. 166

5.36 Data from Fig. 5.35 shown in r_c-V space for a variety of values of the key control parameter χ. Data is shown for (a) simulations and (b) our theoretical predictions. Figure taken from our reference [18]. 167

5.37 Two-dimensional slice through the phase diagram shown in Figure 5.35 for the case $r_c = 3.0$. In the image, theoretical predictions of the combinations of V and χ required to produce an r_c value of 3 are represented by crosses, while circles represent the points in V-χ space for which a critical ratio of 3 is found in simulation. The inclusion of simulated – as opposed to theoretical – results to represent the lower boundary arises due to the fact that the absence of elasticity-induced segregation in the non-fluidised limit is not captured by our simple theoretical model. Solid black lines connecting theoretical and simulated data points are used as a guide to the eye. Open squares and triangles represent experimental data, with triangles representing data sets in which inelasticity-induced segregative effects are apparent and squares corresponding to the cases in which such effects are seemingly absent. For the case of perfect agreement between experiment and theory/simulation, all triangles should fall within the region denoted "Inelasticity-Induced Segregation" with all squares lying external to this region. Figure taken from our reference [18]. 170

5.38 Scale diagrams showing the dimensions of the three differing particle geometries used in experiment: spherical (left), disc-like (horizontal centre) and cuboidal (right). For each particle type, plan (top) and side (bottom) views are shown (due to the symmetry of the particles used, the end view is, clearly, redundant). 172

5.39 One-dimensional particle distributions for both components of various bidisperse-by-shape granular mixtures for which $\nu_A \approx \nu_B$ and $\rho_A \approx \rho_B$ (i.e. particles differ significantly *only* in their geometries. Data is shown for multiple combinations of particle species and driving parameters. Panel (a) shows data for a system of spheres (solid line) and cuboids (dashed line) driven at a frequency of 40 Hz and with an amplitude A = 1.67 mm. Panel (b) represents a system of cuboids (solid line) and discs (dashed line) exposed to the same driving conditions as (a). Panel (c) shows an identical system to (a) with driving parameters f = 80 Hz and A = 0.42 mm, thus providing a dimensionless peak velocity, V, identical to that used in (a), but with a different peak acceleration, Γ. Panel (d) meanwhile again corresponds to a similar particle mixture to that used in (a) and (c), this time producing an equal Γ to that in panel (a) but a differing V through an f-A combination of f = 100 Hz and A = 0.42 mm. In all images shown, N = 1800 and $L_{x,y}$ = 80 mm. Figure taken from our reference [21]. 174

5.40 Experimental data demonstrating the manner in which segregation intensity, I_s, is observed to vary with the driving parameters V and Γ for two differing combinations of particle shape. Open circles are representative of binary systems comprising cuboidal and spherical particles, while open triangles correspond to results obtained from binary mixtures of discs and spheres. For each of these particle combinations, red dotted lines represent data sets for which V is held constant at a value $V = 0.19$ ms^{-1} while Γ is varied and blue dashed lines represent the case in which Γ is held constant at a value $\Gamma = 12$ with the driving velocity V instead undergoing alteration. For all results shown, the particle number and system size are held constant at $N = 2400$ and $L_{x,y} = 60$ mm, respectively, thus ensuring a consistent bed height and aspect ratio. The results presented are clearly suggestive of a strong V-dependence for I_s and, conversely, a negligible influence due to Γ. Figure taken from our reference [21]. 177

5.41 One dimensional vertical packing density profiles from Figure 5.39's panels (c) and (d) replotted alongside their corresponding vertical temperature (T) profiles. In each of the images presented, solid lines correspond to the lower-r_g particle and dashed lines to the higher-r_g particle while blue lines and red lines correspond respectively to the solids fraction and granular temperature of the relevant particle species. Figure taken from our reference [21]. 178

5.42 One dimensional vertical packing profiles for both system components in a variety of binary granular beds comprising particles of equal volume, ν, but which differ in their material densities, ρ, and geometries. Images are shown for the following particle combinations: (a) steel (solid line) and nylon (dashed line) spheres; (b) steel cuboids (solid line) and nylon spheres (dashed line); (c) steel cuboids (solid line) and glass spheres (dashed line); (d) steel cuboids (solid line) and nylon discs (dashed line). The systems shown in images (a)-(c) are all driven with a frequency $f = 65$ Hz and an amplitude $A = 1.03mm$. The bed corresponding to image (d), meanwhile, is driven with $f = 40$ Hz and $A = 3.57$ mm. All systems shown contain a number of particles $N = 1800$. Figure taken from our reference [21]. . . . 180

5.43 Scale diagram of a typical particle used in experiment. Image taken from reference [22]. 183

5.44 Velocity probability density functions for systems with moments of inertia $I = 7.2 \times 10^{-8}$ kgm^2 (black circles), $I = 9.6 \times 10^{-8}$ kgm^2 (blue triangles) and $I = 1.7 \times 10^{-7}$ kgm^2 (red diamonds). Data is shown for both horizontal (x) and vertical (z) velocity components. In all cases shown, the particle number N is equal to 100 and the peak driving velocity V is held constant at 0.68 ms^{-1}. Provided in the insets of each image are the same results plotted on a semilogarithmic scale. Image taken from reference [22]. . . 186

5.45 Log-linear plots of the high-velocity 'tails' corresponding to the velocity profiles shown in Figure 5.44 for (a) the horizontal and (b) the vertical components of particle motion. Linear least-squares fits to the data points shown are included as a guide to the eye. Image taken from reference [22]. 187

5.46 Velocity probability density functions for a series of single particle systems ($N = 1$) driven with an identical peak base velocity ($V = 0.68$ ms^{-1}) to the multi-particle systems depected in Figure 5.44. As with this previous image, data is shown for particles possessing moments of inertia $I = 7.2 \times 10^{-8}$ kgm^2 (black circles), $I = 9.6 \times 10^{-8}$ kgm^2 (blue triangles) and $I = 1.7 \times 10^{-7}$ kgm^2 (red diamonds). Unlike the corresponding image for the $N = 100$ case, however, the various velocity profiles for the single-particle case collapse almost perfectly onto a single curve; the reasons for the striking disparity between these two Figures is discussed at length in the main text. Image taken from reference [22]. 189

5.47 Experimentally obtained x-tracjectory of a single, asymmetrically irradiated particle undergoing free flight in a direction directly parallel to that of gravity. 191

5.48 (a) $E^{\dagger}$, the sum of the time-averaged translational kinetic energy, $\bar{E}$, and gravitational potential energy, E_P, possessed by a granular bed plotted as a function of the moment of inertia, I, of the individual particles comprising each system. Data is shown for beds excited with peak driving velocities $V = 0.41$ ms^{-1} (black circles), $V = 0.49$ ms^{-1} (grey crosses), $V = 0.55$ ms^{-1} (blue triangles), $V = 0.61$ ms^{-1} (orange squares) and $V = 0.68$ ms^{-1} (red diamonds). In all cases, a fixed particle number $N = 100$ is used. Panel (b) shows the same data as presented in (a), this time normalised by the base velocity, V. Panel (c), meanwhile, shows $E^{\dagger}$ as a function of V, for particles with rotational inertiæ $I = 7.2 \times 10^{-8}$ kgm^2 (circles), $I = 8.1 \times 10^{-8}$ kgm^2 (crosses), $I = 9.6 \times 10^{-8}$ kgm^2 (triangles), $I = 1.2 \times 10^{-7}$ kgm^2 (squares) and $I = 1.7 \times 10^{-7}$ kgm^2 (diamonds). In all images shown, linear fits to the data points presented are included as a guide to the eye. Figure taken from reference [22]. 194

Granular materials display a host of fascinating behaviours both remarkably similar to and strikingly different from those exhibited by classical solids, liquids and gases. Due to the ubiquity of granular materials, and their far-reaching importance in multitudinous natural and industrial processes, an understanding of their dynamics is of the utmost importance to modern society.

In this thesis, we analyse in detail two phenomena, one from each of the above categories: granular convection, a behaviour directly analogous to the Rayleigh-Bénard cells observable in classical fluids, and granular segregation, a phenomenon without parallel in classical, molecular physics, yet which is known to greatly impact various physical and industrial systems. Through this analysis, conducted using a combination of the experimental positron emission particle tracking technique and discrete particle method simulations, we aim to improve our knowledge of these processes on a fundamental level, gaining insight into the factors which may influence them, and hence how they may be effectively controlled, augmented or eliminated.

This thesis is dedicated to Hattie Amos, who for the past 8 years has been my inspiration, my comfort through the difficult times and my companion in the good times. She is the reason I strive to do better, and to be better.

Acknowledgements

I would like to begin by thanking Professor David Parker for the extraordinary degree of trust, support, freedom, generosity and genuine kindness he has afforded me throughout my PhD. There are no words which can adequately express my gratitude, and I can only say that I count myself immensely lucky to have had the opportunity to work under such a unique Supervisor.

I would also like to thank those with whom I have collaborated during my study:

Dr. Anthony Thornton of the University of Twente who, in my opinion, represents everything a scientist should be - possessing of a great wealth of knowledge, yet always willing to share that knowledge freely in the hopes of advancing his field, as opposed to achieving personal gain. The tools and knowledge which he has taken the time and effort to provide me with have undeniably had a transformative influence on my research.

Dr. Nicolás Rivas - put simply, an extraordinary mind which belies his years; despite a hugely busy schedule, Nico has always found the time to help me answer scientific questions ranging from the mundane to the almost incomprehensibly abstract, and has never failed to provide a new angle and an impressive insight.

Dr. Thomas Weinhart, whose mathematical and computational knowledge has proved invaluable in some of the pivotal areas of my research, facilitating the deeper exploration and stronger explanation of numerous phenomena detailed within this thesis. I am additionally grateful for his regular help and advice on both technical and scientific matters.

Professor Anthony Rosato of the New Jersey Institute of Technology - a living confutation of the old adage that you shouldn't meet your heroes. His were some of the first papers which introduced me to the field of granular dynamics, and the ability to work alongside such an esteemed member of the granular community has been both an honour and a pleasure.

Finally, I wish to acknowldge the funding received from the Hawkesworth Scholarship, provided by the late Dr. Michael Hawkesworth, without which this research would not have been possible.

1 Introduction

For look! Within my hollow hand,
While round the earth careens,
I hold a single grain of sand
And wonder what it means.
Ah! If I had the eyes to see,
And brain to understand,
I think Life's mystery might be
Solved in this grain of sand.
– Robert William Service

1.1 Granular Materials - An Introduction

Although the words of Robert William Service should perhaps not be taken at face value, the innumerable ways in which granular materials may affect our daily lives nevertheless suggest that there is a kernel (or, dare I say, grain) of truth in the literal interpretation of the latter lines of his poem. Any system comprising a number of discrete, macroscopic objects may be described as a '*granular material*'. These materials are ubiquitous in the world around us; indeed it is likely that you have encountered at least one granular material already today, whether by eating a bowl of cereal, walking along a gravel path or brushing dust from a surface. In addition to these rather mundane examples, granular materials also play significant roles in multitudinous natural and industrial processes, with direct applications in diverse fields ranging from the highly lucrative pharmaceutical [23] and mining [24] industries to the prediction of avalanches [25], earthquakes [26] and other geophysical phenomena [27], food processing [28], agriculture [29] and even space research [30]. In fact, it is estimated [?, 31] that 10% of the world's energy resources are expended in the handling and processing of granular materials. Unfortunately, estimates also show that these processes are, at best, 50% efficient on average, meaning that more than half of this vast amount of energy is simply wasted. A large part of this inefficiency stems from the fact that we simply do not have an adequate understanding of granular materials. It is this lack of understanding, and the considerable potential rewards of filling the void in our knowledge, which, in part, motivates the continuing research into granular materials.

Perhaps a more noble motivation for the study of granular systems is a simple fascination with the plethora of interesting and often unique behaviours they exhibit. Much like the 'classical', molecular materials with which we are all familiar, granular materials may exist in a solid-like, liquid-like or gaseous state, where each of the 'particles' forming a given solid or fluid are themselves macroscopic, solid objects. For those unfamiliar with granular materials, the idea that a collection of solid objects might behave in such a way may seem very far-fetched. However, let us consider for a moment the behaviour of sand, a granular material with which we are all well acquainted: if we compare the decidedly solid-like structure of a sand castle to the liquid-like flow observed within a sand timer and the chaotic, gas-like dynamics of sand grains in a dust devil, the idea begins (I hope) to seem more reasonable. Despite the dissimilarities between the constituents of classical and granular materials, one may observe in granular systems many behaviours analogous to those of their molecular counterparts, for instance convective motion [32, 33] and surface wave patterns [34–36] in fluidised granulates demonstrating a fluid-like behaviour. Conversely, granular systems may also demonstrate behaviours entirely unobserved in molecular materials. A notable example is that of *granular segregation* [37], whereby a granular liquid or gas containing two or more ‘species’ of unlike particles (differing, for instance, in their size, shape, density or other material properties) will spontaneously separate out such that differing particle species occupy different regions of a given experimental volume. If such a behaviour does not immediately seem surprising to you, consider for a moment what might happen if the same process were able to occur in the mixture of particles of which the air around us is composed! Other phenomena unique to granular materials include a lack of energy equipartition between dissimilar particles in a single system [38], violating the zeroth law of thermodynamics [39], and the spontaneous formation of significant spatial inhomogeneities in the density fields of liquid-like and gaseous systems [40–44]. All of these phenomena will be discussed in greater detail in later sections.

So what causes granular systems to differ so greatly from their classical equivalents? The answer to this question is simple (although its consequences are, unfortunately, not): interactions between grains and their surroundings are *dissipative*, and the ordinary (thermodynamic) temperature has no influence on their behaviour [45].

Let us first consider the lack of temperature-dependence of granular systems, which is relatively straightforward to explain: at room temperature, the magnitude of the thermodynamic temperature, $k_B T$, is of the order 10^{-21} J. Consider now an archetypal granular particle; for the current example we will choose specifically a 1mm diameter glass sphere (the smallest used in the experiments described within this thesis). The typical energy scale associated with such a particle is the work required to raise the particle upwards against the Earth’s gravity, g, by a distance equal to the particle’s diameter, d. The value obtained in this manner, $E_P = mgd = 1.28 \times 10^{-8}$ J (with m the particle’s mass) is approximately 12 orders of magnitude greater than the thermodynamic energy scale, meaning that the latter may be safely neglected in any ordinary set of circumstances. In order to be able to draw comparison between the dynamical behaviours of granular and molecular materials, we define instead a *granular temperature*, $T = \frac{1}{2} m \langle c^2 \rangle$ [46] . Here, c

represents the 'fluctuation velocity' of a particle about its mean value, and '$\langle\rangle$' represents an ensemble average over all particles within a system. Throughout this thesis, the word 'temperature' and the symbol T will, unless otherwise stated, be used to refer to the granular, as opposed to thermodynamic, temperature.

Despite the existence of a granular analogy to temperature, one cannot expect the thermodynamic and hydrodynamic theories developed for classical fluids to hold in the granular case, due largely to the inelastic nature of particulate collisions in granular media mentioned previously. It is this dissipative nature which provides what is possibly the most important distinction between molecular and granular systems: while a thermally isolated *molecular* system will maintain its (thermodynamic) temperature *ad infinitum*, a *granular* system will require a continuous energy input in order to maintain a constant (granular) temperature. If the system's energy source is removed, its temperature will decay through a series of energy-dissipating collisions, eventually reaching a state of zero kinetic energy.

There are various manners in which energy may be provided to a granular system; for instance, energy may be provided simply by gravity [47] (e.g. during hopper flow [48]), through contact with a vibrating surface [49, 50] or by placing the granulate within a rotating container [51, 52]. The dynamics, and related phenomena, produced by each method of energisation are so diverse that each may be considered a 'sub-field' of granular physics (for instance, an expert in vibrated systems may have little insight into the behaviours of rotating systems, and vice versa). Therefore, for the sake of simplicity, brevity and clarity, the work presented here focuses solely on vibrated and vibrofluidised granular systems. The main features and notable behaviours of these systems are introduced in the following section, and discussed in greater detail in Chapter 2.

1.2 Vibrated Granular Systems

The choice to study vibrated systems was taken based largely on two factors: Firstly, vibrated granular systems are, in their most basic form, relatively simple. This simplicity allows the study of granular systems on what is often (somewhat confusingly) termed the 'microscopic scale' - i.e. it is possible to investigate the behaviours of *individual particles* within a larger system, as opposed to simply observing the bulk behaviour of the granulate as a whole. This ability to observe individual particle interactions can be extremely useful in the construction of kinetic-theory-like models of granular systems, for instance. In short, simple, vibrated systems may be highly instructive, providing insights into the fundamental behaviours of granular systems that may then be applied to larger and more complex 'real-world' scenarios [53]. Secondly, the vibration of granular materials has numerous applications, in particular in industrial settings. Thus, work performed in this sub-discipline of granular dynamics is often of direct relevance to 'real-world' problems.

Having established *why* vibrated systems are worth studying, we turn our attention next to *how* vibration can energise and even, with adequately strong oscillatory motion, *fluidise* a granular bed. In the experiments discussed throughout this work, a solid, horizontal, plate which vibrates sinusoidally in the vertical (z) direction is used to 'drive' a system of particles resting above the plate[1]. As the plate oscillates, it will collide with particles, causing a transfer of energy. Since the plate may be considered infinitely massive compared to the particles, kinetic energy will clearly be imparted to those particles with which the plate makes contact[2]. These energised particles will then collide with others within the system, transferring energy through the bed. If the input energy is great enough (i.e. if the frequency, f, and amplitude, A, at which the plate oscillates are adequately large), the bed may become *fluidised*, attaining a state whereby the particles

---

[1] The experimental setup used is described in detail in section 3.1.

[2] Since the motion is sinusoidal, the plate may also, in some instances, *remove* energy from colliding particles. Nonetheless, the net effect of the vibrating base is to input energy to the system.

in the system no longer simply oscillate about fixed points but are free to move relative to one another in a manner similar to that observed in the molecules of a liquid [54]. If the energy input is increased further still, the bed may make the transition to a more dilute, gaseous state [41], whereby particles move relatively rapidly, with a considerable mean free path between collisions.

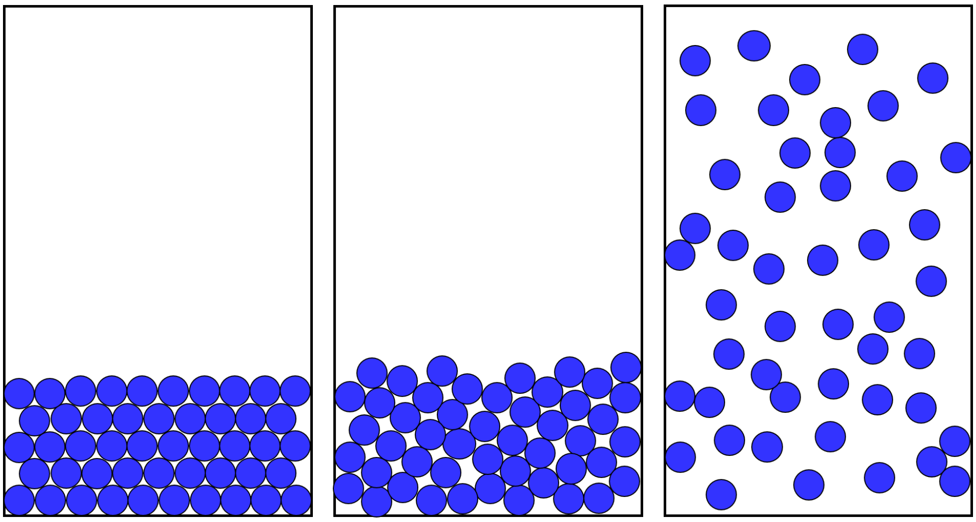

Figure 1.1: Visualisation of a simple, quasi-two-dimensional, vibrated system based on results acquired using the MercuryDPM discrete particle method simulation software (see section 3.3). The images show the system in a weakly-excited, solid-like state (left), a moderately-excited, liquid-like state (centre) and a strongly excited, gaseous state (right). Although the systems discussed throughout this thesis are typically more complex than those represented here in terms of their size and dimensionality, the simplified systems shown nonetheless provide a useful, visual representation of the three major states achievable by a vibrated granulate.

As illustrated in Figure 1.1, the solid-like, liquid-like and gaseous phases of granular matter show a pleasing resemblance to our mental image of the microscopic structure of ‘normal’, molecular solids, liquids and gases. However, the inherent non-uniformity of vibrational excitation combined with the dissipative nature of granular materials leads to the existence of several important behaviours not typically observed in classical fluids.

Consider once again a three-dimensional granular bed which is driven by a single, flat vibrating plate forming the base of the system. Clearly, particles at the bottom of the system, immediately adjacent to the oscillating base, will receive kinetic energy through collisions the plate. These energised particles will then collide with other grains higher up within the system, transferring some of their kinetic energy. This second set of particles will then collide with particles above them, transferring energy still higher within the system, and so on. However, due to the aforementioned inelasticity of such interactions, each set of collisions will result in a fraction of the initial energy being converted to sound and (thermodynamic) heat, where it is effectively 'lost' due to the macroscopic nature of the particles involved [45]. Thus it is that a *temperature gradient* may appear in a granular system - particles near the energising base will become 'hot', possessing high energies and hence large granular temperatures, with this energy gradually being 'damped out' by repeated collisions as the initial impulse travels through the system.

It is interesting to note, however, that the gradients observed are not always monotonically decreasing, as one might intuitively expect; in fact, in many cases, the vertical temperature of a system is observed to initially decrease with height (z) before passing through a minimum and then *increasing* with further increases in z [55–58]. This somewhat counterintuitive 'temperature inversion' may be explained by the presence of gradients in the system's packing density [59, 60] - for strongly excited systems, a system's solids fraction will decrease in a near-exponential [61–63] manner at large heights (see, as an example, Figure 1.2). Thus, despite the fact that the system's *total energy* will decrease monotonically with height, as necessitated by the dissipative nature of the medium, due to the reduced number of particles at large z, the average energy *per particle* may still increase. This behaviour marks a departure from Fourier's law, another of the many interesting distinctions between classical and granular materials. The existence of spontaneous temperature gradients carries several consequences, potentially leading to the onset of convective motion [64], or aiding the separation of particles which differ in their geometric or material properties [65, 66]; these phenomena, which form the main focus of this thesis, and their connection to the inhomogeneous temperatures exhibited by vibrofluidised granular systems will be discussed in detail in subsequent sections.

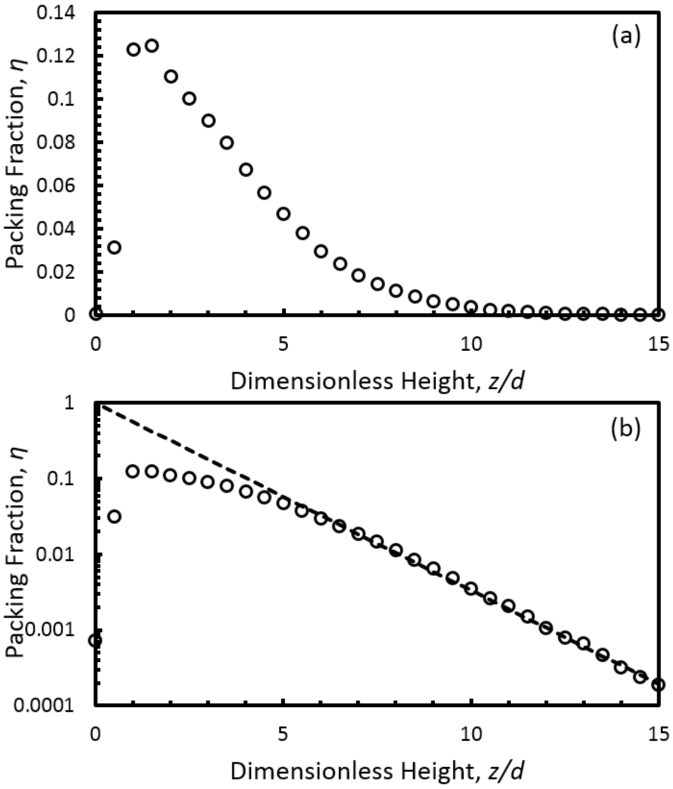

Figure 1.2: Exemplary experimental packing density profile for a single monolayer of 6mm glass particles driven with base acceleration $\Gamma = \frac{4\pi^2 f^2 A}{g} = 17$ (where f and A are, respectively, the frequency and amplitude of vibration), producing a dilute, highly fluidised granular bed plotted on (a) linear and (b) semi-logarithmic axes. The exponential nature of the profile's decay is emphasised in panel (b) through the inclusion of a dotted line representing a 'true' exponential. The images shown correspond to currently unpublished data.

A second noteworthy consequence of the innately dissipative collisions which characterise granular materials is the existence of the *clustering instability* [40], whereby repeated collisions between imperfectly elastic particles lead to localised increases in density. These regions of increased density, known as 'clusters', can affect the behaviour of granular systems in a variety of ways, for instance by altering the observed velocity distributions [67] and even playing a rôle in the '*jamming*' transition of granular systems [68], an important subject which, again, will be more thoroughly addressed in later sections. The manner in which clusters form can be understood as follows: if, in a given region of space within a granular gas, a random fluctuation causes an instantaneous increase in density, this will result in a localised increase in the inter-particle collision rate compared to the rest of the system. While in a molecular system such a fluctuation would be inconsequential, in a granular system (where collisions are inelastic), this increased collision rate will lead to an increased rate of energy dissipation within the high-density region, and hence a reduced temperature. This reduction in temperature will, in turn, create a reduced local pressure, resulting in a migration of particles from the rest of the system towards the region, further increasing the local density and causing the above process to begin anew. Thus, for a freely cooling system, the cluster will grow until it eventually encompasses the entire system, entirely arresting motion. For continuously driven systems, however, the size reached by a cluster will be determined by a balance between the time required for a cluster to form, and the timescale on which these clusters are destroyed by interactions with the system's energy source. For adequately strong driving, systems may be rendered entirely devoid of clusters, allowing the creation of spatially homogeneous systems more reminiscent of classical gases.

Even in the absence of clustering and other spatial inhomogeneities, such as the vertical density profiles arising due to the influence of gravity, vibrated granular systems are *still* found to exhibit behaviours entirely distinct from those of their classical analogues. For instance, granular gases typically exhibit non-Gaussian velocity distributions [69,70], an absence of molecular chaos [71, 72] and temperature anisotropy [73]. However, under the right conditions, it is nonetheless possible to create a granular systems which much more closely mimic their molecular counterparts, as we will see in section 4.1.

A full explanation of the myriad interesting phenomena exhibited by granular solids, liquids and gases would warrant an introductory section longer than most entire PhD theses. Therefore, in the following chapter I focus instead on those phenomena most pertinent to the majority of my research, providing a review of the existing literature and, I hope, a solid background to the new work described in chapters 4 and 5.

2 Overvew of Previous Work

In this chapter, a detailed background of the main phenomena discussed within this manuscript is provided. In the following sections, a summary of the major findings pertaining to the study of granular convection and granular segregation is presented, with reference to the groundbreaking studies which marked each step forward in the field. We begin by discussing the matter of *granular convection*, before moving on to the somewhat more complex issue of *granular segregation.*

2.1 Granular Convection

Of the phenomena discussed within this manuscript, granular convection almost certainly bears the greatest resemblance to the more familiar processes observed within classical fluids. However, as is almost inevitably the case with granular systems, things are slightly more complex than in the classical case. For a start, there are in fact *two main mechanisms* by which convective motion may be induced in a granular system - friction and buoyancy. Although frictionally-driven convection was in fact discovered over a century before buoyancy-driven or 'thermal' convection [74,75], we shall begin by discussing the latter, as it bears a more direct resemblance to the convection observed in molecular fluids.

2.1.1 Buoyancy-Driven Convection

For relatively dilute, strongly driven and hence highly fluidised systems constrained horizontally by fixed, dissipative, vertical walls, one will observe an increased collision rate at these horizontal boundaries which, for reasons similar to those used to explain clustering in the previous section, will lead to a locally increased number density of particles. This cooler, denser region adjacent to the system's sidewalls will, due to buoyancy effects [76–78], 'sink' toward the bottom of the system. Upon reaching the base of the system which, as we recall from previous sections, is in fact the bed's energy source, the descending particles will become energised, and hence rise upward through the centre of the system. This repeated recirculation of particles creates the observed Rayleigh-Bénard-like convection rolls characteristic of wall-induced thermal convection.

Buoyancy-driven convection was first observed in 2001 through the experiments of Wildman *et al.* [75], wherein the dynamics of a three-dimensional, vertically vibrated granular bed were explored using Positron Emission Particle Tracking (PEPT). Their results were later verified by the molecular dynamics simulations of Talbot and Viot [79], who directly demonstrated the importance of sidewall dissipation in determining the presence, strength and direction of thermal convection rolls.

In 2005, Wildman *et al.* [80] provided further insight into the phenomenon of sidewall-enhanced thermal convection through the experimental investigation of an annular system in which the internal and external vertical walls could be independently varied to provide differing degrees of dissipation. It was found that, for the case in which both inner and outer walls were relatively elastic, a single roll would form whose orientation was dependent on the relative dissipation at each wall - the direction of flow would always be downward at the more dissipative wall, as one might expect. For the situation in which wall dissipation was generally higher, however, the formation of a double roll was observed, with particles travelling downwards at each wall and upward in the centre of the channel between them. The study found that the transition from a single- to a double-roll state was also dependent on the number of particles, N, within the system - for fixed driving conditions, an increase in N will result in a greater collision rate, thus providing an additional, indirect manner in which to vary the degree of dissipation within the system.

The 2007 paper of Eshuis *et al.*, *Phase diagram of vertically shaken granular matter* [81], details the various dynamical states exhibited by granular systems possessing differing bed heights and dissipative properties and exposed to varying driving conditions, defining the points at which transitions between these states may be expected to occur. The authors demonstrate that as the dimensionless energy input parameter $S = \frac{4\pi^2 f^2 A^2}{gl}$ (with f and A the frequency and amplitude, respectively, of the base vibrations, l an appropriate length scale corresponding to the particles used, typically taken here as d, the diameter of a spherical particle, and g the gravitational acceleration at the Earth's surface) is increased, a granular system may be observed to progress through a series of different states: for very low excitation (specifically if the acceleration produced by the vibrating base is weaker than that of gravity, i.e. $\Gamma = \frac{4\pi^2 f^2 A}{g} \lesssim 1$), the granular bed will behave simply as a solid, following exactly the motion of the oscillating base plate. As the vibration strength is increased, the bed will begin to 'detach' from the base plate at certain points within the cycle [82, 83], entering either the 'coherent expanded' or 'coherent condensed' state [84, 85] (collectively termed the 'bouncing bed' state) dependent upon the number of particle layers present, and hence the dissipative parameter $\chi = N_L(1 - \varepsilon)$ (where N_L is the number of particle layers and ε the particles' coefficient of restitution) [86]. In these states, the system simply (as the name implies) 'bounces' in synchronisation with the vibrating base, completing one complete 'bounce' for each oscillatory cycle. As the force with which the system is driven increases further still, the bed may then make the transition to one of three differing states, depending again on the depth of the bed, N_L; for small N_L, the bed will be 'vaporised', entering a gaseous phase. For large N_L, the bed undergoes a period-doubling bifurcation and enters a state of 'undulations' [87–89] (alternatively known as 'arches', 'ripples' or '$f/2$ waves'), exhibiting standing wave patterns. For intermediate bed heights, however, the bed is observed to enter a buoyancy-driven convective state. In deeper beds, the convective state may also be achieved by further increasing S, with the bed passing through a density-inverted 'Leidenfrost' state [90] (similar to the eponymous state observed in classical fluids [91]) before becoming susceptible to the convective instability as S is augmented further still. Eshuis *et al.* also discover that the *number* of convection rolls in the system is also sensitive to S - larger S values (i.e. stronger driving) causes a lateral expansion of the convection rolls, naturally leading to a reduction in their number. This finding was later validated using a hydrodynamic model [92].

In the paper *Convection in three-dimensional vibrofluidized granular beds* [93], experimental results acquired using PEPT are compared to hydrodynamic models, demonstrating a reasonable agreement between the two. This study once again provides evidence of the important influence of sidewall dissipation, and also demonstrates an inverse relationship between the rate of convection and the vibrational amplitude with which the system is driven.

2.1.2 Frictionally-Driven Convection

The study of *frictionally-driven* convection has a considerably longer and richer history, perhaps due in part to the fact that it is typically found to occur at comparatively lower vibration strengths, which were more easily accessible to early experimenters. First documented by Faraday in 1831 [74], the phenomenon of granular convection was not the subject of any significant research until a considerable resurgence in interest in the late 20th Century.

Perhaps the first truly quantitative study of granular convection, and the first to relate its origins to frictional effects, was conducted by Laroche *et al.* [94], who posit that convective motion is strongly reliant on fluidisation due to the presence of interstitial air. This idea is directly contradicted by the work of Evesque and Rajchenbach [95] who state that the fluid (or lack thereof) surrounding a granular medium in no way affects the onset of convective motion. These juxtaposed findings may, perhaps, be explained by the considerable differences in system geometry and typical particle size between the two experiments. Evesque and Rajchenbach were the first to successfully demonstrate that the onset of convection was determined by the value $\gamma = \omega^2 A$ (with $\omega = 2\pi f$), now more commonly cited in the literature in its nondimensional form, $\Gamma = \frac{\omega^2 A}{g}$.

The molecular dynamics simulations of Gallas *et al.* [96] showed that there are in fact *several* mechanisms by which granular convection may occur, specifically detailing two particular causes: spatial heterogeneities in the amplitude at which the system is driven, and the presence of frictional lateral boundaries. The former convective mechanism is thought to occur due to the existence of a *resonant frequency* for which convection is maximal, the specific value of this resonance being determined by the dissipative coefficient of the bed's constituent particles. The latter, frictionally driven mechanism may be explained by the fact that during the upward phase of the base's oscillatory motion, the granular bed becomes compressed, exerting a relatively increased pressure on the sidewalls of the system. This pressure creates, in turn, a significant shear force which acts in opposition to the upward motion of the particles. On the downward stroke, however, the bed is able to relax and expand, resulting in a smaller frictional force from the system's side boundaries as the bed descends. The resultant imbalance in the shear force during the upward and downward phases of the base's motion gives a *net downward drag* at the walls of the system. Thus, particles are forced downward at the edges of the container, meaning that a net upflow of particles is necessary in the bed's central region in order to satisfy the law of conservation of mass flow, setting up convective motion within the setting. Gallas *et al.* also make the important observation that the convection rolls observed are independent of initial conditions, showing that convection is not a transient effect.

Ehrics *et al.* [97] pioneered the use of magnetic resonance imaging (MRI) techniques to observe the convective motion of vibrated beds. Unlike previously used optical techniques, the application of MRI allowed the *internal* dynamics of the system to be probed, and hence the shape and depth-dependence of the flow to be detailed for the first time. Their results demonstrated the presence of a thin, rapidly flowing layer near the system's walls, and showed the upward flow rate of the central region to possess an approximately exponential depth-dependence.

Further MRI investigations were conducted by Knight *et al.* [98], this time being combined with visual analysis. An explanation for the depth-dependent flow rate observed in [97] was provided, stating that the fact that particles may join the upward flow at *any height* naturally leads to a flow velocity which increases with height. They also show that the *radial* variation in flow rate exhibits a form which may be fitted either by a hyperbolic cosine or a modified Bessel function. Evidence is also provided for the fact that interstitial air is of negligible effect on convective motion within the system, which is instead dominated by particle-wall interactions, in agreement with previous findings. It is also demonstrated that the geometry of the container is also influential in the form of the convective flow, with container size determining the width of the downward-flowing region of the bed.

Knight's 1997 paper *External boundaries and internal shear bands in granular convection* [99] extends the study of convection to systems with non-vertical walls. Knight demonstrates that as walls are canted outward from the vertical, the average flow velocity is found to decrease until, upon reaching a *critical angle*, the direction of flow is entirely *reversed.* This novel observation of inverse convection is explained by the presence of a 'ratcheting effect' whereby the bed's expansion during free flight leads to particles near the outer edge of the system recolliding with the wall at a *higher point*, creating a net upflow near the container walls. Knight also further explores the rôle of friction within the system, concretely demonstrating that - as expected from previous studies - less frictional sidewalls result in weaker convection currents. Demonstrated also was the fact that, for the case of strong, continuous driving and relatively smooth walls, reversed convection rolls may also be observed in systems with vertical side-boundaries due to another previously unobserved mechanism resulting from the presence of *period-doubling bifurcations* within the system. As discussed above, 'normal' frictionally-driven convection arises due to shear between particles and the system's walls as the bed rises and falls in synchronisation with the vibrating base of the system. For stronger driving, however, the bed particles will no longer lift-off from and return to the system's floor with a single, constant flight time; rather, a cycle of one shorter and one longer flight time will repeat every two oscillatory periods. For the case in which two adjacent regions of the granular bed exhibit differing periodic behaviour, an *internal shear band* may potentially form. If the downward drag experienced by particles at the interface between these two neighbouring regions is greater than that at the system walls, then the sense of the system's convective flow will be inverted. A final significant result arising from this set of experiments is that the direction of flow is observed to be *independent of time* - i.e. it is determined only by the inherent properties of the system. This is a result of considerable importance for studies conducted using PEPT, as will become apparent in section 3.2 of this thesis.

In 2000, Hsiau and Chen [100] used image processing techniques to perform a quantitative analysis of the motion of particles within a vibrofluidised, two-dimensional system. By dividing the computational volume into a series of bins, each of identical width ΔY, the *dimensionless flow rate*, J, could be determined as:

$$J = \frac{\sum |V_y \Delta Y|}{W\sqrt{gd}} \tag{2.1}$$

where W is the container width and d the diameter of a particle. Through use of the parameter J, the dependence of the convective flow rate on various system parameters could be investigated. In particular, it was shown that there exists a power law relation between flow velocity and the peak velocity of the vibrations driving the system. The height of the centre position of convection cells was also found to decrease with increasing velocity amplitude.

Finally, the coexistence of, and competition between, both of the main forms of convection - buoyancy-driven and shear-driven - is discussed by Risso *et al.* [101]. In their study, molecular dynamics (MD) simulations are used to demonstrate that, dependent on the solids fraction of a system, convection may be observed in the absence of friction if particles are inelastic, but also for the converse case of perfectly elastic yet frictional particles. They also demonstrate that thermal convection is not solely dependent upon the coefficients of restitution of particles and their surroundings, but also on their frictional properties; in this instance, friction simply acts as an additional form of dissipation, equivalent to a decreased elastic coefficient.

2.2 Granular Segregation

The segregation and mixing of granular materials has, over the past few decades, received considerable attention from the granular community. This interest is perhaps in part due to the considerable importance of this behaviour to various industrial processes [102–105], but also to the fascinating nature of this phenomenon which is unique to the granular state of matter. Considering the subject matter of this thesis, my discussion of granular segregation will, for the sake of brevity, be limited to that arising due to vertical vibration; however, it is nonetheless worth briefly noting that the separation of differing particle species may also occur in many other situations, for instance in rotated systems [106], chute flows [107] or during discharge from a hopper [108].

As I have previously mentioned, segregation may occur due to differences in various material properties possessed by particles, most notably size [109,110], density [111,112], restitution coefficient [20, 113] or shape [114]. There exist multiple mechanisms underlying the segregative behaviours caused by each of these factors, the dominant mechanism(s) for a given system being determined by various parameters, such as density, temperature distribution or driving strength. Due to the abundance of these potential mechanisms, and their not-inconsiderable complexity, I shall address each relevant segregation-inducing particle property individually.

2.2.1 Size Segregation

We begin by discussing segregation due to differences in the physical size of particles, as this is indisputably the most thoroughly researched and well-understood segregative mechanism observable in vibrated granular systems, having been actively studied since the mid 20^{th} century [115]. Early work demonstrated that large particles rise through a bed of smaller particles for a range of driving frequencies, f, [37] and that the degree of segregation observed increased with driving amplitude, A, [116]. In 1973, experiments by Ahmad and Smalley [109] determined the acceleration, $\Gamma = \frac{4\pi^2 f^2 A}{g}$, to be the most critical variable influencing a system's segregative behaviour, demonstrating also that a larger ratio between particle sizes results in an increased degree of segregation.

It was the 1976 paper by Williams [117] which first proposed the mechanism of '*percolation*', one of the main, widely-accepted causes of size-segregation in vibrated granulates. The process of percolation occurs when a granular bed composed of two or more differing sizes of particle is subjected to some form of disturbance - e.g. through the application of vibration - which causes a rearrangement of particles within the system. Such a rearrangement may lead to the presence of 'gaps' between particles, allowing particles above to fall down, filling the voids created. Clearly, these voids will be preferentially filled by smaller particles, leading to a tendency for small particles to descend and large particles to ascend through the system. Of course, such a mechanism can only be expected to apply for the case in which the volumes of the voids are comparable to or smaller the size of the larger particle species, i.e. for relatively dense systems and/or relatively large disparities in particle size.

Monte Carlo simulations by Rosato *et al* [110, 118] further elucidated the influence of void-filling mechanisms on the upward motion of large particles through a system of smaller particles, and hence the corresponding segregation of bidisperse-by-size systems. They explain their findings in terms of the relative probability of a large particle moving upward or downward; as a granulate is vibrated, voids will naturally occur within the system. Since any void is more likely to be filled by a relatively small particle, larger grains will clearly tend to migrate upwards as they are 'pushed' from below by the small particles which will preferentially fill any small voids created beneath them. In order for a large particle to move *downwards*, one must rely upon the relatively improbable formation of a void large enough to accommodate the large particle's volume. Hence, a larger particle's net motion will be upward through the system. It was this work by Rosato *et al.* which coined the term 'Brazil Nut Effect' (BNE) to describe this phenomenon, referencing the fact that one often observes, in a container of mixed nuts, that the (larger) brazil nuts are predominantly found at the top of this particular type of granular bed, likely due to the processes described above.

In 1993, *Knight et al.* [119] were the first to propose a direct link between convective motion and size-segregation. They suggest a mechanism whereby both large and small particles are transported upward through a convective system at an equal rate, yet larger particles, upon reaching the top of the system, become 'trapped', as they are unable to re-enter the relatively thin downward stream of the convective flow. Since this segregation mechanism clearly relies on the fact that the large particles in the system are of greater diameter than the width of the downward-flowing convective stream, this places certain limitations on the range of applicability for this theory – i.e. the size ratio between particles must be adequately great, and downward-flowing region adequately narrow as to prevent the re-entrainment of the larger particle species. Studies of wider systems [120], where the width of the downward stream of convection rolls is correspondingly increased, the breakdown of this theory is indeed observed; in such situations, convection can in fact be observed to *enhance mixing*, i.e. reduce segregation [121]. Nonetheless, in situations where system parameters are adequate to produce the above-mentioned convection-related size-separation, the rate at which segregation occurs is typically considerably faster than for cases in which convection is absent [122, 123].

The 2001 paper *Reverse Brazil Nut Problem: Competition between Percolation and Condensation* [124] proposes another new mechanism, termed '*condensation*', capable of explaining the tendency of particle mixtures to segregate. Their hypothesis draws on the findings of earlier works in monodisperse systems [125, 126] wherein it is shown that, within such a system, there exists a *critical temperature*, T_c, below which a fully-fluidised system will begin to exhibit regions of solid-like behaviour near the base of the system, the degree of solidification increasing as the system's temperature further decreases below T_c – a process termed condensation. It is suggested that, for a binary system, if the two particulate components possess different critical temperatures, and the temperature of the system as a whole lies between these two values, one particle species will begin to condense and hence migrate toward the bottom of the system while the other remains fluidised, leading to segregation. The title of this article stems from the fact that the mechanism described may, in some instances, lead *larger* particles (representing the Brazil nuts in our hypothetical bag of mixed nuts) to *sink downwards* through the system as opposed to rising upwards as would be expected from the earlier work of Rosato and his colleagues.

Work by Sanders *et al.* investigates the possibility of an attractive force between intruders in a granular bed. Their initial, simulational investigation [127] concerns the idealised situation in which a system of inelastic but frictionless particles is exposed to vertical vibration, allowing the situation to be assessed on a fundamental level. Their results show that large, neutrally buoyant particles immersed in a fluidised system of smaller particles experience an attractive force towards one another, leading to a novel, horizontal segregation. They explain the observed effective attraction by an asymmetry in the repulsion of large particles during the upward stroke of vibrations and the attractive force arising from the greater number of 'host particles' external to, as opposed to in between, the intruders during recollision with the system's base. This attractive force is found to persist in experimental situations, when additional microscopic system properties, such as friction, are reintroduced [128]. Moreover it is found, both in experiment and simulation [129, 130], that by varying the properties of the waveform used to drive the system, the strength of the attractive force between particles may be altered, or even reversed – i.e. a weak repulsion between large intruders may be produced.

For more dilute systems, there exist still more mechanisms by which segregation may occur; perhaps the most relevant mechanism to such systems is that of *thermal diffusion*, whereby the presence of a temperature gradient in a granular mixture will produce relative motion between differing species along the direction of the gradient. In these dilute systems where simple, binary particle collisions can be assumed, several attempts have been made to explain the segregation observed in such systems using kinetic theory. The first study to employ these kinetic theory techniques was performed by Hunt and Hsiau [131], who demonstrated that for a system exhibiting a spatial variation in temperature, large particles will migrate towards regions of low temperature and small particles towards regions of high temperature. However, much like the work of Luding and Hong [124], their theory was developed under the assumption of energy equipartition between differing species. In subsequent works [10, 132], however, this assumption was shown to be rather dubious – in reality, systems comprising multiple species will typically exhibit non-equipartition, with heavier and/or larger particles generally possessing higher temperatures.

While Garzó and Dufty [133] successfully developed a hydrodynamic theory for binary systems capable of accounting for the effects of energy nonequipartition, the first attempt to directly apply such a model to the issue of segregation was made by Galvin *et al.* [134]. In their paper, it is demonstrated that the presence of non-equipartition results in the existence of additional components of the forces known to drive segregation. As with the case of equipartition, these segregative forces are related to diffusive behaviour arising due to the presence of temperature gradients.

Further work by Garzó [135] provides an explicit expression for the *thermal diffusion factor*, a parameter which characterises the steady-state segregation observed parallel to a temperature gradient by determining the point at which the species separation caused by thermal diffusion will be balanced by the 'normal' diffusion which acts to oppose this segregative behaviour. Work by Brey *et al.* [136], meanwhile, provides a parameter $\phi = \frac{m_S T_L}{m_L T_S}$ which may be used to predict the direction of segregation. Here m_χ is the mass of a single particle of species χ and T_χ the average granular temperature for this species.

In summary, the degree of size-segregation exhibited by a given granular system is likely to be determined by a combination of the above factors, the dominant mechanism(s) being decided by the bed's state – in particular its density and temperature, and the distributions thereof – which in turn are dependent on factors such as the strength with which the bed is driven, its size, and its material properties. Despite considerable efforts to establish how the relevant mechanisms will compete in a given situation [137–139], and hence what the expected direction and degree of segregation may be, the subject still remains far from fully understood.

2.2.2 Density Segregation

We discuss next the matter of density-driven segregation, almost certainly the second most thoroughly investigated segregative mechanism, and one of the major foci of this thesis. Like size segregation, the phenomenon has been known to the scientific community for several decades, although the volume of research produced within this time is comparatively diminutive.

It was noted in 1973 by Ahmad and Smalley [109] that for the case of vertically vibrated systems in which particles differ both in size and density, an increase in the material density of a larger particle led to a slower ascent and a correspondingly reduced final degree of segregation, with the inverse being true for a decrease in density. Such a finding is perhaps predictable based on our knowledge of simple buoyancy in molecular fluids, whereby one would indeed expect a light object to rise more quickly through a dense medium than a similar but comparatively heavier object.

Somewhat more surprisingly, work by Shinbrot and Muzzio [140, 141] demonstrates that, under certain conditions, systems may in fact exhibit an *inverse buoyancy*, whereby large but heavy 'intruder' particles may rise towards the top of a granular mixture while similarly large, light particles are observed to sink! They propose an explanation for their findings based on the greater inertia possessed by heavier particles – for deep beds excited with large amplitudes, a given particle will, on the 'up-stroke' of the oscillatory motion, be launched upward. Particles with greater inertia (i.e. heavier particles) are more likely to penetrate further upward through the bed, creating a wake which will be filled by lighter particles, much like the percolation mechanism described previously, leading this heavier particle to, over a series of vibration cycles, rise through the system. The paper does not, however, provide an explanation for the inverse case, where large, light particles are found to sink. This reverse buoyancy was later shown to occur also in systems outside the tracer limit, i.e. with multiple particles of each species [124, 142].

In 2004, it was shown by Huerta and Ruiz-Suárez [138] that while in the limit of low-frequency driving ($f = \mathcal{O}(1)$ Hz) one may observe, dependent on the system details [143–145] either the Brazil Nut Effect (whereby larger particles rise) *or* the more counter-intuitive Reverse Brazil Nut Effect (whereby large particles *sink*), only the former of these is observed for higher driving frequencies. It is this high-frequency regime which forms the main focus of this thesis.

Under the condition of high-frequency vibration and randomised (i.e. non-convective), fluid-like motion in the absence of strong temperature gradients, the segregative behaviour observed in granular systems in fact emulates very closely the situation of classical, Archimedean buoyancy [146]. Indeed, the research of Huerta *et al.* demonstrates that, for systems obeying the aforementioned constraints, the linear relation between buoyancy forces and object volume expected from Archimedes' principle is closely observed. It is also shown that an increase in the energy with which the bed is excited leads to an augmented buoyancy force. In addition to this simple buoyancy force, research by Trujillo *et al.* [147] shows that systems may experience an additional, *pseudothermal* buoyancy force due to the presence of differing granular temperatures between species.

If the constraint of a homogeneous temperature distribution is relaxed, we must once again consider the presence of segregation due to thermal diffusion [131,133–136], which affects systems which are bidisperse-by-density as well as those which are bidisperse-by-size, as discussed previously. The condensation mechanism of Hong, Quinn and Luding [124] described in the previous section is also dependent not only on the size of particles, but additionally their mass (and hence density). Specifically, the ratio between particles' critical temperatures, T_c, is predicted to follow the relation:

$$\frac{T_c(A)}{T_c(B)} = \frac{m_A d_A}{m_B d_B} \tag{2.2}$$

where $T_c(\chi)$ is the critical temperature of a species χ, with m_χ the mass and d_χ the diameter of this particular particle type.

In addition to the studies discussed above, which deal with systems where both the density *and size* of particles are varied, a number of works exist in which the effects of density are more effectively isolated (although, as will become apparent in the following section, effects due to particle elasticity may still be present).

Shi *et al.* [148] investigate binary beds of monosized, spherical particles, observing a generally incomplete segregation in the vertical direction (i.e. that parallel to the direction of excitation) with, as one might expect, the lighter particles dominating the upper regions of the system. They find that the degree of segregation exhibited varies linearly with the ratio of particle densities used, with complete segregation being observed for ratios $\frac{\rho_H}{\rho_L} \gtrsim 4$ (where ρ_H and ρ_L are, respectively, the densities of the heavy and light particles comprising a given system). They also find particle elasticity to play a negligible rôle in the observed segregative processes.

For the case in which convective motion is also present, thus introducing horizontal, as well as vertical, inhomogeneity to the systems under investigation, the situation becomes still more complex. Unlike for the case of size segregation, particles differing only in their mass will both be equally likely to become entrained in the thin, downward-flowing convective streams near the walls of convective systems, eliminating the relatively simple segregation mechanism proposed by Knight *et al.* [119]. In such monosized system, convective motion is found, dependent on the systems under investigation, to promote both the mixing *and* separation of differently massive particle species.

Work by Yang [112] suggests that, for a range of driving parameters and bed heights, the presence of convection consistently leads to the acquisition of a well-mixed final state; the variation of the system's control parameters is found to affect only the *rate* of mixing, which is observed to occur more rapidly for shallower and/or more strongly excited beds.

Conversely, work by Tai *et al.* [149] finds that heavier particles tend to migrate toward the centres of convection rolls, resulting in segregation patterns more complex than the relatively simple cases discussed previously, where segregation occurs predominantly in the vertical direction. Although the authors do not suggest a specific mechanism underlying the segregation patterns detailed, they note that they believe the granular temperature to play a significant rôle in their observations.

Work by Burtally *et al.* [150,151] explores the behaviour of fine ($d \sim 100\mu$m) particles, whose behaviour is, due to their small sizes, considerably influenced by effects arising due to interstitial air – unlike the previous studies mentioned, where the large particle sizes and masses render air effects negligible. Their work provides insight into the rôle of air effects, but also convective motion within granular systems, demonstrating that in vacuum, where significant convective flow is present throughout the experimental system, the granulate under investigation acquires a well-mixed final state. In the presence of interstitial air, however, the system's segregative behaviour is markedly different, not only to the mixed state exhibited by the systems under vacuum conditions, but also to any of the situations previously described. Specifically, a sharply defined, mobile layer of consisting almost entirely of heavier (brass) particles is found to exist either on top of a layer of lighter (glass) particles, or 'sandwiched' in between two such layers. Their unusual observations are thought to be due to the fact that the viscous damping caused by air in the system will more strongly retard the motion of glass particles than (denser) brass particles, allowing this latter particle species to be, on average, more kinetically active. The increased dynamics of the brass particles lead to a greater dilation in brass-rich regions, which will act to 'draw in' particles. Since the brass particles in the system are more active, a higher proportion of such particles will migrate towards the already brass-rich region, while glass-rich regions become extremely densely packed, and hence hard for the brass particles to enter, leading eventually to the observed segregation. The findings of Burtally *et al.* were later reproduced simulationally by Zeilstra *et al.* [105,152].

In 2010, work by Lim [153] explored the influence of the vibrating base used to drive a system on both its segregative behaviours and its dynamical state. The introduction of a 'bumpy' base, as it is termed by the author, is found to have little effect on the segregation of a bidisperse-by-density system for the case of vertical oscillations, despite altering other system properties, such as temperature anisotropy. This seems somewhat contradictory to the experimental findings of Liao et al., who suggest that the segregation rate of a binary granular system shows a strong dependence on the 'bumpiness' of a system's base. However, Liao *et al.* [154] attribute the influence of their base roughness to a decrease in the energy transfer from their vibrating base to the bed of particles under investigation – in other words, the use of an increasingly bumpy base at fixed vibrational parameters strength is effectively equivalent to a reduction in driving strength, which would, as well known from previous studies, affect the rate of segregation within a system. Thus, it is possible that the discrepancy between these two articles may, perhaps, be explained by the fact that the reduction in energy input noted by the experimental work of Liao et al. may have been less pronounced, or indeed entirely absent, from the simulational work of Lim. Both papers seem to agree, however, that the base topography itself has little *direct* impact on the segregative behaviours of granulates exposed to excitation from such a base.

Recent work by Rivas et al. [155–157] concerns the situation of a shallow, quasi-two-dimensional system of monosized particles, wherein vertical vibration causes segregation in the horizontal plane. The researchers detail an unusual, cyclic segregation: starting with an initially well-mixed system, a number of small, dense clusters of relatively heavy particles will rapidly appear when the system is exposed to vibration. This clusterisation arises due to energy non-equipartition within the system, which leads the lighter particles to exert a greater pressure than the heavier particles, thus inducing the observed separation of the differing species. The dense masses of heavy particles formed are then observed to coalesce, tending towards the formation of a single, large cluster at the horizontal centre of the system, albeit with some ‘inclusions’ of lower-density particles. As this agglomeration of heavy particles progresses, the cluster begins to move as a single, solid body, with the majority of its kinetic energy in the vertical component. Once the system has reached a critical degree of clusterisation/segregation, a collision between a heavy particle which forms part of a cluster and an energetic, light particle may cause the high vertical energy of the heavier grain to be transferred to the lateral directions. This particle may then collide with a neighbouring sphere within the cluster, causing a similar conversion of vertical to horizontal motion, leading to a ‘chain reaction’ of such collisions, the end result of which is a disintegration of the cluster (i.e. an abrupt ‘re-mixing’ of the bed) and a considerable spike in the horizontal energy of the system. Such an occurrence is termed a sudden chain energy transfer event. Such events are observed to occur for a wide range of system parameters, showing this to be a robust phenomenon. It will be shown later in this thesis (see section 4.1) that similar phenomena may even occur for fully three-dimensional systems [15].

2.2.3 Inelasticity-Induced Segregation

Although long known to exert a significant influence on the dynamics of particulate systems [158] and, indeed, their segregative behaviours [37], the effect of particle elasticity on the mixing and separation of granular mixtures has only recently received any significant attention from the granular community.

The first paper to directly address the effects of particle inelasticity on the segregation of granular systems was published in 2006 by Serero *et al.* [113], whose hydrodynamic theory predicts the existence of a form of segregation arising solely due to differences in particles' dissipative properties. Their model suggests that when equally massive, equally-sized particles which differ only in their coefficients of restitution, ε, are exposed to a temperature gradient, the less elastic species will tend to migrate towards regions of lower temperature.

Further evidence of the existence of a purely inelasticity-related segregation mechanism was provided by the simulations of Brito *et al.* [19] who, based on their observations, propose a novel physical mechanism capable of explaining dissipation-driven segregation. Their hypothesis states that relatively inelastic particles, whose species is denoted 'B', will, when forming part of a binary system alongside more elastic 'A' particles, develop a region of increased packing density in their immediate vicinity. The 'excess mass' surrounding particles of species A relative to species B is defined as:

$$\delta m = \int_{d}^{\infty} dr 2\pi r \left[\rho_B(r) - \rho_A(r)\right] \tag{2.3}$$

with $\rho_\chi(r)$ the total particle density surrounding a particle of species χ with diameter *d*. In addition to the effectively increased mass of less-elastic particles, Brito *et al.* also observe a localised decrease in temperature. The authors refer to the low-temperature, high-density region encompassing dissipative particles as a ‘cold droplet’. The combination of the relatively high mass and low temperature possessed by these cold droplets will, clearly, cause them to sink through the system, thus leading to the inelasticity-induced segregation predicted by Serero and his colleagues. The mechanistic theory presented by Brito *et al.*, although simple, forms the cornerstone of much of the new work relating to inelasticity-driven segregation presented within this thesis.

The horizontal segregative clustering mechanism investigated by Sanders et al. and Lui et al. [127–130] and described earlier in this chapter is also found to be strongly dependent on the relative elasticity of particles [159]. As previously noted by Brito *et al.*, dissipative particles may modify the local density and kinetic energy of neighbouring particles; Lui *et al.* here show that this local modification may also, for large, relatively elastic particles, result in a local reduction in density and increase in energy, an effect which is enhanced when two intruder particles are found in close proximity. Since the attractive force between intruder particles is reliant on an increased energy possessed by host particles in the immediate vicinity of intruders, this force can be reduced, and indeed its polarity reversed, through a reduction in the coefficient of restitution, ε, of the intruder species. The rôle of particle dissipation in this manner of segregation is further explored through the simulations of Yan *et al.* [160], who provide strong evidence that ε is in fact a key determining factor in the degree of clustering, and hence species-separation, observed.

In 2009, Brito and Soto [20] went on to discuss the interplay between their recently noted inelasticity segregation and other, competing separation mechanisms. In this paper it is shown that, dependent on the parameters of the systems under investigation, the inelasticity-induced segregative mechanism can successfully compete with – and even dominate – both buoyancy-driven segregation and the Brazil nut effect. In other words, both size- and density-segregation can, under the right set of circumstances, be overcome by the often overlooked inelasticity-segregation. This is an important result, as it calls into question the findings of numerous previous works on the topic of segregation – in particular experimental studies, where ε cannot easily be individually controlled – wherein only particle mass and diameter are considered.

Further work by Serero *et al.* [161] extends the theory of [113] to allow for a greater range of particle elasticities, providing also a detailed analysis of the influence of gravity in vertically vibrated systems. Their results for dilute systems agree well with the findings of Brito *et al.* [19], with more dissipative particles tending towards the container's lower region. Serero *et al.* additionally show [162] that even if two particulate species forming a granular bed share an identical size, mass and average coefficient of restitution, if the *distribution* of ε values varies between species, the system may be subject to a "*stochasticity-induced*" segregation. Specifically, it is observed that particles whose ε values during repeated collisions demonstrate a higher standard deviation will be found to concentrate in higher-temperature regions.

The existing literature shows a marked lack of experimental research directly concerning the matter of inelasticity-related segregation, most likely due to the difficulty of effectively isolating ε – in experiment, it is, for obvious reasons, extremely challenging to vary the elastic properties of a particle without simultaneously altering either its other material properties or its geometry. One of the major foci of this thesis is to remedy this issue, providing a much-needed experimental comparison for the theoretical and simulational studies detailed above.

2.2.4 Geometrically-Induced (Shape) Segregation

Despite the fact that, as with the previously discussed segregation mechanisms, the geometry of particles has long been known to affect their segregative properties [163], our understanding of shape-related demixing remains startlingly limited. There are, arguably, two main contributing factors to this dearth of knowledge; the first is the fact that simulational models of non-spherical particles are notoriously complex and computationally expensive. The second is the ill-defined meaning of the word 'shape'. This term in fact incorporates a number of properties possessed by an object, each of which may individually affect the dynamical and segregative behaviours exhibited by a granular system; examples include particles' angularity [164], elongation [165], maximal solids fraction or packing density [166], surface area and aspect ratio [167] and nonconvexity [168], to name but a few. Thus, it is hard to directly quantify 'shape' as a whole, and hence correspondingly difficult to design and conduct a systematic, experimental study of this multifaceted parameter. Instead, one can only analyse and attempt to understand the individual components which comprise a particle's shape one by one in the hopes of, eventually, building up a complete picture. This, in itself, is no mean feat, as a variation in grain geometry will, in the vast majority of cases, result in the alteration of multiple particle properties. Although the field of granular dynamics is, seemingly, only just beginning this process, the advent of new and more powerful simulational techniques makes this eventual aim seem an increasingly feasible prospect.

In 2003, Abreu *et al.* [166], through a series of Monte Carlo simulations, performed what is arguably the first true systematic study of segregation due to particle geometry in a vibrated system. Although research concerning shape effects on the segregation of granular systems had been performed previously [169], these early studies did not adequately separate particle shape and size (or, rather, volume), making a definitive analyses of effects due solely to geometry near impossible. Abreu *et al.*, however, rigorously maintain the volume, and hence mass, of their simulated particles, varying only the elongation, and therefore aspect ratio, $\mathcal{A}$, of the spherocylindrical grains modelled. While the results presented show no evidence of a simple, direct relationship between the elongation of a particle and its segregative properties, the porosity (i.e. solids fraction) of a particle species, which is shown to be dependent on $\mathcal{A}$, seemingly plays a clear and definite rôle. Specifically, particle species whose geometry allows them to achieve a greater packing density at a given set of vibrational parameters will tend to segregate towards the base of the system; the greater the disparity in porosity, the greater the observed rate of segregation.

Experimental work by LaMarche *et al.* [170] demonstrates a form of segregation mediated by *entropic ordering* [171]. In their paper, they draw parallels between the granular system under investigation and the solvents and solutes of classical, molecular and colloidal systems, with a bed of small, spherical grains acting as the solvent while a number of flat, hexagonal plate-like particles provide an analogue for the solute. Through variation of the frequency, f, and acceleration, Γ, with which the system is driven, as well as the volume fraction, φ, of spheres, the authors observe three distinct segregation patterns in addition to a well-mixed state. Specifically, the bed demonstrates a state in which the hexagonal plates form a close, hexagonal packing, a state in which multiple, stacked columns of these plates are formed (reminiscent of the 'discotic' state observed in colloidal systems [172]) and a state in which the disc-like particles simply segregate towards the centre of the system in a disordered manner. The existence of these ordered states, which exist within well-defined regions of $\Gamma - \varphi$ phase space presents a striking parallel to the behaviours of colloidal systems, suggesting that a thermodynamic framework for granular materials may be within the realms of possibility.

Work by Caulkin, Jia *et al.* uses a simple geometrical algorithm to predict the packing [173] and segregative [174] properties of granular materials varying in the shapes and sizes of their constituents. They propose that the rate of segregation exhibited by a system (and indeed its existence) is primarily determined by the mobility between particles of differing properties, with only an indirect dependence on the precise physical mechanism causing these relative motions. They note specifically that smaller particles in a binary system are, in effect, *more mobile* than larger particles due to their reduced collision probability, and suggest that it is this increased mobility which creates segregation; the qualitative agreement observed between their experimental results and their simulations provides a degree of support for their hypothesis. The authors posit that the same should apply to particles of differing shape, even if their volumes are held equal, due to differences in their surface/projection area – a long, thin particle, for instance, may possess a greater ability to navigate through small gaps within a system than a more equally-dimensioned particle such as a sphere or cube. It is worth noting, however, that the results presented consider only the case of relatively dense, non-fluidised beds excited by a series of discrete taps as opposed to continuous driving – a very different situation to that which forms the main area of interest of this thesis.

Unlike the majority of studies regarding geometrically-induced segregation, Monte Carlo simulations by Roskilly *et al.* [175] consider not only the case of relatively dense systems, but also that of more strongly excited and hence dilute systems. Their findings for relatively closely-packed regimes agree well with the findings of Abreu *et al.* [166], the results obtained being consistent with the idea that particle species possessing more porous packings will segregate upward through a given system, provided that the material densities and volumes of all particles are equal. For lower-density beds, however, Roskilly et al. hypothesise that a different mechanism plays the determining rôle in the segregation experienced by systems of differingly-shaped particles. Specifically, they suggest that the segregative behaviours of more dilute systems are predominantly dependent on differences in the "*effective size*" of particles. This quantity is taken as the radius of gyration, r_g, possessed by a particle or, more accurately, the average value of r_g taken across its three major axes of rotation. The radius of gyration may, in turn, be determined from the moment of inertia, I, of a particle as $r_g = \sqrt{\frac{I}{m}}$, where m is the mass of a single grain. They observe that, in a manner analogous to the relatively simple case of size segregation, higher-r_g particles will tend to segregate towards the top surface of a vibrated system, with the inverse being true for particles possessing smaller "effective sizes". In section 5.4 of this thesis, we put this finding to the test in an experimental situation.

3 Methodology

In this chapter, we begin by discussing the details of the experimental systems explored within this thesis, including the methods used to create our vibrofluidised beds, and introduce the main parameters which may determine the behaviours of the resultant dynamical system (section 3.1). We then detail, in section 3.2, the means through which the movement of a single particle through such a bed may be tracked (section 3.2.1), and how this single-particle motion may be used to infer whole-field behaviours pertaining to the system in its entirety (section 3.2.2). Finally, in section 3.3, we describe the manner in which the experimental system is recreated using discrete particle method simulations.

3.1 Experimental Setup

The basic experimental setup, common to the majority of the individual experimental studies which make up this thesis, is as follows: a cuboidal container with fixed, rigid walls is affixed to the top of an LDS V721 electrodynamic shaker, such that it may be vibrated sinusoidally in the vertical direction. The container's horizontal dimensions are, in all cases, equal, i.e. $L_x = L_y$, creating a degree of symmetry within the system and thus simplifying analysis. The vertical dimension, L_z, meanwhile, is chosen, for all systems used, to be adequately large that collisions between particles and the container's upper boundary are statistically improbable, allowing us to consider the granular beds explored as 'open' systems. Within the container is housed a bed of N particles. As the system is vibrated, these particles are energised by collisions with the system's base. Using different combinations of $L_{x,y}$ and N, it is possible to analyse systems of varying resting depth or 'layer number' (N_L), and aspect ratio ($\mathcal{A} = \frac{N_L}{L_{x,y}/d}$), and hence study the differing behaviours exhibited by systems under these various conditions.

While the material of the sidewalls bounding the system in the horizontal direction is varied throughout the experiments performed, the base of the system is, in all instances, composed of stainless steel. The use of a steel base acts to reduce the influence of triboelectric effects within the system [148], which may otherwise alter the dynamics observed in an undesirable manner. The large particle sizes generally used (typically, beds comprising spherical particles of diameter $d \geq 3$ mm are investigated) also aid in the reduction of the influence of static charge on the system, whilst also allowing additional effects due to interstitial air to be safely neglected [105]. The suppression of interstitial air and triboelectric effects is highly beneficial to the experiments performed, as it allows us to more precisely isolate the effects of the parameters under investigation.

Since the main focus of this thesis is on the *steady-state* behaviour of vibrated granulates, the frequency, f, and amplitude, A, at which systems are driven are, unless specifically stated otherwise, held constant throughout each individual experimental data set. Across data sets, however, a wide range of driving parameters frequencies and amplitudes, and hence a wide range of dimensionless driving accelerations, $\Gamma = \frac{4\pi^2 f^2 A}{g}$, and dimensionless shaking strengths, $S = \frac{4\pi^2 f^2 A^2}{dg}$ (with g the acceleration due to gravity), are explored. This allows the investigation of a wide range of system states and hence a number of differing dynamical behaviours. Further details relating to the steady-state nature of the system may be found below in section 3.2.2. Feedback from an accelerometer attached to the base of the vibrating system is used to maintain a constant, and accurate, driving frequency and amplitude. Through the use of this feedback loop, the dimensionless peak acceleration produced by our shaker varies by, at most, ±0.005, an error of less than 1% for all driving strengths used throughout this thesis.

A range of differing particle properties are also explored throughout the work which forms this thesis. Particles with differing sizes, densities (ρ), elastic properties (ε) and frictional properties (μ) are utilised in experiment, as are various binary and ternary combinations of differing particle types. Unless otherwise stated, however, the particles used can be assumed uniformly spherical in all cases.

3.2 Positron Emission Particle Tracking (PEPT)

3.2.1 The Physics of PEPT and its Application to Granular Systems

Positron emission particle tracking is a technique, developed at the University of Birmingham, which allows the position of a single[1], radioactive particle which emits pairs of back-to-back γ-rays (i.e. γ photons whose trajectories are separated by $180° \pm 0.5°$) to be tracked in three-dimensional space.

In order to extract data from a given system using PEPT, one requires an appropriate detector (in our case an ADAC *Forte* dual-headed gamma camera - see Fig. 3.1) and a tracer particle 'labelled' with a β^+-emitting radioisotope. When investigating granular media, the tracer particle is typically chosen to be physically identical to all other particles within the system, such that its dynamical behaviour may be considered representative of that of all other particles in the system; the importance of this matter will become apparent later in this section.

Positron emission is a subtype of β-decay which occurs when a particular atom is unstable due to a proton-rich nucleus. In order to achieve increased stability, a proton (p) is converted into a neutron (n), accompanied by the release of a positron (β^+) and an electron neutrino (ν_e), resulting in a net decrease in the nucleus' proton number relative to the number of neutrons, as required.

---

[1] PEPT can, in fact, also be used to track multiple particles; however, since the inclusion of additional tracers acts to reduce the spatial resolution of the data acquired, only single tracers are utilised for the experiments performed as part of the work presented here. The interested reader may find further information regarding the use of PEPT to track multiple particles in our references [176–179].

Figure 3.1: The modified dual-headed positron camera used to acquire PEPT data.

β^+ activity can be induced in the chosen tracer particle via one of two main methods: direct activation, or indirect activation. In order to achieve *direct* activation, a grain is irradiated by a high-energy charged particle beam from the University's cyclotron, such that interactions between the beam and atoms within the tracer material produce a suitable β^+ emitting isotope. The two such reactions most commonly used in the work discussed here are the conversion of oxygen atoms within glass particles to Fluorine-18 and the conversion of iron atoms within steel particles to Cobalt-55. In the former, a Helium-3 beam produces the relevant positron emitting isotope, ^{18}F, through the reactions:

$$^{16}\mathrm{O}(^{3}\mathrm{He},\mathrm{p})^{18}\mathrm{F} \tag{3.1}$$

and:

$$^{16}\mathrm{O}(^{3}\mathrm{He},\mathrm{n})^{18}\mathrm{Ne} \rightarrow^{18}\mathrm{F} \tag{3.2}$$

In the latter, a proton beam induces β^+ activity as follows:

$$^{56}\mathrm{Fe}(\mathrm{p}, 2\mathrm{n})^{55}\mathrm{Co} \tag{3.3}$$

Of course, these are only two examples of the materials in which the desired β^+ activity may be produced. In general, the only qualifiers which determine whether or not a given particle may be labelled via direct activation are a) whether the material in question possesses an element which may be successfully converted to a positron emitter and b) whether this material can withstand the high temperatures experienced during the irradiation process. In reality, the determining factor tends to be this latter criterion, as the majority of commonly available materials contain at least one element suitable for conversion to a β^+-emitting isotope.

For cases in which direct activation is not possible, or is otherwise undesirable, particles may instead be labelled via indirect methods. In this case, the typical procedure is to produce a dilute solution of ^{18}F, through the activation of the oxygen molecules of the H_2O as described in equations 3.1 and 3.2, which can then be adsorbed onto the surface of particles [180–182]. Although tracers of almost any material may be created using this method, it carries one distinct disadvantage as compared to direct activation, namely that the activity may be largely limited to an adhered layer on the tracer particle's surface. Thus, particularly in highly frictional systems, it is possible that the active material may become spread throughout the system, limiting the accuracy with which the particle motion may be tracked for reasons which will become apparent later in this section. Such issues can, however, be largely avoided through careful experimental procedure.

Once a tracer has been created, its motion may then be tracked and recorded; the emitted positrons will rapidly annihilate with electrons in the surrounding medium of the tracer, typically on a timescale $\mathcal{O}(100)$ picoseconds. The annihilation of these particle-antiparticle couples results in the emission of a pair of 511 keV γ-rays, whose trajectories

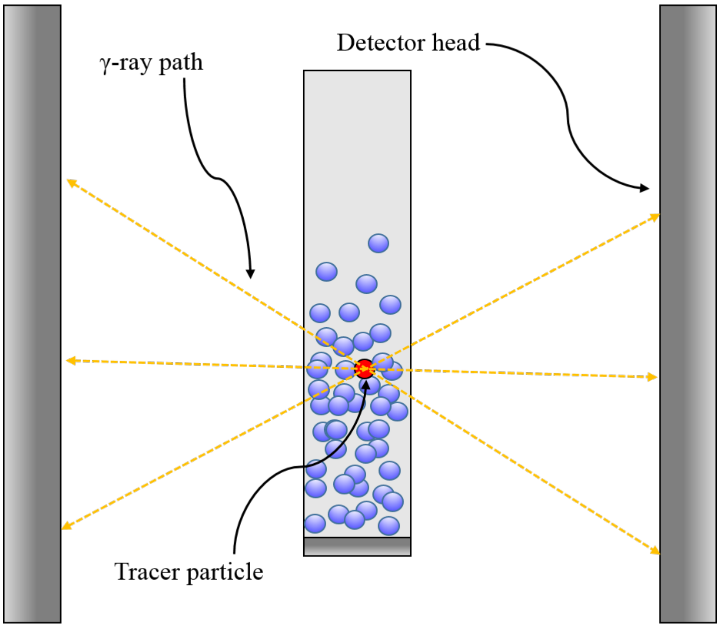

Figure 3.2: Schematic diagram illustrating the triangulation of a tracer particle's spatial position (not to scale). For clarity, the tracer particle is here highlighted in red, although in reality the tracers used are both visually and physically identical to all others in the system. Since the trajectories taken by γ rays produced via electron-positron annihilation events are known to be effectively collinear, if a pair of γ photons are detected by the camera's opposing detectors within a predefined 'resolving time', the path between the two detection events can be recreated. The point of intersection of multiple such γ-ray paths can, as illustrated, be used to determine the spatial position of the tracer particle.

are separated by $180° \pm 0.5°$ due to the conservation of momentum. If the two γ-rays produced by an electron-positron annihilation event are detected near-simultaneously by the two heads of the positron camera (providing a 'coincidence event'), the positions on each detector face at which the γ interactions occur is recorded.

The two detector heads which form our positron camera each consist of a single, 16 mm thick sodium iodide (NaI) crystal of surface area 590×470 mm^2 which is optically coupled to an array of 55 individual photomultiplier tubes. When an interacting (γ) photon causes scintillation within one of the NaI crystals, its centroid can be determined from the relative signal strength from the numerous photomultipliers present. Through this method, the interaction coordinates of a single incident γ-ray may be determined to a resolution of approximately 6 millimetres [183, 184].

Since we know that the γ photons in which we are interested have been emitted 'back-to-back' (i.e. their trajectories both fall along the same vector) the path taken by the γ-ray can be reconstructed, as schematically illustrated in Fig. 3.2. Of course, for highly active tracers, not all coincidence events will be 'true' coincidences. A 'coincidence event' is defined as the detection of any two γ-rays within 7.5 nanoseconds of one another, leading to the possibility of various anomalies such as 'random coincidences', whereby entirely unrelated γ-rays happen to strike the two detector faces within this resolving time, or 'scattered pairing', whereby one or both of the γ-rays emitted by an annihilation event are scattered within the system, and the software falsely assumes that the line connecting the two points at which the photons are detected corresponds to the origin of the photons. In order to aid comprehension, exemplary visual illustrations of these false coincidences are provided in Fig. 3.3.

Clearly, through the acquisition of a number of (true) coincidence events in rapid succession, the position of the tracer may be triangulated. For a stationary particle, its position may be determined to an arbitrary accuracy. A moving tracer, meanwhile, may be located with an accuracy of the order of millimetres, the precise resolution

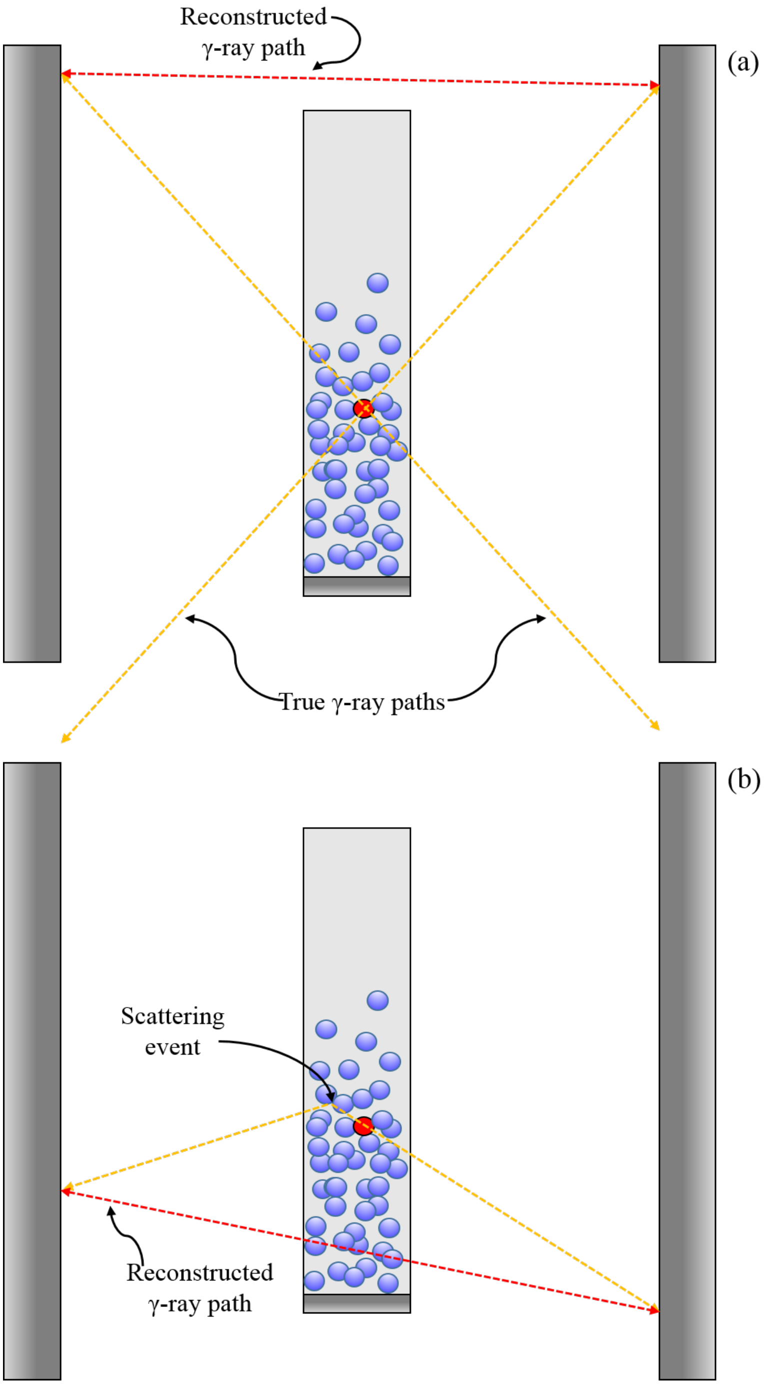

Figure 3.3: Schematic diagram providing a visual illustration of commonly encountered false coincidence events (the system shown is not to scale). Image (a) shows a *random* coincidence, whereby two entirely unassociated γ rays happen to be detected within the resolving time, τ_r. Panel (b), meanwhile, shows a false coincidence whereby one of the two emitted photons becomes scattered, causing it to deviate from its initial, collinear path.

being dependent on various parameters, including the density of the system, the typical velocity of the tracer, and its activity. Specifically, a slow-moving tracer may be located 50 times per second with an accuracy of ~ 100μm while the position of a tracer moving at 1 ms^{-1} may be recorded to within ~ 0.5 mm 250 times per second [183]. The temporal resolution with which data may be acquired is similarly dependent on these parameters; this time resolution is typically of the order of milliseconds, as suggested by the figures quoted above.

In order to minimise the negative influence of anomalous events on the accuracy of PEPT data, an algorithm [185] is employed to discard as many of these false coincidences as possible before data processing is undertaken. For each triangulation event, the algorithm is implemented as follows:

1. The algorithm determines a *minimum distance point*, i.e. the point in space closest to which all of the reconstructed paths corresponding to coincidence events are found to pass.
2. The coincidence events corresponding to the paths which lie furthest away from this point are discarded.
3. A new minimum distance point is then determined from the remaining coincidence events.
4. This process is repeated in an iterative process until only a user-defined fraction, f_{opt}, of the original points remains.

As mentioned above, the acquisition of a series of successive triangulation events may be used to record the three-dimensional motion of a tracer particle, i.e. its position and velocity. If the tracer particle used is physically identical to all others within the system, and the system itself exists in a non-equilibrium steady state (NESS), the principle of ergodicity may be exploited such that the time-averaged motion of this single particle may be considered representative of the behaviour of the system as a whole [186]. Thus, PEPT may be used to experimentally measure various important quantities pertaining to the dynamics of a granular bed. Detailed below are the manners in which the quantities most relevant to the work discussed in this thesis may be obtained from PEPT data.

3.2.2 Extracting Whole-Field Data from PEPT

Ensuring a Steady State

Since the use of PEPT data to determine whole-field information is reliant on the steady-state nature of the system under investigation, it is of paramount importance that all systems studied do indeed adhere to this prerequisite. This being the case, several measures are taken to ensure a NESS for the entire duration over which PEPT data is extracted.

Firstly, for each data set recorded, the experimental system is vibrated for a period of time adequate to allow the system to reach its steady state *before* data acquisition begins. The time required for a system to achieve a steady state can be predicted using DPM simulations (see section 3.3), although in all cases the duration of the initial vibration is chosen to be considerably longer than the time period extracted from simulations in order to guarantee, as far as possible, that the system will indeed reach its NESS.

Once data has been acquired, the existence of a steady state can be confirmed by subdividing the data into a series of short, overlapping 'segments' in time and ensuring that the system's state and behaviour remain consistent for all segments obtained.

The validity of PEPT data and the steady-state nature of the systems under investigation can also be substantiated by comparison with simulations, as discussed further in later sections.

Packing Density and Density Fields

For steady state, monodisperse systems in which ergodicity is assumed, the fraction of time, F, spent by any single particle in a given region may be expected, in the limit $t \to \infty$, to be directly proportional to the average density of particles in that same region. Of course, in practice, the realisation of an experiment of infinitely long duration is somewhat unfeasible! However, if the consistency checks detailed in the preceding section show adequately small variation in F and its distribution between various time segments of the obtained data and/or repeated experiments, the aforementioned direct proportionality can nonetheless be safely assumed. The small variations which *are* observed between repeated experiments and the individual times slices thereof may be used to provide a measure of the uncertainty in our results, which are inherent in any granular system due to the random nature of the dynamical behaviours of the individual particulate constituents. Thus, the time-averaged packing density, η, for a region or 'cell' of volume V_c within a granular bed may be determined from PEPT data as:

$$\eta = \frac{N\pi d^3 F}{6V_c} \tag{3.4}$$

where N is the number of particles in the system as a whole, and F is the fraction of time spent by the tracer in the particular volume V_C. By subdividing the computational volume into a series of equally sized cells, it is therefore possible to plot the spatial variation of a system's packing. For instance, by choosing V_c such that each cell represents a horizontal 'slice' of thickness dz through the container volume at a given height, z, it is possible – for adequately small dz – to create a one-dimensional density profile. Alternatively, by depth-averaging through one of the system's horizontal dimensions and subdividing the resultant 2D projection of the system into a series of 'pixels' of size $dx \times dz$, one can create a two-dimensional density field. Exemplary images of such density plots may be seen in Fig. 3.4.

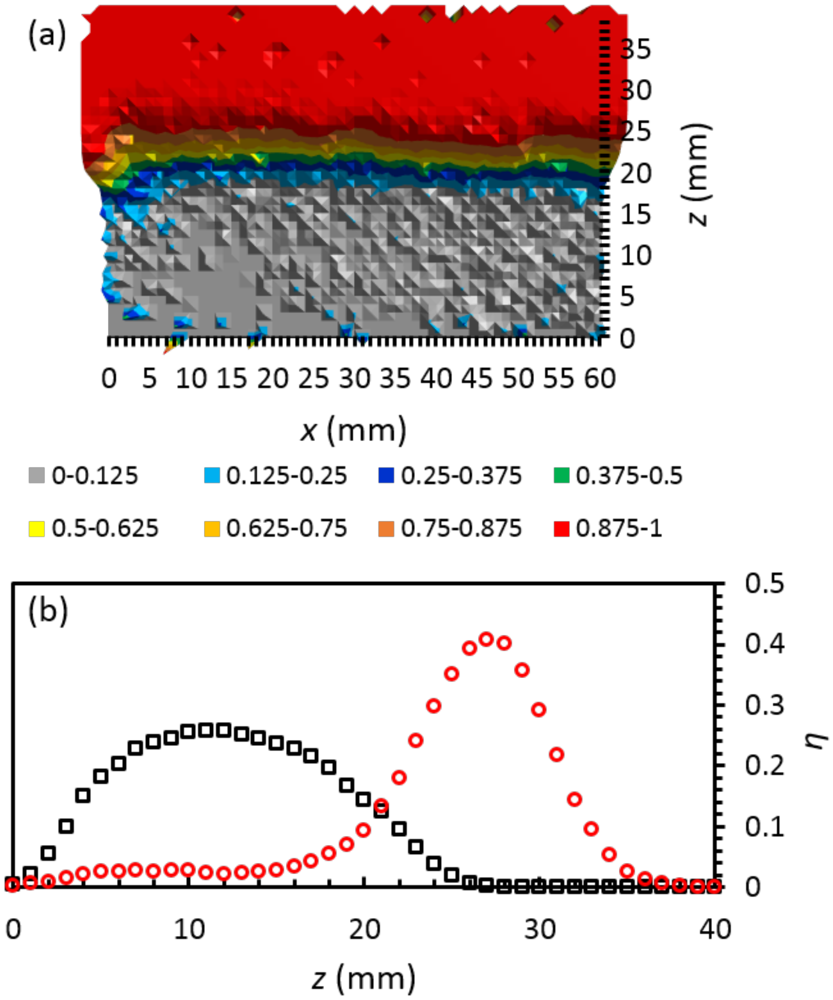

Figure 3.4: (a) Two-dimensional particle concentration distribution for the (light) polyurethane component of a binary mixture of equally sized (heavy) steel and polyurethane particles. The volume fraction of polyurethane particles in a given region of two-dimensional space can be determined using the colour key provided in the image. (b) One-dimensional packing profile for both light (red circles) and heavy (black squares) components of the system shown in (a).

Mean Squared Displacement and Self-Diffusion

Mean squared displacement, often abbreviated to MSD and, for the purposes of this thesis, assigned the symbol M, is a useful measure of the relative ease with a particle may move through a system. The MSD is defined as:

$$M = \langle |\mathbf{r}(t) - \mathbf{r}(t = 0)|^2 \rangle \tag{3.5}$$

where $\mathbf{r}$ is a particle's position vector and, hence, $|\mathbf{r}(t) - \mathbf{r}(t = 0)|$ represents the net distance moved by a particle from its initial position after a time t. For PEPT data, a single MSD 'trace' may be obtained by choosing an arbitrary data point as the trace's start point, and then simply recording the distance moved by the tracer from this original point for each subsequent data point. By averaging over a number of such traces, each with a different data point as its starting position, one may obtain a value of M.

Once M has been calculated as a function of t, the long-time mean squared displacement behaviour may be used to determine the self-diffusion coefficient, D, from the equation:

$$D = \lim_{t \to \infty} \frac{1}{6t} \langle |\mathbf{r}(t) - \mathbf{r}(t = 0)|^2 \rangle \tag{3.6}$$

In order to assure an accurate value for D, only data corresponding to the central region of a given system is used in calculations, to ensure that the mean squared displacement behaviour is not influenced by the finite size of the container. An illustration of the possible effects of such confinement may be seen in Figure 3.5; here we see examples of $M(t)$ for both a relatively large container ($L_{x,y}$ = 120 mm) and a comparatively small system ($L_{x,y}$ = 25 mm). For the latter system, we clearly see that the mean squared displacement approaches a point of saturation, due to the presence of fixed lateral boundaries which prevent any further migration away from the tracer's starting position. For the former, however, the linear trend indicative of simple Fickian diffusion is maintained for considerably longer.

In order to calculate the diffusivities of systems in which there exists a net motion (e.g. convective systems), it is simply necessary to subtract, at each timestep, the appropriate mean flow corresponding to the region of the system (i.e. the current ‘pixel’) in which the relevant data points lie.

Velocities, Velocity Distributions and Velocity Fields

The calculation of particle velocities from PEPT data is, in essence, trivial, as one can directly access information regarding the tracer’s spatial position at a given point in time from PEPT data. However, simply determining the particle’s pseudo-instantaneous velocity from two consecutive data points often results in considerably larger error margins than are desirable. Instead, it is generally prudent to instead take an average over several consecutive data points. The optimal number of data points over which to average is dependent on the system under investigation – since PEPT cannot detect particle collisions, any average taken over a series of data points during which a collision has occurred will, clearly, provide an erroneous value of the instantaneous velocity. This being the case, it is necessary to ensure that the typical timestep over which velocities are calculated is considerably shorter than the typical collision rate between particles. Thus, velocity values acquired from PEPT are most accurate in relatively dilute systems.

One of the main uses of velocities acquired in the above manner is the production of velocity probability density functions (vPDFs). These distributions may be acquired by dividing all data points into a series of appropriately sized bins dependent on their velocity values and normalising by the total number of points. The resultant probability distributions, examples of which may be seen in Fig. 3.6, provide valuable information regarding the system’s dynamical behaviour; for instance, comparing distributions for the x, y and z components of velocity will give an indication of the degree of anisotropy within the system [187, 188], while the kurtosis of the distribution (i.e. its deviation

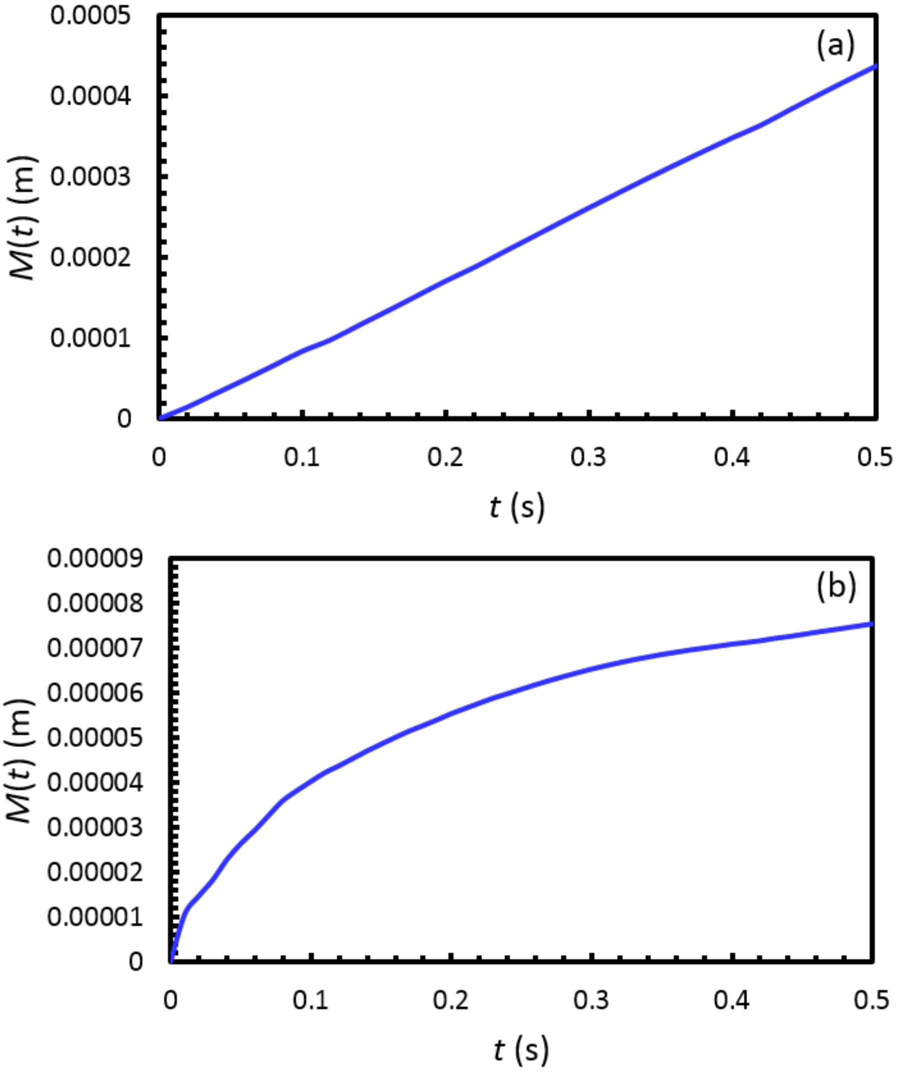

Figure 3.5: Mean squared displacement, $M(t)$, as a function of time for vibrofluidised granular beds housed in containers of horizontal extent (a) 120 mm and (b) 25 mm.

from the Gaussian form) is of significant interest to the granular community [189–196] due, at least in part, to its implications for the successful application of kinetic theory to particulate systems.

PEPT data may also be used to determine the *mean* velocities for a system, or for any given region of the experimental volume. By subdividing the computational volume into a series of cells, as described above for the creation of density fields, one may calculate the average particle velocity within each region of the experimental system throughout the duration of an experiment, and thus produce a velocity vector field, such as that shown in Fig. 3.7. Again, these fields may be used to investigate various aspects of a system's behaviour; of particular relevance to this thesis is the ability of these fields to provide useful visual illustrations of convective motion (or the lack thereof) within a system, and indeed quantitative measurements of the strength of convection within a system, as will be further discussed below.

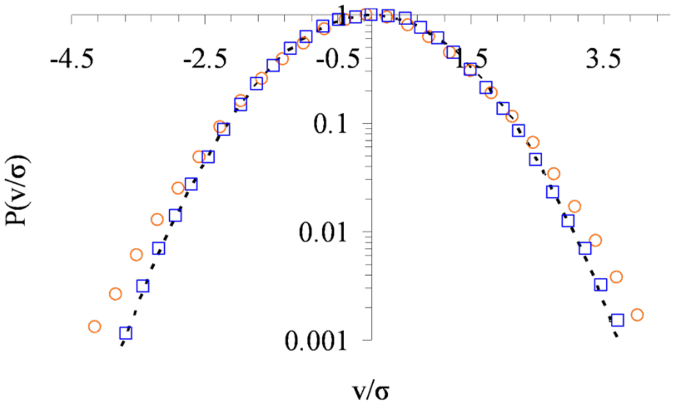

Figure 3.6: Examples of velocity distributions acquired from PEPT data. Data is shown for two highly excited granular systems, one of which exhibits a near-Gaussian velocity distribution (blue squares), as would be expected of a similar *molecular* system, while the second demonstrates the augmented high energy 'tails' typical of granular systems (orange circles). A dashed line corresponding to a true Gaussian is included as a guide to the eye. For the interested reader, the context and significance of this image may be found in our reference [1].

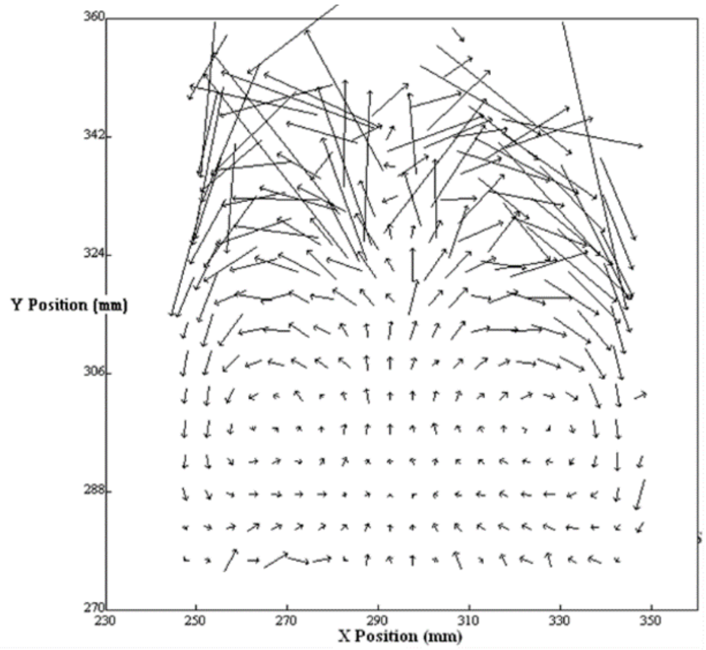

Figure 3.7: Two-dimensional, depth-averaged velocity field showing the steady-state particle flow for a vertically vibrated system in which strong convective flow is present.

Granular Temperature and Temperature Fields

The granular temperature, i.e. the fluctuating kinetic energy, of a system may be determined in several manners; the choice of the method by which T is calculated from PEPT data depends on the state of the system under investigation.

For very dilute systems, where the mean collision rate is considerably lower than the mean detection rate, T can be calculated directly from the velocity values whose origins are explained above. In order to produce a temperature field by which the spatial distribution of T may be displayed, one first needs to subdivide the experimental volume into a series of cells in a similar manner to that described above for density and velocity fields. For each cell, the localised mean velocity, $\bar{v}$, may be calculated. The individual velocity values corresponding to the n data points falling within this cell may then be used to calculate the local temperature as:

$$T = \frac{1}{2} m \frac{\sum_{i=1}^{i=n} (v_i - \bar{v})^2}{n} \tag{3.7}$$

where v_i is the velocity corresponding to the i^{th} data point within the cell and m, as usual, is the particle mass.

When determining quantities such as T from PEPT data, it is important to consider the errors inherent to the technique, in particular the absence of a reliable collision detection routine. Since PEPT cannot detect the presence of particle collisions, any velocity values calculated over a series of data points corresponding to a time period during which one or more collisions has occurred will, clearly, produce an errorneous value. This being the case, in order for velocities, and hence granular temperatures, to be directly calculated from particles' ballistic trajectories, the temporal resolution of the PEPT data must be adequately high compared to the mean collision rate within a given system that erroneous velocities such as those described above represent only a small fraction of the velocities measured.

For higher-density systems, where the presence of particle collisions substantially affects the accuracy of velocity data, another method is required in order to reliably calculate T. Under these circumstances, T is most accurately calculated from the system's mean squared displacement behaviour, determined as described above. Specifically, a value of T may be obtained through a determination of the mean squared speed, $\langle c^2 \rangle$ achieved by performing a 2nd order polynomial regression on the ballistic region of the mean squared displacement [197].

Convective Flow Rates

As well as providing a qualitative illustration of convective motion within a granular system, as may be seen in the middle panel of Fig. 3.8, the velocity fields detailed earlier in this section may also be used to determine a quantitative measure of the strength of convection within the system. In order to quantify convection strength, we use a parameter J, analogous to that used by Hsiau and Chen [100]. In order to calculate J, we first identify the position of the vertical centre of convection for the system under investigation. We then take a thin 'slice' through the computational volume at this height, and divide this slice into a series of cells. For each of these N_c cells, the mean velocity in each spatial direction may be calculated, as described above. By exploiting the fact that, at the system's vertical convection centre, the horizontal components of velocity may be assumed equal to zero, the mean convective flow rate may be determined as:

$$J = \frac{\sum\limits_{i=1}^{i=N_c} |v_z^i| \eta^i}{2N_c} \tag{3.8}$$

where v_z^i and η^i are, respectively, the mean vertical (z) component of velocity and the local packing density corresponding to the i^{th} cell. The divisor of two arises due to the fact that the above equation takes the sum of both upward- and downward-flowing regions.

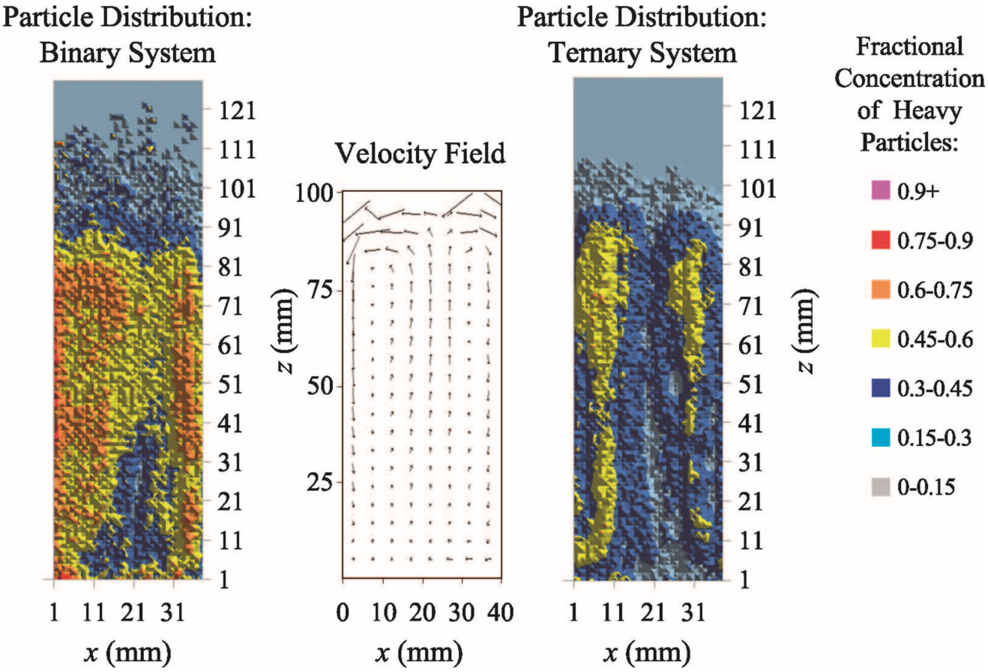

Figure 3.8: Plot showing a typical, convective velocity field for a dense, narrow granular system (centre) and its influence on the distribution of differently massive particles in binary (left) and ternary (right) systems. Data is taken from our reference [2], which is discussed in detail in section 4.4.

Segregation Intensity

PEPT data may also be used to quantify the degree of steady-state segregation, or *segregation intensity* [198,199], I_s, achieved by a binary, ternary or polydisperse granular bed. For clarity and ease of comprehension, I will first discuss the determination of I_s with reference to the relatively simple case of a binary mixture of monosized particles, before explaining how the process may be extended to more polydisperse systems.

In order to investigate a binary system, two identical runs are conducted, one using a tracer of species A and the second a tracer of species B. It should be noted that while it would be possible to perform a single run with two tracer particles, the addition of an extra tracer will reduce the accuracy with which either particle may be located [200]. Thus, although more time consuming, it is generally favourable to perform individual, single-tracer runs. Since we are discussing here only steady-state, ergodic systems, time-averaged values such as the residence time fraction, F, and hence the particle density, η, for each species may be directly compared. As such, it is possible to determine, for any given region of the system under investigation, the local *fractional concentration*, ϕ, of a particular particle species. By subdividing the computational volume into a series of individual cells and, for each of these i cells, calculating the local concentration, ϕ_i of one of the species present, the segregation intensity may be determined using the equation:

$$I_s = \left[\frac{\sum_{i=1}^{i=N_c} (\phi_i - \phi_m)^2}{N_c} \right]^{\frac{1}{2}} \tag{3.9}$$

where N_c, as usual, is the total number of cells within the computational domain, and ϕ_m is the mean concentration of the relevant particle species for the system as a whole. Throughout this thesis, we normalise the value of I_s such that for systems in which complete segregation is achieved, $I_s = 1$, with a value $I_s = 0$ corresponding to a perfectly mixed system. The necessary normalisation constant is simply equal to the I_s value of the relevant system for the case of complete segregation (i.e. the maximum achievable value of I_s). Such a normalisation allows the direct comparison of differing systems, whilst also allowing the simple and easily comprehensible fractional representation of I_s.

In order to investigate the segregative behaviours of granulates possessing greater degrees of polydispersity, i.e. systems comprising n individual species, it is simply necessary to conduct a series of n individual data sets using PEPT, each run using a tracer of a different species.

Ensuring Ergodicity

In order to ensure that the whole-field data presented are reliable and accurate, it is necessary to perform certain validity checks. Such checks are typically performed by subdividing a given data set or 'run' taken over a period t_r into a series of individual, shorter data sets of length Δt_r. If the whole-field quantities calculated (e.g. density or temperature distributions) remain consistent across each segment of the original data set, we can assume that these quantities are indeed representative of the system's true steady-state behaviour.

Figure 3.9 shows a typical example of the reproducibility expected for an accurate PEPT data set.

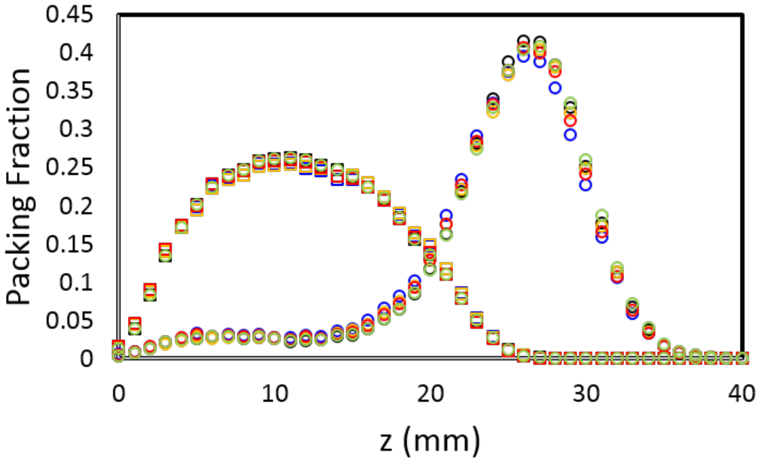

Figure 3.9: Vertical packing density profiles for both components of a binary bed comprising nylon (circles) and steel (squares) spheres driven with a dimensionless acceleration $\Gamma = 14$. Data is shown for a full data set of length $t_r = 4800$ s (red) as well as for a series of individual 'segments' of this data set, each of length $\frac{t_r}{10}$ (blue, green, orange and black) corresponding to various points chosen to span the entirety of t_r.

3.3 Simulations - the MercuryDPM Code

In addition to experimental results acquired using positron emission particle tracking, additional data were obtained from discrete particle method (DPM) simulations [201–203], in order to validate and elucidate observations made using PEPT. The use of simulational methods also allows the study of various aspects of the system's behaviour which are inaccessible to PEPT, in particular the observation and measurement of time-dependent properties and the investigation of systems' transient behaviours, i.e. during their evolution towards a final steady state. Moreover, the inclusion of simulations allows a greater degree of control over the physical properties of the particles and systems under investigation than is achievable in experiment.

The simulations discussed within this thesis are produced using the open-source software package *MercuryDPM*, developed at the University of Twente [204–207]. Simulations such as those performed as part of the work discussed here are often referred to as DEM or *discrete element method* simulations. However, since MercuryDPM is specifically designed to model particulate systems, placing particular emphasis on contact models [208], the optimisation of contact detection for highly polydisperse-by-size systems [209] and coarse graining which is performed *in-code* (as opposed to during post-processing) [210,211], the simulations discussed here are more appropriately termed *DPM* or *discrete* ***particle*** *method.* MercuryDPM was originally developed to model chute flows of granular materials [205,212,213] and later extended to handle other system geometries such as rotating drums [214] and, of course, vibrated beds.

Having provided a brief overview of the MercuryDPM code, the finer details of the algorithm may now be discussed, beginning with the precise manner in which particle contacts are modelled.

A granular or particulate system is modelled as a series of i particles, each possessing a position, $\mathbf{r}_i$, a velocity, $\mathbf{v}_i$, an angular velocity, ω_i, a density, ρ_i, and a diameter, d_i. Since, in this thesis, we consider exclusively monosized granulates, we can simply consider a single diameter, d. The particles defined in the above manner are treated as being spherical and soft, and contacts between particles are assumed to occur at single points. The distance between two particle centres i and j is denoted $r_{ij} = |\mathbf{r}_i - \mathbf{r}_j|$. The *branch vector*, i.e. the vector from the centre of a particle to its point of contact with a second particle, is defined as $\mathbf{b}_{ij} = -(d_i - \delta^n_{ij})\hat{\mathbf{n}}_{ij}/2$, where δ^n_{ij} is the *overlap* between particles (defined below). The unit normal vector, meanwhile, is taken as $\hat{\mathbf{n}}_{ij} = \frac{\mathbf{r}_i - \mathbf{r}_j}{r_{ij}}$ with the relative velocity between particles simply given as $\mathbf{v}_{ij} = \mathbf{v}_i - \mathbf{v}_j$.

Two particles are considered to be in contact if they possess a positive overlap, i.e. $\delta^n_{ij} > 0$, where δ^n_{ij} is defined as:

$$\delta^n_{ij} = \max(0, \frac{d_i + d_j}{2} - r_{ij}) \tag{3.10}$$

At the point of contact, the relative velocities between particles in the normal and tangential directions are taken as:

$$\mathbf{v}^n_{ij} = (\mathbf{v}_{ij} \cdot \hat{\mathbf{n}}_{ij})\hat{\mathbf{n}}_{ij} \tag{3.11}$$

and

$$\mathbf{v}^t_{ij} = \mathbf{v}_{ij} - \mathbf{v}^n_{ij} - \omega_{\mathbf{i}} \times \mathbf{b}_{ij} + \omega_{\mathbf{j}} \times \mathbf{b}_{ji} \tag{3.12}$$

respectively. It should be noted that the form provided for the relative tangential velocity, $\mathbf{v}^t_{ij}$, applies only for the case of equally-sized particles. Since the assumption of size-uniformity holds for all systems discussed within this thesis, this simplified formulation of $\mathbf{v}^t_{ij}$ given in equation 3.12 is more than adequate.

For the studies detailed here, particle contacts are – unless otherwise stated – assumed to be linearly viscoelastic, with normal and tangential forces calculated using a spring-dashpot model with a linear elastic and linear dissipative contribution [201,208,213,215].

The choice to implement the spring-dashpot model as opposed to a Hertzian force model is taken due to the fact that while both can accurately recreate the steady state behaviours of granular systems [212, 216], the former is consdierably more computationally efficient. In fact, in the systems studied here, direct comparisons of equivalent simulational data sets utilising Hertzian and spring-dashpot contact models have shown results to be effectively independent of the specific form used [13].

For our chosen model, the relevant forces exerted on particle i by particle j may be given as:

$$\mathbf{f}^n_{ij} = k^n \delta^n_{ij} \hat{\mathbf{n}}_{ij} - \gamma^n \mathbf{v}^n_{ij} \tag{3.13}$$

and

$$\mathbf{f}^t_{ij} = -k^t \delta^t_{ij} - \gamma^t \mathbf{v}^t_{ij} \tag{3.14}$$

Here, $k^{n,t}$ are the relevant spring constants and $\gamma^{n,t}$ the relevant damping constants, while δ^t_{ij} is the elastic tangential displacement. δ^t_{ij} is defined to be zero at the initial time of contact, with its evolution from this point in time given by:

$$\frac{d}{dt}\delta^t_{ij} = \mathbf{v}^t_{ij} - r^{-2}_{ij}(\delta^t_{ij} \cdot \mathbf{v}_{ij}) r_{ij} \tag{3.15}$$

In this equation, the second term corrects for the rotation of the contact, ensuring that $\delta^t_{ij} = 0$ for the case $\hat{\mathbf{n}}_{ij} = 0$. In order to satisfy the inequality $|\mathbf{f}^t_{ij}| < \mu |\mathbf{f}^n_{ij}|$ – i.e. to simulate the sliding observed between particles when the ratio of normal to tangential force exceeds the microscopic friction coefficient, μ – the magnitude of δ^t_{ij} is appropriately truncated.

For central collisions, i.e. those in which tangential forces are negligible, the collision time, t_c, and restitution coefficient, ε, for a particle interaction may be related to the spring-dashpot properties via the relations:

$$t_c = \frac{\pi}{\sqrt{\frac{k^n}{m_{ij}} - \left(\frac{\gamma^n}{2m_{ij}}\right)^2}} \tag{3.16}$$

and

$$\varepsilon = \exp\left(-\frac{t_c \gamma^n}{2m_{ij}}\right) \tag{3.17}$$

with $m_{ij} = \frac{m_i m_j}{m_i + m_j}$ the reduced mass.

The *total force* acting on particle i during a collision is a combination of the contact forces $\mathbf{f}_{ij}^n$ and $\mathbf{f}_{ij}^t$ given in equations 3.13 and 3.14 for all j particles with which i is in contact as well as external forces which, for the studies detailed within this thesis, arise due solely to the influence of gravity, g. Once the necessary forces and torques have been determined, the resultant relations can be integrated in time using the Velocity Verlet [217] and forward Euler methods [218], adopting a timestep $\Delta t = t_c/50$.

When used to provide verification and validation of PEPT data, care is taken to implement exact experimental values of the various system parameters. The system's energy-providing base is simulated as a simple, flat, infinitely massive wall which undergoes sinusoidal oscillation in the vertical direction. In all cases where direct comparison is drawn between experiment and simulation, the reader may assume that – unless otherwise stated – the particle number (N), system size (L_x, L_y, L_z), resting bed height (N_L), particle diameter (d), particle density (ρ) and hence mass (m), driving frequency (f), amplitude (A) and hence dimensionless driving acceleration (Γ), peak velocity (V) and non-dimensional shaking strength (S) are taken as the corresponding experimental values. Wherever possible, known experimental values or experimentally measured values of the various particle-wall and particle-particle restitution coefficients (ε_w, ε) and frictional coefficients (μ_w, μ) are also implemented. For binary and ternary systems, the relative concentration (φ_χ) of each particle species used in experiment is also matched in simulation. Unless specifically noted to the contrary, composite systems are modelled as possessing an initially perfectly-mixed state.

In addition to values of ε and μ, the frictional spring-dashpot model used to determine the normal and tangential forces acting between particles in contact requires also a predefined contact time, t_c. In order to increase the speed of simulations, a contact time of $t_c = 10^{-5}$ s is typically used. For most particle materials investigated, such a value is unrealistically large, and as such carries the potential to underestimate the energy lost during collision and hence produce inaccurate or anomalous results [219]; however, for each of the simulational studies detailed within this thesis, repeated tests using t_c values an order of magnitude below and up to two orders of magnitude above this value are conducted in order to assess the sensitivity of each system to the specific t_c values used. In all cases discussed here, the system's behaviour is observed to be invariant of the specific t_c implemented. Further evidence of the limited influence of t_c is provided by the generally excellent agreement observed between simulations and their corresponding experiments, specific examples of which may be found throughout chapters 4 and 5. A demonstration of the close correspondence between simulation and experiment may also be seen in Figure 3.10 below.

It is particularly interesting to note that the DPM simulations shown in 3.10 even reproduce the unusual behaviour of the various packing density profiles at small z. This represents a useful example of the fact that not only may experiments be used to validate simulations, but a close agreement between simulation and experiment can often provide a degree of support for the existence of physical phenomena which may otherwise be ascribed to artefacts in experimental data. It is firstly important to note that the zero point of the profiles shown in 3.10 is shifted by $\frac{z}{d} = 0.5$ in order to account for the fact that PEPT will typically locate the *centre* of the particles tracked – i.e. the low-z behaviour observed is not due to a lower detection rate below a height of $0.5d$. Rather, the comparatively low packing fraction at small z is thought to be evidence that the bed is in either a 'bouncing bed' or undulatory state [81], meaning that the bottom-most layer of particles in the bed will periodically leave its surface, leading to a lower residence time and hence the reduced time-averaged packing density observed.

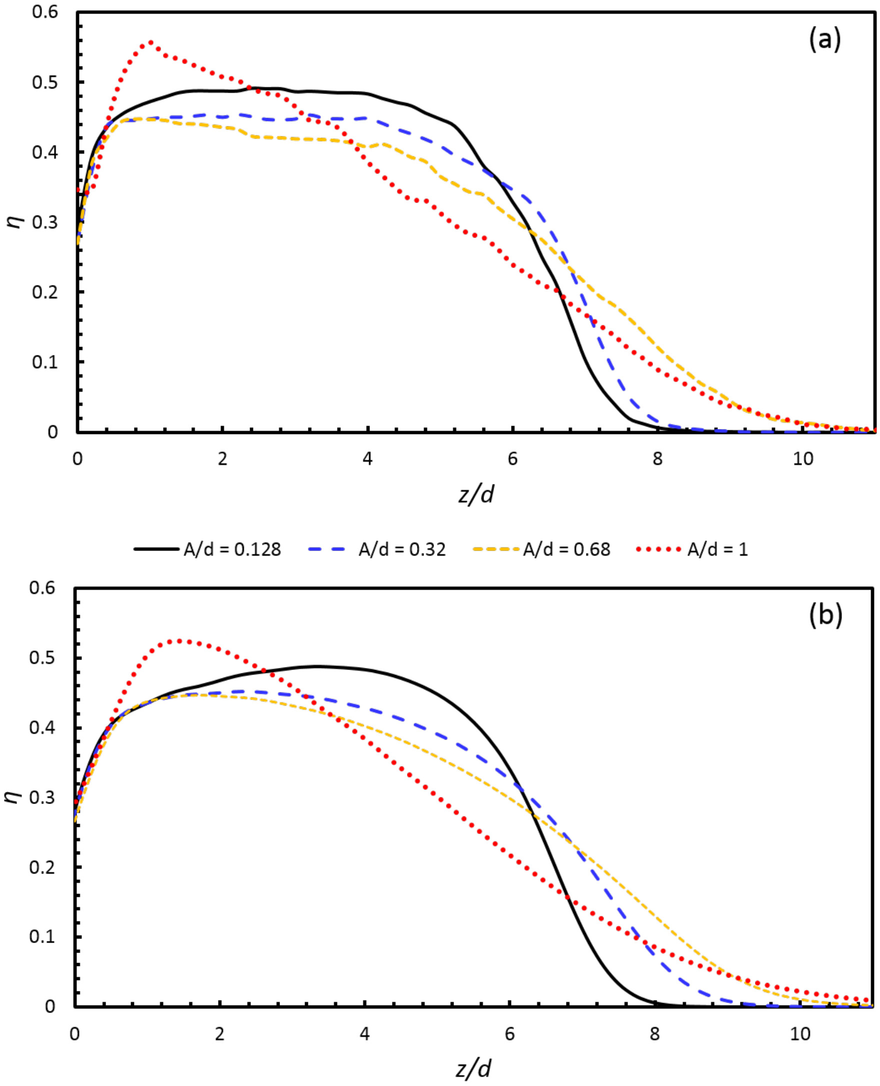

Figure 3.10: Experimental (a) and simulational (b) packing density profiles for a vertically vibrated bed of 3 mm diameter stainless steel particles. The bed has a dimensionless depth of $N_L = 6$ particle layers, and is driven at a fixed dimensionless energy input $S = \frac{4\pi^2 f^2 A^2}{gd} = 5.44$ produced using various combinations of A and f, as specified in the legend provided in the image. The strong agreement shown here provides a powerful example of the advantage of directly modelling the vibrational motion of the base of a system as opposed to simply approximating the base's energy input using a static '*thermal wall*', an assumption often used in other simulation models [3–6]; were such an approximation used here, the simulated profiles would all be identical!

4 Convective Flow, and its Influence on the Dynamical and Segregative Behaviours of Granular Systems

In this chapter, we discuss the dynamics of systems in which convective motion, be it buoyancy-driven or frictionally-induced, plays an important rôle. We first discuss the relatively simple case of monodisperse systems, demonstrating various methods by which the strength of convection within a system may be deliberately altered through the variation of controllable system parameters, detailing how the different convective flow rates achieved affect the state and behaviours of the systems under investigation. We then expand our analysis to binary and ternary systems, illustrating the effects of convective flow on the manners in which particles with differing properties are distributed within the experimental domain, and how energy is shared between these differing particle species.

4.1 Thermal Convection in Monodisperse Systems – The Rôle of Sidewall Dissipation

In order to test the influence of sidewall dissipation on the convective flow set up within a laterally constrained, vibrated granular bed, an experimental system was constructed whereby the material of the sidewalls bounding the system, and hence the particle-wall coefficient of restitution, ε_w, could be altered whilst holding constant all other relevant system parameters. The particles forming the granular bed were 5mm in diameter, and composed of soda-lime glass ($\rho = 2750$ kgm^{-3}). The system used to house these particles comprised a square-based cuboidal container of dimensions $L_x \times L_y \times L_z = 100 \times 100 \times 200$ mm, giving the system a dimensionless width $W^* = W/d = 20$. The sidewalls of the system are detachable, such that they may be removed and replaced in between runs to allow an exploration of the impact of sidewall dissipation on the system's dynamics. In order to allow a variety of ε_w values to be explored, numerous different sidewall materials with strongly disparate elastic properties were tested, as may be seen from Table 4.1.

Table 4.1: Effective inelasticities for the various materials used as system sidewalls.

Material	Effective Inelasticity, ε_w
Mild Steel	0.70 ± 0.006
Stainless Steel	0.68 ± 0.024
Copper	0.58 ± 0.008
Brass	0.52 ± 0.010
Tufnol	0.39 ± 0.012
Clear Perspex	0.33 ± 0.014
Lead	< 0.01

The "*effective inelasticities*" [10] shown in Table 4.1 represent a measure of the average kinetic energy lost by a particle upon collision with a wall, including energy losses not only due to inelasticity, but also friction and energy transferred to the rotational modes. The ε_w values were determined using high-speed photography, the values shown in the table corresponding to an average being taken over a large number of individual collisions, with the quoted errors corresponding to the standard deviation over the range of results obtained. Specifically, for each sidewall material investigated, a single, flat sheet composed of the relevant material and of equal thickness to the sidewalls themselves was placed horizontally, and a single glass sphere dropped onto the plate from an initial height h_1. The subsequent motion of the sphere as it repeatedly collides and recollides with the horizontal plate is then recorded and, for each individual drop test, a value of the effective coefficient of restitution determined as $\varepsilon_w = \sqrt{\frac{h_2}{h_1}}$ [220], where h_2 is the height of the particle's first bounce after initially being released from the original height h_1. In fact, from a single data set with a large enough h_1, it is possible to acquire several measurements of ε_w by measuring the apex height of multiple subsequent bounces and simply generalising the aforementioned formula to $\varepsilon_w = \sqrt{\frac{h_{i+1}}{h_i}}$. For each wall material, repeated measurements were taken at a variety of initial drop heights ranging from 0.1 to 1.0 m.

Of course, the viscoelastic nature of the particles used in experiment means that their restitution coefficients are inherently velocity-dependent [221]. As such, for collision velocities outside the range explored in our preliminary investigations, variance on the presented values is likely to be greater than the error-values included. Nonetheless, the *relative* inelasticities of the particle species used are likely to remain similar (i.e. the brass component of a bed should, on average, always be more disipative than the glass component etc.) meaning that the qualitative trends presented and discussed here should still provide a useful insight into the systems studied.

Inelastic interactions may also be affected by the aging of particles, and indeed the walls of the system itself [222]. However, the biggest disparity in behaviour is observed between new and aged particles (as opposed to aged and further aged particles). As such we have chosen in our experiments to deliberately'age' our particles prior to their use by simply vibrating each batch at high intensity for a period of at least 6 hours.

The experimental system was vibrated, unless otherwise stated, at a fixed frequency $f = 70$ Hz with an amplitude $A = 1.93$ mm, providing a dimensionless acceleration $\Gamma = 38.0$ and a non-dimensional energy input of $S = 14.7$, adequate to ensure a fully fluidised system for all particle numbers, N, and hence bed heights, N_L, explored. The high frequency of the driving oscillations ensures that the system's centre-of-mass motion has no phase dependence, i.e. that the bed dynamics are decorrelated from the specific motion of the driving [223], allowing the system's base plate to simply be treated as an energy source [224].

In order to obtain adequate statistics, data sets were recorded over a time period $t_{run} \geq 2700$ s, the specific value chosen to ensure that, in all instances, the duration over which data is acquired is at least two orders of magnitude greater than the timescale of convection[1].

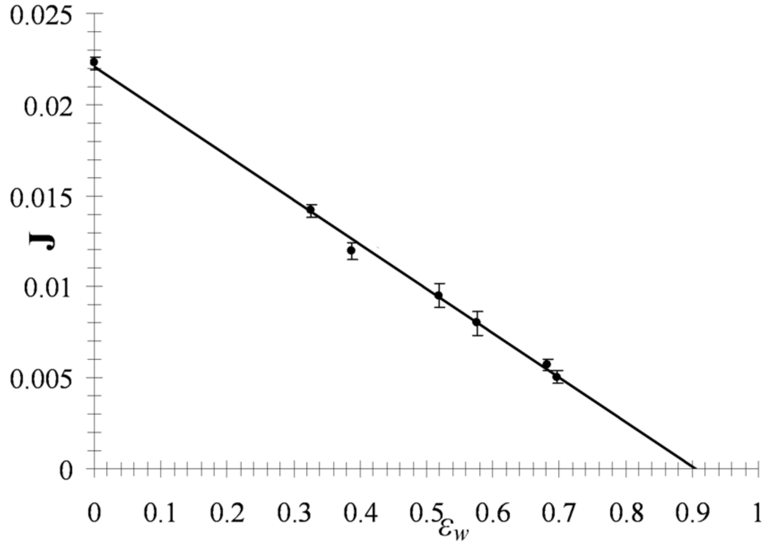

Figure 4.1: Convective flow rate, J, in ms^{-1} as a function of effective sidewall inelasticity, ε_w for the case $N = 863$. Figure taken from our reference [7].

For the above-described system, the variation of convection strength, quantified by the parameter J (as discussed in section 3.2.1) with ε_w can be seen in Fig. 4.2. This figure possesses several noteworthy features; firstly, and most obviously, it clearly demonstrates a monotonic decrease in the convective flow rate, J, with increasing sidewall elasticity, as may be expected from previous studies [79]. Less predictable, however, is the seemingly linear relationship between the two parameters, for which there is, as of yet, no convincing theoretical explanation, despite the persistence of such a relationship over a

---

[1] For each system, an initial test run was conducted in order to obtain an estimate of the relevant convection rate, with this value then being used to determine an appropriate t_{run}. The appropriateness of the run length could later be confirmed from the final data set.

range of particle numbers and indeed particle materials (see Fig. 4.8). It is additionally interesting to note the ε_w value corresponding to the x-intercept of the assumed linear relation (i.e. the point at which convection within the system would be expected to cease). For all systems comprising solely glass particles, the zero-convection value of ε_w is approximately equal to 0.9. Considering that the inter-particle coefficient of glass is also typically determined to be ~ 0.9 (the precise measured value varying between studies [10, 225, 226]), it is tempting to suggest that the cessation of convective motion at this point is due to a simple balance between wall and particle restitution coefficients. However, similar observations do not hold in systems of steel particles, or indeed for binary glass-steel combinations, as may be seen from Fig. 4.8 in the following section. In reality, the point at which sidewall and interparticle dissipation balance – and hence wall-driven convection will be suppressed – will be also heavily dependent on the differing *collision rates* for the particle-wall and particle-particle case. Although the ability to predict the zero-convection point for a given system is beyond the scope of the current work, it is certainly a potentially interesting avenue to explore in the future.

A final important aspect of the trend observed in Fig. 4.1 is the extent of the influence of ε_w on the system's convective behaviour – in this example, the convection strength, J, varies by more than a factor of four over the range of parameters tested. Indeed, under certain circumstances, a variation in ε_w can – even when all other system parameters are held constant – act to induce convection in otherwise non-convective systems or, alternatively, frustrate convection in previously convective systems, as demonstrated in Figure 4.3. In short, it is clear that the alteration of sidewall dissipation allows an impressive degree of control over the convective behaviours of a vibrofluidised granular system.

The relationship between convective flow rate and *particle number*, N (see Figure 4.2), is comparatively more complex in terms of the general (non-monotonic) trend observed, yet can be relatively easily explained, at least in a qualitative manner. At low

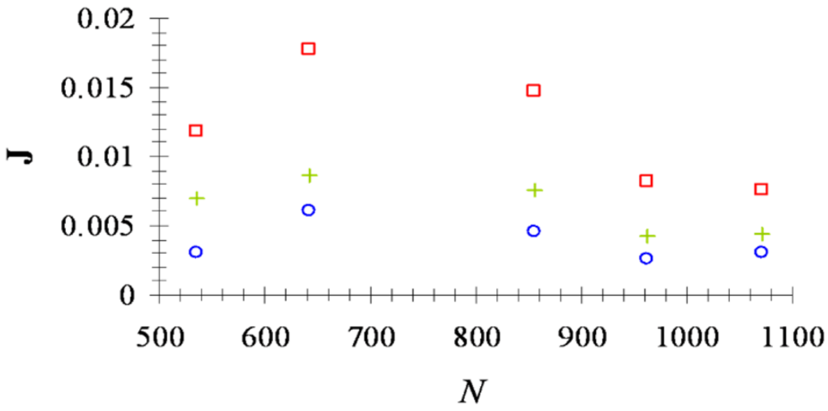

Figure 4.2: Convective flow rate as a function of particle number, N, for steel (blue circles), copper (green crosses) and perspex (red squares) sidewalls. Figure taken from our reference [7].

N, the bed will, by definition, be relatively dilute, meaning that the energy input per particle may be expected to dwarf the energy lost through dissipative collisions at the system's sidewalls, resulting in relatively weak convection (i.e. small J). For large particle numbers, meanwhile, dissipation will be significant throughout the system, meaning a smaller differential in dissipation between the outer and inner regions of the system; moreover, in more densely packed systems, frictional effects will become increasingly prevalent, leading eventually to a transition from buoyancy-driven to frictionally-driven convection, the latter of which may be expected to be relatively weak in our smooth-walled systems. Thus, one might indeed anticipate the presence of a maximum in J for middling values of N, as observed.

In addition to their influence on the convection observed within the granular bed, the horizontal boundaries also influence several other important system properties, such as the spatial variation of the granular temperature, T, and the observed distribution of particle velocities. As discussed in section 2.1, the temperature distribution within an open vibrofluidised granular bed under the influence of gravity is generally found to

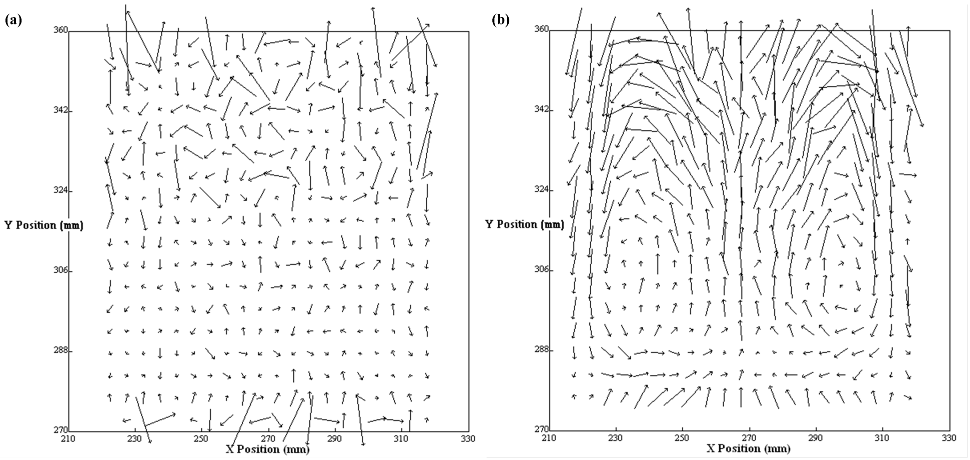

Figure 4.3: Velocity vector plots in the x-z plane for $N = 321$ particles in two equally-sized, identically-driven systems differing only in the material of the sidewalls used to constrain the system laterally. Images are shown for (a) mild steel ($\varepsilon_w = 0.70$) and (b) tufnol ($\varepsilon_w = 0.39$) sidewalls. Velocity values are averaged over the z-dimension.

be inhomogeneous [227]. Specifically, for relatively dilute, strongly fluidised systems, one typically observes a vertical gradient which initially decreases with height, z, before passing through a minimum and increasing for large z, where the system becomes more dilute and hence less dissipative. Our results show that the degree of inhomogeneity exhibited by a granular system may be directly affected by its sidewall properties, not only in the horizontal direction, as one would naturally expect [228], but also in the vertical direction, as illustrated in Fig. 4.4. Specifically, it is found that although, for all sidewall materials, the general trend in T is found to remain roughly constant for small heights (z) within the bed, a significant divergence is observed at larger heights, where systems bounded by more elastic walls are found to possess steeper gradients in T and generally higher temperatures. In order to confirm that this observation is indeed robust, and not simply an artefact in the experimental PEPT data, a theoretical continuum model was used to confirm the ε_w-dependence observed. In order to produce the theoretical curves shown in Fig. 4.4, the hydrodynamic framework of Brey *et al.* [57]

was modified to include a density dependent "*effective coefficient of restitution*", ε^*, incorporating both sidewall (ε_w) and inter-particle (ε) coefficients of restitution. The density-dependence arises due to the fact that as a granular bed becomes more dilute, the relative probability of particle-sidewall collisions to particle-particle collisions will increase. Specifically, the form of the effective coefficient of restitution was taken as:

$$\varepsilon^* = \frac{\alpha\nu\varepsilon + \varepsilon_w}{1 + \alpha\nu} \tag{4.1}$$

where ν is the local number density of particles, and α is a constant. Despite the simplicity of this addition to the model of [57], the results nevertheless provide a pleasing qualitative agreement with our experimental findings, as may be seen from Fig. 4.4, providing support for the validity and robustness of our observations. Figure taken from our reference [7].

In addition to the spatial inhomogeneity of the temperature within our system, it is additionally observed that – as is typical of vertically vibrated systems – T is also *anisotropic*, with particle temperatures displaying, in all cases, larger vertical (T_z) than horizontal ($T_{x,y}$) components. Since, due to the symmetry of the container under investigation, the horizontal temperature components may be expected to be – and indeed are found to be – equal, for the remainder of this section we will simply consider a generalised horizontal temperature, T_h. Our investigation of systems' average anisotropy, characterised by the ratio T_z/T_h for the average T of the system as a whole, shows two main results. Firstly, it is found that denser (i.e. higher N) systems are typically more isotropic. This makes sense, as the increased inter-particle collision rate within a more densely-packed bed will naturally result in a more rapid transferral of the kinetic energy provided by the base in the vertical direction to the horizontal modes [189], resulting in a reduced disparity between T_z and T_h. The increase in T_z/T_h with less elastic sidewalls can be simply explained by the fact that dissipative interactions between particles and the system's lateral boundaries will, clearly, remove energy predominantly from the

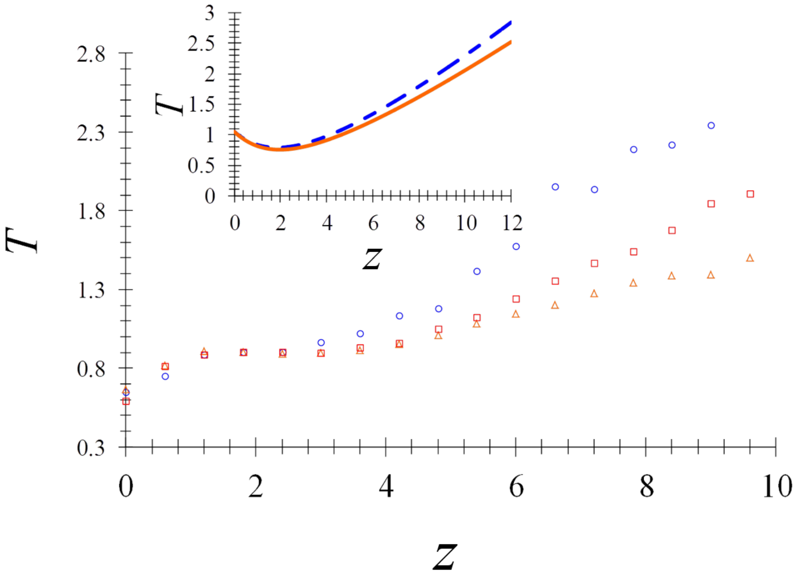

Figure 4.4: Vertical temperature profiles for the case N = 963, normalised in each case by the average temperature of a particle taken over all data points. Profiles are shown for systems with sidewalls composed of mild steel (blue circles), lead (orange triangles) and perspex (red squares). Aside from this variation in sidewall material, all systems shown are identical in terms of their driving, size and indeed all other major variables. Inset: theoretical temperature profiles for cases equivalent to steel ($\varepsilon_w = 0.7$ – dashed curve) and perspex ($\varepsilon_w = 0.33$ – solid curve).

horizontal direction, thus exacerbating the observed anisotropy. The increased influence of ε_w for more dilute systems, meanwhile, can be explained by the fact that less dense systems will, as previously discussed, be subject to an increased proportion of particle-sidewall collisions; moreover, in lower density beds where particle velocities will, on average, be higher, these collisions will remove comparatively more energy, due to the velocity-dependence of particles' dissipative properties [229, 230]. Although the general, decreasing trend between T_z/T_h and ε_w is perhaps not surprising, the degree to which this effect is evident is nonetheless noteworthy – simply changing the sidewall material can alter the degree of anisotropy observed within a system by upwards of 30%. It is lastly interesting to note that our results for all ε_w tested converge to non-unity value with increasing N, in agreement with the predictions of van der Meer *et al.* that T_z will always exceed T_h in a system exposed to vertical vibration.

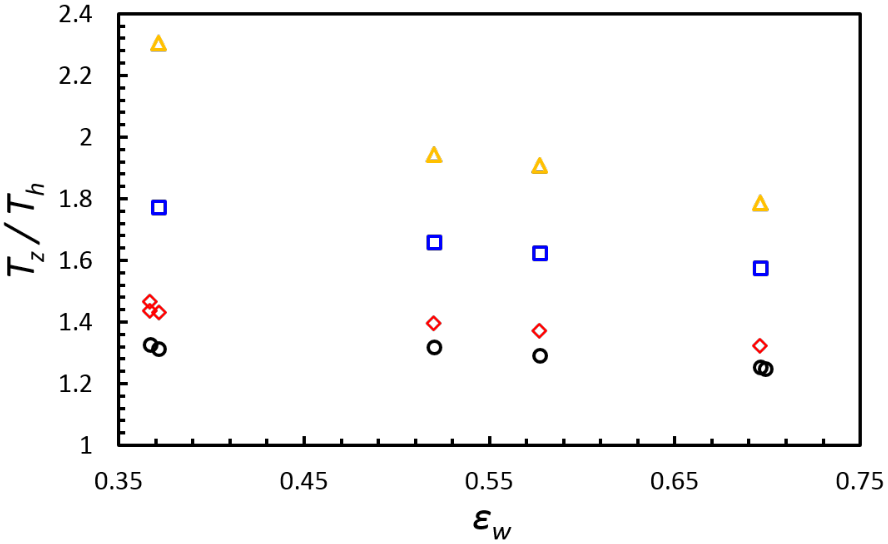

Figure 4.5: Variation of the ratio of vertical to horizontal temperature components (T_z/T_h) for systems with varying particle number, N, and sidewall elasticity, ε_w. Data is shown for beds of size $N = 321$ (orange triangles), $N = 428$ (blue squares), $N = 642$ (red diamonds) and $N = 856$ (black circles). Figure taken from our reference [7].

Our final area of investigation concerns the velocity distributions displayed by beds bounded by differingly dissipative horizontal boundaries. Previous investigations by van Zon *et al.* [231] have shown that, for highly constrained, quasi-two-dimensional systems, the frictional dissipation possessed by the sidewalls may significantly influence the distribution of particle velocities exhibited by a vibrated system, with systems possessing more frictional (and hence dissipative) walls evincing stronger deviation from the Gaussian form.

As evidenced by Figures 4.7 and 4.6, an increase in sidewall dissipation seems, for our strongly excited, three-dimensional system, to act in a manner analogous to an increase in wall friction in the system described by van Zon *et al.*, with lower-ε_w systems demonstrating a peaked distribution and increasingly non-Gaussian high energy tails. This is an important result, as it provides strong evidence that sidewall effects are not simply limited to the domain of narrow, quasi-two-dimensional or otherwise highly constrained systems, but also exert significant influence on fully three-dimensional systems more representative of most 'real-world' applications. This result is even more remarkable when we consider the fact the data shown in Figures 4.6 and 4.7 is taken exclusively from the central region of the bed, showing still more definitively that the influence of a container's sidewalls may pervade the entire system, as opposed to being limited to the immediate vicinity of the walls themselves. The extension of the sidewall influence on particle velocities in the interior of the system may, perhaps, be explained as follows: for the case of highly dissipative boundaries, one will – as previously discussed (see section 2.1) – typically observe an increased particle density near the walls of the system, as compared to the case of more elastic side-boundaries. Since in the systems under investigation particle number is, by definition, conserved, this will clearly lead to a relatively *decreased* density in the centre of the system and, hence, an increase in the probability of particles achieving greater velocities, thus explaining the augmented high-energy tails observed for systems bounded by more dissipative sidewalls.

Since PEPT is incapable of directly recording particle collisions, one must consider the possibility that the non-Gaussian profiles observed may simply be due to erroneous data. Denser regions of the system will, clearly, experience an increased collision rate relative to more dilute regions. A high collision rate may result in particle velocities being calculated across a period of time during which one or more collisions have taken place, therefore potentially creating a falsely low average velocity in higher-density regions of the bed and a correspondingly high velocity in more dilute regions, thus creating erroneous high-energy tails in the distribution. However, a simple calculation of the typical free time between collisions based on Enskog theory shows that this time is more than an order of magnitude higher than the data acquisition rate for the current experiments, meaning that such effects should have limited impact on our results. Moreover, results from our prior studies [1] have demonstrated that PEPT can successfully reproduce near-Gaussian profiles for other systems possessing similar packing density dsitributions.

4.2 Thermal Convection in Binary Systems – The Interrelation of Convection and Segregation

Having elucidated the various manners in which the alteration of a system's sidewall material may affect its dynamical properties, we now extend our investigation to the case of granular mixtures – will the effects reported in the previous section have an impact on the distribution of particles within a binary system?

In order to answer the above question, a binary bed comprising a 50:50 mixture of $d = 5$ mm glass ($\rho = 2500$ kgm^3) and steel ($\rho = 7850$ kgm^3) particles was introduced to the system described in the section 4.1. For the sake of clarity and brevity, the subscripts H (for 'heavy') and L (for 'light') will be used to denote the various properties possessed by the steel and glass beads, respectively; for instance T_H represents the temperature possessed by the heavier, steel species. For the main experiments discussed here, the

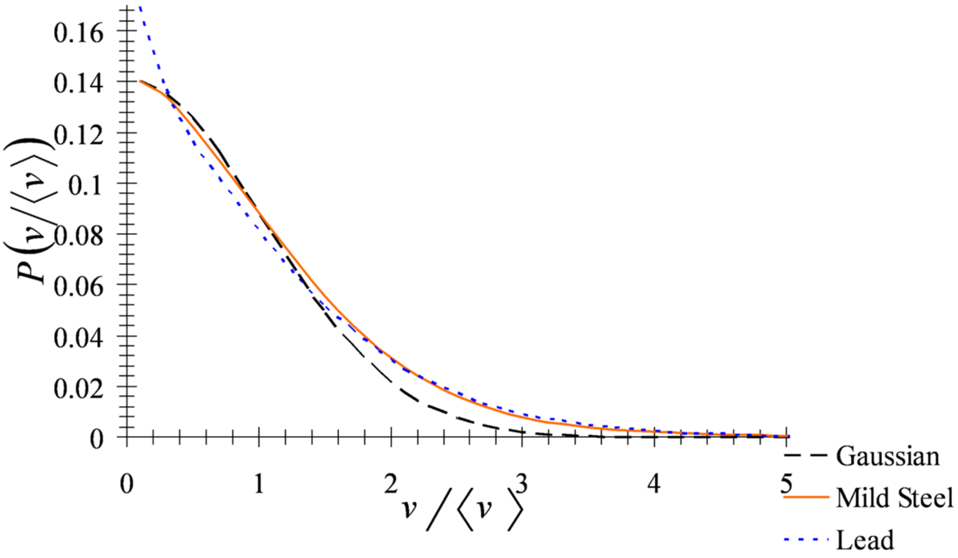

Figure 4.6: Velocity probability density function (vPDF) for the extremal values of particle elasticity explored in experiment, shown alongside a corresponding Gaussian distribution (black dashed line). Data is shown for systems with sidewalls composed of mild steel (solid orange line) and lead (blue dotted line). In all cases, a particle number $N = 856$ is used. Figure taken from our reference [7].

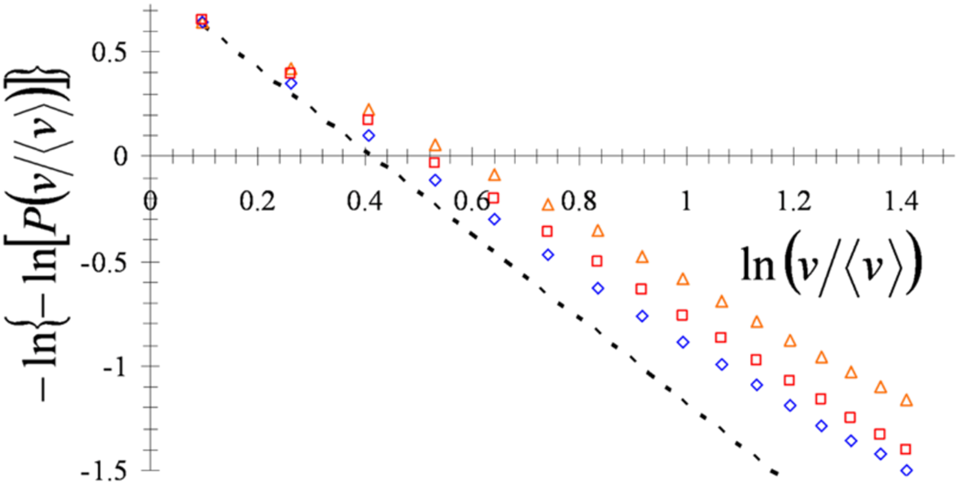

Figure 4.7: Double-logarithmic plot of the high-$|v|$ region of the vPDFs for the case $N = 642$. Data is shown for lead- (orange triangles), tufnol- (red squares) and steel-walled (blue diamonds) systems, with a Gaussian distribution represented by a dashed line. Figure taken from our reference [7].

system is excited with a driving frequency of 70 Hz and an amplitude of 1.17 mm, providing a dimensionless acceleration $\Gamma = 23$ and shaking strength parameter $S = 5.4$. Throughout all experiments performed, the particle number is held constant at 1000, i.e. $N_H = N_L = \frac{N}{2} = 500$, providing a dimensionless resting bed height, N_L, of approximately 2.5 particle layers.

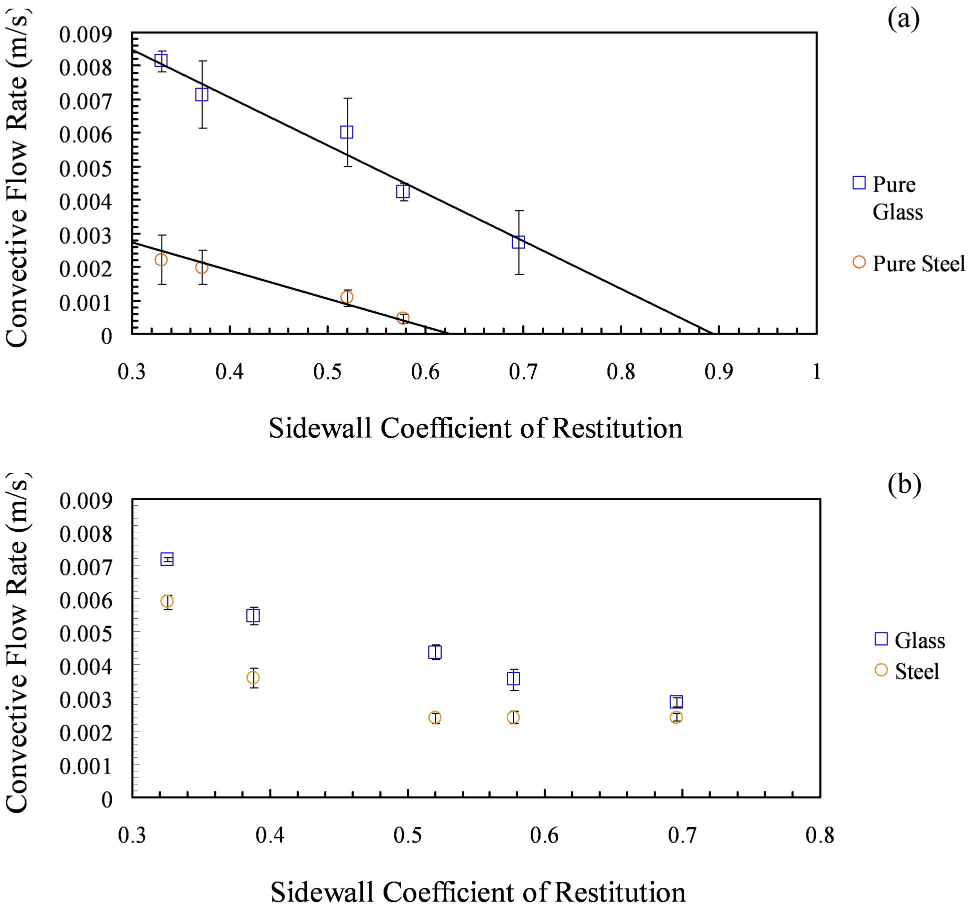

Figure 4.8: Variation of convective flow rate, J, with sidewall elasticity, ε_w, for (a) monodisperse systems of glass (L) and steel (H) spheres and (b) a bidisperse mixture of these materials. In all cases the particle number $N = 1000$, with $N_H = N_L = \frac{N}{2}$ in the binary case. Figure taken from our reference [8].

Before directly discussing the influence of sidewall dissipation on the segregative behaviours of our vibrofluidised bed, we must first address the issue of whether our findings from the preceding section may be expected to apply also to binary systems and, if so, how the observed relationship between convective flow rate, J, and sidewall elasticity, ε_w, might vary for the bidisperse case. Information pertaining to this matter may be seen in Figure 4.8, which compares the convective behaviours of equivalent monodisperse and bidisperse beds.

While the previously observed increase in J with decreasing ε_w holds for relatively dissipative side-boundaries, as the sidewall coefficient of restitution increases, the flow rate seemingly approaches an asymptotic minimal value. It is additionally notable that the (heavier and more dissipative) steel particles achieve this minimal value more quickly (i.e. at a lower ε_w value) than their comparatively light and elastic glass counterparts. The existence of such a plateau implies that for binary, as opposed to monodisperse, beds, there exists an inherent minimal value of convection strength, J. While the authors might speculate as to a cause for this behaviour, we decline to do so at this juncture, as further work is necessary to provide an adequate degree of support for any hypothesis drawn.

A comparison of Figure 4.8's panels (a) and (b) also reveals that, in the binary case, the typical convective flow rate for a glass particle is slightly reduced as compared to the case of a monodisperse system of such particles, while the convection strength for steel grains shows a considerable increase in the mixed system. This latter observation may be relatively simply explained by the differing elastic properties possessed by glass and steel particles: although estimates of particles' ε values vary considerably between studies, it is generally agreed that, for a given impact velocity, glass particles may be expected to possess a higher ε (i.e. be more elastic) than equivalent steel spheres [10, 225, 232]; indeed, our own experimental measurements (which are discussed in detail in section 5.1) produce the same result. This being the case, we hypothesise that the reduced dynamics observed for a binary glass-steel system as opposed to an equivalent unary ('pure') glass bed may correspond simply to the lower *average* coefficient of restitution in this second case. A similar argument may be used to explain the *increased* kinetics of the bidisperse system relative to the (more dissipative) pure-steel bed.

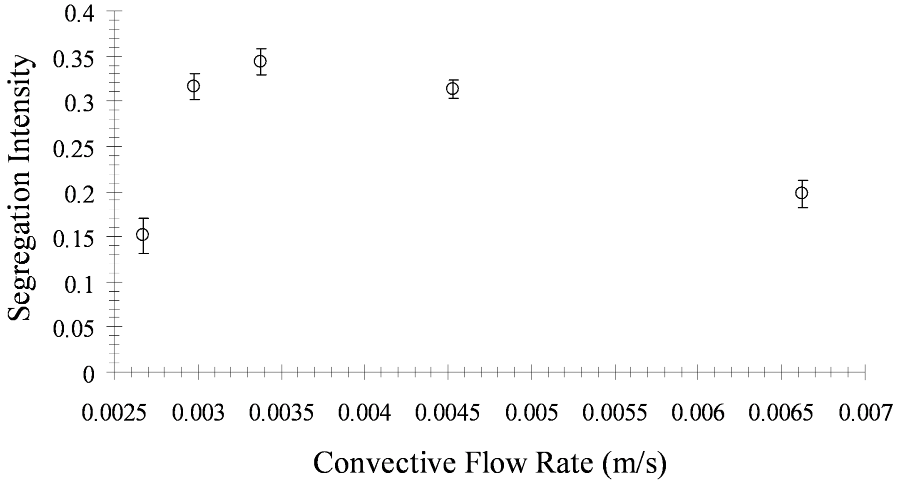

Figure 4.9: Segregation intensity, I_s, (as defined in section 3.2.2) as a function of the system's average convective flow rate for a 50:50 by volume binary mixture of glass and steel particles. In this image, I_s remains unnormalised, such that a value $I_s = 0.5$ represents complete segregation, while $I_s = 0$, as usual, indicates perfect mixing between species. Figure taken from our reference [8].

Figure 4.9 shows, perhaps somewhat surprisingly, a distinct absence of the simple, monotonic relation between convection strength and segregation that one might expect from previous studies of convective granular mixtures [112, 233–237]. We do not here intend to imply that previous studies are flawed or incorrect – indeed, results similar to those of [112, 233–237] can be reproduced in our own system by considerably reducing the driving strength, V, or augmenting the bed depth, N_L. Rather, this is emphatic evidence that there exists a stark distinction between the dynamical behaviours of dense, weakly fluidised systems and highly excited, gaseous systems, demonstrating the necessity that those in the field of granular physics do not naively assume findings from one dynamical regime to be directly transferrable to others. Also notable from Figure 4.9 is the *significant variation* in the degree of segregation exhibited by the system across data sets, despite the fact that the systems to which each of the data points correspond are entirely identical in all aspects other than the walls by which the system is bound. This is a significant result, as it strongly suggests the degree of segregation/mixing within a system may be controlled without necessitating the alteration of the properties of the particles forming the bed *or* the manner in which the system is excited. Such a finding may potentially prove highly useful in industries where segregation is an issue as, clearly, it would be undesirable to change the properties of a product purely to promote/reduce mixing. Similarly, in many cases it may be incommodious or indeed impossible to alter the manner in which beds are excited – for instance in the case of vibration during transportation, which is known to cause the unwanted separation of granular mixtures [105].

Although, as previously stated, the relationship between I_s and J does not obey a simple, monotonic trend, that is not to say that the observed behaviour cannot be understood. Our data show that, in actual fact, the individual particle species of which the system is composed may possess *different flow rates*, even when part of the same system. While there exists no direct, consistent relationship between the degree of segregation observed and the convective flow rate of either individual particle species or, as we have already discussed, the average or total[2] convection rate, $\bar{J}$, for the system as a whole, the same is not true for the *ratio* of flow rates between species, $\tilde{J} = \frac{J_L}{J_H}$.

The influence of the ratio of convection rates between species, $\tilde{J}$, on I_s may be seen in Fig. 4.10(a), which shows a monotonically increasing relationship between the two parameters. The decreasing gradient of the plot for large $\tilde{J}$ implies that there exists a maximal extent to which the bed may become segregated which, considering the dilute

---

[2] Throughout this thesis, the terms "*average convective flow rate*" and "*total convective flow rate*" are used interchangeably to describe the value of convection strength ($\bar{J}$) calculated as described in section 3.2.2 using data for *both heavy and light* particles simultaneously – i.e. particle velocities are summed for both species, and averaged over the combined total number of data points for both data sets. While the term "*average*" is perhaps more technically accurate, it is felt that the phrase "*total convective flow rate*" better conveys the fact that $\bar{J}$ incorporates both/all components of the granular mixtures under investigation.

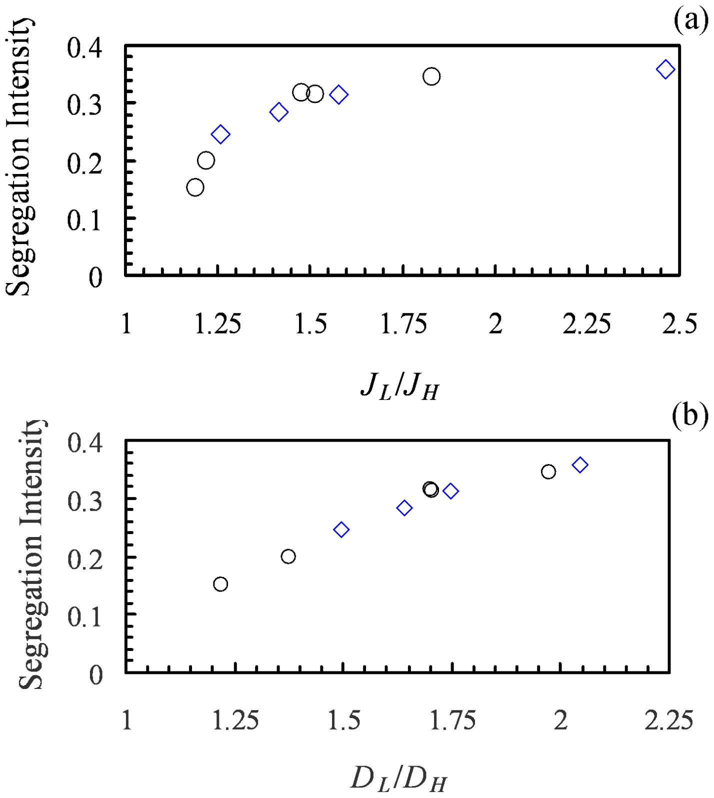

Figure 4.10: Segregation intensity, I_s, as a function of (a) the convection rate ratio, $\frac{J_L}{J_H}$, and (b) thel diffusivity ratio (i.e. the ratio of self diffusion coefficients, $\frac{D_L}{D_H}$). Data is shown for the case in which convective and diffusive motion is varied through alteration of the system's driving parameters (diamonds) as well as for the situation in which the system's dynamics are altered through a variation in sidewall material (circles). Figure taken from our reference [8].

nature of the systems investigated is not surprising – due to the large void space present, it is highly probable that a percentage of light particles (which will tend to segregate upwards) will simply 'fall through' the system without interacting with other particles [238, 239], thus inevitably causing a degree of remixing, even in conditions highly favourable to segregation.

The contradistinction of the trends observed in Figures 4.9 and 4.10(a) can be understood, on a qualitative level, due to the fact that denser and therefore, in our case, heavier particles are less likely to be pulled into a convective stream [138]. Thus, the initially confounding observation that mixing is improved for both the strongest *and weakest* total convection strengths can be explained as follows: in the limit of very weak total convection, there will, implicitly, exist only a small disparity in particles' individual convection rates. In the opposite, high-$\bar{J}$ case, both particles species will be equally likely to be successfully entrained in the convective flow, once again leading to similar J values for both species. Hence, both high and low $\bar{J}$ correspond to the same lower limit of $\tilde{J}$. For the case of more moderate total convection strength, however, one may expect lighter species to exhibit considerable convective motion while heavier species remain relatively unperturbed, resulting in a significant disparity between the convection strengths corresponding to each component of the bed. A visual illustration of the differing degrees of segregation observed for each of the cases described may be seen in Fig. 4.11.

We now propose a mechanism by which systems exhibiting more strongly differing convection strengths may, as observed, be expected to produce a greater separation of particle species. The theoretical work of Garzó [133, 135] provides evidence that, for dilute, highly fluidised systems such as those currently under investigation, the extent of segregation observed within a system is determined (as discussed in section 2.2) by a balance between the separation of particle species arising due to thermal diffusion, and the remixing of particles due to 'ordinary', Fickian diffusion. Garzó's theory, however,

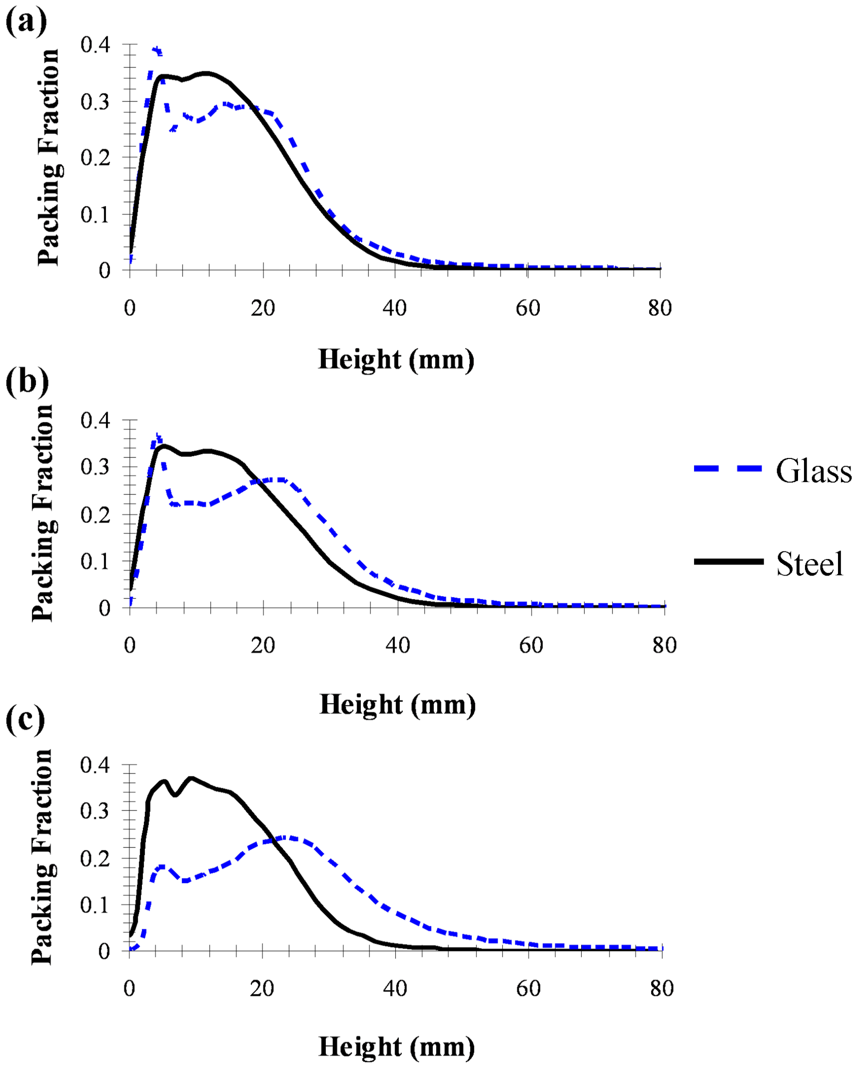

Figure 4.11: One-dimensional packing profiles providing a visual illustration of the vertical segregation observed for binary systems of glass and steel particles with horizontal boundaries constructed of (a) steel (ε_w = 0.70), (b) perspex (ε_w = 0.33) and (c) brass (ε_w = 0.58). All other system parameters are held constant for all images shown. Figure taken from our reference [8].

was developed under the assumption of a convection-free bed. We posit that, in convective systems, there exists a third, pseudo-diffusive component due to convection [240]. Further, we propose that the decreased likelihood of heavier particles being 'swept up' into the convective stream will lead to a relatively reduced 'diffusivity' for this species, which will naturally act to create a greater imbalance between the diffusive processes favouring segregation, and those opposing it. The greater the disparity between species' convection rates, the greater this inequality becomes, thus explaining the enhanced segregation for systems in which $\tilde{J}$ is larger. The monotonically increasing trend observed in Fig. 4.10(b)) between I_s and $\frac{D_L}{D_H}$ is indeed what we would expect based on the preceding arguments, providing a measure of support for this hypothesis. However, further work is required in order to definitively confirm the true mechanism underlying our observations.

Having established a cogent argument supporting the concept that the ratio of convective flow strengths is a determining factor in the segregative behaviours of a dilute vibrofluidised bed, we next provide evidence that $\tilde{J}$ is in fact the *dominant factor* affecting the steady state segregation reached by the systems investigated – as discussed at length in the previous section, the alteration of a system's sidewall properties does not only influence convective flow, but may additionally impact a number of other quantities pertaining to the state and dynamics of a system. This being the case, our observations may, potentially, be ascribed to other sources, as opposed to arising predominantly from the variation of $\tilde{J}$, as has been hypothesised thus far.

In order to provide a resolution to the above quandary, a series of experimental runs were conducted using fixed values of sidewall elasticity, ε_w, and varying the convective behaviours of the system by altering the frequency, f, and amplitude, A, of driving. Specifically, values in the ranges $50 \leq f \leq 90$ and $0.66 \leq A \leq 1.69$ were used. The specific combinations of f and A implemented were deliberately chosen so as to also allow a large range of dimensionless driving accelerations, Γ, and input energies, S, to be explored. Amazingly, the data points acquired in this manner were shown to collapse onto the same curve as those acquired with fixed driving and varied ε_w. This result strongly suggests a lack of strong, direct dependence on the system's driving parameters (f, A, Γ, S) *or* any previously unaccounted for wall effects. Moreover, since considerable variations in temperature, density and the spatial distributions thereof are a natural consequence of such large variations in the excitation of the system, the observed collapse also implies a minimal dependence on these quantities. In summary, our findings strongly suggest that the relative convection rate, $\tilde{J}$, between particle species is in fact the primary criterion in determining the degree of segregation exhibited by our systems.

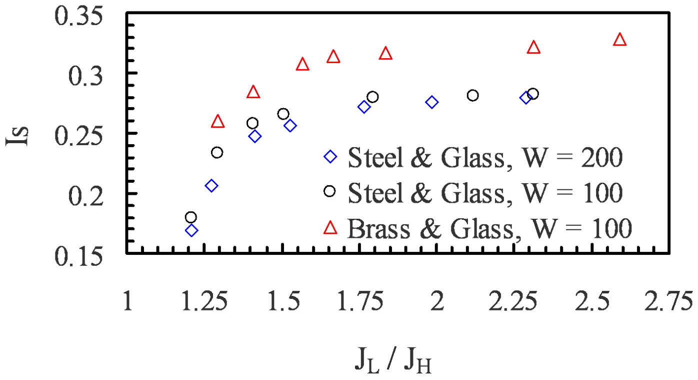

Figure 4.12: Simulated data showing the relationship between segregation intensity, I_s, and the ratio of convective flow rates, $\frac{J_L}{J_H}$, for various particle combinations and system widths (Note: in the published paper from which this image originally appeared, the width of the system was denoted 'W' as opposed to '$L_{x,y}$' as is the case in the current work). Figure taken from our reference [8].

Further investigations of the system, intended to both validate and extend our experimental findings, were undertaken using discrete particle method simulations produced using MercuryDPM. The code was set up as described in detail in section 3.3, with the simulations emulating as closely as possible the experimental situation through the implementation of all known experimental parameters. Although the simulations were not found to *quantitatively* reproduce the exact I_s values associated with each given $\tilde{J}$ value, a pleasing agreement was observed between the general trend produced by the simulations and that corresponding to the PEPT data (see Figure 4.12), lending credence to the validity of our experimental findings.

Additional simulations were also performed taking, for the H particles, known experimental values of the restitution coefficient ($\varepsilon = 0.61$) and density (ρ = 8500 kgm^{-3}) corresponding to *brass*, as opposed to steel, particles. The general trend in I_s vs $\tilde{J}$ observed was once more found to remain consistent with our initial findings, as may be seen from Fig. 4.12. However, several differences were also noted between the systems comprising brass and glass particles and those composed of steel and glass particles. Firstly, as shown in Fig. 4.12, the magnitude of the observed segregation is, for all $\tilde{J}$ values, increased as compared to the steel-glass case. This is to be expected, as brass particles are both heavier *and* more dissipative than their steel counterparts, meaning that they will naturally have a greater tendency to segregate due to both density- *and* elasticity-driven mechanisms. It was also found that although the *total* convection rate, $\bar{J}$, is somewhat diminished for the brass-glass case, the *ratio of convective flow rates*, $\tilde{J}$, is comparatively increased for a given set of system parameters. The observed increase in $\tilde{J}$ is to be expected from our previous hypothesis – the greater ρ and lower ε possessed by brass particles, as compared to steel particles, means that they will be still harder to 'drag' into the convective stream, further exacerbating the difference in flow rate between these brass spheres and the glass grains making up the remainder of the bed, as discussed above. The decrease in total convection rate, meanwhile, can likely be explained in the framework of our discussion in section 4.1: for beds of glass and brass particles, as opposed to those comprising glass and steel constituents, the system's average coefficient of restitution will be comparatively lower. As discussed in sections 2.1 and 4.1, wall-induced thermal convection is driven by a differential between the particle density and temperature near the side-boundaries of the system and the corresponding values of these quantities in the system's central region. Moreover, as shown in the previous section, the more significant the difference between the particle elasticity, ε, and that of the bounding walls, ε_w, the greater the disparity in density and temperature between the inner and outer regions, and the stronger the convection produced. By introducing the brass particles to the system and lowering the average, particle-particle restitution coefficient, we reduce the contrast between ε_w and ε, leading to the observed reduction in overall convection strength. Support for this origin of the reduced $\bar{J}$ for brass-steel systems was provided by conducting a series of simulations in which the density of the H species was held at the relevant value ($\rho = 7850$) for steel particles and only the restitution coefficient varied to the relevant value for brass, whereupon similar effects on $\bar{J}$ were observed as for the 'true' brass-glass case. The qualitative differences noted here between glass-steel and glass-brass systems were later confirmed experimentally. As it is challenging, in an experimental situation, to create convection within more internally dissipative systems – or at least to create adequately strong convection that the measured J values remain statistically significant compared to the noise inherent to experimental measurements – only a limited number of experimental data points could be successfully acquired. Nonetheless, the experimentally observed variations in the typical degree of segregation, I_s, the absolute and relative values of convection strength, $\bar{J}$ and $\tilde{J}$, were found to correspond closely to those seen in simulation.

In order to test the robustness of our observations, a series of simulations were conducted for the case of a larger system. Specifically, the implemented values of L_x, L_y and L_z were doubled, leading to a four-fold increase in the container's base area. In order to maintain consistency between results obtained from this new system and those previously discussed, the number of particles in the system was also increased by a factor of four, such that the resting bed height, N_L, and hence the key dissipative control parameter, $F_d = N_L(1-\varepsilon)$ [61], remain constant. The highly similar behaviour observed for the $W = 100$ mm and $W = 200$ mm cases (see Fig. 4.12) provides further evidence that *direct* wall effects (i.e. as opposed to the *indirect* effects occurring due to the convective motion which, in turn, arises due to the sidewalls) do not play a significant rôle in the bed's segregative behaviours. The close correspondence of the trends also lends further weight to the validity of our findings.

An additional advantage to the inclusion of simulations in our work is that they allow us to investigate also the *time-dependent* behaviours of our systems, a feat which, although not impossible, is not easily achieved using PEPT – in particular for the case of multi-component systems. Our analysis shows that despite the considerable variation in the *magnitude* of segregation, I_s, with $\tilde{J}$, a similarly large variation in the *rate* of segregation, was not observed. Indeed, the typical segregation timescale, τ_s (defined as the time taken for the system to evolve from its initially perfectly mixed state to its final, steady-state I_s value) was found to remain approximately constant for all ε_w, and hence $\tilde{J}$, values tested. To be more precise, any observed variations in τ_s with $\tilde{J}$ were found to be insignificant compared to the innate statistical fluctuations arising due to the nondeterministic nature of a system's evolution towards its equilibrium distribution (i.e. its steady segregated state). It is finally worth noting the impressively short time required for a system to achieve steady state segregation, with $\tau_s = \mathcal{O}(10\text{s})$ in all tested cases. Considering also that both experimental and simulational data sets suggest a typical convective timescale of the order of 1 s, it appears that only a few convective cycles are required in order for a system to achieve its equilibrated state. Although, as previously mentioned, τ_s cannot be accurately determined from PEPT data, visual observations of the experimental system certainly support this result.

4.3 Thermal Convection in Binary Systems – Energy Non-Equipartition

So far we have established that the sidewalls of a system may significantly influence not only the convective and segregative behaviours of a granulate but also play a vital rôle in determining the spatial distribution of granular temperature and the manner in which this temperature is distributed between the various components of motion. We now pose the question of whether an alteration in ε_w might additionally alter the temperature distribution between *particle species*?

The experimental system used to investigate the partition of energy between species is identical to that described in section 4.2 in terms of its total particle number (N), as well as the fractional concentration of heavy (steel) and light (glass) particles, the typical driving parameters (f, A, Γ and S), the dimensions ($L_{x,y,z}$) and wall materials of the containers used.

Early studies of monosized binary systems [10] suggested that the distribution of energy, and hence temperature, between differing particle species was determined solely by the particles' mass ratios, specifically noting an independence of the driving velocity, the particle elasticity (and the ratio thereof), the relative number of each particle species and even the bed's packing density. Later studies [144, 228, 241, 242], however, provide strong evidence of an additional dependence on particles' elastic properties, yet continue to observe the previously noted constant temperature ratio between the two species throughout the experimental volume for any given system, even those in which the spatial distribution of temperatures is highly non-uniform [136]. It is notable from the aforementioned studies that the general consensus in the field is that only the material properties of the particles themselves can influence the manner in which energy is partitioned between dissimilar particle species. In this section, we attempt to challenge this assumption, demonstrating that the variation of a system's sidewall properties, and hence the convective and segregative behaviours of a granular bed, can in fact alter the distribution of energy between unlike particles.

As may be seen from Figures 4.13 and 4.14, the alteration of the sidewalls bounding the system has a definite and significant effect on the distribution of energy between particle species, despite the fact that the densities, $\rho_{H,L}$, and elastic properties, $\varepsilon_{H,L}$

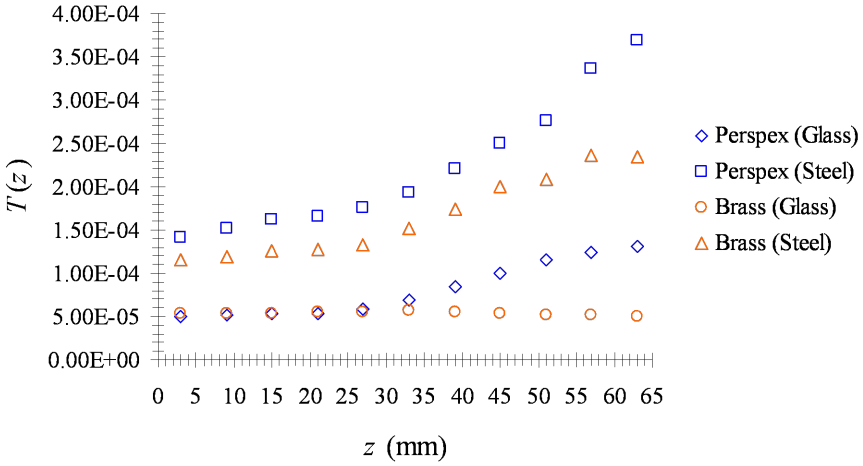

Figure 4.13: Local granular temperature, $T(z)$ (measured in Joules), plotted as a function of z, the height from the system's base. Data is shown for each of the individual components of a glass/steel binary mixture for systems bounded by both brass (ε_w = 0.52) and perspex (ε_w = 0.33) sidewalls, as indicated in the Figure – in each case, the legend provides this information as *[wall material] ([particle material])*. Figure taken from our reference [9].

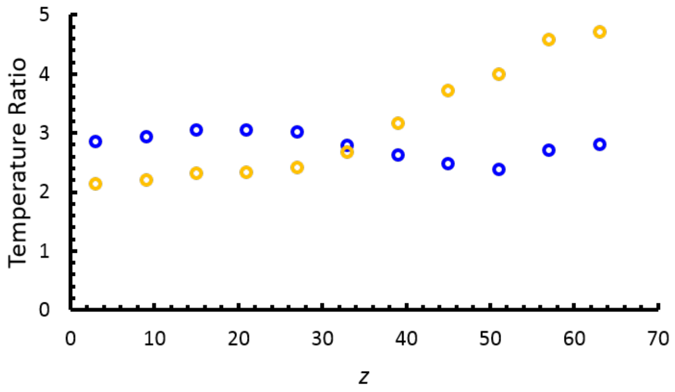

Figure 4.14: Variation with height, z, of the granular temperature ratio, $\gamma = \frac{T_H}{T_L}$, for the data shown in Figure 4.13. Here, blue circles represent the ratio for a perspex-walled system and orange circles that of a brass-walled system. It is interesting to note from this Figure that the temperature ratio within the bulk of the material ($z \lesssim 30$ mm) remains relatively constant, as expected from previous studies [10], yet varies significantly for large z. This is likely due to the fact that the upper regions of the system exist in the dilute Knudsen regime where the system's dynamics are governed by differing processes [11, 12].

of the particles under investigation remain unchanged, as indeed do all other major system parameters. The effect of varying ε_w on the distribution of particle energies and temperatures is, however, not straightforward, and indeed displays some rather unexpected and counterintuitive results; firstly, it is notable from Fig. 4.13 that, for the cases shown, the system with the *more* dissipative sidewalls possesses a notably *higher average temperature.* A second somewhat surprising observation is that, as may be inferred from Fig. 4.15, better mixed systems seemingly exhibit a *greater disparity in temperatures* between particle species! Since this latter observation is of more direct relevance to our main area of discussion, we shall begin by addressing this matter.

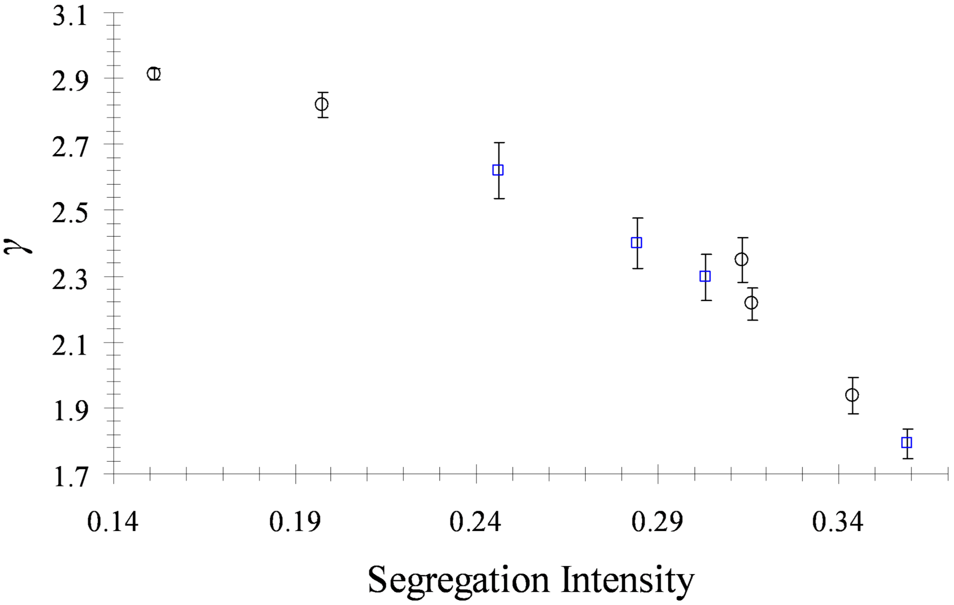

Figure 4.15: Temperature ratio, $\gamma = \frac{T_H}{T_L}$, as a function of segregation intensity, I_s. Data is shown for the case in which I_s is altered due to a variation in sidewall dissipation (circles), as well as that in which the degree of segregation is altered through a change in the system's driving parameters (squares). In both cases, all other system parameters are held constant. Figure taken from our reference [9].

Before specifically discussing the influence of sidewall-induced convection and segregation on the inter-species partition of kinetic energy, it is firstly important to ensure that the observed differences in the distribution of energy between differently massive particles can indeed be attributed directly to the convective motion and resultant degree of species-separation, and not to other variations in the system's state that may arise due to a variation in sidewall dissipation – namely the spatial distribution of packing density, η, and temperature, T. It is firstly worth noting that previous studies of systems similar to that described here [10, 136] have reported that the specific forms of density and temperature profiles are *unimportant* in the determination of the temperature ratio $\gamma = \frac{T_H}{T_L}$ in which our interest lies. A clear demonstration of this independence may be seen in Figure 4.16, which shows, for two exemplary systems, a near-constant value of γ throughout the bulk of the granular bed despite considerable variation in both the local number density for the system as a whole, as well as the local volume fraction or *concentration*, φ, of each individual species. This observation agrees well with the findings of previous studies, as discussed above.

Further evidence that J and I_s, as opposed to other system properties, play the dominant rôle in determining γ (at least for the case of a constant $\frac{\rho_H}{\rho_L}$ and $\frac{\varepsilon_H}{\varepsilon_L}$) can be seen in Fig. 4.15. Here, in a manner similar to that discussed in relation to section 4.2's Figure 4.10, we observe the collapse onto a single curve of data corresponding to varied wall dissipation ($0 \lesssim \varepsilon < 0.7$) and varied driving conditions ($0.88 < S < 18.6$), strongly implying a lack of direct dependence of γ with these parameters, and further strengthening the argument that specific values of, and indeed spatial distributions of, η and T are similarly inconsequential.

Now that we may assume, with some certainty, that the relative temperature, γ, possessed by particles is primarily dependent on the convective motion, and hence degree of segregation, I_s, exhibited by the system, we now attempt to explain the origin of this dependence, and its somewhat unexpected *decrease* with increasing species separation. As with the work performed in the previous section, the observed degree of energy partition shows no direct dependence on the *absolute* convective strength, $\bar{J}$, but *does* demon-

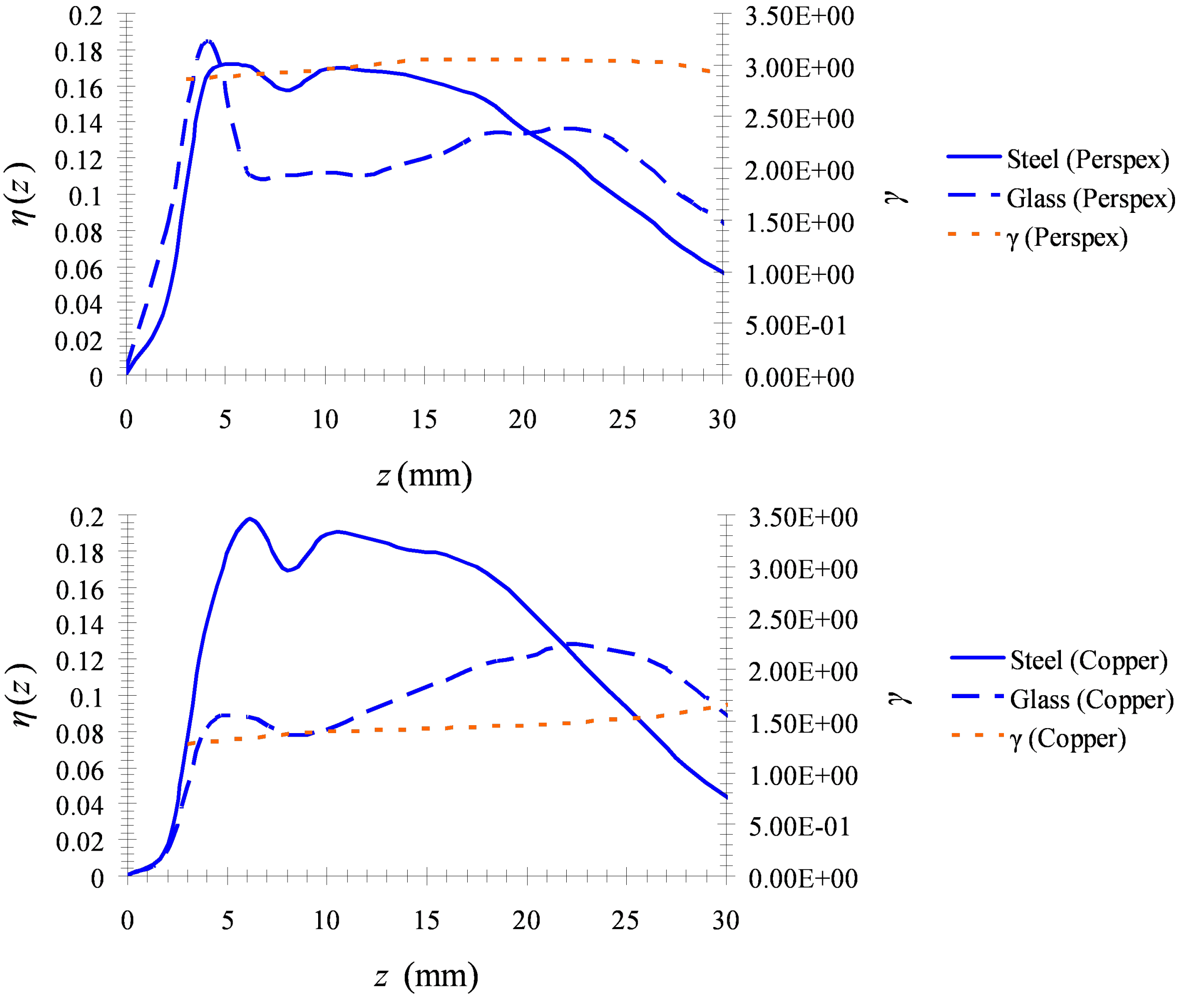

Figure 4.16: Experimentally acquired packing profiles for the steel and glass components (blue solid and dashed lines, respectively) of a binary bed shown alongside the corresponding temperature ratio, $\gamma = \frac{T_H}{T_L}$, between the two species (orange dotted lines). The upper image shows data for a perspex-walled system ($\varepsilon = 0.33$), while the lower image corresponds to an otherwise identical system bounded instead by copper walls ($\varepsilon = 0.58$). Figure taken from our reference [9].

strate a monotonic relationship with the *relative* convection strength between species, $\tilde{J}$, and hence, by definition, I_s. It is this latter parameter which we believe gives rise to the observed energy partition behaviour shown in Figure 4.15. We posit that an increase in the level of species separation, I_s, (i.e. a less well-mixed system) will lead to a relative *decrease* in the number of collisions between unlike particles and, correspondingly, a comparative *increase* in same-species interactions. Previous, theoretical work [243] suggests that an increasing proportion of *inter-species* collisions will lead to an augmented temperature, T_H, for the system's heavier component – hence leading to a greater value of $\gamma = \frac{T_H}{T_L}$ for simple binary systems such as ours. Conversely, a greater proportion of *intra-species* interactions may be expected to provide a relative increase in the temperature of lighter and/or less dissipative particles – resulting in a *decrease* in γ. Thus, for better-mixed (lower I_s) systems where inter-species interactions are more dominant, one would indeed expect a greater disparity between heavy and light particles, with the inverse being true in more segregated systems. Our findings agree well with these expectations, as is apparent from Figure 4.15.

It is additionally interesting to note the *form* of the relationship between γ and I_s, which seemingly demonstrates a tendency toward an *asymptotic maximum* as the system approaches a state of perfect mixing ($I_s = 0$). Intriguingly, the approximate value to which γ tends corresponds closely to the mass ratio of the glass and steel particles used in experiment, $\frac{m_H}{m_L} \sim 3.13$, implying that complete mixing between particle species leads to an equilibration of particles' *fluctuating velocities*, as opposed to kinetic energies or temperatures. On close inspection, it is noticeable that the γ value of the asymptote is in fact likely to be slightly below the ratio $\frac{m_H}{m_L}$, although this is perhaps to be expected due to the relatively decreased elasticity of the steel particles compared to their glass counterparts. Of course, further study is required to confirm whether an equilibration of these fluctuation velocities is indeed the origin of the observed behaviour, or whether the correspondence between $\frac{m_H}{m_L}$ and the asymptotic maximum of $\frac{T_H}{T_L}$ is merely coincidental.

If our hypothesis is indeed correct, this finding could potentially prove useful in the formulation of future hydrodynamic models of convective, binary systems through the provision of a *known boundary condition*, $\gamma = \frac{m_H}{m_L}$ for the limiting case in which both particle species exhibit equal convective flow rates and complete mixing.

We lastly discuss the surprisingly non-monotonic relationship between the total temperature of the bed and the degree of dissipation provided by the system's sidewalls, a matter which we briefly touched upon earlier in this section, whereupon we noted that, under certain circumstances, a system with *more dissipative* side-boundaries may possess an overall *higher temperature*. Clearly, one would intuitively expect that the introduction of an additional source of energy dissipation to a system would result in a decrease in its overall temperature, and while this is certainly the case for certain situations, this presumption does not hold in others. Unlike the previously discussed temperature *ratio* between particle species, the *total temperature* shows no clear-cut dependence on either I_s *or* $\bar{J}$ individually (as evidenced by Figure 4.17). Rather, we propose that it is a *combination* of convective and segregative effects which determines the temperature of the system for a given, fixed driving strength. For the current situation, in which the heavier particles are also more dissipative, one may expect the internal dissipation of the system to be minimised when the system is well mixed, as in a segregated state, a greater proportion of more dissipative particles will exist near the base of the system, effectively reducing the energy input to the system. This may, in part, explain the increase in total temperature, T_{tot}, observed for very low and very high total flow rates (see Fig. 4.17), which (as discussed in the previous section) correspond to the most completely mixed systems. The fact that, for similarly well-mixed systems, the greatest value of T_{tot} in fact occurs for that with the *most dissipative sidewalls* may be further explained by the fact that these sidewalls produce the strongest convective flow (as detailed in section 4.1); not only are highly convective systems more 'active', which will naturally lead to the acquisition of higher temperatures [244], but the strong convective flow also causes a small but significant *expansion* of the (more dissipative) steel component of the bed, resulting in a reduced average dissipation within the system's bulk [67].

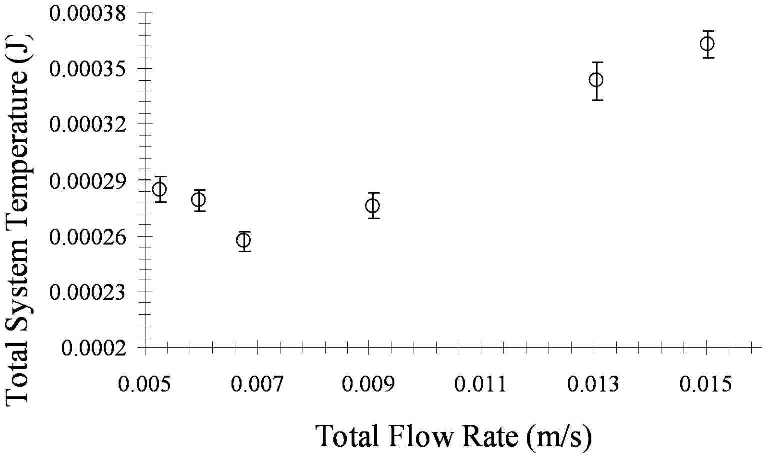

Figure 4.17: Temporally and spatially averaged *total* temperature ($T_H + T_L$) for both components of a glass/steel binary system as a function of the system's total flow rate ($J_H + J_L$). Here, data is shown only for the case of varied ε_w, as opposed to varied driving strength, as the latter will additionally influence the energy input to the system, hence obscuring the J-dependence with which this image is concerned. Figure taken from our reference [9].

4.4 Frictionally Driven Convection and Segregation in Unary, Binary and Ternary Systems

In the final section of this chapter, we extend our investigation to the case of ternary beds and the situation of frictionally-driven (as opposed to buoyancy-driven) convective flow. For this investigation, we choose a total particle number $N = 6000$ and a system of dimensions $L_x \times L_y \times L_z = 40 \times 40 \times 200$ mm, providing a dimensionless resting bed height of $N_L = 33.8$. This N_L value is considerably increased compared to the values used in previous studies, resulting in an increased influence of friction within the system, and hence the introduction of the previously unexplored frictionally driven convective flow. In order to ensure consistency between experiments investigating monodisperse, bidisperse and ternary systems, particles of equal size ($d = 3$ mm), but differing density, are used, and the total particle number, N, is held constant for all degrees of polydispersity, thus ensuring that the total resting bed depth remains constant for all systems explored. Specifically, in the binary case, we choose $N_A = N_B = \frac{N}{2} = 3000$ (i.e. $N = 6000$), while in the ternary case we take $N_A = N_B = N_C = \frac{N}{3} = 2000$ (providing, once again, a total particle count of $N = 6000$).

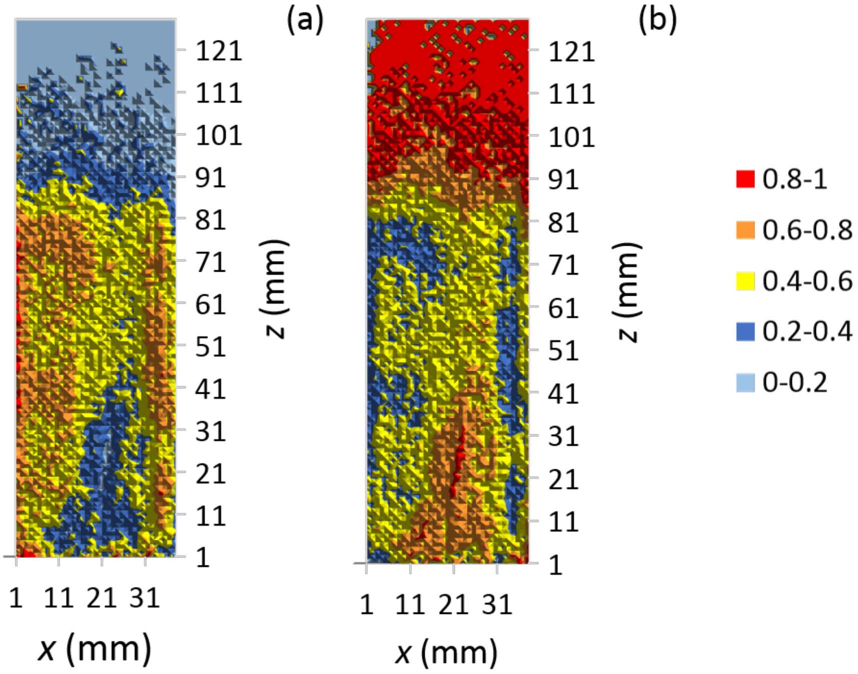

Figure 4.18: Two dimensional particle concentration plots showing the spatial distribution of light (L) polyurethane particles (image (a)) and heavy (H) steel particles (image (b)) within a system comprising a 50 : 50 mixture of these two species. The system shown here is driven with a fixed dimensionless acceleration $\Gamma = 11$. In each image shown, the local fractional concentration, ϕ, of the relevant species can be determined from the colour key provided. Figure taken from our reference [2].

In our experiments, three differing species of particle are used: steel ($\rho = 7850$ kgm^{-3}), glass (ρ = 2500 kgm^{-3}) and polyurethane (ρ = 1200 kgm^{-3}). For the sake of brevity and clarity, the steel, glass and polyurethane particles are simply referred to as 'heavy' (H), 'medium' (M) and 'light' (L), respectively, throughout this section. We explore unary systems of each of the above species (L, M, H), as well as all three possible binary combinations thereof (LM, LH, MH) and, finally, ternary systems comprising all three particle classes (LMH).

As with previous experiments, the system is vibrated sinusoidally in the vertical direction. In the current experiment, the frequency of vibration is held constant at a value f = 40 Hz, while the amplitude of vibration is varied in the range $A \in (0.776, 2.64)$ mm, thus providing a range of dimensionless accelerations $\Gamma \in (5, 17)$ and dimensionless shaking strengths $S \in (1.29, 15.0)$. By exploring the system's behaviour over this considerable range of excitation strengths, we can ensure that our findings are robust and generalisable or, where this is not the case, specifically expound the range of validity of our observations.

It is immediately obvious from Figures 4.18 and 4.19 that the equilibrium distribution of particle species within *denser* systems exhibiting *frictionally driven* convection differs markedly from the relatively simple, vertical segregation observed in the dilute, highly fluidised systems discussed in previous sections[3]. The images presented in these Figures show some striking and unexpected features – of particular note is the fact that, for the system shown in Fig. 4.19, the heaviest (H) particle species possesses a slightly *higher steady-state vertical centre of mass position*, h, than either of the lighter (M, L) species, in seeming defiance of the principle of potential energy minimisation [245]. The origin of this initially surprising observation becomes much clearer, however, when one compares the particle concentration distributions shown in Figure 4.19 to the corre-

---

[3] Note that in the binary (ternary) concentration fields shown, the data presented correspond to a combination of two (three) time-averaged data sets, each produced using a different tracer particle. The inclusion of data obtained from *all species present* ensures a more accurate representation of the system than would be achievable by tracking only one species and inferring the behaviour of the other species present.

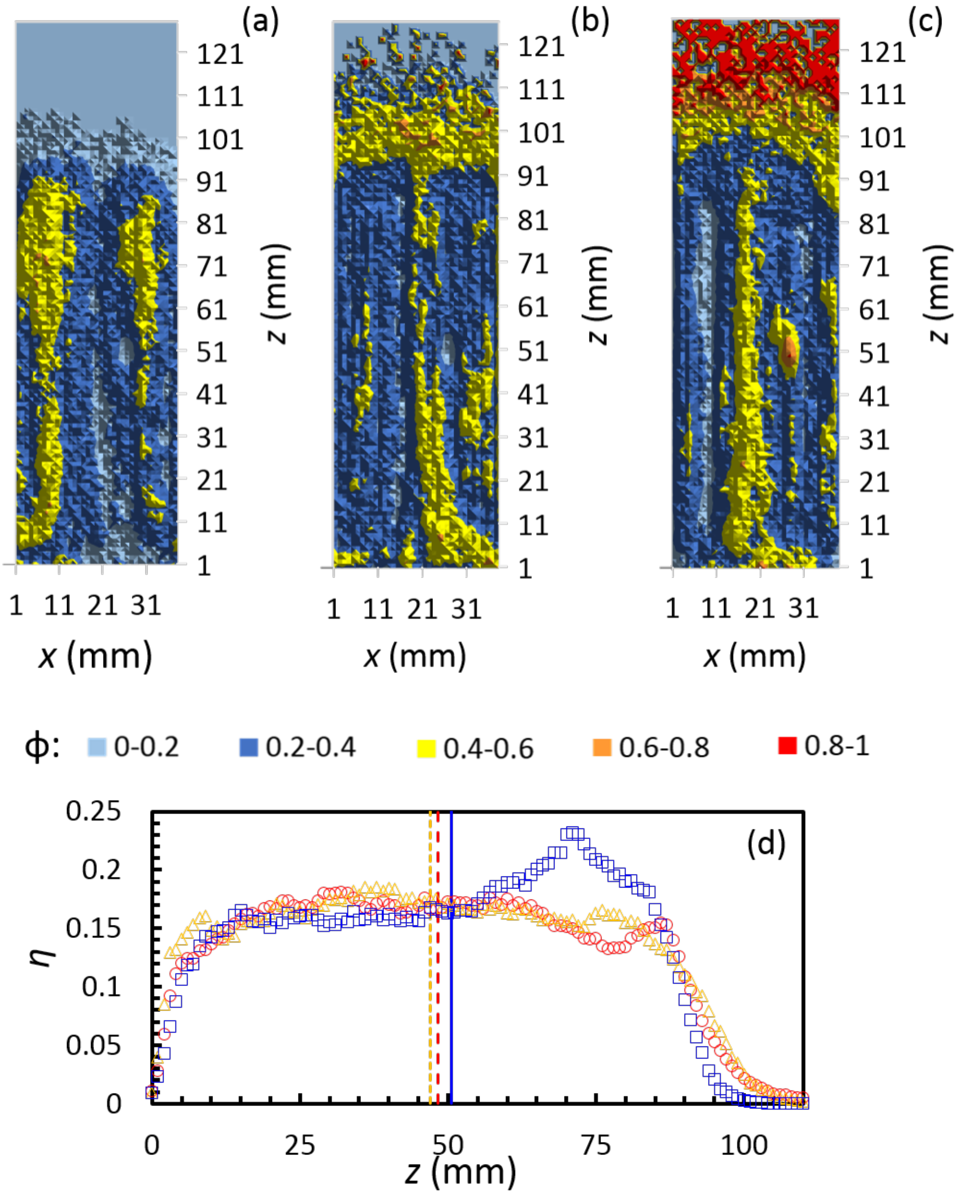

Figure 4.19: *Top:* Two-dimensional particle concentration plots showing the spatial distributions of steel (H) particles (image (a)), glass (M) particles (image (b)) and polyurethane (L) particles (image (c)) for a $\frac{1}{3}:\frac{1}{3}:\frac{1}{3}$ mixture of these species. The system is driven with an acceleration $\Gamma = 11$. In each image shown, the local fractional concentration, ϕ, of the relevant species can be determined from the colour key provided. *Bottom:*Image (d) shows one-dimensional projections of the data presented in panels (a)-(c), with blue squares corresponding to H particles, yellow triangles representing M particles and red circles denoting the local packing fractions of the L species. The positions of the time-averaged vertical mass centres of each species are marked by solid, dotted and dashed lines for the H, M and L species respectively. Figure taken from our reference [2].

sponding velocity vector fields shown in Figure 4.20. It is immediately notable from a comparison of these figures that the heaviest (or, in the case of binary systems, heavi*er*) particles tend to occupy spatial regions corresponding to the *centres* of the convection cells present. The lightest/lighter particles, meanwhile, are largely excluded from these regions, existing predominantly in the fast-flowing outer regions of the cells, i.e. at the edges and centre of the system. A dilute and highly energetic 'gas' comprising almost exclusively light (L) species particles is also typically observed in the uppermost region of the container, while a large proportion of L and M particles (if present) are generally found near the system's base.

This rather complex distribution of particles can, perhaps, be explained in terms of the findings of previous studies. Firstly, it has been previously demonstrated [112, 149] that heavier particles may indeed be expected to migrate toward the centres of convection rolls. Although a direct explanation of this behaviour has, to the best of our knowledge, never been provided in the literature, we tentatively propose a possible mechanism underlying our observations; as touched upon briefly earlier in this section, the distribution of particles within a physical system may be expected to tend toward its lowest energy state, allowing mechanical stability to be achieved. This being the case, it makes sense that the *heaviest particles* will migrate towards regions in which flow is *slowest* (i.e. near the convection centres), thus minimising kinetic energy. Through a similar argument, one may also expect the lightest particles to predominantly occupy the fastest-flowing regions of the bed. The fact that the uppermost and lowermost regions of the bed are also dominated by lighter particles may similarly be explained by the known tendency of lighter or smaller particles to preferentially occupy regions of high temperature [131,246] – in this case the very dilute region at the top of the bed, and the region at the bottom of the container, directly adjacent to the system's energy-providing base (see Fig. 4.21). The combination of these effects provides a coherent explanation for the observed distribution of particle species in both the binary and ternary cases.

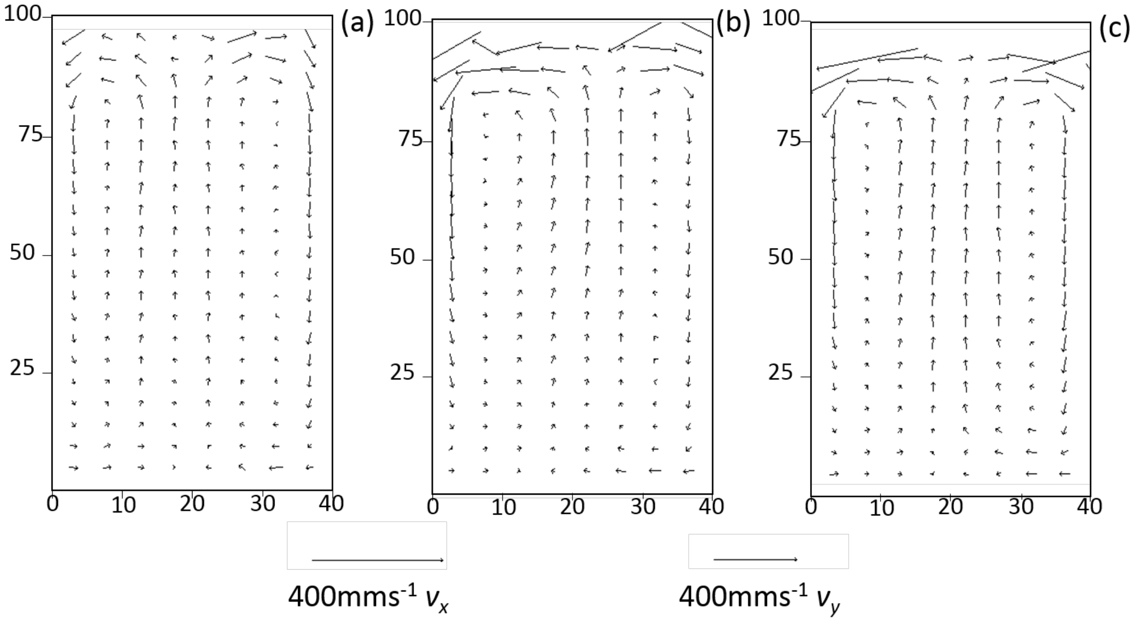

Figure 4.20: Experimentally acquired depth-averaged velocity vector fields shown for the system's x-z plane (note that the image refers to the vertical dimension as 'y' due to the differently defined coordinate system used in the original publication from which this image is taken). Data is shown for monodisperse (M), binary (MH) and ternary (LMH) systems in panels (a), (b) and (c) respectively. In all cases, the system is driven with a fixed dimensionless acceleration $\Gamma = 11$, the total particle number N is held constant and – for the binary and ternary systems – the volume fractions of all particle species are held equal to one another (i.e. $N_M = N_H = 3000$ for image (b), $N_L = N_M = N_H = 2000$ in image (c)). Figure taken from our reference [2].

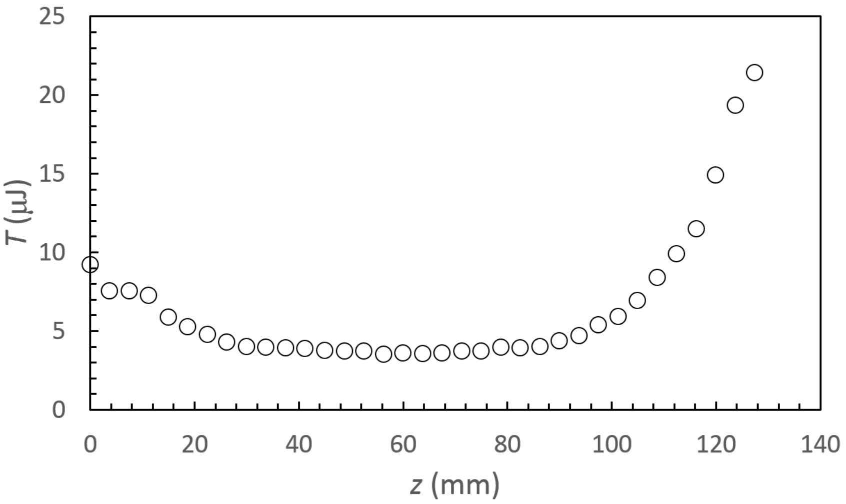

Figure 4.21: Experimentally acquired one-dimensional vertical temperature profile for a ternary system driven with an acceleration Γ = 14; the T values shown represent the average across all three particle species for each region of the experimental system. The form of the profile shown is typical of that exhibited by all systems studied, with a relatively large temperature at small and large heights, z, with a near-constant, lower-T region throughout the main bulk of the bed. Figure taken from our reference [2].

An important question to address, both concerning the validity of the above hypothesis and our understanding of granular systems in general, is whether the observed segregation does indeed, as suggested, arise sue to convective motion within the system, or whether in fact the inverse is true – i.e. the convective flow observed is the result of an instability caused by the segregation of differently massive particle species[4]. Compelling evidence in support of the former possibility is provided by Figure 4.20, which shows a remarkable similarity in the flow fields for both the mono- and poly-disperse cases. The persistent presence of convective flow in a unary system where segregation is, by definition, impossible, strongly suggests that it is convection which leads to segregation, and not vice-versa.

Arguably the most important result pertaining to this current area of investigation is not the specific form of the distribution of particle species *per se*, but rather the remarkable similarity in the distributions for binary and ternary systems. This observation carries potentially important implications, providing an indication that findings from the extensive existing literature concerning *binary* systems may be relatively simply extended to the relatively unexplored case of ternary systems, and even those exhibiting higher degrees of polydispersity.

Notable also is the consistency in the distribution of particle species observed across a wide range of driving parameters as well as numerous differing combinations of particle density and elasticity and, of course, differing degrees of polydispersity. Indeed, the general, qualitative behaviours described here were found to remain consistent over the full range of driving strengths and particle combinations explored. Such an observation lends credence to the validity and robustness of our observations. Moreover, the generality of our findings allows the prediction, at least on a qualitative level, of the steady-state particle distribution for any similar system – the heaviest species present will occupy the slowest-moving regions of the system with the lightest dominating the

---

[4] As will become apparent in the next section, there undoubtedly exists *some* form of interrelation between convective motion and the particular form of segregation discussed here.

most dynamic regions, and any intermediate species occupying the areas possessing more moderate kinetic energy. Such a knowledge may, in the future, prove highly useful to the formulation of a theoretical framework for convective, polydisperse granular systems

4.5 Summary

In this chapter, we have discussed the manners in which the frictionally-driven and buoyancy-driven convective behaviours of vibrofluidised granulates are affected by various controllable parameters and how, in turn, these convective phenomena affect various other properties of the systems under investigation.

For the case of buoyancy-driven or 'thermal' convection, we have demonstrated the existence of a monotonic relationship between the strength of convection, J, and the coefficient of restitution, ε_w, possessed by a system's lateral boundaries. We have shown that the changes in J resulting from an alteration in ε_w may directly affect the degree to which a binary system separates into its individual components and that the combination of segregation and convection may additionally alter the partition of kinetic energy between unlike particle species.

For the case in which the behaviour of the system was dominated by frictional, as opposed to collisional, interactions, we observed a markedly different form of segregation, with heavier particles migrating towards the centre of convection rolls, as opposed to simply occupying the lower regions of the system, as one might expect from simple buoyancy arguments. Similar segregative behaviour was exhibited for both binary and ternary systems, providing a clear indication that the transition from the binary to the ternary case does not fundamentally alter the physical mechanisms underlying the separation of distinct particle species in composite granular beds.

In the next chapter, we focus more directly on the issue of segregation itself, for the relatively simple situation of non-convective systems.

5 Density-Driven and Inelasticity-Induced Segregation in Non-Convective, Monosized Granulates

In this section, we discuss in detail the origins, dependencies and effects of density- and inelasticity-related segregation in the idealised case of systems possessing zero bulk motion. We begin by analysing the influence of a system's geometry, filling height and, hence, packing fraction on the maximal degree to which a bidisperse, monosized granular system may segregate, and the speed with which this maximal segregation is achieved. Building upon the knowledge gained from this investigation, we then detail a method by which the separation of a binary mixture may be optimised and accelerated through an exploitation of the history-dependent nature of dense granular systems. We next examine the degree to which particles' collisional dissipation may affect the segregative behaviours of a system, exploring the competition between inelasticity- and density-induced segregative mechanisms and determining the range of parameter space for which the influence of particle elasticity on segregation becomes negligible. Having explored the various control parameters which affect particle segregation, we next focus on how segregation may influence other important system properties, in particular the energy possessed by a granular bed. Finally, we extend our analysis to the situation in which particles are no longer uniformly spherical, looking into the little-understood effect of particle geometry on the dynamics and segregative properties of granular systems.

5.1 Density-Driven and Inelasticity-Induced Segregation – The Influence of Packing Density and System Geometry

It is well known [247, 248] that the packing density of a granular bed can strongly affect its physical properties and dynamical behaviours. Despite this fact, there exists surprisingly little information in the literature regarding the precise impact of a system's packing fraction on its segregative behaviours, at least for the situation of monosized granulates differing in their material properties.

The packing density, η of a system can be altered in a variety of ways, for instance by varying the strength with which the system is driven [249] (i.e. adjusting A and/or f for the case of vibrated systems) or by changing the (resting) depth of the bed, N_L [250]. Since a variation in the driving frequency and amplitude of a system will often give rise to changes other than a simple alteration in packing density – thus introducing possible complications into our analysis – we choose instead to adjust η by altering the dimensionless resting bed height, N_L. Specifically, we choose to vary N_L by keeping the total particle number, N, *fixed* whilst adjusting the lateral extent ($L_{x,y}$) of the container used to house the granular bed under investigation. The decision to vary N_L is due to the fact that, in the numerous industrial process where segregative and mixing processes play a pivotal rôle, a variation of N is likely to be undesirable as this will, clearly, affect the output rate of a given product. A visual representation of the typical manner in which the packing density, η, is found to vary with N_L, for a variety of different systems, may be seen in Figure 5.1.

The basic experimental set-up remains largely as described in section 3.1. In all cases, monosized binary systems containing equal numbers, and hence volumes, of each particle species are investigated. Specifically, we choose once again $N_A = N_B = \frac{N}{2} = 500$. Square-based ($L_x = L_y$) cuboidal containers of horizontal extent $L_{x,y} \in (25, 160)$ mm are used, providing a range of dimensionless resting bed heights $N_L \in (0.98, 40.0)$. The

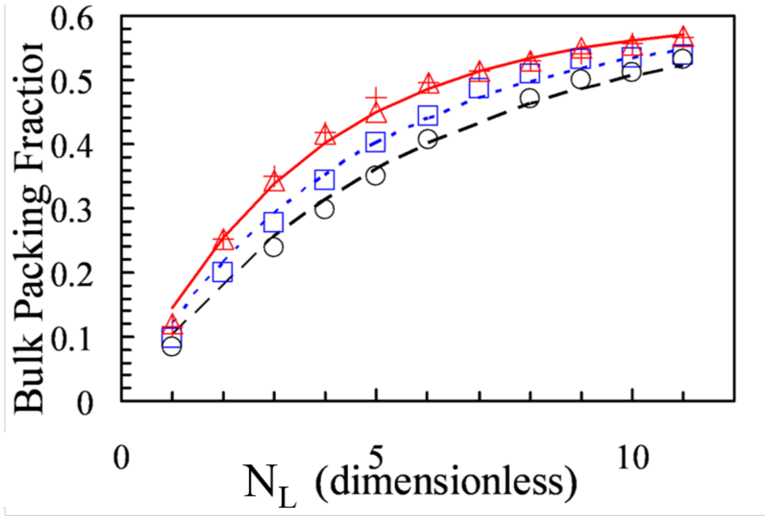

Figure 5.1: Variation of the system's bulk packing fraction with the dimensionless resting bed height, N_L. Data is shown for monodisperse systems comprising glass (circles and dashed line) and brass (triangles and solid line) spheres, as well as a binary mixture of brass and glass particles (squares and dotted line). In each case, discrete points represent experimental data, while continuous lines correspond to simulational data. Data is also shown (crosses) for simulations in which particles possess the density of glass particles but the restitution coefficient of brass particles, demonstrating a seeming mass-independence which will be further evidenced and discussed in greater detail in section 5.4. Figure taken from our reference [13].

system is driven, unless otherwise stated, at a fixed vibrational frequency of 70 Hz and an amplitude of 0.86 mm.

In order to frustrate frictionally-driven convection, 0.5 g of graphite powder is added to each system to act as a lubricant, thus reducing surface friction for both particle-particle and particle-wall contacts [231, 251]. Of course, this reduction in frictional effects is not sufficient in itself to *guarantee* the absence of convection - in particular for the case of shallower systems where frictional effects on convection are already minimal. This being the case, the absence of convective motion is specifically ensured for each individual data set. In each instance, two checks are carried out in order to assess whether or not convection is present: firstly, the time averaged velocity fields are analysed to check for the presence of coherent, non-random motion within the system. Secondly, for each data set, fast fourier transforms (FFTs) of the tracer particle's horizontal and vertical motion are analysed; the presence (or lack thereof) of distinct peaks in the resultant power spectra provide evidence of the existence (or absence) of coordinated motion, such as convection, within the system. This second check is particularly useful due to the fact that *metastable* convection rolls may be difficult to visualise using the velocity fields produced from PEPT data. Although the existence of a peak in the FFTs produced is not necessarily an indication of convection specifically, the presence of *any* form of correlated motion within the system is nonetheless undesirable, as we wish to investigate vibration-induced segregation on a fundamental level, i.e. exploring the simplest systems possible, namely those in which particle motion is effectively randomised. Figure 5.2 shows exemplary FFTs for both the situation in which motion is random and uncoordinated, reminiscent of a molecular gas (red line), and the case in which the motion of the bed as a whole is correlated with that of the vibrating base of the system (blue and black lines). Any data sets demonstrating evidence of convective flow, or indeed any form of bulk motion, are discarded.

Aside from a reduction in friction, the addition of graphite powder may alter the contact properties of particles in other manners, for instance by increasing adhesion, altering their contact area or simply adding an additional material with differing properties – all of which may subtly affect the inelasticity of particle interactions [252, 253]. Due to the large size of the particles involved and the relatively small volume of graphite introduced, the effects are unlikely to be highly significant, yet the possibility that our results may be affected must not be ignored. Nonetheless, since an equal volume of graphite is introduced to *all systems tested*, the general qualitative trends discussed here should still be valid.

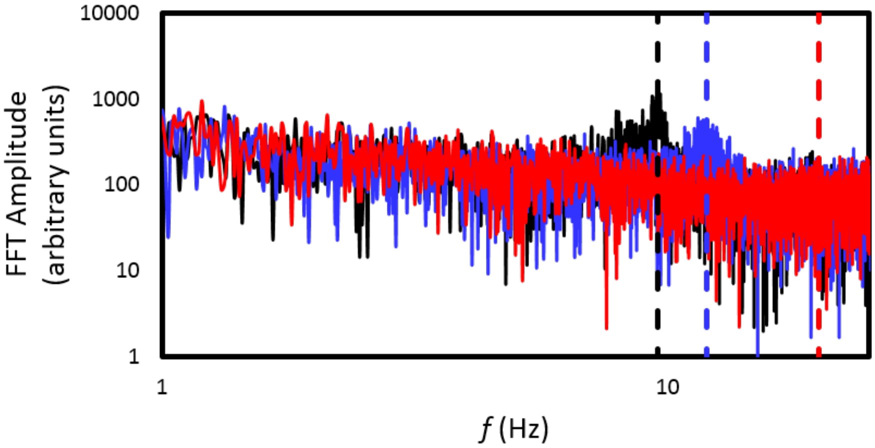

Figure 5.2: Power spectra corresponding to the vertical centre of mass motion of a bed with dimensionless height N_L = 6 driven with a fixed dimensionless peak energy S = 1.83. Results are shown for systems in which the desired S value is achieved using various differing combinations of driving frequency, f, and peak amplitude, A. Specifically, we show here the cases f = 9.55 Hz, A = 5 mm (black), f = 11.9 Hz, A = 4 mm (blue) and f = 19.9 Hz, A = 2.4 mm (red). In all cases, the power spectra themselves are represented by continuous, solid lines while vertical dashed lines are used to demarcate the position on the horizontal axis pertaining to the relevant driving frequency of each given system. All data presented is acquired from experiment. Figure taken from our reference [14].

5mm spheres composed of various materials, and hence possessing a range of material densities, ρ, and effective elasticities, ε, (see section 4.1) are used in experiment. A list of the materials used, and the corresponding particle properties, may be found in table 5.1. Since, in this current chapter, we will discuss in detail the effect of particles' dissipative properties, we define two separate effective elasticities for particle-particle collisions – one for *intra-species* collisions ($\varepsilon_{\alpha\alpha}$) and another for *inter-species* collisions ($\varepsilon_{\alpha\beta}$). For the MercuryDPM simulations used to recreate the experimental system, the effective elasticity for collisions between unlike particle species is determined as the geometrical average of the intra-species coefficients for each particle type, i.e.:

$$\varepsilon_{\alpha\beta} = \frac{\varepsilon_{\alpha\alpha} + \varepsilon_{\beta\beta}}{2} \tag{5.1}$$

Although such a formulation may seem overly simplistic, it is in fact a natural consequence of the spring-dashpot model of particle restitution (see section 3.3), and is found to produce excellent agreement with experimental results across all data sets analysed.

Table 5.1: Effective elasticities, $\varepsilon_{\alpha\alpha}$, and material densities, ρ, for the various particles used in experiment.

Particle Material	Material Density, ρ (kgm^{-3})	Effective Elasticity, $\varepsilon_{\alpha\alpha}$
Glass (G)	2500	0.83
Aluminium (A)	2700	0.69
Steel (S)	7850	0.79
Brass (B)	8500	0.61

Figure 5.3 shows the variation of a system's segregation intensity, I_s, with the ratio of particles' material densities, $\frac{\rho_H}{\rho_L}$, for a number of different experimental and simulated situations. We discuss first the relatively simple case corresponding to simulations in which segregation within the system arises solely due to density differences between particles (i.e. particles possess equal ε values). Here, we see an initially increasing trend between I_s and $\frac{\rho_H}{\rho_L}$ which approaches an apparent plateau for relatively large density ratios. The existence of such an asymptotic maximum in I_s for relatively dilute systems such as those described here is perhaps not surprising; the presence of considerable void space within the system will, naturally, lead to a certain probability of particles

simply ‘falling through’ the system without interacting with other particles [107, 254], thus leading to an inevitable degree of re-mixing as lighter particles at the top of the system re-enter the lower regions which one would expect to be predominantly occupied by particles of the heavier species.

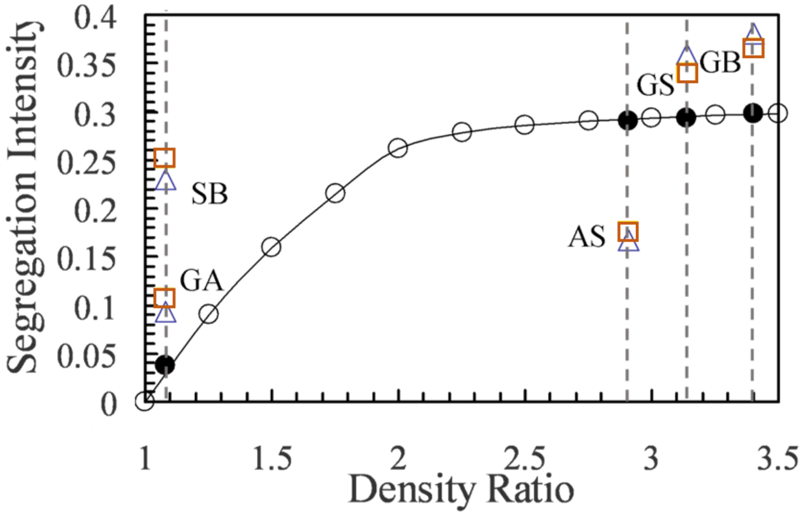

Figure 5.3: Segregation intensity as a function of the density ratio, $\frac{\rho_H}{\rho_L}$, between heavy (H) and light (L) particle species for a system of resting depth $N_L = 2.5$. Experimental data (open triangles) and simulational results (open squares) are shown for various binary combinations of the materials shown in table 5.1; the specific pairings of particle species are demarcated using the abbreviations provided in the table. Results are also shown (solid circles) for simulations in which the experimental *density* values are maintained, but the *effective elasticities* of particles are held constant at a value $\varepsilon_{\alpha\alpha} = \varepsilon_{\beta\beta} = 0.91$, thus demonstrating the case of *purely density-driven* segregation, and its distinction from the situation in which elasticity-induced segregative effects are also present. Additional results (open circles) are included for simulations in which, as before, $\varepsilon_{\alpha\alpha} = \varepsilon_{\beta\beta} = 0.91$, but the density ratio is instead varied by holding the density of the lighter component constant at 2500 kgm^{-3} whilst varying ρ_H to produce the desired density ratios. In this image, I_s is not normalised, and a value $I_s = 0.5$ corresponds to a fully segregated system. Figure taken from our reference [13].

Notable also from the equal-elasticity case is the collapse onto a single curve of the filled circles – representing the case in which ρ_L possess a constant value of 2500 kgm^{-3}

and only ρ_H is varied – and empty circles – denoting the situation for which both ρ_L and ρ_H are altered, their precise values corresponding to the various combinations of material density available in experiment. This collapse clearly suggests that while the density *ratio* of particles plays a significant rôle in their segregative behaviours, the same does *not* hold true for the *absolute values* of ρ, i.e. the *average* density of the system. The invariance of I_s with $\bar{\rho} = \frac{\rho_H + \rho_L}{2}$ will be further discussed later in this chapter (see section 5.4).

We turn our attention now to the case in which both $\frac{\rho_H}{\rho_L}$ *and* $\frac{\varepsilon_H}{\varepsilon_L}$ are varied. Immediately notable for this situation is the marked deviation from the trend observed for purely density-driven segregation, providing a clear demonstration of the *profound impact* of the oft-overlooked inelasticity effects on the segregation of vibrofluidised systems. This pronounced deviation persists even for large $\frac{\rho_H}{\rho_L}$ values, where one might intuitively expect elasticity effects to be dwarfed by those due to density differences; in fact, the presence of elasticity effects even allows the previously discussed plateau in I_s to be overcome. This observation may, perhaps, be explained by the fact that an increase in dissipation for the heavier component will lead to a comparatively reduced void space in the lower part of the bed, thus reducing the degree of remixing discussed previously. Evidence for the validity of this hypothesis may be seen in Figure 5.4, which shows the variation with ε_H of the average void fraction for the lower region of a system (specifically, $z < h$) alongside the observed segregation intensity.

The influence of differing particle elasticities is perhaps best illustrated through a comparison of a binary glass/steel system and an equivalent aluminium/steel system. As may be observed from Figure 5.3, for the case in which elasticity effects are discounted, one would anticipate the segregation intensity to vary between the two cases by only $\sim 1\%$. When the particles' effective inelasticities are considered, however, I_s is observed to increase by more than 100% between the glass and aluminium cases. This large discrepancy between results can, in fact, be relatively easily explained. For the equal-ε case,

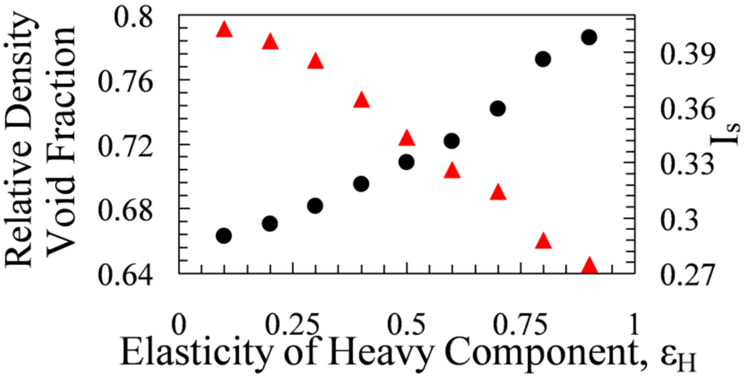

Figure 5.4: Segregation intensity, I_s, (red triangles) and average void fraction for the *lower half* of the system (black circles) as a function of ε_H, the effective elasticity of the system's heavier component. In this instance, the bed height is once more equal to 2.5 particle diameters, while the density ratio $r = \frac{\rho_H}{\rho_L}$ is now held constant at $r = 4$. As with the previous image, an I_s value of 0.5 corresponds to a fully-segregated system. All data shown is derived from DPM simulations. Figure taken from our reference [13].

segregation is due entirely to differences in density and, since the ratio $\frac{\rho_H}{\rho_L}$ does not vary significantly between the glass/steel and aluminium/steel cases, no significant difference in I_s is observed. When differences in particle inelasticity are considered, however, we observe two contrasting situations for the glass/steel and aluminium/steel systems – in the former, the heavier species is also more dissipative, while in the latter the heavier particles are actually more elastic. Thus, for the steel/glass bed, both density-driven and inelasticity-induced segregative mechanisms act in unison, providing greater segregation than would be achieved from density differences alone. For the aluminium/steel system, however, the two segregative processes act in opposition, providing a reduced I_s as compared to the equal-elasticity case. The strong influence of particle elasticity on system behaviour is clearly observable in both experiment and simulation. A further example of the considerable influence of inelasticity effects on system behaviour may be seen in Figure 5.5, which demonstrates the fact that even systems in which particles are identical in terms of their sizes, masses *and* frictional properties can exhibit significant segregation based solely on differences in particle restitution.

The complex interrelation between density and inelasticity effects, and the fact that it is very difficult in 'real life' to vary one of these properties without influencing the other, makes it extremely difficult to experimentally isolate either one of these parameters, and hence near impossible to observe any clear trends between I_s and either $\frac{\rho_H}{\rho_L}$ or $\frac{\varepsilon_H}{\varepsilon_L}$ in the laboratory. However, the strong agreement shown between experiment and simulation in Figure 5.3 and further evidenced in 5.6, which shows similar data for a denser system, means that we may now confidently rely on our simulational results to accurately elucidate the relevant relationships.

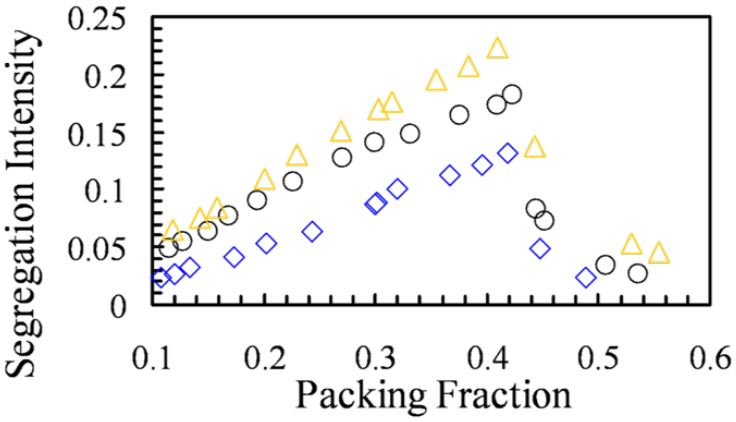

Figure 5.5: I_s as a function of packing fraction, η, for the case in which segregation is due solely to inelasticity effects (i.e. $r = 1$; specifically, $\rho_A = \rho_B = 2500$ kgm^{-3}), illustrating the considerable variation in the strength of inelasticity-induced segregation for systems of differing system density. Data is shown for systems in which the elasticity of the different system components varies by a factor of 1.5 (blue diamonds), a factor of 2 (black circles) and a factor of 4 (orange triangles); in all instances, the effective elasticity of the less-dissipative component is held constant at a value $\varepsilon = 0.95$. For both images, $I_s^{max} = 0.5$. Figure taken from our reference [13].

Now that we have established the presence of both density- and inelasticity-related segregative processes in our system, we next discuss how each of these mechanisms are affected by the packing density of the granular beds undergoing segregation. Figure

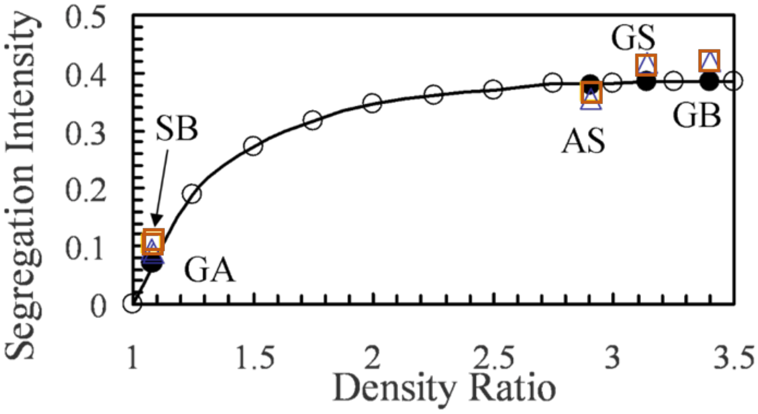

Figure 5.6: Segregation intensity, I_s, as a function of the density ration $r = \frac{\rho_H}{\rho_L}$ for the case of a bed with resting height $N_L = 10$. All symbols used are as defined in Figure 5.3. Figure taken from our reference [13].

5.6 shows an image equivalent to that given in Figure 5.3 for the case of an increased bed height, N_L, and hence – since all other system parameters are held constant – a correspondingly augmented bulk packing fraction, $\bar{\eta}$ (defined as the average value of η taken over a height equivalent to twice the vertical centre of mass position of an excited bed in a steady state). Clearly, the increase in $\bar{\eta}$ has had several noteworthy effects on the system; firstly, the asymptotic maximum value of I_s for the case of purely density-driven segregation is considerably increased compared to the lower-density case. Secondly, the influence of particle inelasticity is significantly reduced. Finally, the time taken for the system to reach its equilibrium distribution – i.e. its final segregated state – is considerably increased, as may be clearly seen from Figure 5.7.

Having determined the specific manners in which the packing density of a system may affect its behaviours, we now proceed to further investigate each of the observations described above in order to explain their origins and elucidate the specific forms of their relations to the system's solids fraction.

We firstly discuss the matter of the relationship between the maximal, plateau value of I_s achievable by a system and the packing density of said system. For low and moderate

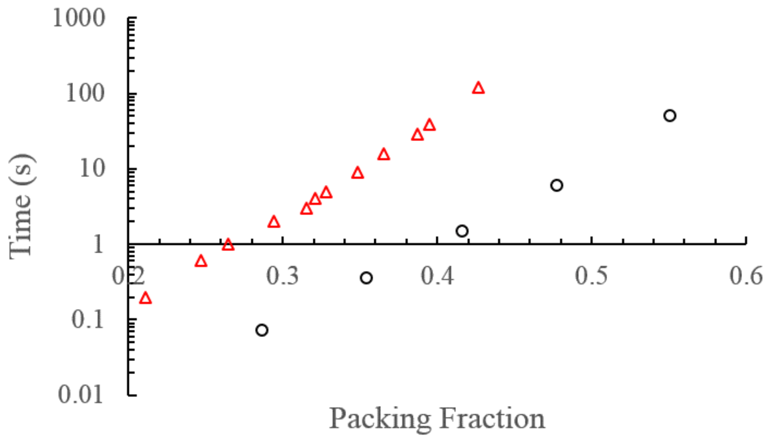

Figure 5.7: Log-linear plot of the time required for a simulated system to reach its steady segregated state (red triangles) shown alongside the time required for a single, light particle in an experimental system to rise from the base to the free upper surface of a vibrated bed comprising purely heavy particles (black circles). Figure taken from our reference [13].

packing fractions, the observed relationship between I_s^{max} and $\bar{\eta}$ is relatively simple, as is the explanation of its origin. For packing fractions $\lesssim 0.45$ (i.e. less than ~ 70% of the maximal packing achievable for a bed of spherical grains [255–257]) one observes a monotonically increasing relationship between I_s and $\bar{\eta}$. This increasing trend can, in general terms, be attributed to two factors: firstly, the decrease in void space with increasing $\bar{\eta}$ and, secondly, the fact that as $\bar{\eta}$ increases, the system will experience increased buoyancy forces, which act to promote segregation, and a decreased diffusivity, which will result in a corresponding decrease in the rate of re-mixing [258]. It is interesting to note that the sharp downturn in I_s with decreasing packing density occurs approximately at the point for which the system's mean free path becomes approximately equal to the particle diameter.

For the case in which the system under investigation is more tightly horizontally constrained, resulting in the bed possessing a greater resting height, N_L, and aspect ratio, $\mathcal{A} = \frac{N_L}{L_x/d}$, leading in turn to a higher average packing, one observes a markedly

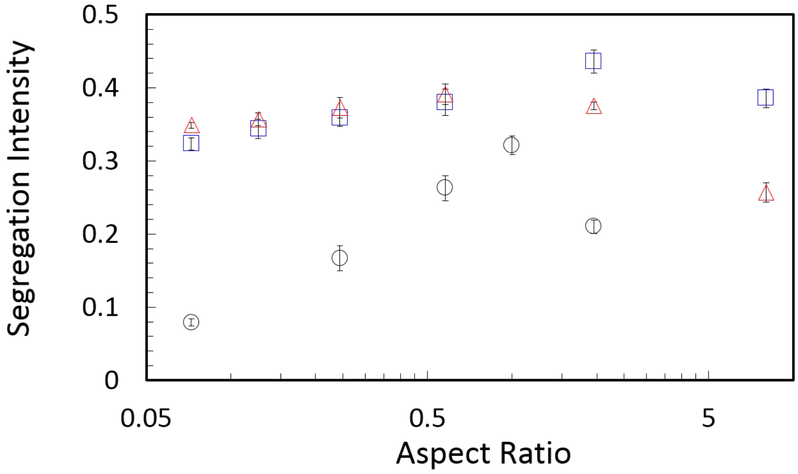

Figure 5.8: Variation with aspect ratio, $\mathcal{A} = \frac{N_L}{L_x/d}$, of the degree of segregation, I_s, exhibited by a given binary system of $N = 1000$ particles, driven with a constant frequency $f = 70$ Hz and amplitude $A = 1.06$ mm. Data is shown for three different combinations of particles: glass and steel (blue squares), glass and brass (red triangles) and aluminium and steel (black circles). A 50:50 ratio of the relevant species is utilised in all cases. Figure taken from our reference [15].

different behaviour – segregation intensity begins to *decrease* with $\bar{\eta}$. The effect of increasing aspect ratio on I_s is clearly illustrated in Figure 5.8.

One probable origin for the observed decrease in species-separation with increasing η in densely packed, high aspect ratio beds is the greater presence of *localised clustering.* Specifically, it is known that a system's packing becomes increasingly inhomogeneous as the degree of dissipation within the system becomes greater [259], either due to an increased packing [260], or simply due to the presence of more dissipative particles – explaining, perhaps, why brass/glass and steel/aluminium systems undergo the transition from an increasing to a decreasing relation between I_s and η or, equivalently, $\mathcal{A}$ than the equivalent glass/steel system. If the rate of at which a system undergoes clusterisation is comparable to or greater than the rate at which segregation is achieved, it is highly likely that the clusters formed will incorporate *both* particle species present in the system, thus hindering the relative motion between grains and limiting the completeness with which the system components can become separated [66,153,261]. It is additionally worth noting that, since in higher aspect ratio systems there will exist a reduced relative contact area between particles and the energy-inducing vibrating base, the formation of force networks [262–265] – which will further hinder relative motion within the bed – will become increasingly prevalent as the ratio of energy-providing particle-base collisions to energy-lowering particle-particle collisions decreases [266]. Evidence of the increased clustering – and the resultant reduction in I_s – for denser, higher-$\mathcal{A}$ systems as described above may be seen in Figure 5.9. It should be noted that the clusters described here are distinct from the 'cold droplets' discussed in relation to inelasticity-induced segregation.

A final interesting observation to be drawn from the higher-density systems explored is the strong implication of the existence of sudden chain energy transfer events (SCETEs), or a similar phenomenon, in the systems explored. SCETEs, as briefly discussed in section 2.2.2, have been previously observed both in simulation [157] and experiment [155], but only for quasi-two-dimensional beds; the results provided here represent a

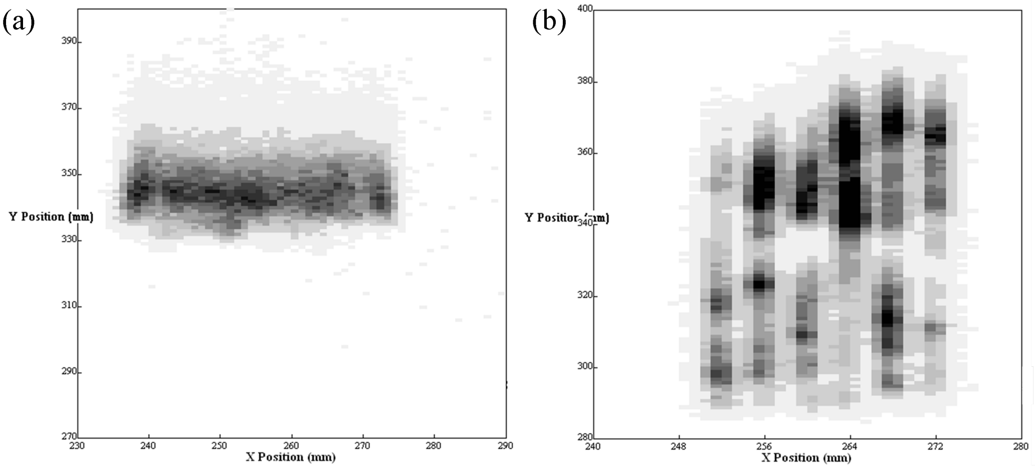

Figure 5.9: Two dimensional spatial packing density distributions for two otherwise identical glass/steel systems with aspect ratios (a) $\mathcal{A} = 1.95$ ($N_L = 15.6$) and (b) $\mathcal{A} = 8$ ($N_L = 40$). Darker shades are representative of regions of comparatively higher packing. In both images, the container's base (not visualised by PEPT) coincides with a vertical position of 284 mm. It is important to note that in the research paper from which this image is taken, the vertical coordinate was denoted 'y' as opposed to 'z' as is the case for the majority of this thesis. Figure taken from our reference [15].

first indication that analogous dynamical behaviours may also be present in fully three-dimensional beds.

Figure 5.10 compares the typical trajectory of a single, light tracer particle of two systems, identical in terms of their total particle number, aspect ratio (and hence resting bed height) and the strength with which they are driven, differing only in the bed composition – the granulate shown in (a) comprises a $50:50$ mixture of glass and steel particles while that shown in (b) consists of an equivalent mixture of glass and *brass* particles. Despite the similarities between the systems, the highly contrasting images presented indicate strongly differing dynamics within the two beds: for the glass/steel case, one simply observes an initial transient as the light, glass particle migrates upward through the bed before, for the remainder of the data set, remaining predominantly within the upper region of the system, making only occasional, infrequent excursions into the lower bulk of the bed. This behaviour strongly indicates that the bed in question is exhibiting simple, and relatively complete, steady-state segregation, as is typically observed and discussed throughout this thesis. Contrastingly, for the glass/brass system, one observes a repeating cycle of relatively slow upward transits through the system followed by sudden, sharp drops in $z^*(t)$ as the particle apparently 'falls through' the bed. This result is somewhat counterintuitive, as one might understandably expect a higher degree of segregation for the glass/brass system, due not only to the increased mass ratio between particles but also the differences in inelasticity – the brass particles are both heavier *and* more dissipative than the steel, meaning that both density-driven and inelasticity-induced segregative mechanisms should act more strongly to promote segregation in the glass/brass case than the glass/steel incidence.

While one might immediately assume the above-described motion to be due to the presence of convective flow within the system, there exist several convincing arguments suggesting that this is not the case. Firstly, no convective motion is apparent in the velocity vector fields corresponding to the system shown in Fig. 5.10 – or indeed any

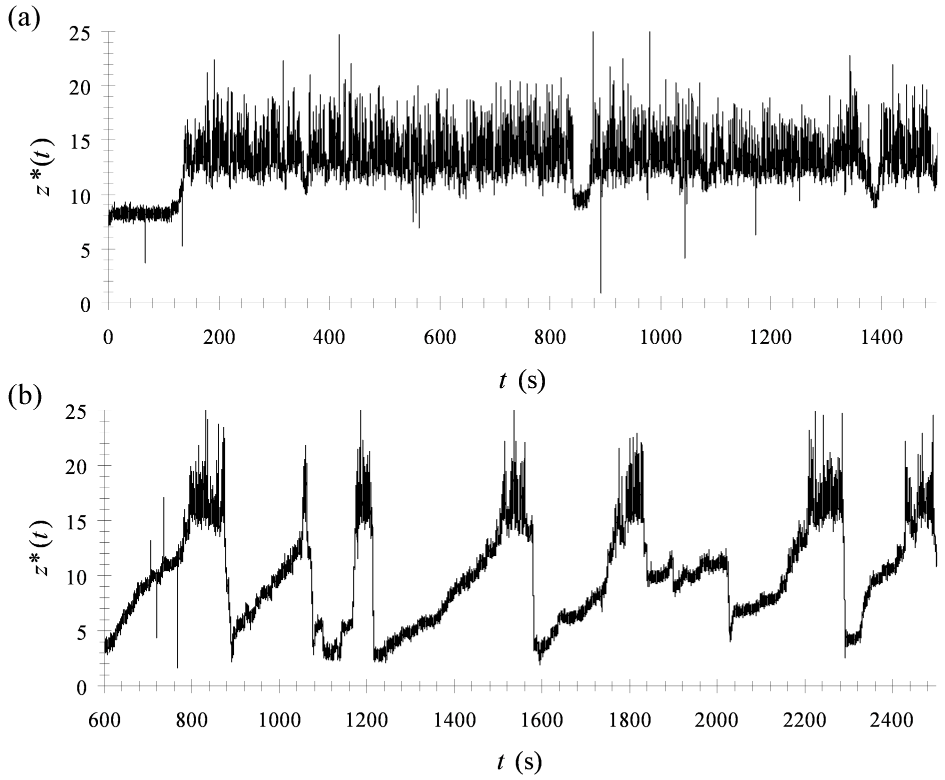

Figure 5.10: Vertical position of a single, glass tracer particle within a binary bed of (a) glass and steel and (b) glass and brass with, in both cases, an aspect ratio $\mathcal{A} = 1.95$, shown as a function of time. The vertical position is here shown as a dimensionless quantity, $z^* = \frac{z}{d}$, with d the particle diameter. Figure taken from our reference [15].

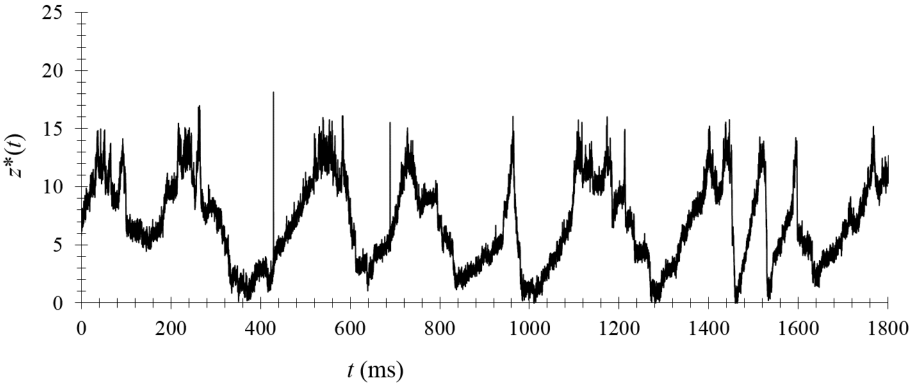

Figure 5.11: Time evolution of the vertical position of a single *brass* tracer in a binary glass/brass system with aspect ratio $\mathcal{A}$ = 1.95.

other systems exhibiting similar behaviour. Secondly, the upward and downward transits show little or no consistency in their duration, as would be expected for the case of convective flow [267]; this lack of periodicity can be further confirmed through analysis of Fast Fourier Transforms (FFTs) of the particle motion. Thirdly, and perhaps most importantly, the downward transits observed are found to occur at seemingly arbitrary points in the system's x-y plane, whereas for the case of convection one would expect the regions of downward flow to be well-defined [268], and in particular a preponderance of downward transits near the system's horizontal boundaries [269].

So, if the tracer's cyclic z-trajectory cannot be attributed to convective flow, what else might be its root cause? We posit that the sudden downward transits experienced by the light, glass tracer particles occur during periods of rapid decompaction as a dense region of brass particles undergoes a SCETE or 'explosion', as it was alternatively termed by the original authors. Since, in the bed's segregated state, one finds the system to be divided into a relatively dilute region of glass particles residing atop a relatively dense region of brass particles, such an 'explosion' may well explain the sudden drops in height observed for the glass tracer particle. Figure 5.11 also shows evidence of such sudden, sharp motion being exhibeted by the brass component of the system. In the case of brass particles, as one would expect from our hypothesis, the downward transits are (compared to the glass case) more likely to occur at lower regions of the system, and therefore are often smaller and less pronounced.

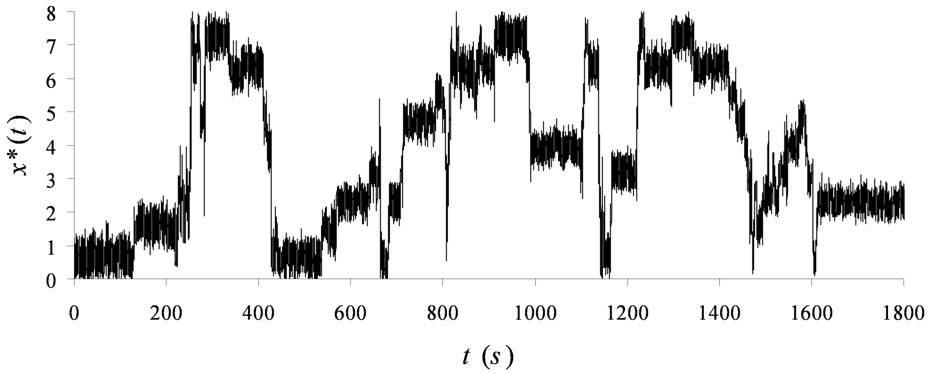

Figure 5.12: Evolution with time of the horizontal (x) position of a single *brass* tracer particle in a bed of glass and brass spheres of aspect ratio $\mathcal{A}$ = 1.95. The horizontal position is normalised by the particle diameter, d, to give the dimensionless variable $x^*(t)$. Figure taken from our reference [15].

The SCETE hypothesis is supported by several factors; firstly, as may be inferred from Figure 5.10, the sudden drops in particle height seemingly only occur at points in time where the system has achieved near-complete segregation. This observation agrees well with the findings of Rivas *et al.* [155, 157], who show that SCETEs require a system to have achieved a significant degree of separation. Secondly, our results show support for the existence of the sharp increases in horizontal mobility and kinetic energy associated with SCETEs, evidence of which may be seen in Figure 5.12; here, we see that the brass tracer particle typically exhibits only limited motion, simply oscillating about a fixed point in a manner indicating that the particle is 'trapped', or 'caged', within a densely-packed structure or cluster. However, the particle will sporadically display a sudden, considerable increase in its horizontal mobility, as would be expected in a system undergoing a SCETE, before relatively quickly becoming quasi-static once more as the tracer finds and becomes trapped within another cluster of particles. It is also worth noting that the typical timescale, and indeed the variance of this value, agree closely with the observed timescales on the 'drop events' visible in Fig. 5.10 are observed to occur. An additional attempt to verify the existence of SCETEs in our three-dimensional set-up uses a system with a reduced particle number yet maintaining a relatively large aspect ratio; the reduction in N reduces the duration required for the tracer to fully explore the system, meaning that accurate data can be produced on a reduced timescale as compared to the full-scale system. This allows PEPT to successfully reproduce spatial packing density distributions for the periods pseudo-steady state behaviour in between successive SCETEs. Examples of the density fields produced may be seen in Figure 5.13; each individual image shown corresponds to time-averaged data acquired in the interval between two successive 'spikes' in $x(t)$ as observed in Figure 5.12. Since the evolution of the system is clearly stochastic in nature, the time period between two SCETEs will naturally vary in length; the time windows shown in Figure 5.12 therefore differ slightly, but are all approximately equal to 500 s (the longest time period between events routinely observed in our system). For comparison, a series of 2D density profiles calculated over 500 s time intervals but corresponding to the glass component of a similar system in the *absence* of SCETEs may be seen in Fig. 5.14. The consistency observed between these images provides support for the idea that the clusters shown in 5.13 are indeed present within the system, as opposed to simply being artefacts of the PEPT technique.

The images shown in Figure 5.13 provide clear evidence of clustering within the system, as may be seen from the localised regions of increased density. More importantly, however, the *spatial positions* of the observed clusters are found to vary considerably between images, despite the fact that all data presented in Figure 5.13 are taken from a *single data set* – each image shown corresponds to a different temporal period lying between two 'energy spikes' as observed in the relevant plot of $x(t)$ vs. t. Our results

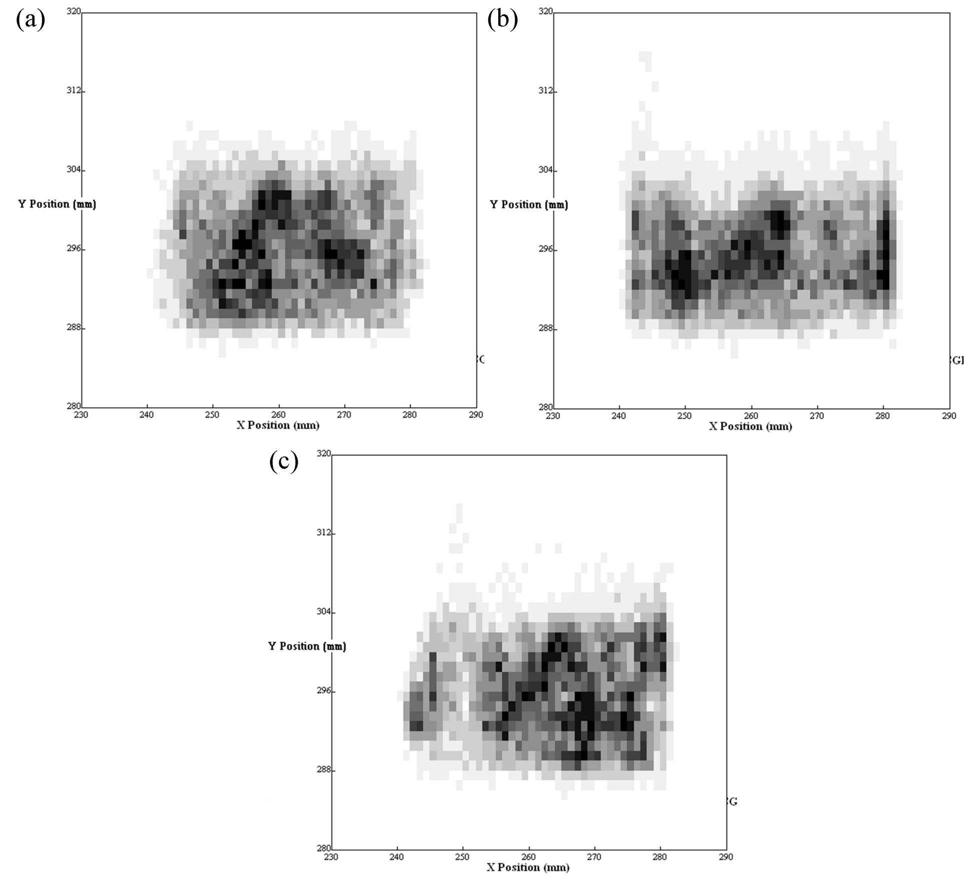

Figure 5.13: Two dimensional packing density distributions for a system of aspect ratio $\mathcal{A} = 1.13$ comprising a 50 : 50 mixture of 6 mm glass and brass particles. Panels (a), (b) and (c) correspond to data acquired from a single experimental run for different intervals in time, as described in the main text. In the images, darker regions represent areas of increased particle density while lighter shading represents more dilute regions. Figure taken from our reference [15].

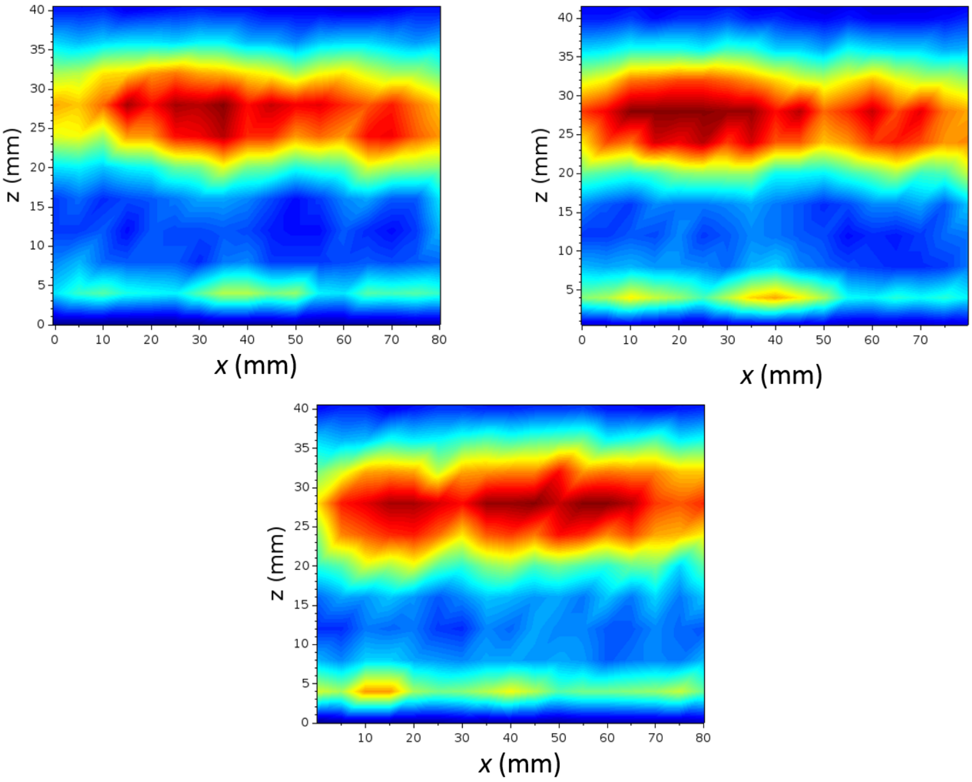

Figure 5.14: Two dimensional packing density distributions for a system of aspect ratio $\mathcal{A} = 1.13$ comprising a 50 : 50 mixture of 6 mm glass and *steel* particles. Each image shown corresponds to a different, non-overlapping 500 s period of a single data set. In this image, red corresponds ti regions of high packing and blue to regions of low particle density.

imply that these spikes cause a significant rearrangement of the system, as may be expected in the case of a SCETE, where clusters will disintegrate during an explosion and subsequently reform in arbitrary new positions.

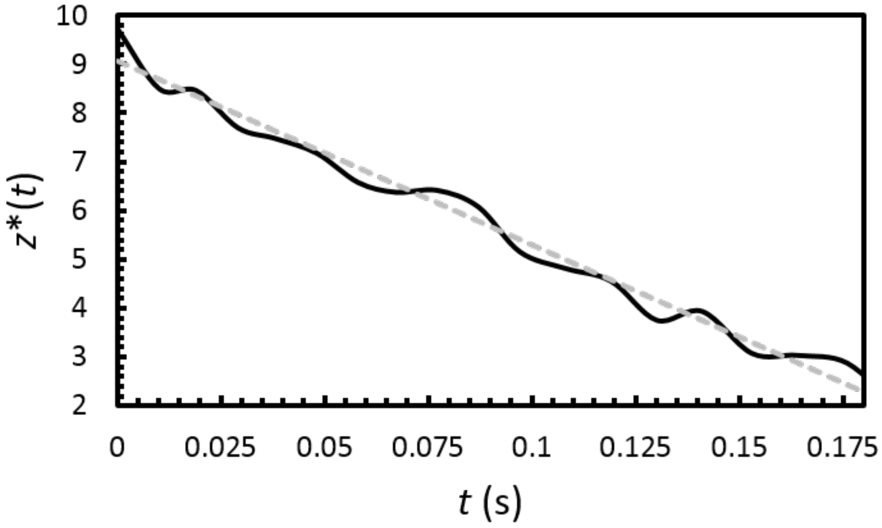

Figure 5.15: Vertical position vs. time for a single glass particle in a glass/brass system of aspect ratio $\mathcal{A}$ = 1.95. Data is shown over a period of time corresponding to a single downward transit through the system.

It is finally interesting to analyse more closely the individual transits made by particles during the potential SCET events. Figure 5.15 shows a typical such transit for a single glass particle in the glass/brass system shown in previous figures. From this Figure, we clearly see that falling particles follow an approximately linear (as opposed to quadratic) general trajectory, showing that these descending particles are not simply in free-fall through the system, but still collide with other grains during their downward motion. Indeed, evidence of these collisions can be directly observed in the deviations of the particle's path about its mean, linear trajectory.

While the combination of results presented above does not represent indisputable evidence of the existence of sudden chain energy events in our system, our observations nonetheless provide a strong suggestion that these events may indeed occur in three-dimensional systems as well as the pseudo-two-dimensional beds in which they were originally discovered. Whatever the cause of the unusual behaviour observed within our system, the variable dynamics and segregative behaviours exhibited by otherwise highly similar systems demonstrate unequivocally that, in future research concerning systems such as those explored here, one must carefully assess whether a given system is in a truly steady state or simply exhibiting metastability before conducting analysis.

5.2 Exploiting Hysteresis to Accelerate Segregation

In the previous section we observed the important rôles played by material density and inelasticity in the segregation of vibrofluidised systems, and that the resultant degree of species-separation is strongly dependent on the packing density of the bed under investigation which, in turn, is directly affected by various controllable system parameters. In particular, it was shown that more closely-packed (i.e. deeper and/or more weakly driven) systems exhibited *more complete* but *slower* segregation than comparatively dilute systems. This raises an interesting question – might it be possible, by varying the packing density of a system, to exploit both the rapid but incomplete segregation observed in low-η beds *and* the slower but more complete segregation observed in denser systems in order to achieve maximal separation in a reduced timeframe?

For instance, Figure 5.16 shows that a system may achieve approximately 80% segregation in less than two seconds, while the acquisition of an entirely segregated state requires $\mathcal{O}(100)$ s. Therefore, one would naturally expect that by achieving the initial $\sim$ 80% segregation with the system in a dilute state and then simply completing the process by subsequently increasing the system's packing density, the time required to produce a fully-segregated system may be drastically reduced.

In order to test this theory, we use the following procedure: a binary system of fixed size and particle number is excited with an initially high energy input (thus producing

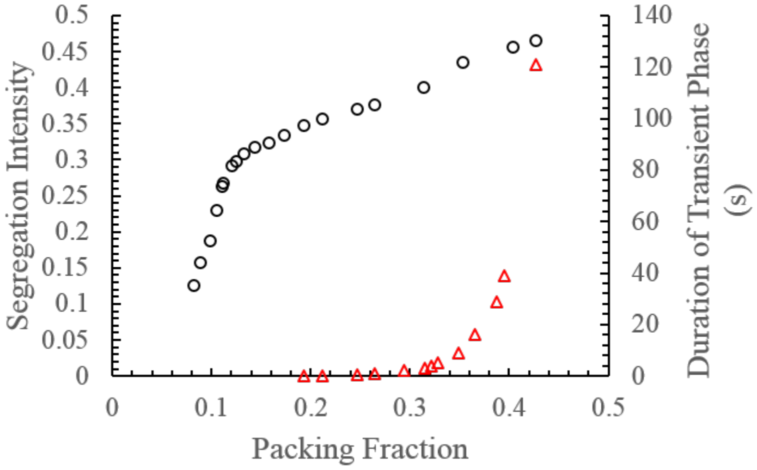

Figure 5.16: Variation of the steady-state segregation intensity, I_s, achieved by a binary mixture (black circles) and the time required (red triangles) for a given system to reach this equilibrium distribution with the bulk packing density, η, of the granular bed under investigation. The data shown here pertain to the case in which segregation is purely density-driven , i.e. $R = \frac{\varepsilon_H}{\varepsilon_L} = 1$. The density ratio, r, between species is equal to 5, ensuring that all systems are capable of achieving complete segregation if other system parameters allow. Figure taken from our reference [13].

a dilute, strongly fluidised bed in which a rapid initial segregation may be achieved) before reducing the strength with which the system is driven, allowing it to relax into a higher-density state and thus complete the segregative process. Specifically, we hold the frequency constant, achieving the desired change in driving strength by varying the *amplitude* of the driving oscillations from an initial, high value, A_i, to a reduced value, A_0. The time period, τ_i, over which the initial, harsh excitation is applied is, in all cases explored, less than 3 seconds; the system is then excited with the diminished amplitude A_0 until the system has reached its equilibrium distribution, i.e. its final, steady state degree of segregation. In both experiment and simulation, the transition between A_i and A_0 is effectively instantaneous, unless specifically stated otherwise and the values of A and f (and hence Γ and S) on either side of this transition are held constant. For conciseness, we term systems excited in this manner *initially strongly driven* or 'ISD'.

In order to assess the degree to which the procedure described above expedites the segregation process, comparison is drawn in all cases with an equivalent *continuously driven* (CD) system, identical in terms of size, geometry, particle number, bed composition and oscillatory frequency, differing only in that the driving amplitude is held constant at A_0 for the entire duration of the run – i.e. there is no initial, strong excitation at A_i.

A direct comparison of CD and ISD driving may be seen in Fig. 5.17. The plot shown in this figure clearly shows a considerable increase in the rate at which the ISD system achieves maximal segregation, as expected from our above rationale. However, the image additionally demonstrates an even more remarkable feature – the differences in the evolution of the two systems' mass centres implies that the CD and ISD beds exhibit strongly differing dynamics even *after* the ISD system's driving strength is reduced to match that of the CD system. Since, after the initial reduction in A from A_i to A_0 the two systems are effectively identical other than in the history of their driving, the divergence in the beds' dynamical behaviours strongly implies the presence of *hysteretic effects* [270,271] within the system. Even more remarkable, considering our present aims, the history-dependent behaviour observed acts to *further increase* the rate of segregation above and beyond the increase expected based on the assumption of a non-deterministic system.

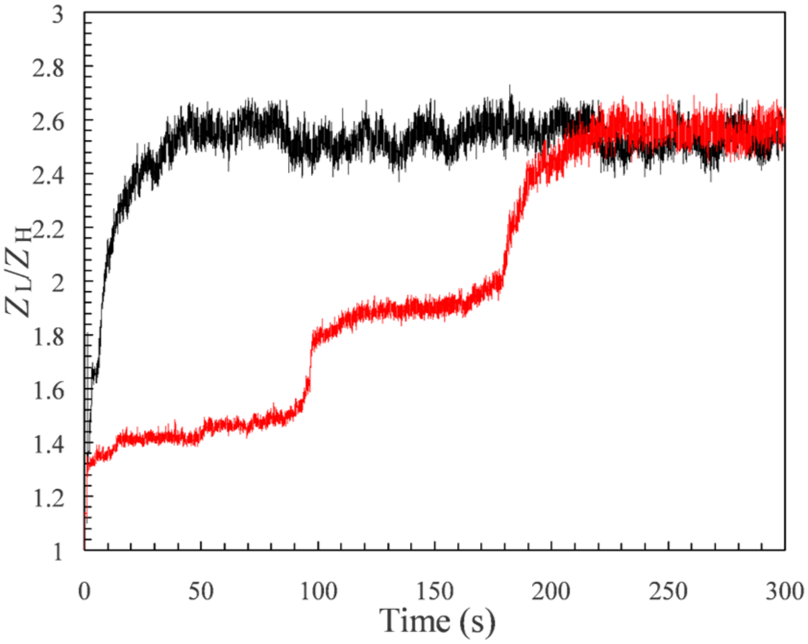

Figure 5.17: Comparison of the time-evolution of the centre of mass ratio for light and heavy particles, $\frac{Z_L}{Z_H}$, for two otherwise identical systems exposed to initially strong driving, ISD, (black line) and continuous driving, CD, (red line), the definitions of which are provided in the main text. For both ISD and CD systems, $N_L = 24.4$, Γ_0, the steady-state peak acceleration, is equal to 17 times the strength of gravity and the density ratio $r = 5$. Clearly, a larger ratio $\frac{Z_L}{Z_H}$ represents more complete segregation. Figure taken from our reference [13].

Specifically, for the case shown in Fig. 5.17, we see that while the ISD system undergoes segregation in a relatively smooth, continuous fashion, indicative of a well-fluidised system in which segregation is buoyancy-driven [146], the equivalent CD system exhibits ‘step-like’ behaviour, suggesting that segregation occurs as a series of discrete particle rearrangements [122, 272], implying a less mobile, more solid-like state [138]. The contrasting behaviour between the two systems is found to persist over many repeated experiments, showing this to be a robust phenomenon. Indeed, hysteretic effects arising from differences in systems' initial driving conditions are observed for a range of system parameters, producing a variety of interesting effects which will be discussed in detail through the course of this section.

We first focus, however, on providing a basic, qualitative explanation for the possible physical origins of the specific behaviours observed in Fig. 5.17. We propose that the differences between the two systems can, perhaps, be explained as follows: the strong excitation experienced by the ISD system during its initial phase creates a highly dilute granular fluid whose density distribution may be expected to be relatively spatially uniform [250]. As A is sharply reduced from A_i to A_0, the bed rapidly 'cools' and condenses into its lower-energy state, in a manner analogous to the rapid quenching required for the supercooling of a molecular liquid [216]. Continuing the analogy, if the initial state is devoid of the density inhomogeneities which typically trigger clusterisation in granular materials (here representing a parallel for the impurities in classical fluids which form the 'seeds' of crystallisation) and the bed cools at such a rate that the its contraction occurs on a timescale shorter than that required for significant clusterisation to occur [273], one may expect the final state achieved to be more spatially homogeneous, and hence more mobile [274, 275] than an equivalent CD system.

History-Dependence of the Dynamics of Monodisperse Systems

Having presented a tentative explanation for the differences in behaviour between ISD and CD systems, we now attempt to provide support for our hypothesis. We consider first the case of monodisperse systems, which provide a somewhat simplified situation in which to probe the existence of specific hysteretic effects. Analysis of monodisperse systems of steel and glass particles with various bed heights, N_L, driven with various shaking strengths, S, shows that hysteretic effects are only significant for systems possessing bulk packing fractions, η above a critical threshold value $\eta_c \sim 0.42$. Evidence for this

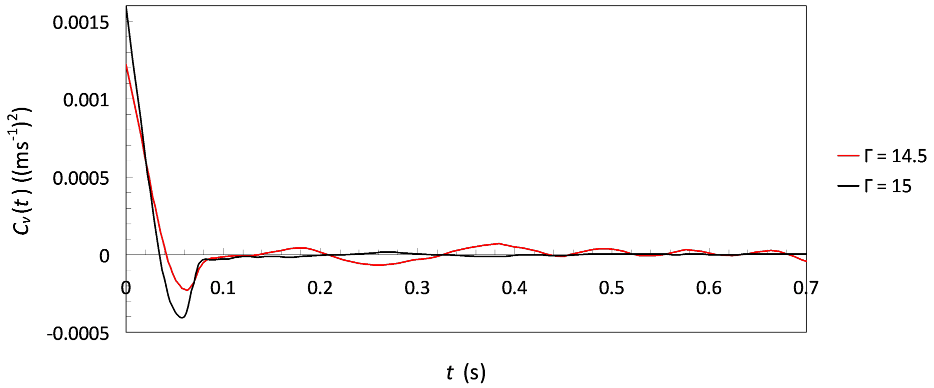

Figure 5.18: Experimentally acquired velocity autocorrelation functions, $C_v(t)$, for a bed of height N_L = 7 driven with a constant peak acceleration Γ_0 = 14.5 (solid red line) and Γ_0 = 15 (solid black line). Figure taken from our reference [16].

transition point can be seen in Figures 5.18 and 5.19; Figure 5.18 shows the velocity autocorrelation functions, $C_v(t)$, for two near-identical, *continuously driven* systems distinct only due to the slight difference in the strength with which they are driven. The velocity autocorrelation function (VACF) provides a measure of the rate at which a particle's velocity becomes decorrelated from its original value, i.e. how much 'memory' of its initial conditions a system retains. Thus, $C_v(t)$ can be used as an indicator of a system's potential history-dependence.

The velocity autocorrelation function may be determined from PEPT data as follows: firstly, particle velocities corresponding to each PEPT data point are calculated as described in previous sections. The entire data set is then divided into a series of overlapping, one second 'traces', with each data point forming an individual 'start point' of a trace, with a start time t_s corresponding to the t-value of the current data point . The velocity correlation for the i^{th} trace is given, for a single cartesian component, as:

$$C_v^i = v(t + t_s)v(t) \tag{5.2}$$

Data points corresponding to each individual VACF trace are binned with a 1 ms time interval, and the overall velocity autocorrelation function, $C_v(t)$, determined by averaging over all of the individual VACFs computed.

In the image shown, we see that the VACF corresponding to the more strongly driven – and hence dilute – system decays relatively rapidly to zero, where it subsequently remains, suggesting the bed's dynamics to be relatively chaotic and history-independent [72]. The more weakly driven system, on the other hand, exhibits a periodic fluctuation in its VACF, indicative of the fact that the system retains some memory of its initial conditions even after multiple particle collisions. The observed oscillation in $C_v(t)$, whose period spans several times the mean particle collision rate, corresponds closely to the observations of Campbell [276] for a sheared granular system. In this paper, it is proposed that such periodic structure is evidence of particles undergoing a repeated, coordinated motion within a bed possessing an ordered microstructure. This pattern of collisions was indeed observed to persist over $\mathcal{O}(100)$ collisions. The presence of a periodicity in the velocity autocorrelation functions corresponding to our system agrees well with our proposition that its behaviour is indeed history-dependent. It must be borne in mind, however, that for the relatively dense systems discussed here, the error on the velocity values used to calculate $C_v(t)$ will be considerable; specifically, approximately 30% of the calculated velocities are likely to be affected by undetected collisions. As such, the results discussed above, while interesting, must be treated cautiously. Therefore, in the remainder of this section, we focus our discussion instead on more reliably calculated quantities.

Figure 5.19 shows comparisons of the mean squared displacement (MSD) behaviour for equivalent ISD and CD systems for beds possessing packing fractions slightly below ($\eta \approx 0.41$ – image (a)) and slightly above ($\eta \approx 0.43$ – image (b)) the critical density η_c. It is clear from the images shown that *below* the threshold the diffusive behaviour of both systems is approximately consistent, suggesting a lack of significant history-dependence.

For the denser system, however, one observes a definite disparity between the mean squared displacements observed within the two systems, indicative of the presence of hysteretic effects. For the remainder of this section, since our main interest lies in the behaviours of hysteretic systems, we shall discuss exclusively those systems for which $\phi \gtrsim \phi_c$.

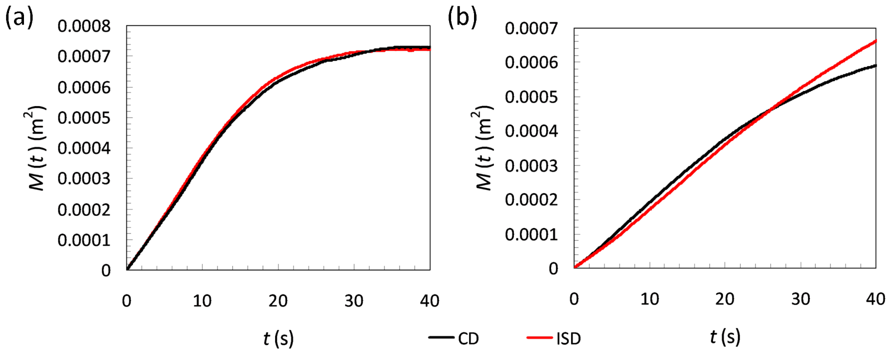

Figure 5.19: Comparison of experimental mean squared displacements, $M(t)$, for continuously driven (CD) and initially strongly driven (ISD) systems of resting height $N_L = 7$ driven with dimensionless acceleration $\Gamma_0 = 14.5$ (panel (a)) and $\Gamma_0 = 15$ (panel (b)). The ISD systems are initially driven with peak acceleration $\Gamma_i = \frac{3}{2}\Gamma_0$ for a period of two seconds. Figure taken from our reference [16].

Figure 5.20 shows mean squared displacement data for a system of the same resting depth, N_L, as those shown in Figs. 5.18 and 5.19 but exposed to comparatively weak driving, resulting in a more densely packed bed. In this denser case, the history-dependent nature of the system is more pronounced, with the two systems, identical in all aspects other than their initial driving, displaying highly disparate dynamics. The ISD system shows the mean squared displacement behaviour characteristic of simple, fluid-like dynamics, exhibiting ballistic behaviour at small t before crossing over to diffusive behaviour [277, 278]. Conversely, for the CD system, the relationship between $M(t)$ and t passes through a plateau of subdiffusive behaviour in between the ballistic and diffusive regions, a trend more reminiscent of supercooled or glassy molecular systems [279]. The existence of such an inflection indicates the presence of *caging effects* [280, 281] within the continuously driven bed. Further evidence of the presence of this 'caging' – a term used to describe the situation wherein particles become temporarily 'trapped' in a cell (or cage) formed by their nearest neighbours [282] – may be seen in Figure 5.21; this Figure shows the variation with time of the horizontal (x) position of the tracer particle for each of the systems shown in Figure 5.20. The considerable dissimilarity between the tracer's motion within each system once again highlights the considerable impact of initial strong driving on a system's subsequent dynamics. Most relevant to the current discussion, however, is the presence, for the case of continuous driving, of extended time periods during which the tracer's position simply oscillates around a fixed point in space. This behaviour provides support for our inference from the corresponding plot of $M(t)$ vs. t that particles within the system are subject to caging effects – i.e. repeatedly becoming confined by their neighbours, before breaking free and subsequently becoming caged once more by a new set of neighbours [283]. This behaviour is in stark contrast to that exhibited by the tracer within the equivalent ISD system, whose trajectory approximates Brownian motion, indicating classically diffusive behaviour.

Another remarkable observation to be drawn from the systems discussed above is that despite their vastly differing dynamics, the packing density remains surprisingly consistent between the CD and ISD cases, as illustrated in Figure 5.22. Indeed, under certain conditions, an ISD system may in fact possess a *higher packing density* than its CD counterpart, yet still maintain *greater mobility* and faster dynamics, in direct contrast to the conventional wisdom within the field, which suggests that increasingly dense systems should in fact become *less mobile* [281]. Evidence of the simultaneously increased mobility and greater packing fraction for an ISD system, as compared to an equivalent CD system, may be seen in Figure 5.23 – here, the relatively small plateau value of $M(t)$ for the ISD case implies a reduced free volume, i.e. a tighter packing [284].

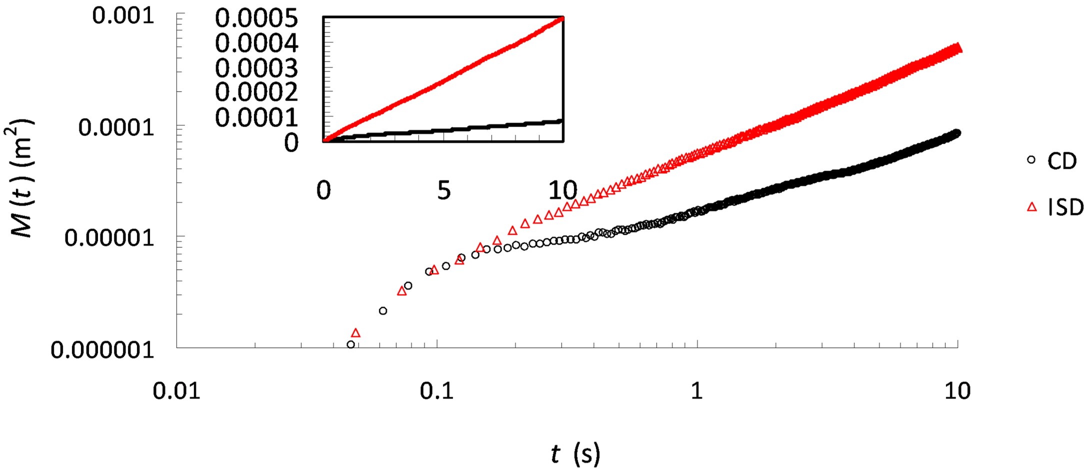

Figure 5.20: Experimentally acquired mean squared displacement, $M(t)$, as a function of time for a monodisperse bed of steel particles bed with a resting depth of $N_L = 7$ particle diameters which is excited with a steady state dimensionless acceleration $\Gamma_0 = 13$. Data is shown for equivalent continuously driven (black circles) and initially strongly driven (red triangles) systems. In the ISD case, the system is initially excited for a period of two seconds at a peak acceleration $\Gamma_i = \frac{3}{2}\Gamma_0 = 19.5$. The inset of the image shows the same data presented on a linear, as opposed to log-linear, scale, emphasising the increased mobility for the ISD case. Figure taken from our reference [16].

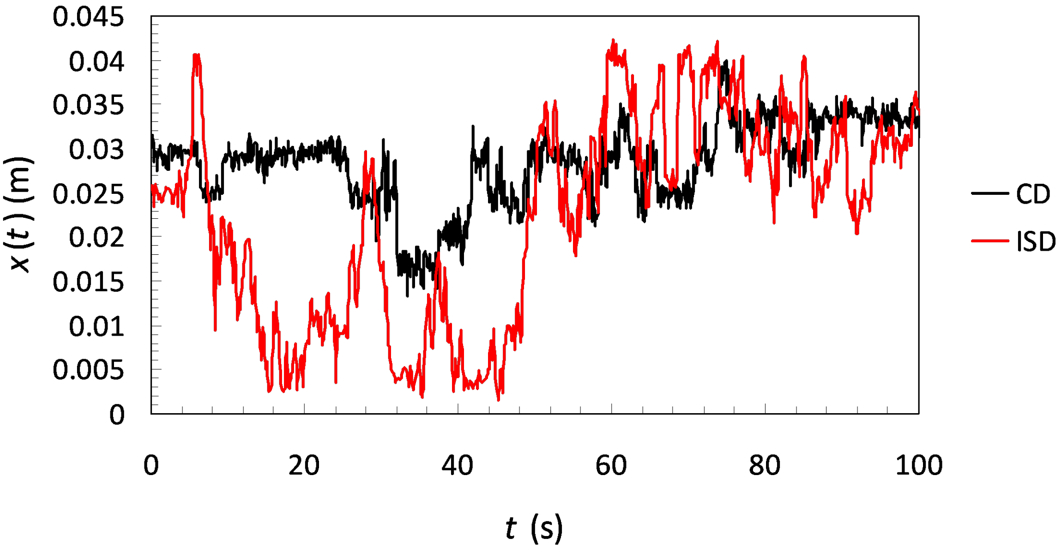

Figure 5.21: A typical example of the evolution with time of the (horizontal) x-position of a single tracer particle within the continuously driven (black line) and initially strongly driven (red line) systems detailed in Figure 5.20 above. Figure taken from our reference [16].

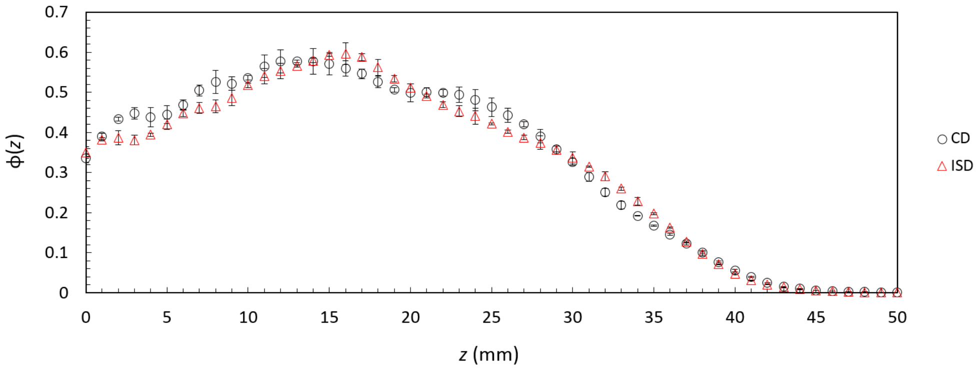

Figure 5.22: Experimentally obtained vertical packing density profiles for the same systems as discussed in Figures 5.20 and 5.21. Figure taken from our reference [16].

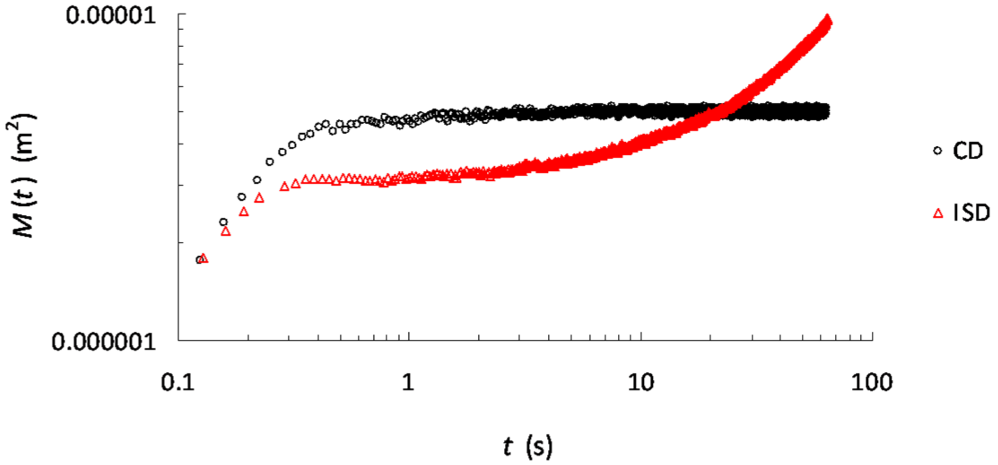

Figure 5.23: Mean squared displacement behaviour corresponding to a pair of experimental granular systems identical in terms of their steady-state driving ($\Gamma_0 = 13$), resting bed height ($N_L = 12$) and other relevant properties, differing only in the manner of their original excitation – one bed, represented by red triangles, is initially vibrated at an increased acceleration $\Gamma_i = 19.5$ for a two second period while the other, represented by black circles, is driven continually at Γ_0. Figure taken from our reference [16].

As the system's density increases further from the threshold value for hysteresis, η_c, the differences in the steady-state dynamics of the continuously driven and initially strongly driven systems become still more pronounced. Figure 5.24 shows the mean squared displacement behaviour for a bed of height $N_L = 12$ particle diameters for both CD and ISD excitation; included also in this image is a comparison of the typical evolution of the particle's typical horizontal motion within the system, which perhaps better captures the strongly divergent dynamics of the two differently driven systems. From the MSD behaviour shown in panel (a) of this Figure we see that, although both ISD *and* CD systems now show a point of inflection in $M(t)$ (i.e. both systems may be expected to demonstrate caging effects to some degree), the subdiffusive plateau for the CD case is greater in length than for the ISD system demonstrating that, in the former system, particles remain caged for longer periods of time [285]. This inference is well supported by the particle trajectories shown in panel (b), which show the ISD tracer to spend considerable periods of time simply oscillating about a fixed point while the tracer corresponding to the equivalent ISD system is typically observed to move through the system more freely, becoming caged only for comparatively short durations.

As the system's packing density becomes greater still, approaching the maximal solids fraction for a system of spheres, the form of driving (ISD or CD) used to excite otherwise identical systems can even represent the difference between a mobile and a "*jammed*" state, wherein particle motion is entirely arrested and the system becomes permanently locked in a single configuration [286] (see Figure 5.23). Although the hysteretic nature of systems close to the jamming transition is well known to affect the packing densities and stress distributions acquired by a system in its final, jammed state [287–289], the ability of a system's initial driving conditions to determine its ultimate *dynamical state* – i.e. whether the bed is static or mobile – is, to the best of our knowledge, a novel observation.

Having described the numerous ways in which the initial driving conditions of a system

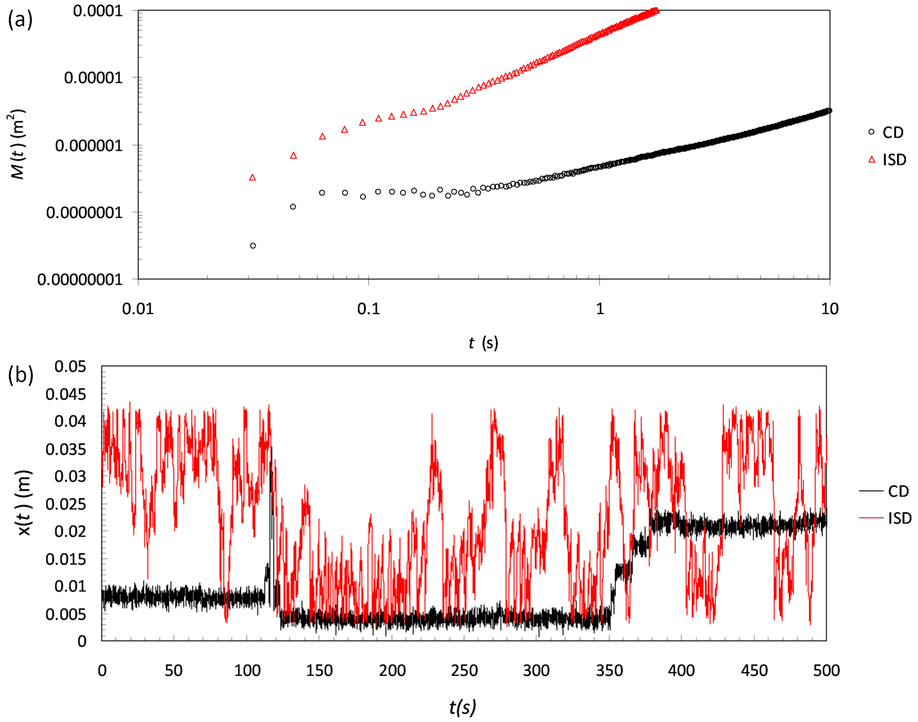

Figure 5.24: Experimental results showing (a) the variation with time of the mean squared displacement, $M(t)$, for particles within a pair of corresponding initially strongly driven and continuously driven systems and (b) the evolution with time of the relevant tracer particle's horizontal position in the x-direction for the same CD-ISD dyad. For both ISD and CD systems, $N_L = 12$ and $\Gamma_0 = 14.5$, with an initial driving acceleration $\Gamma_i = 21.75$ in the ISD case. Figure taken from our reference [16].

may affect its subsequent steady-state behaviour, we must now address the question of *why* these effects are observed. In particular, we must attempt to explain the counter-intuitive results noted above whereby denser (or equally dense) beds may exhibit *faster dynamics* than comparatively dilute systems, in direct contradiction of the generally expected monotonically decreasing relation between bed density and system mobility [290]. The answer to this question perhaps lies in the work of Watanabe and Tanaka [291] who propose that the slowing dynamics of a system approaching the jamming transition may be due to the increasing presence of *medium-range crystalline order* (MRCO) [292, 293] within the bed. Indeed, they show that the decrease in mobility of a system approaching jamming may be explained *solely* by the greater presence of MRCO within the bed. In other words, the oft-observed correlation between increasing bed density and slowing dynamics may only be an *indirect link* – greater levels of MRCO cause slow dynamics, the existence of MRCO is increasingly likely in denser systems, therefore more compact systems typically exhibit slower dynamics. If it is indeed true that the degree of MRCO clustering alone may be responsible for the slowing dynamics of our systems, then our above discussion regarding the reduced heterogeneity of ISD, as compared to CD, systems may well be able to explain our results.

The hypothesis that systems possessing reduced MRCO (i.e. more spatially homogeneous beds) will exhibit greater mobility also resolves the seemingly contradictory situation in which systems are both more dense *and* possess faster dynamics: if one is to consider a granular medium as a conglomeration of randomly packed particles and particulate clusters [274], a greater number of clusters and/or a larger typical cluster size will exacerbate the presence of defects in the bed. This will, by definition, result in an increased void space, and hence a *reduced average packing density* for the system. Hence, it is perhaps not surprising that, under certain circumstances, a system possessing less (MRCO) clustering may be simultaneously more mobile and more dense than a similar system in which clusters are more prevalent.

Although the above proposal provides a pleasing explanation of our observations, it still remains for us to provide direct evidence that MRCO clustering is indeed present in our systems. To this end, we turn to an analysis of the various *structural properties* associated with our systems; firstly, we introduce the *radial distribution function*, $g(r/d)$, which provides a measure of the average number of particle centres, $N_{ave.}$, falling within a spherical shell of thickness $\Delta(r/d)$ at a distance r/d from the centre of a given particle [294]. For our purposes, the radial distribution function, as extracted from our simulated systems, can be defined as:

$$g(r/d) = \frac{N_{ave.}}{4\pi(r/d)^2\Delta(r/d)} \tag{5.3}$$

The form of the radial distribution function can be used to determine the physical state of a granular system [295]; in particular, the presence of distinct peaks in $g(r/d)$ at radii $r/d = \sqrt{2}$ and $r/d = \sqrt{3}$, as may be seen for the continuously driven system represented in Figure 5.25, are indicative of the presence of crystalline structure within the bed. The comparatively smooth radial distribution function for the otherwise identical ISD system provides a considerable measure of support for our hypothesis that it is the relatively homogeneous, crystal-free nature of the ISD systems which allows their faster dynamics. Further support is provided through analysis of the *coordination number*, and the differences therein between equivalent CD and ISD systems. The average coordination number, $\langle Z \rangle$, is a measure of the mean number of contacts or 'nearest neighbours' per particle [296], and can be simply defined as:

$$\langle Z \rangle = \frac{\sum\limits_{i=1}^{i=n} Z_i}{N} \tag{5.4}$$

where Z_i is the number of contacts belonging to the i^{th} particle within the system. For a disordered bed of equally-sized particles, one would expect an average coordination number $4 \lesssim \langle Z \rangle \lesssim 6$ [297, 298] and a normal distribution of Z values [266], as is indeed observed for the ISD system shown in Fig. 5.25 (b). As a system becomes more ordered, however – as would be expected in the presence of substantial medium-range crystalline ordering – the distribution will become less uniform, and $\langle Z \rangle$ will attain higher values [299, 300], as exhibited by the corresponding CD system.

The final evidence suggesting the presence of MRCO in our system may be seen in Fig. 5.26, which shows the presence of localised regions of increased packing within the bed, indicative of the existence of crystalline order within these segments of the experimental volume. It is worth noting that data corresponding to the below image were acquired over a particularly long duration (τ_{run} = 32400 s) in order to allow the tracer to fully explore the experimental volume in spite of the slow dynamics of the bed.

It is interesting to note that, as may be expected from our supercooling analogy, the steady-state dynamical behaviour of our ISD systems is also dependent on the *rate* at which the initial, strong driving (A_i, Γ_i). is reduced to the final, steady-state value (A_0, Γ_0). Although the results discussed up until this point all correspond to the situation of an effectively instantaneous transition between A_i and A_0, additional data was also obtained for the case in which the initial driving was linearly reduced to its final value over a period of 5 seconds. In this case, the steady state dynamics achieved by the system and, more relevantly, the differences in dynamical behaviour between ISD and CD systems, are observed to vary significantly depending on the details of the bed in question – in some instances, the differences between ISD and CD systems were found to be as pronounced as for the case of an instantaneous reduction in A_0. Conversely, for other cases the slower reduction in initial driving strength is seemingly adequate to negate the supercooling-like effect discussed above, resulting in near-identical behaviour for ISD and CD beds. In still other instances, the behaviour is found to lie somewhere in between, with definite, yet less marked, differences in particle mobility between the differingly driven systems. These differences are perhaps not surprising when put in the context of our arguments from earlier in this section – dependent on the driving details and resting

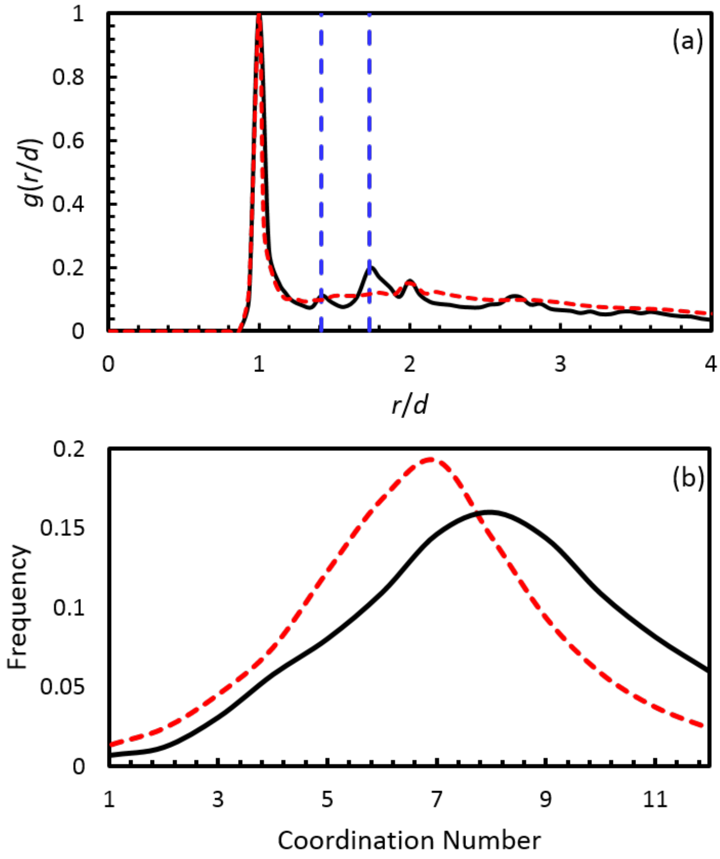

Figure 5.25: (a) Radial distribution function, $g(r/d)$, for an ISD-CD dyad with Γ_0 = 14 (Γ_i = 21 for the ISD system) and N_L = 10. (b) Coordination number distributions for the case Γ_0 = 13 (Γ_i = 19.5), N_L = 8. In both images, results pertaining to the CD system are represented by a solid black line, while those corresponding to the ISD system are depicted as dashed red lines. The marked variations in the two quantities shown between the equivalent CD and ISD systems provide a clear illustration of the differing degrees of crystalline order within the differently driven systems. All data shown correspond to DPM simulations. Figure taken from our reference [16].

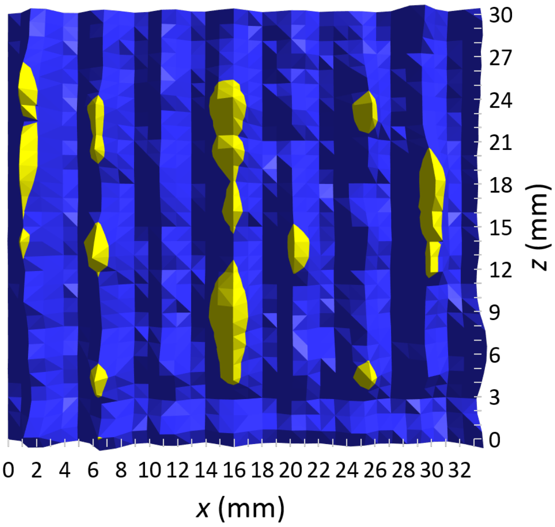

Figure 5.26: Two-dimensional spatial packing density distribution for an experimental continuously driven (CD) system of depth $N_L = 14$ excited with a peak dimensionless acceleration $\Gamma_0 = 14$. Regions of the bed for which the local solids fraction exceeds the random close-packed value $\eta = 0.63$ are highlighted in yellow, while areas in which the packing density falls below this value are shown in blue. The presence of multiple, localised regions for which $\eta > \eta_{rcp}$ provides a strong indication of the presence of crystalline structure within the system. Figure taken from our reference [16].

height of the bed in question, the timescale of cluster formation ($\tau_{cluster}$) within the bed may vary significantly. Thus, in some instances this timescale will still be considerably greater than the (now increased) relaxation timescale (τ_r) of the bed, leading as before to a significant divergence between the steady-state dynamics of ISD and CD systems. In other cases, where $\tau_r \gg \tau_{cluster}$, the initial strong driving will have no appreciable impact on the subsequent dynamics, leading to similar steady states for both ISD and CD. Finally, when the two timescales τ_r and $\tau_{cluster}$ are comparable, one may still expect a reduction in clustering, albeit less emphatic than for the case $\tau_r \ll \tau_{cluster}$. Similar observations may also be expected by keeping the system parameters (and hence $\tau_{cluster}$) constant and varying instead the duration over which A_i, Γ_i are reduced. Although our results are not substantial enough to make any reliable assertions regarding the precise relationships between the systems' control parameters, the rate of decrease of driving strength and the resultant bed dynamics, this is certainly a topic worthy of future research.

History-Dependence of Binary Systems and their Effects on Segregation

Having discussed in detail the effects of initial excitation strength on the subsequent dynamical and physical state of various monodisperse granulates, we now attempt to use these observations to provide a more thorough treatment of our findings regarding the segregation of binary systems described at the beginning of this section.

We quantify the segregation rate of a system using two parameters; for simulated systems we record the time evolution of the centres of mass (h) of both the heavy (H) and light (L) components of a given bidisperse bed. The ratio $\frac{h_L}{h_H}$ provides a measure of the degree to which a system is segregated with, for the case of an equal-volume mixture as described here, $\frac{h_L}{h_H} = 1$ representing a perfectly mixed system and $\frac{h_L}{h_H} = 3$ representing an entirely segregated system[1]. Of course, this latter value represents a highly idealised

---

[1] It should be noted that this only holds true for the case of simple, vertical, buoyancy-driven segregation, as is indeed present in the systems described here.

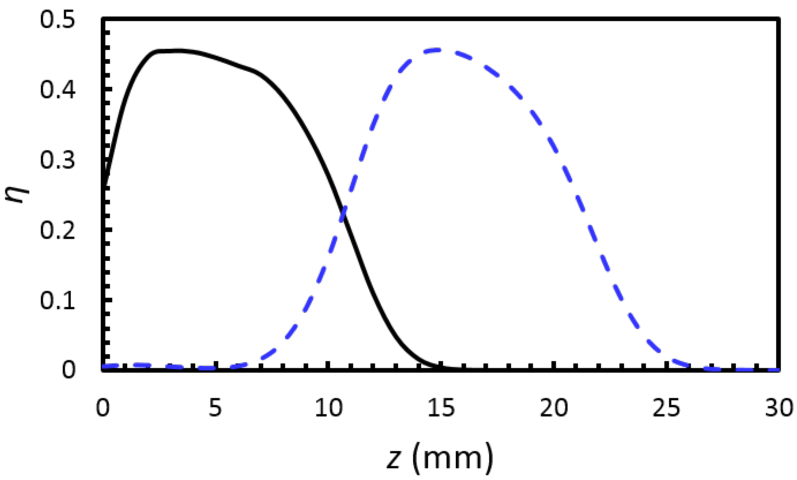

Figure 5.27: Simulated one-dimensional vertical packing profiles for the heavy (solid black line) and light (dashed blue line) components of a binary system of depth $N_L = 7.4$ whose components vary in density by a ratio $\frac{\rho_H}{\rho_L} = 8$. The system is driven with a peak dimensionless acceleration $\Gamma = 3.5$ and a peak driving velocity $v = 0.14$ ms^{-1}.

case - in reality, a fully-segregated system will possess a centre of mass ratio $\frac{h_L}{h_H} \sim 2.5$ due to the inevitability of a small degree of overlap at the interface between light and heavy particles (see Figure 5.27). For experimental systems, meanwhile, we analyse the vertical position of a single, light tracer particle in a bed of heavier particles as a function of time. Although the rise rate, τ_{rise}, of the single tracer during its ascent through the system is, clearly, not directly equivalent to the measure of segregation used in our simulated systems, where information corresponding to all particles within the bed may be simultaneously measured, by comparing the trends in the two quantities with various system parameters, we can provide some degree of validation for results obtained from our simulations. Similarly, there exist certain parallels between the single-particle dynamics observed within our experimental systems and the segregative behaviours of the corresponding simulated beds.

Figure 5.28 shows the vertical trajectory of a single, glass tracer particle in a bed

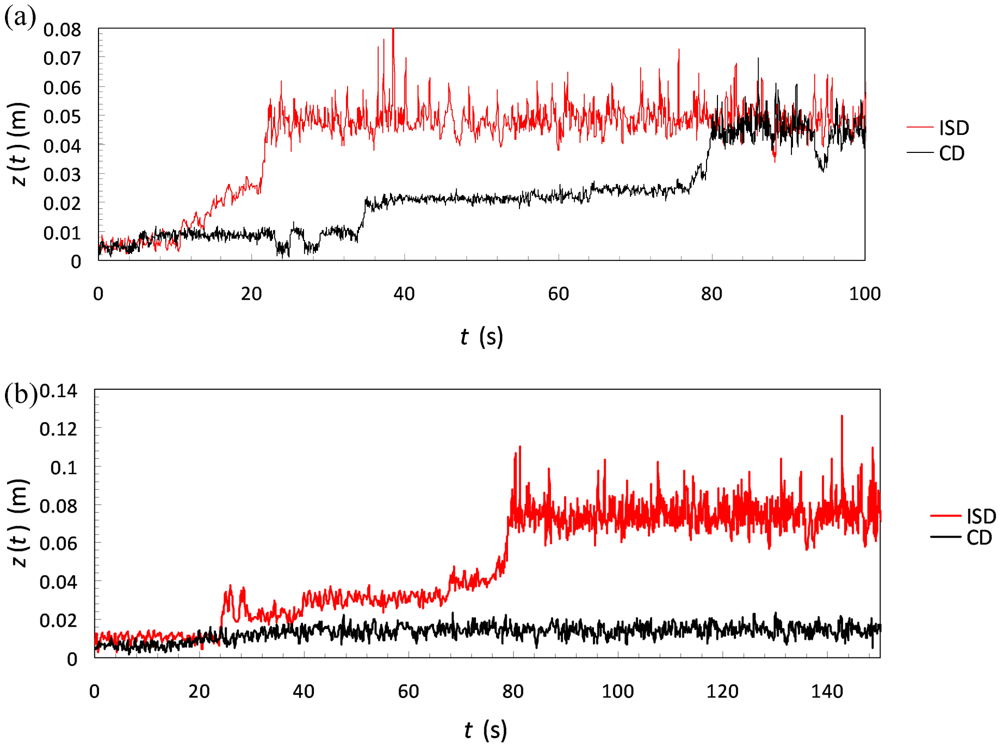

Figure 5.28: Experimental data plotting the variation with time of the vertical (z) position of a single glass (ρ = 2500 kgm^{-3}) sphere as it rises upward through a bed of equally-sized steel (ρ = 7900 kgm^{-3}) spheres. In each case, data is shown for both continuously driven (black lines) and initially strongly driven (red lines) systems with otherwise identical parameters. In panel (a), we see the behaviour of a bed of height $N_L = 7$, while the data shown in panel (b) corresponds to a bed with $N_L = 12$. In both cases, the steady-state driving acceleration, Γ_0, is equal to 13, with an initial driving $\Gamma_i = \frac{3}{2} \cdot \Gamma_0 = 19.5$ for the ISD systems in each of the two panels. Figure taken from our reference [16].

of equally-sized steel spheres. Aside from the inclusion of the glass tracer, the system shown in panel (a) is identical to that described in Figure 5.20 above, and the system corresponding to panel (b) is equivalent to that shown in Figure 5.23. Image (a) shows two important features: firstly, the upward transit of the light particle is considerably faster in the ISD system, indicative of the accelerated segregative processes expected. Secondly, the particle's ascent is smoother in the ISD than the CD case, the latter of which displays a more step-like rise, agreeing well with the results of our simulations as discussed earlier in this section and visually demonstrated in Figures 5.17 and 5.29. The denser case shown in image (b), meanwhile, once again demonstrates the ability of initial strong driving to 'mobilise' a system which would ordinarily be jammed, the immobile nature of the CD system evidenced by the lack of movement in any spatial dimension despite being continuously excited for a period of 7200 seconds. To ensure that the system was in a truly jammed state, repeated runs were conducted with the tracer particle initially placed in various regions of the bed; in all cases, both the resulting PEPT data and visual inspection confirmed the system to be entirely immobile aside from an initial transient period of densification when the system is first subjected to vibration. This observation demonstrates that ISD can even induce segregation in systems which would not normally undergo separation, a finding of potential value to industry.

Figure 5.29 shows data extracted from simulations of systems possessing driving parameters and bed heights identical to the experimental cases shown in Fig. 5.28, differing only in the composition of the granulate – instead of the single glass tracer immersed in a bed of steel particles used in experiment, the simulations implement a fully bidisperse bed, specifically a 50:50 ratio of monosized steel and glass particles.

A comparison of the corresponding experimental and simulational systems shows a remarkable similarity in the observed dynamical and segregative behaviours of the beds, despite the lack of direct equivalence in the quantities used to illustrate these behaviours. Specifically, for the more dilute system, we observe for both experiment and simulation

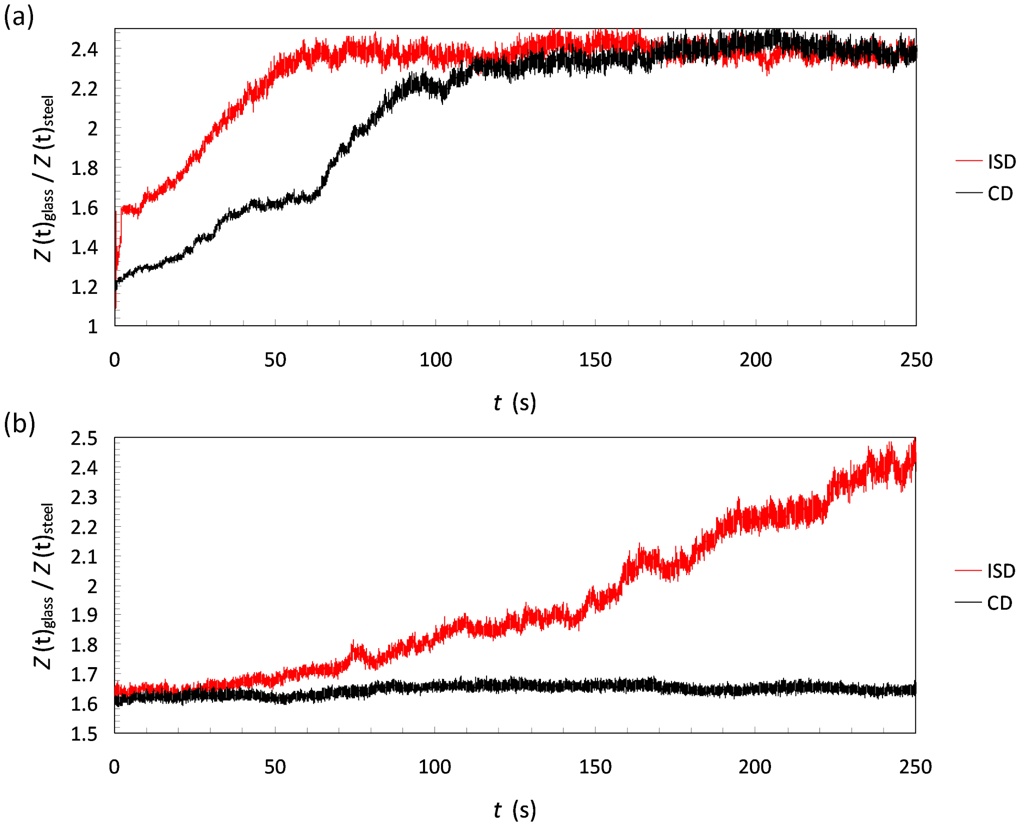

Figure 5.29: The centre of mass ratio, $\frac{Z_L}{Z_H}$ – an indicator of segregation – shown as a function of time for simulated ISD and CD systems with driving parameters and bed depths identical to those in Figure 5.28. Figure taken from our reference [16].

a relatively smooth increase in z and $\frac{h_L}{h_H}$ for the ISD case as compared to the discontinuous stepwise increase observed for the CD case. For the denser case, meanwhile, simulation and experiment once again agree in their demonstration of a jammed CD system and a mobile ISD system in which evidence of caging effects may be seen. The close correspondence between the experimental single-particle rise dynamics and the simulated evolution of $\frac{h_L}{h_H}$ provides strong support for the validity and robustness of our observations.

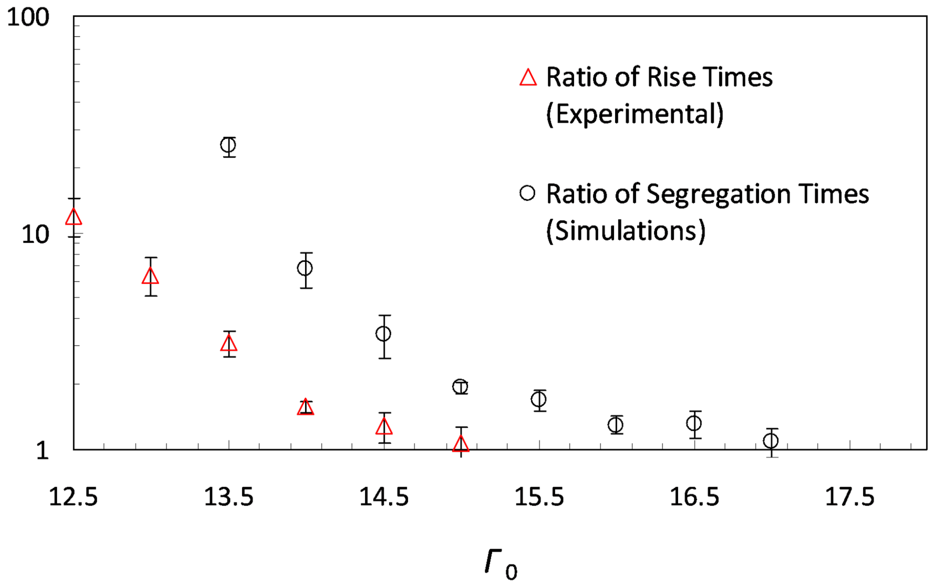

Figure 5.30: A visual illustration of the extent to which initial strong driving is found, on average, to accelerate the separation of particle species in a vibrated binary system for a range of steady-state driving strengths, Γ_0, and hence differing packing fractions, η. Shown here is experimental data, in the form of a ratio between the time taken for a single (light) glass particle to rise from the base to the free surface of a bed of (heavy) steel spheres for equivalent CD and ISD systems, and simulational data, presented as a ratio of the necessary times for complete (steady-state) segregation to be achieved by the two members of a CD-ISD pair. Figure taken from our reference [16].

A direct comparison of the extent to which ISD driving may, for a range of driving parameters, expedite the ascent of a single particle rise in an experimental system and the segregation of a simulated bed may be seen in Figure 5.30. Although the absolute timescales are – as one would expect – different for the experimental and simulational cases, the similarity in the observed trends provides additional verification of our hypotheses regarding the ability of initial strong driving to affect the subsequent dynamics of a binary system and, hence, accelerate the segregation thereof.

In summary, we have shown that the hysteretic nature of a dense, vibrofluidised granulate may be exploited in a variety of manners, most notably to prevent jamming, reduce caging and accelerate segregation – three matters of great relevance to numerous industrial processes. Despite the considerable length of this section, there remains much scope for future research stemming from this area of study; for instance the optimisation of the magnitude and duration of the initial, strong excitation of the system may provide still more impressive time and energy savings in processes which require segregation.

5.3 Suppressing Inelasticity-Induced Segregation

Although in this chapter we have already touched briefly on the matter of inelasticity-induced segregation, until now we have focussed predominantly on systems of steel and glass particles, whose coefficients of restitution are both relatively high and relatively similar to one another, thus largely suppressing any inelasticity-related species-separation. While the ignorance of specific inelasticity effects on systems' segregative behaviours may be acceptable in such cases, where differences in particle mass dwarf those in particle dissipation, the same cannot be said for all systems; as discussed in the previous section, effects due to particles' elasticities – and the ratio thereof between differing particle species within a system – can create serious complications in the analysis of binary and polydisperse systems, for instance by causing significant deviations from predictions based only on differences in particle size and density, or masking trends in behaviours caused by other particle properties. Therefore, it is of the utmost importance for researchers to be able to establish whether or not significant elasticity-related segregative effects are to be expected in a given system.

The aim of the work described in this section is to establish a manner in which one can predict, for any given vibrofluidised system, whether or not inelasticity-induced segregation is likely to play a significant rôle in the dynamical behaviour of said system. As has been discussed earlier in this thesis, there exists a pair of dimensionless control parameters, $S = \frac{\omega^2 A^2}{gd}$ and $\chi = N_L(1 - \varepsilon)$, by which one can fully describe a system's state. By creating a phase diagram highlighting the regions of S-χ parameter space[2] for which inelasticity effects become negligible, we provide a widely generalisable reference by which future researchers may easily determine whether or not they need consider these effects. Such an ability may, for instance, be used to plan experiments so as to avoid elasticity effects, to simplify theories (or more accurately determine their ranges of validity) or to explain discrepancies between seemingly contradictory findings in existing and future literature.

The experiments performed as a part of this current investigation utilise, once again, a set up largely similar to that described in section 3.1. A range of bed heights, N_L, were produced by varying both the container's horizontal extent, $L_{x,y}$, in the range $25 \leq L_{x,y} \leq 100$ as well as the number of particles housed within the container, specifically $N \in (2400, 6700)$. The particles used here are all spherical and of 3 mm diameter. The ability to vary N_L in two distinct manners is highly advantageous, as it allows a comparison of systems possessing equal N_L values created using different combinations of N and $L_{x,y}$, hence enabling us to assess the generality of our observations, and indeed the validity of χ as a true state variable.

A range of driving frequencies, $f \in (40, 100)$ Hz, and peak amplitudes, $A \in (0.388, 1.71)$ mm are explored, the lower limit of f chosen such that the frequency of oscillation is always adequately large to ensure that the bed dynamics are decorrelated from the vibratory motion of the container base [224].

---

[2] In the current section, we in fact largely refer to the parameter $V = \sqrt{S} = \frac{\omega A}{\sqrt{gd}}$ as opposed to S.

In experiment, we explore various binary combinations of glass, aluminium, stainless steel and chrome steel particles, with an equal-volume mixture of the relevant species ensured in all cases. 0.5 g of graphite powder is added to each system investigated as a means of reducing friction, and hence further isolating effects due to particle inelasticity.

Simulated systems, as usual, mimic their experimental counterparts through the inclusion of exact experimental parameters where possible, with $L_x, L_y, L_z, N, d, A, f, \rho$ and ε all implemented as their known values. The particle-wall restitution coefficient, ε_w is taken as the experimentally-determined value (0.59) for a collision between a glass sphere and the system walls; although the precise value of ε_w may be expected to vary for particles of differing material properties, preliminary data sets exploring a range of ε_w values show relatively little impact on the system's behaviour so long as the wall dissipation remained adequately low to prevent the formation of wall-induced thermal convection rolls. The coefficient of friction is taken as $\mu = 0$, in order to emulate the effects of lubrication in the experimental system. The validity of this choice for μ was tested by conducting repeated runs for a range of V and χ spanning the range used in experiment. It was observed that the variation of μ produces no fundamental change to the system's dynamics; rather, an increase in μ is, for the systems investigated, effectively equivalent to a decrease in ε. Since the ε values used correspond to *effective elasticities* as determined by Feitosa and Menon [10] (and discussed in greater detail in section 4.1), energy losses due to friction are already incorporated into the parameter meaning that, for the systems explored here, the use of $\mu = 0$ makes physical sense. It should be noted, however, that we explore predominantly *fully fluidised* systems – for systems in a more solid-like state, the assumption $\mu = 0$ is less likely to be valid.

In addition to the simulations and experimental work performed, we also attempt to construct a simple theoretical framework through which one may predict, for a system with known V and χ, whether or not inelasticity-induced segregation may be expected to significantly impact the behaviour of a bidisperse granulate. As we have discussed previously, for a well-fluidised system devoid of strong temperature gradients, one may expect segregation to be governed by simple, Archimedean buoyancy forces [146]. For the case of a *monosized* binary granulate such as those described here, the segregative behaviours exhibited will be largely determined by three factors: density, or equivalently mass, differences between particle species, the dissipative properties of differing particles, and the average packing density, η, of the bed as a whole. Clearly, with no other segregative effects present, a difference in particle density, i.e. a non-unity ratio $r = \frac{\rho_H}{\rho_L}$, will result in a tendency for the system to segregate, as heavier particles will preferentially migrate to the lower regions of the system while lighter particles are more likely to rise upward. It is highly useful to note at this point that the segregated state of a system can in fact be *fully characterised* by the parameter r defined above without any knowledge of the absolute values of each individual component [17]. This fact is clearly demonstrated in Fig. 5.31, which shows the particle distributions produced in a series of simulated systems in which all parameters – including the ratios $r = \frac{\rho_H}{\rho_L}$ and $R = \frac{\varepsilon_H}{\varepsilon_L}$ – are held constant, with the exception of the individual ρ values of the particles used, and hence the average particle density, $\bar{\rho}$. The image shows that despite a significant variation in the absolute density (and hence mass) values involved, so long as the *ratio of these densities* remains consistent, the segregation produced is effectively unaltered. Although this decoupling of a system's total mass (or, equivalently, average density) may initially seem somewhat surprising, it is in fact easily understandable, as both in simulation and, due to the feedback from our accelerometer (see section 3.1), in experiment, our granular beds are in effect driven by an infinitely massive wall.

The influence of the second factor which plays a determining rôle in the segregation observed within our systems – the bulk density, η – may also be fairly simply understood: the more dense the system, the higher the buoyancy forces acting on particles due to the increased mass of a given displaced volume [301]. The effects of particles' elasticities, and the ratios thereof between cohabiting species, meanwhile, are somewhat more subtle – as

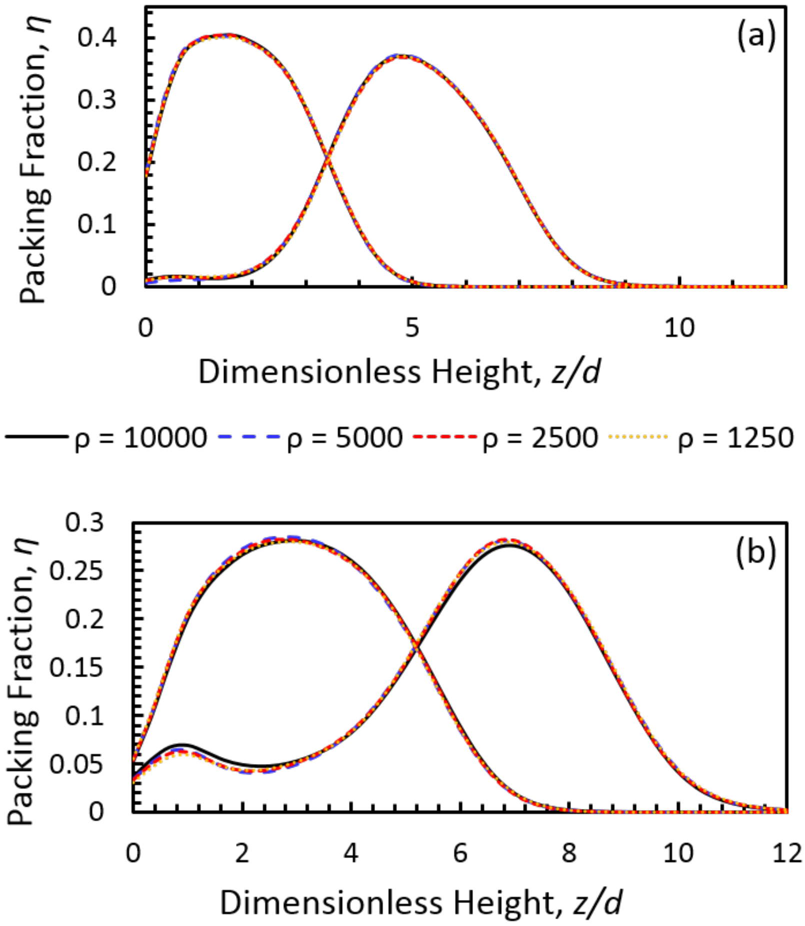

Figure 5.31: One-dimensional vertical packing distributions for both heavy (H) and light (L) components of a binary granular bed the case $N_L = 5.4$, $\varepsilon_H = \varepsilon_L = 0.83$ and $r = \frac{\rho_H}{\rho_L} = 4$. Data is shown for dimensionless driving accelerations $\Gamma = 3.5$ (panel (a)) and $\Gamma = 11$ (panel (b)). In each panel, particle distributions are shown for systems in which the *average* particle density varies from $\bar{\rho} = 1250$ kgm^{-3} ($\rho_L = 500$ kgm^{-3}, $\rho_H = 2000$ kgm^{-3}) to $\bar{\rho} = 10000$ kgm^{-3} ($\rho_L = 4000$ kgm^{-3}, $\rho_H = 16000$ kgm^{-3}). Figure taken from our reference [17].

discussed at length in previous sections (see, for example, sections 2.2, 2.2.3) differences in more dissipative particles' *effective weights* may lead such particles to 'sink' downward through the system [19, 20].

For binary systems in which both differences in ρ *and* ε are present – a situation more-or-less inevitable in any 'real-world' scenario – one may observe a competition between the two segregative mechanisms (e.g. if the heavier species is more elastic) or, conversely, one may find that the two forces act in unison (e.g. if the heavier particles are also more dissipative). However, our results strongly suggest that if the density ratio $r = \frac{\rho_H}{\rho_L}$ is adequately high, effects due to inelasticty differences are, seemingly, entirely negated. It is this observation which forms the basis of our theoretical arguments; in the following, we attempt to provide an explanation for the observed R-independence at high r, and use our hypothesis to explicitly determine the required 'critical' density ratio, r_c, above which one may predict inelasticity effects to become negligible for a given system density, η.

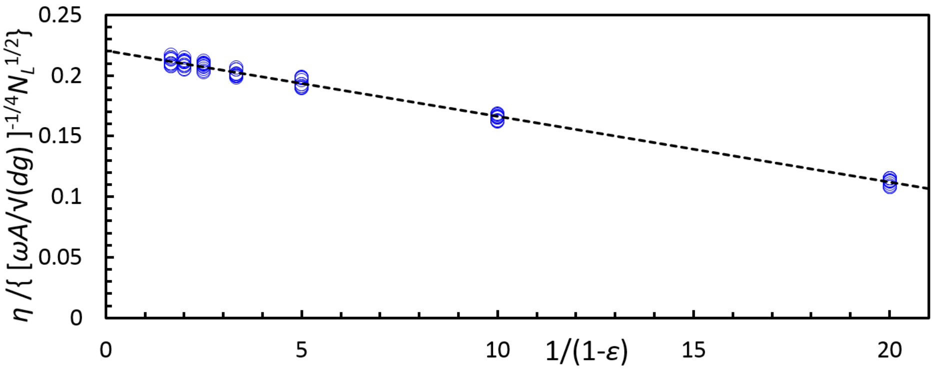

Figure 5.32: Plot showing the relationship connecting the average packing density, η, of a simulated, monodisperse granular system and the effective elasticity, ε, of the particles forming the bed. Data is shown for a range of driving parameters and bed heights, whose values span the ranges used in experiment. The η values are normalised by a factor $N_L^{\frac{1}{2}}(\omega A/\sqrt{dg})^{-\frac{1}{4}}$, whose significance is explained in the main text. Figure taken from our reference [18].

As may be deduced from existing theory [53, 61, 62], and further evidenced by the empirical data provided in our Figure 5.32, the packing density of a system can be related to the particle elasticity, ε, as:

$$\eta(N_L, f, A, \varepsilon) = \alpha - \frac{\beta}{(1-\varepsilon)} \tag{5.5}$$

with $\alpha = a{\cdot}F(N_L, f, A)$ and $\beta = b{\cdot}F(N_L, f, A)$, where a and b are constants. The normalisation factor used in Figure 5.32 corresponds to a function $F(N_L, f, A) = N_L^{\frac{1}{2}}(\omega A/\sqrt{dg})^{-\frac{1}{4}}$ empirically determined from our data. An interesting feature of Figure 5.32, or rather the linear relation it depicts, is that there exists a finite value of $\frac{1}{1-\varepsilon}$ at which the trend will intercept the x-axis. Since, clearly, a negative density for such a system is physically impossible, this intercept represents the point at which the theory presented must break down, suggesting specifically that the observed relation cannot be valid for $\varepsilon \gtrsim 0.98$. The physical significance of this intercept, although not discussed as part of this thesis, is nonetheless a subject worthy of future investigation

Following from equation (5.5), it may similarly be expected that two systems which are identical in terms of their driving, size and bed height but differ in their average particle elasticity will possess a ratio of packing densities given by:

$$\frac{\eta_1}{\eta_2} = \frac{a - b/(1-\varepsilon_1)}{a - b/(1-\varepsilon_2)} \tag{5.6}$$

where η_X and ε_X represent, respectively, the mean packing fraction and elasticity of system X and the constants a and b retain their definitions from the previous equation. In the scenario presented by Brito *et al.* [19, 20], it is proposed that an inelastic particle will modify the packing density of particles within a volume of diameter $\sim 3d$ in its immediate vicinity. If we assume equation 5.6 to hold, on a local level, for single systems comprising two differing particle species (as opposed to two separate, monodisperse systems) we can determine, from Archimedes' principle, the necessary conditions for which a *light* particle will migrate toward the *lower regions* of the container. If we define the *effective density*, $\tilde{\rho}_X$, of a particle of species X as the average ρ possessed by such a particle and those immediately surrounding it, an L particle may be expected to sink if the inequality:

$$\frac{\eta_L}{\eta_H} > \frac{\tilde{\rho}_H}{\tilde{\rho}_L} \tag{5.7}$$

is satisfied. Here, η_X represents the local packing density expected of particle species X. Consider now a granular mixture comprising two species, L and H, whose properties are such that $\rho_H > \rho_L$ and $\varepsilon_H > \varepsilon_L$. In such a system, the limiting case – i.e. the situation most favourable to the descent of the lighter but more dissipative species – is that in which all particles within an L-species particle's sphere of influence are of the opposite (heavier) species. If the average density, $\tilde{\rho}_L$, of such a conglomeration of particles is still insufficient to allow the L particle to penetrate downward into a pure region of H particles, one can reliably assume that the relative particle elasticity, R, between the two system components will have *no influence* on the steady-state separation achieved by the system. This being the case, we conjecture that inelasticity-induced segregation may be safely neglected for any systems which fulfil the condition:

$$\frac{\tilde{\rho}_h^{max}}{\tilde{\rho}_l^{max}} > \frac{\eta_l}{\eta_h} \tag{5.8}$$

where the superscript '*max*' denotes the situation in which all grains within the particle of interest's region of influence are of the comparatively heavy species, thus representing for the L species a cluster of maximal weight and for the H species a region of localised monodispersity.

For a known η value and density ratio, r, the local density, $\tilde{\rho}$, of a given system component can be estimated by determining the typical number of grains falling within the vicinity of a given particle and taking the average ρ of all particles within this region.

By assuming the situation in which all surrounding particles are of the H species, $\tilde{\rho}^{max}$ can then be calculated without the necessity of any additional system information. Thus, with only a knowledge of η and $r = \frac{\rho_H}{\rho_L}$, it is possible to predict whether or not a system's equilibrium distribution is likely to be subject to the influence of inelasticity-induced segregative behaviours.

Although the above is only a very simple theory, reliant on several disputable assumptions, we observe nonetheless a pleasing agreement with experimental and simulational results, as will be clearly highlighted in the remainder of this section.

In order to validate our theory, a large number of simulations were performed over a broad range of V-χ parameter space. So as to allow for comparison between theory and simulation, the critical ratio, r_c, of particle densities above which inelasticity effects are suppressed was determined. This was achieved as follows: for a given combination of V and χ, simulations were performed using a range of density ratios, $r = \frac{\rho_H}{\rho_L}$. For each of these density ratios, five individual combinations of ε_H and ε_L were tested, giving ratios $R = \frac{\varepsilon_H}{\varepsilon_L}$ of 9, 3, 1, $\frac{1}{3}$ and $\frac{1}{9}$. Inelasticity effects were deemed to be negligible if the segregation intensity (I_s) values for all five cases were found to agree to within 5%. Determining r_c is then simply a case of establishing the lowest ratio r for which this consistency in I_s is achieved. Although the 5% margin of error used may at first seem somewhat arbitrary, this choice of threshold value in fact arises due to the fact that the typical variation in I_s values acquired from repeated simulations of *identical systems* is $\lesssim 5\%$ – i.e. if the variation in I_s values across the tested R values is less than 5%, this fluctuation is not statistically significant, and one can safely assume ε-effects to be unimportant. It is additionally worth noting that our results are not strongly sensitive to the precise margin of error chosen, owing to the fact that when inelasticity effects *are* present, their influence is generally highly pronounced, with variations in I_s typically $\gtrsim 25\%$.

The above process was repeated for numerous V-χ pairings, and hence a variety of η

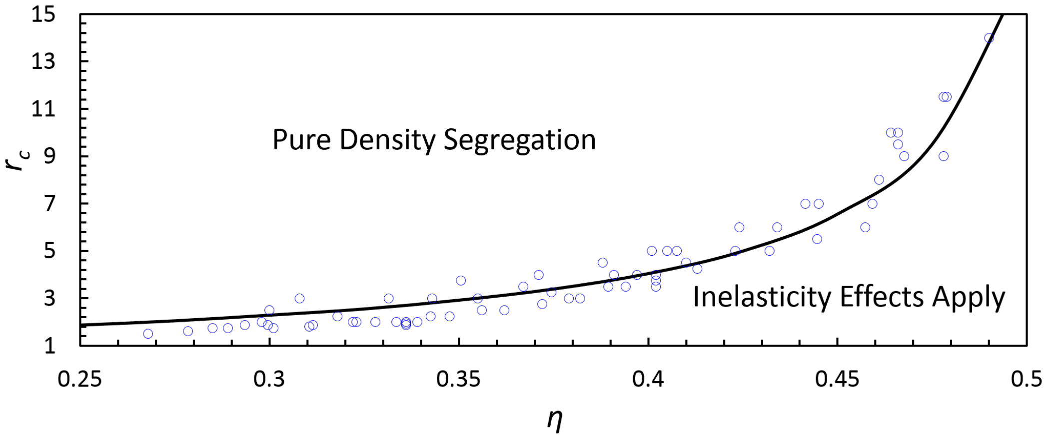

Figure 5.33: Plot of the critical ratio, r_c, of particle densities above which segregative effects due to differences in particle elasticity may be neglected as a function of the average packing density, η, of a binary granular bed. Open circles represent data from simulations while the (theoretical) solid line corresponds to the situation for which the inequality in equation (5.8) becomes balanced, i.e. the boundary dividing regions for which inelasticity effects may and may not be ignored. Figure taken from our reference [18].

values, allowing the phase diagrams presented in Figures 5.33 and 5.35 to be produced. Figure 5.33 shows a comparison of our theoretical predictions of the critical ratio density r_c with results acquired from simulation over a range of system packing fractions, η. The agreement demonstrated in this image not only provides support for the theory presented here but, since the construction of our theory relies heavily on the work of Brito *et al.*, also represents strong evidence that the phenomenon proposed by these researchers does indeed accurately describe the mechanism underlying inelasticity-induced segregation.

While the agreement between theory and simulation is generally strong, simulated data is observed to deviate more significantly from the theoretical predictions for more dilute systems; specifically, the theory is observed to systematically overestimate r_c for $\eta \lesssim 0.3$. The minor disagreement observed is thought to be due to the fact that the localised pockets of high density ('cold droplets') surrounding dissipative particles possess *finite lifespans*. In more dilute systems, such clusters of particles will evanesce more frequently

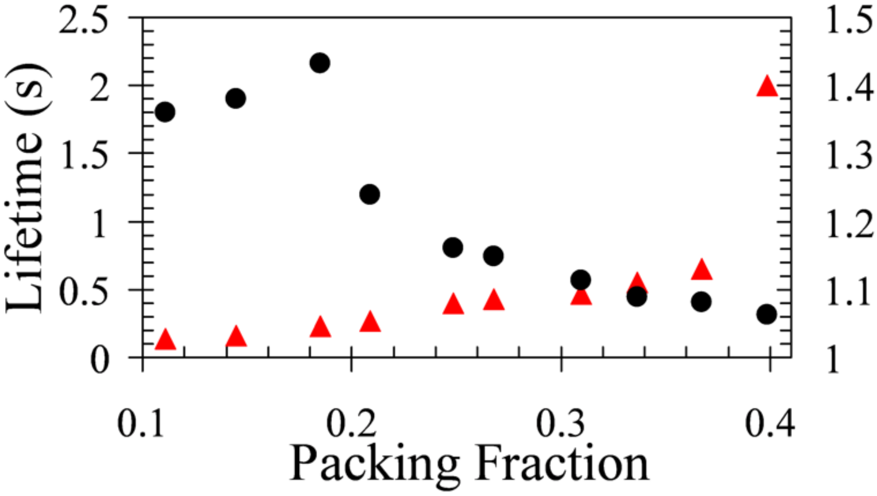

Figure 5.34: Variation with packing fraction, η, of the typical lifespan (red triangles) of the localised regions of high density or '*cold droplets*', the existence of which is believed [19,20] to facilitate inelasticity-induced segregation within vibrofluidised systems such as ours, and the local packing density of these droplets as compared to the system's average η value (black circles). The data shown corresponds to the situation $N_L = 2.5$, $\rho_A = \rho_B = 2500$ kgm^{-3} and $\varepsilon_A = 3 \cdot \varepsilon_B = 0.9$. Figure taken from our reference [13].

due to a relatively increased collision rate with the system's energising base [11, 302], as may be seen from our Figure 5.34. Hence, for lower η, the shortened cold-droplet lifetime will result in a weaker segregation than predicted by our theory, which does not account for the above-discussed effects.

The presence of cold droplets within our system can be easily observed from simulation data by identifying regions of increased density ($\eta_{local} \geq 1.2\eta_{average}$ [19]) surrounding a given dissipative particle. The lifespan of a given droplet can then be determined by identifying the specific particles belonging to this high-density region and recording the number of time steps for which they remain in close proximity, i.e. the average particle separation corresponds to the average packing density of a clustered region. The lifetime of a particle is defined simply as the duration of time between a droplet's initial formation and its dispersal by the system's vibrating bed.

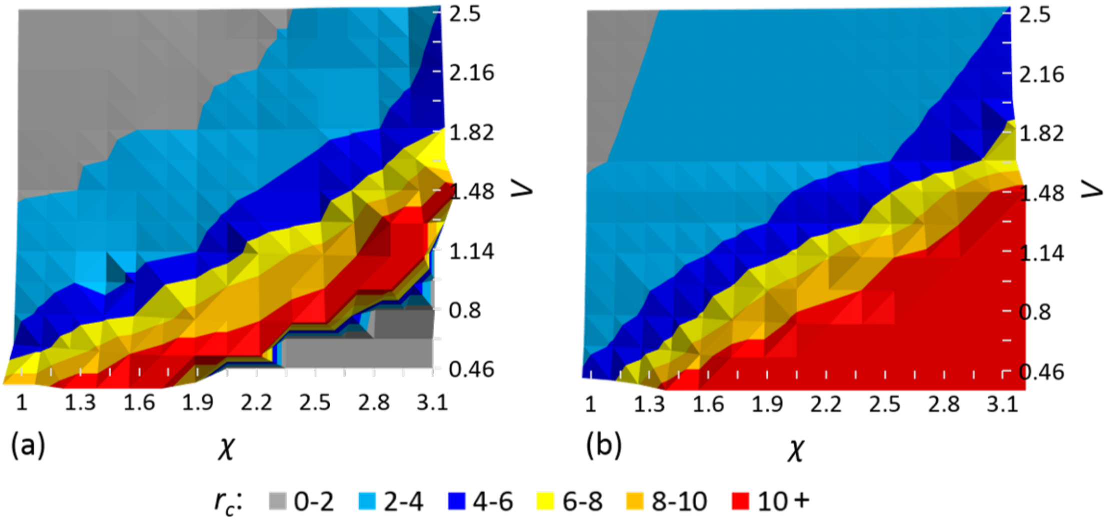

Figure 5.35: Phase diagram showing, for various combinations of the key dissipative control parameter χ and key excitation control parameter V the minimal necessary ratio, r_c, for which inelasticity effects on segregation are fully suppressed. Panel (a) shows data acquired from DPM simulations, while panel (b) presents the relevant theoretical predictions based on the framework presented above. Figure taken from our reference [18].

Although the ability to predict the presence or absence of an ε-related influence on a system's segregative behaviours based solely on said system's packing density may, in itself, prove highly useful in the analysis of *existing* data, its use as a *predictive tool* remains somewhat limited by the fact that η is not a directly controllable parameter. In order to remedy this issue, an additional phase diagram (see Figure 5.35) was also produced. Here, the necessary density ratios (r_c) above which inelasticity effects become suppressed are presented in V-χ parameter space (as opposed to simply as a function of η), with V and χ both known, controllable variables. An alternate representation of the data shown in Figure 5.35 may be seen in Figure 5.36, where results are instead presented in the r_c-V phase space for a variety of differing χ values.

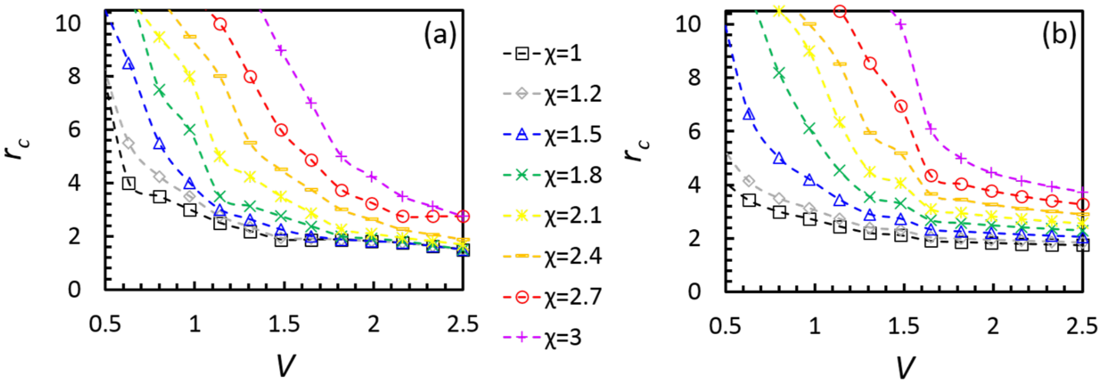

Figure 5.36: Data from Fig. 5.35 shown in r_c-V space for a variety of values of the key control parameter χ. Data is shown for (a) simulations and (b) our theoretical predictions. Figure taken from our reference [18].

Values of the critical density ratio, r_c, obtained from simulation and theory are found to agree to within a range $|r_c^{sim} - r_c^{theory}| < \frac{3}{2}$ throughout the majority of the V-χ parameter space. However, in the low-V, high-χ limit, one can clearly observe a significant discrepancy. Specifically, this observed disagreement is found to occur in regions of phase space for which $\eta \gtrsim 0.5$. The stark divergence of simulation and theory observed at $\eta \sim 0.5$ provides a useful indication of the range of validity for the theoretical framework presented here.

The breakdown of our theoretical model for high-density systems is certainly not overly surprisng, as in the dense limit a system is unlikely to be fully fluidised; since our theoretical framework is reliant upon the assumption that segregation arises due to Archimedean buoyancy forces, and these forces directly apply only in fluidlike systems, it is entirely understandable that when the condition of fluidisation is no longer fulfilled, our theory can no longer be expected to hold.

Having discussed at length the agreement shown between theory and *simulation*, we turn our attention now to the *experimental* results obtained. Unlike in simulation, the precise control and individual variation of particle density and elasticity is highly difficult to achieve in practical, experimental situations. Therefore, in order to assess the degree to which our theory agrees with experiment, we must adopt a different approach to that used in our comparison with simulated data. The experimental validation of our theory was performed as follows: two experimental bidisperse systems were prepared – a 50:50 mixture of stainless steel (H) and glass (L) spheres and a similarly composed bed of chrome steel (H) and aluminium (L) particles. Both systems are identical in terms of particle number, size and geometry, and are housed in identical containers, ensuring also a consistent resting bed depth, N_L. The materials used are chosen such that in both cases the ratio $r = \frac{\rho_H}{\rho_L} \approx 3.0 \pm 0.1$; *however*, while in the former (glass/steel) case $\varepsilon_H < \varepsilon_L$, in the latter (aluminium/steel) case, the inverse is true – i.e. $\varepsilon_H > \varepsilon_L$. This careful choice of material properties allows a more-or-less direct comparison of systems for which inelasticity-related and density driven segregative mechanisms compete, and those in which they act in unison.

In Figure 5.37 we see a two dimensional 'slice' through the phase diagram presented in Figure 5.35, showing the isoline for the case $r_c = 3$. For various discrete points in V-χ phase space, experimental data sets are obtained for systems driven with a dimensionless peak velocity V 0.1 above and below the theoretical value expected to produce an r_c value of 3 for a given χ. Since r_c denotes the transition point between the presence and suppression of inelasticity effects on segregation, one would expect that – if our theory is correct – experimental data sets acquired using V values *above* the theoretically predicted 'critical driving', V_c, should show a significant influence due to ε (i.e. $I_s(glass/steel) > I_s(aluminium/steel)$) while those for which $V < V_c$ should produce approximately identical steady state particle distributions (i.e. $I_s(glass/steel) \approx I_s(aluminium/steel)$). Specifically, as was the case in our comparison of simulation and theory, inelasticity effects are deemed negligible if the relevant I_s values are found to agree to within 5%. For cases in which experimental data was found not to match our expectations from the theoretical framework, additional data sets were acquired using a driving strength $V = V_c \pm 0.2$, $V = V_c \pm 0.3$ etc. until the transition point was successfully determined.

As may be seen from Fig. 5.37, the agreement between theory, simulation and experiment is, in general, relatively strong, with the notable exception of data for the case of large χ and small V (i.e. the high-density limit). The deviation observed here between experiment and simulation may perhaps be explained due to the imperfect modelling assumption $\mu = 0$; while such an assumption seems reasonable for more dilute, fluidised systems, in the case of highly dense systems the presence of phenomena such as jamming and caging may, as discussed in section 5.2, significantly affect segregation. Since these effects are highly dependent on frictional interactions between particles, it is perhaps unsurprising that our frictionless model does not accurately reproduce the behaviour of tightly packed systems.

To summarise, in this section we have formulated a simple theoretical framework by which one may predict, from known, controllable parameters, the presence or absence of significant inelasticity-induced segregative effects in a given granular system. The validity of the framework developed has been tested against experimental results as well as discrete particle method simulations, with strong agreement observed in both cases over a wide parameter space. This strong agreement not only underlines the

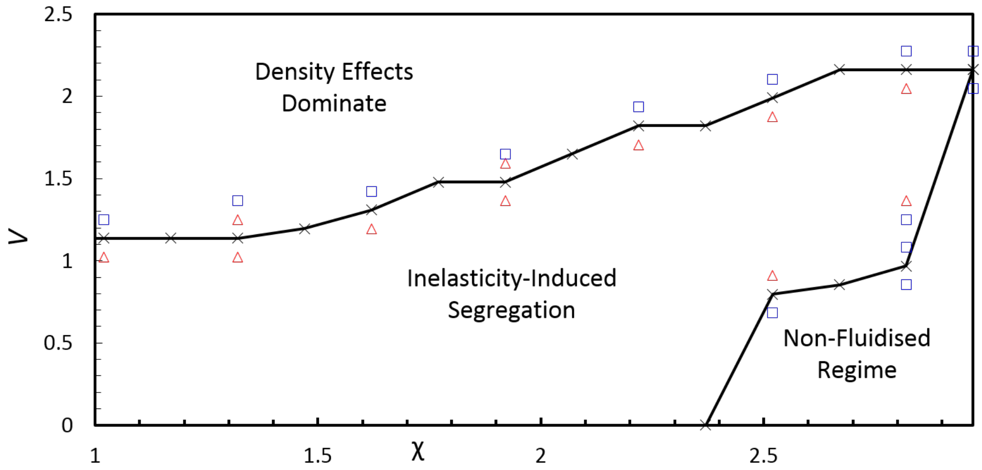

Figure 5.37: Two-dimensional slice through the phase diagram shown in Figure 5.35 for the case r_c = 3.0. In the image, theoretical predictions of the combinations of V and χ required to produce an r_c value of 3 are represented by crosses, while circles represent the points in V-χ space for which a critical ratio of 3 is found in simulation. The inclusion of simulated – as opposed to theoretical – results to represent the lower boundary arises due to the fact that the absence of elasticity-induced segregation in the non-fluidised limit is not captured by our simple theoretical model. Solid black lines connecting theoretical and simulated data points are used as a guide to the eye. Open squares and triangles represent experimental data, with triangles representing data sets in which inelasticity-induced segregative effects are apparent and squares corresponding to the cases in which such effects are seemingly absent. For the case of perfect agreement between experiment and theory/simulation, all triangles should fall within the region denoted “Inelasticity-Induced Segregation” with all squares lying external to this region. Figure taken from our reference [18].

potential value of our theory in various industrial and research applications, but also confirms, to within a reasonable doubt, the hypotheses of Brito *et al.* [19, 20] regarding the origins of inelasticity-segregation in vibrofluidised granulates. This is a particularly important result with regards to this thesis, as much of the work presented relies to some degree on the validity of this model. In the next section, we explore another relatively under-researched segregative mechanism – that which arises due to differences in particle geometry – and show, amongst other results, how inelasticity effects can still play a major rôle even in systems comprising considerably more complex particles and particle interactions.

5.4 Segregation and Energy Transfer in Systems of Non-Spherical Particles

As discussed in section 2.2.4, the concept of 'shape' is rather ambiguous and ill-defined, with numerous individual physical properties, each of which may individually affect a particle's dynamics, contributing to a particle's 'shape'. Therefore, in this section, we focus specifically on a single, clearly-defined quantity – the *radius of gyration*, r_g, which has long been used in various scientific disciplines as a measure of a particle's "*effective size*" [303–305] in granular, colloidal and molecular systems. Previous simulational work [175, 306] has shown r_g to play a crucial, indeed dominant, rôle in the segregation of relatively dilute systems comprising particles of varying geometry.

The radius of gyration is a fascinating quantity, as particles possessing equal masses and volumes (ν) can, due to various differences in their geometry, possess vastly different moments of inertia (I), and hence highly divergent r_g values or 'effective sizes'. In this section, we describe two experiments in which the strongly differing dynamical and segregative behaviours exhibited by particles of *equal volume* but contrasting radii of gyration are explored.

We begin by investigating the segregation of dilute binary systems comprising various combinations of equally-voluminous simple geometrical shapes – spheres, discs and cuboids – whose behaviours are seemingly governed by the relative r_g values of particles. The potential origins of this hypothetical rotational inertia-driven segregation are then probed through the study of a series of monodisperse systems composed of particles possessing a more complex geometry, carefully designed to isolate the effects of r_g as fully as possible. The geometries of the simple geometric shapes are provided in Figure 5.38, while details of the more complex may be found later in this section, where the experiments performed using these objects are discussed in greater detail.

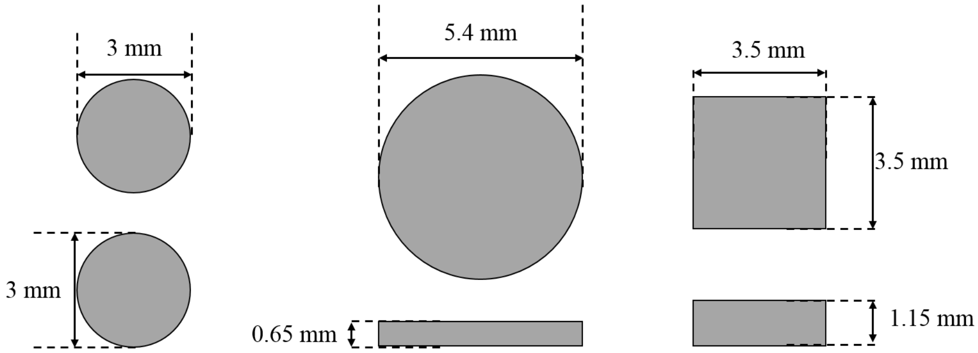

Figure 5.38: Scale diagrams showing the dimensions of the three differing particle geometries used in experiment: spherical (left), disc-like (horizontal centre) and cuboidal (right). For each particle type, plan (top) and side (bottom) views are shown (due to the symmetry of the particles used, the end view is, clearly, redundant).

As mentioned above, our first area of study concerns the segregation of particles with differing geometries but approximately equal volumes, specifically $\nu = 14.4 \pm 0.5$ mm^{-3}. Despite their near-identical ν-values, the particles used possess markedly different radii of gyration, r_g, with the cuboidal and disc-like particles respectively possessing values of r_g 1.3 and 1.6 times that of the equivalent sperical grains. For the purposes of the discussion presented here, the quoted r_g values are taken as the average value of the radii of gyration corresponding to a given particle's three major rotational axes. A series of binary systems, each containing $N_H = N_L = \frac{N}{2}$ particles, with $N \in (1000, 3000)$, are analysed, with combinations of particle species exploring all possible permutations. The beds studied are housed within square-based cuboidal containers of width $L_{x,y} \in (25, 100)$ mm, all of height 200 mm.

A variety of oscillatory frequencies and amplitudes are used to drive the system, with each parameter range spanning a decade, specifically $10 \leq f \leq 100$ Hz and $0.67 \leq A \leq 6.7$ mm. The wide f-A phase space utilised allows the dimensionless excitation parameters Γ and S to be varied independently which enables us to determine which of these parameters is most suitable for characterising the states of the systems explored. It is ensured that, in all cases, the combinations of f and A (and hence S and Γ) used to drive the system are adequate to ensure a highly excited, gaseous state. By ensuring that the beds explored are all relatively dilute, we actively suppress the maximal packing fraction related segregative mechanism proposed by Abreu *et al.* [166], thus further isolating effects due to r_g.

Figure 5.39 shows examples of the equilibrium distributions achieved by different particle combinations and for a variety of driving parameters. It is immediately apparent from this Figure that for all particle combinations and particle numbers as well as all f-A combinations explored, particles possessing greater radii of gyration are found to segregate towards the upper regions of the system; this observation is found to hold true for all recorded data sets, including those not explicitly presented here. It is perhaps worth noting, however, that the *magnitude* of this segregation varies considerably with the aforementioned system parameters. This result agrees well with those derived from the simulations of Roskilly *et al.*, who similarly observed a series of partially segregated systems in which the higher-r_g particles possess a higher average centre of mass position.

A second notable feature of our results is that, for frequencies $f \gtrsim 20$ Hz, the degree of segregation exhibited by a given system is not only seemingly independent of the specific combination of f and A at which the system is vibrated, but additionally shows

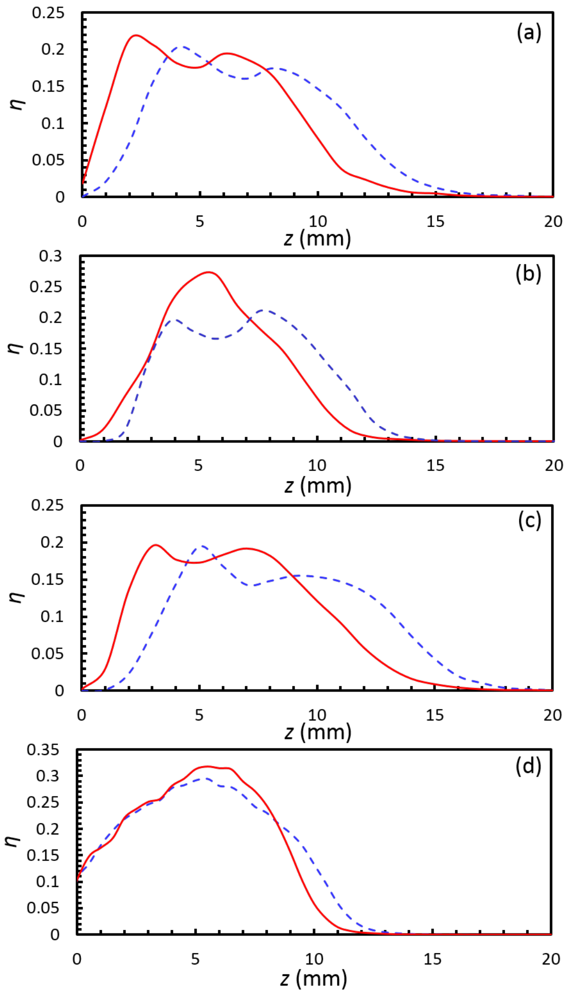

Figure 5.39: One-dimensional particle distributions for both components of various bidisperse-by-shape granular mixtures for which $\nu_A \approx \nu_B$ and $\rho_A \approx \rho_B$ (i.e. particles differ significantly *only* in their geometries. Data is shown for multiple combinations of particle species and driving parameters. Panel (a) shows data for a system of spheres (solid line) and cuboids (dashed line) driven at a frequency of 40 Hz and with an amplitude $A = 1.67$ mm. Panel (b) represents a system of cuboids (solid line) and discs (dashed line) exposed to the same driving conditions as (a). Panel (c) shows an identical system to (a) with driving parameters $f = 80$ Hz and $A = 0.42$ mm, thus providing a dimensionless peak velocity, V, identical to that used in (a), but with a different peak acceleration, Γ. Panel (d) meanwhile again corresponds to a similar particle mixture to that used in (a) and (c), this time producing an equal Γ to that in panel (a) but a differing V through an f-A combination of $f = 100$ Hz and $A = 0.42$ mm. In all images shown, $N = 1800$ and $L_{x,y} = 80$ mm. Figure taken from our reference [21].

an apparent invariance with the peak acceleration, Γ. Our findings suggest that, for the systems under investigation, the key control parameter determining a system's I_s is the peak velocity, V[3].

Visual evidence of the observed Γ-invariance (and, similarly, V-dependence) displayed by our systems is provided in Figure 5.39[4]. A comparison of panels (a) and (c) shows that, as Γ is varied from $\Gamma = 10.8$ to $\Gamma = 27.0$ at fixed $V = 0.42$ ms^{-1}, the observed profiles remain remarkably similar, and the integrated quantity I_s varies by only a factor of 1.08 as Γ is increased 2.5-fold. The observed variation in I_s is comparable in size to the magnitude of statistical fluctuations between repeated data sets taken from identical systems, strongly suggesting that the segregation occurring within our systems is indeed independent of Γ. It should be emphasised that the *only difference* between these two systems is in their driving. The same is true for Figure 5.39's images (a) and (d), where Γ is now held constant between the two cases at a value $\Gamma = 10.8$, while V varies by a factor of two, from $V = 0.42$ ms^{-1} to $V = 0.21$ ms^{-1}. In this instance, I_s varies by more than a factor of 3 between the two systems. The considerable disparity between the fixed-Γ and fixed-V cases provides evidence that the velocity V is indeed the appropriate control parameter with regards to segregation. This finding certainly makes physical sense as, for dilute systems such as those discussed here, the main quantities which directly affect segregation – namely packing density and granular temperature – are expected to scale with V [219, 307–309]. In fact, for *all systems* tested in which $f > 20$, we find that a variation in Γ between 5.4 and 26.9 at fixed V provides little or no appreciable alteration in I_s. Conversely, a variation in V from 0.19 to 0.66 ms^{-1} results in very significant variations in I_s, with segregation intensities ranging from $I_s = 0.07 \pm 0.02$ to $I_s = 0.39 \pm 0.03$.

The breakdown in the observed Γ-invariance for small f can, perhaps, be explained

---

[3] In the current section, V is taken as the unnormalised, *dimensional* velocity $V = \omega^2 A$ in alignment with the original publications, and the images thereof, discussed and included in this section.

[4] Further, more complete and quantitative support for this observation is also provided later in this section where we discuss systems of particles differing both in shape and density.

by the fact that, at these lower frequencies, the dynamics exhibited by the bed become sensitively dependent on the *specific form* of the applied vibrations - i.e. particle motion can no longer be assumed to be decoupled from that of the oscillating wall driving the system [224], but may instead become correlated with this oscillatory motion [34, 310–318]. If particle and base motion do indeed begin to exhibit coordinated motion then, clearly, one must also consider the precise values of f, A and (hence) Γ alongside V. However, in this current work we are interested in analysing the *fundamental* behaviours of the system; as such, we focus on the less-complex high-frequency case, for which the vibrating base can be treated simply as an energy source [224] and, since $E \propto V^2$, we can safely assume the bed dynamics and segregative behaviours to be predominantly, if not solely, controlled by V as opposed to other driving parameters.

In spite of the strong evidence suggesting the determining rôle played by V in the segregation exhibited by our systems, there seemingly exists no clear, monotonic relationship between I_s and V, as may be seen from Figure 5.40. This is perhaps to be anticipated, as the segregation exhibited by a system is sensitively dependent on several variables, in particular the granular temperature, T, and packing density of a system (as well as the distributions thereof), which in turn are directly related to V by non-trivial relationships. This being the case, while the concept of V as the relevant control parameter still seems logical, a simple relationship between the two parameters V and I_s cannot be realistically expected. Nonetheless, it is hoped that, with further research, a concrete – albeit complex – relationship connecting segregation intensity and peak vibrational velocity may be successfully established.

Having established the basic segregative behaviours exhibited by our system, we now attempt to provide a cogent explanation of their origins. In Figure 5.41, we are shown one-dimensional packing profiles for a pair of bidisperse-by-shape granular mixtures which give, in each case, the spatial distribution of each particle species alongside their corresponding (granular) temperature profiles. For both species in both systems, we see

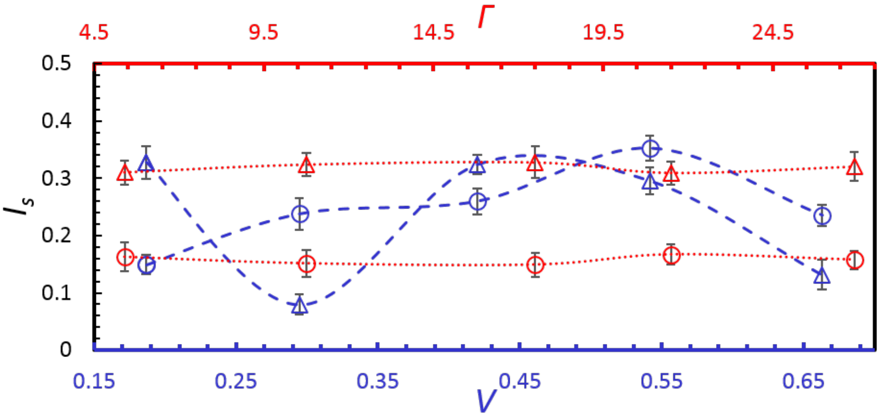

Figure 5.40: Experimental data demonstrating the manner in which segregation intensity, I_s, is observed to vary with the driving parameters V and Γ for two differing combinations of particle shape. Open circles are representative of binary systems comprising cuboidal and spherical particles, while open triangles correspond to results obtained from binary mixtures of discs and spheres. For each of these particle combinations, red dotted lines represent data sets for which V is held constant at a value $V = 0.19$ ms^{-1} while Γ is varied and blue dashed lines represent the case in which Γ is held constant at a value $\Gamma = 12$ with the driving velocity V instead undergoing alteration. For all results shown, the particle number and system size are held constant at $N = 2400$ and $L_{x,y} = 60$ mm, respectively, thus ensuring a consistent bed height and aspect ratio. The results presented are clearly suggestive of a strong V-dependence for I_s and, conversely, a negligible influence due to Γ. Figure taken from our reference [21].

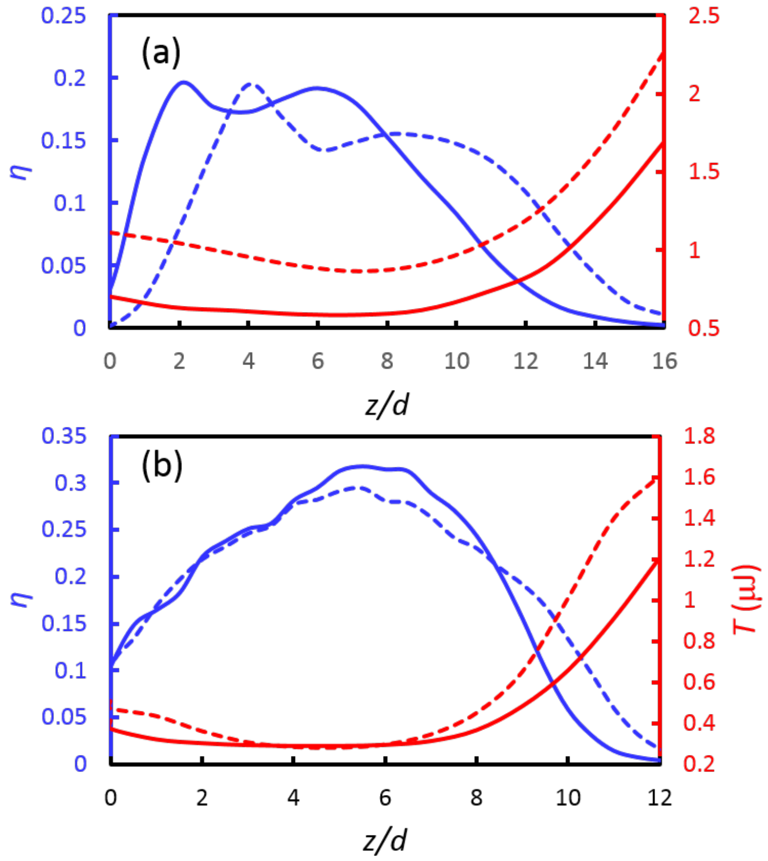

Figure 5.41: One dimensional vertical packing density profiles from Figure 5.39's panels (c) and (d) replotted alongside their corresponding vertical temperature (T) profiles. In each of the images presented, solid lines correspond to the lower-r_g particle and dashed lines to the higher-r_g particle while blue lines and red lines correspond respectively to the solids fraction and granular temperature of the relevant particle species. Figure taken from our reference [21].

that the general, qualitative form of the temperature profiles matches our expectations for a dilute, vibrated granular system [319], with T initially decreasing with height, z, before passing through a minimum and increasing with z for large heights. This general form is in fact maintained for all systems studied. However, although the same trend in T with z is observed for all particle species, there typically exists within each system a distinct disparity in the magnitude of T between the two species present, with particles possessing larger radii of gyration invariably obtaining higher average temperatures. This important observation can perhaps be explained through analogy with the experimental findings of Wildman *et al.* [132], who demonstrate a similar non-equipartition of energy within systems of uniformly spherical particles which are bidisperse-by-*size*. Wildman *et al.* show that the modified collision and dissipation rates within their system lead to larger particles possessing greater temperatures. We posit that, due to their larger *effective sizes*, higher-r_g particles will be subject to an alteration in collision and dissipation rate similar to that experienced by larger particles in [132], thus achieving higher temperatures, as observed. Hence, due to the additional segregation-inducing forces which arise in systems where particle species possess unequal temperatures [134], we may expect to witness the separation of the differing components of our system. Specifically, since – as proposed by Brey *et al.* [136] – a particle of species 'A' will rise if the inequality $\frac{m_B T_A}{m_A T_B} > 1$ is fulfilled, and in the case discussed here $m_A = m_B$, it follows that the particle type possessing the higher granular temperature should segregate towards the upper regions of the bed, as is indeed observed. It is additionally worth noting that, for the systems tested, as the ratio $\frac{m_B T_A}{m_A T_B}$ tends to unity, the observed degree of segregation, I_s, tends to 0, lending further support to our hypothesis.

Now that the matter of purely geometry-driven segregation has been discussed at length, we next aim to address the question of how this mechanism of species separation compares to other sources of segregation. Specifically, we turn our attention to systems comprising particles which differ both in geometry *and density* yet still maintain equal volumes, ν. To this end, we explore muliple systems comprising combinations of particles with identical geometries to those discussed throughout this section, but composed of differing materials, namely nylon (ρ = 1100 kgm^3) and glass (ρ = 2500 kgm^3), in addition to the chrome steel (ρ = 7900 kgm^3) particles discussed previously. A selection of images from systems composed of particles providing a variety of shape/density combinations may be seen in Figure 5.42.

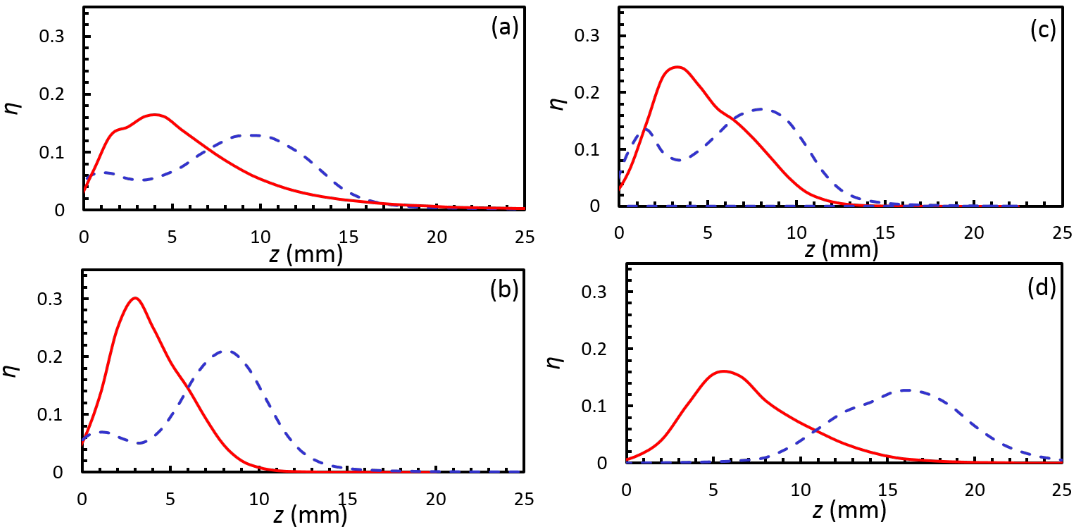

Figure 5.42: One dimensional vertical packing profiles for both system components in a variety of binary granular beds comprising particles of equal volume, ν, but which differ in their material densities, ρ, and geometries. Images are shown for the following particle combinations: (a) steel (solid line) and nylon (dashed line) spheres; (b) steel cuboids (solid line) and nylon spheres (dashed line); (c) steel cuboids (solid line) and glass spheres (dashed line); (d) steel cuboids (solid line) and nylon discs (dashed line). The systems shown in images (a)-(c) are all driven with a frequency f = 65 Hz and an amplitude A = 1.03mm. The bed corresponding to image (d), meanwhile, is driven with f = 40 Hz and A = 3.57 mm. All systems shown contain a number of particles N = 1800. Figure taken from our reference [21].

Perhaps the most notable feature of Figure 5.42 is the fact that, in all cases, the upper regions of the system are dominated by the *lighter* particle species, irrespective of the relative r_g values of the particles concerned. This observation holds true for all systems tested, strongly implying that, at least for the systems investigated here, segregative effects due to particle geometry are *decidedly secondary* to those arising from differences in particles' relative densities. It is additionally interesting to note that, on a qualitative level, the particle distributions of mixed density and shape systems resemble much more closely those produced by systems of uniformly spherical particles with differing densities (e.g. Fig. 5.42 (a)) than those produced by systems comprising particles of equal density but differing geometry (Figs. 5.40 (a)-(d)). This admittedly simple observation is nonetheless valuable, as it provides a clear demonstration that the introduction of non-spherical geometries to a granular system does not inherently invalidate the existing knowledge in the field regarding segregation which is largely based on systems comprising exclusively spherical particles.

Despite our above assertion, there exist nonetheless certain key discrepancies between the results produced by purely spherical (PS) systems and those attained from geometrically non-uniform (GNU) systems, as is readily observable from Fig. 5.42. A comparison of Figs. 5.42 (a) and (b), for instance, yields an intriguing and rather counterintuitive result: the steel cuboid / nylon sphere system depicted in image (b) displays significantly stronger segregation than the purely spherical steel/nylon mixture shown in image (a) (I_s = 0.67 as opposed to I_s = 0.42 for the PS system). This is somewhat unexpected due to the fact that, unlike in system (a), where both species share identical geometries and hence segregation is solely governed by density differences, in system (b) we would expect, from our previous observations, that there exists an additional segregative mechanism due to the disparity in particles r_g values which should act to *oppose* the density driven segregation – i.e. one would naturally anticipate a *reduced* I_s relative to system (a) as opposed to the marked increase observed. This result provides still further evidence of the relatively weak strength of the segregative mechanisms directly associated with particles' radii of gyration, but also demonstrates the existence of additional manners in which particle geometry may affect system behaviour.

The unusual behaviour described above – which is, in fact, common to all systems studied – is thought to arise due to the fact that the non-spherical particles possess an increased number of degrees of freedom as compared to their spherical counterparts. This increase in $N_{D.o.F.}$ manifests itself as an effective decrease in the elasticity of the non-spherical grains, as a higher proportion of translational kinetic energy is in essence 'lost' to the rotational modes, resulting in a lower average granular temperature for systems involving such particles, and hence an increase in the bed packing density [227]. This increase in η, in turn, will lead to an increase in buoyancy forces within the system, and hence the greater degree of segregation observed. Although this proposal may at first seem slightly speculative, a measure of support for its validity may be seen in Figures 5.42 (a)-(c), where an increased η for the GNU systems ((b) and (c)) relative to the PS system shown in (a) is clearly observable, despite the identical driving parameters, particle number and system size used in all three cases.

In order to provide a deeper understanding of the influence on system dynamics of the interplay between translational and rotational motion for particles possessing differing rotational inertia, we turn our attention now to the investigation of a series of *monodisperse* systems composed of non-spherical particles whose geometries are carefully designed such that the various species studied differ almost exclusively in their I (and hence r_g) values, remaining near-identical in all other aspects. The particles used are depicted schematically in Figure 5.43.

The particles used are simply constructed from a pair of stainless steel hexagonal nuts affixed to a rod of length l = 20 mm, also composed of stainless steel. By varying the distance ΔX separating the hexagonal nuts whilst ensuring that the two remain equidistant from the particle's centre (hence maintaining symmetry), various particle classes possessing significantly differing moments of inertia yet consistent centre of mass positions may be created. The manner in which our particles are formed ensures that

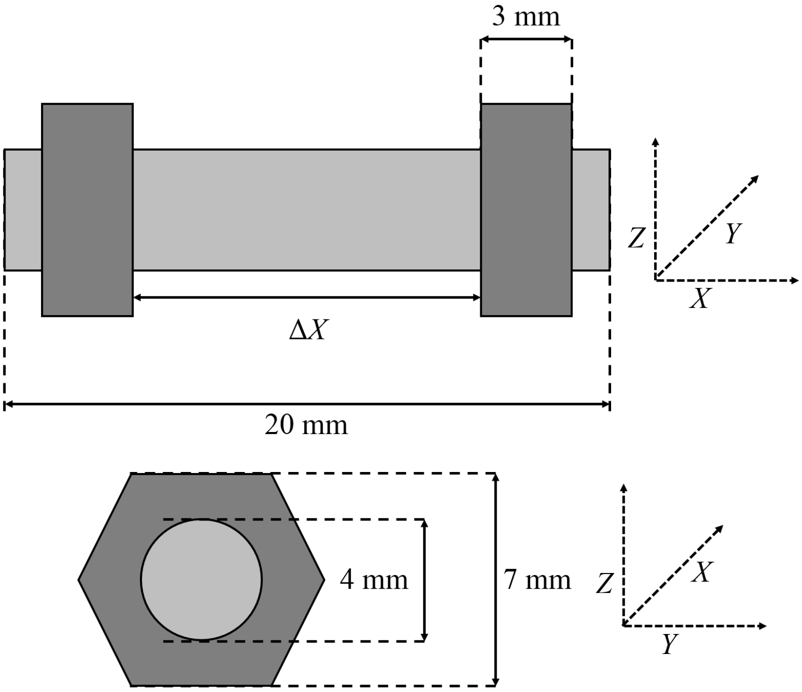

Figure 5.43: Scale diagram of a typical particle used in experiment. Image taken from reference [22].

Table 5.2: Spatial dimensions of particles used in experiment alongside their moments of inertia, I, for rotation about the Z (or, equivalently, Y) axes as shown in Fig. 5.43, and their corresponding radii of gyration, r_g. The definition of ΔX may also be seen in this Figure.

Class	ΔX **(mm)**	I **(kgm^2)**	r_g (mm)
I	0.0 mm	7.2×10^{-8}	5.0
II	3.0 mm	8.1×10^{-8}	5.3
III	6.0 mm	9.6×10^{-8}	5.8
IV	9.0 mm	1.2×10^{-7}	6.4
V	14.0 mm	1.7×10^{-7}	7.6

effects due to I, and hence r_g, are isolated as far as possible, by guaranteeing that each of the particle species used are identical or near-identical in terms of all other relevant properties which may affect their dynamical behaviours. For instance, all particle types maintain approximately equal masses and volumes ($m = 3.9 \times 10^{-3}$ kg and $\nu = 3.7 \times 10^{-7}$ m^{-3}, respectively); all particles are constructed entirely of stainless steel, thus eliminating variation in their densities, elasticities and frictional properties; all particles possess a fixed total length, l, further ensuring consistency in the effective restitution coefficient of the particles, which is known to be affected by the elongation of grains [320]; the large size of the particles used and the choice of their material as stainless steel will ensure an absence of cohesive forces between particles and therefore, by definition, a lack of variation in this parameter between particle species [169]; this choice of size and material, in conjunction with the system's steel base, will additionally provide a similar lack of triboelectric forces [148] and interstitial air effects [105] within the system; the cross sectional areas of particles are identical in all major planes meaning that no particle species should be more or less likely to become entrained in convective streams than any other [321]. Finally, the maximal achievable packing fractions of all particle species used – which may affect segregation, albeit predominantly in the limit of much denser systems than explored here [166] – are approximately equal.

Due to the nature of the particles used, moments of inertia about their X-axes are equal for all species used, with a value $I_X = 4.53 \times 10^{-9}$ kgm^2. Since this value is, for all classes of particle, at least an order of magnitude smaller than the rotational inertia corresponding to the Y and Z axes and, additionally, $I_Y = I_Z$ we will, throughout the remainder of this section, use the symbol I to denote particles' rotational inertia about the Y (or, equivalently, Z) axes, and, for the sake of simplicity, discuss our results in terms of this parameter. The I values corresponding to all particle classes used in experiment are introduced in Table 5.2.

The experiments corresponding to the current area of investigation are all conducted using a fixed system size ($L_{x,y} = 120$, $L_z = 250$ mm) and particle number ($N = 100$), with the peak velocity of the driving oscillations varying in the range $V \in (0.41, 0.68)$ ms^{-1}, these values being achieved using a fixed frequency of $f = 40$ Hz and a range of amplitudes $1.63 \leq A \leq 2.72$. The upper and lower bounds of the excitation strengths used are determined, respectively, by the maximal driving achievable using our apparatus and the minimum energy input by which a fully gaseous state may be successfully achieved for all particle species tested.

Figure 5.44 shows a series of velocity probability density functions (vPDFs) for various monodisperse systems of particles possessing differing rotational inertiæ, I. Data is shown for both the vertical and horizontal components of particles' translational motion; it should be noted that, due to the symmetry of the square-based cuboidal vessel used to contain the beds under investigation, the vPDF for v_y is not shown, as the distributions of particle velocity in the x and y directions are identical. In order to ensure the absence of wall effects, the vPDFs shown correspond to data acquired solely from the central region of the container; specifically, only data points which lie at least a particle length from the system's walls are used in our calculations. In order to acertain whether the velocity distributions acquired in this manner are indeed accurate and representative of the system's behaviour, vPDFs were produced using data from regions of Cartesian

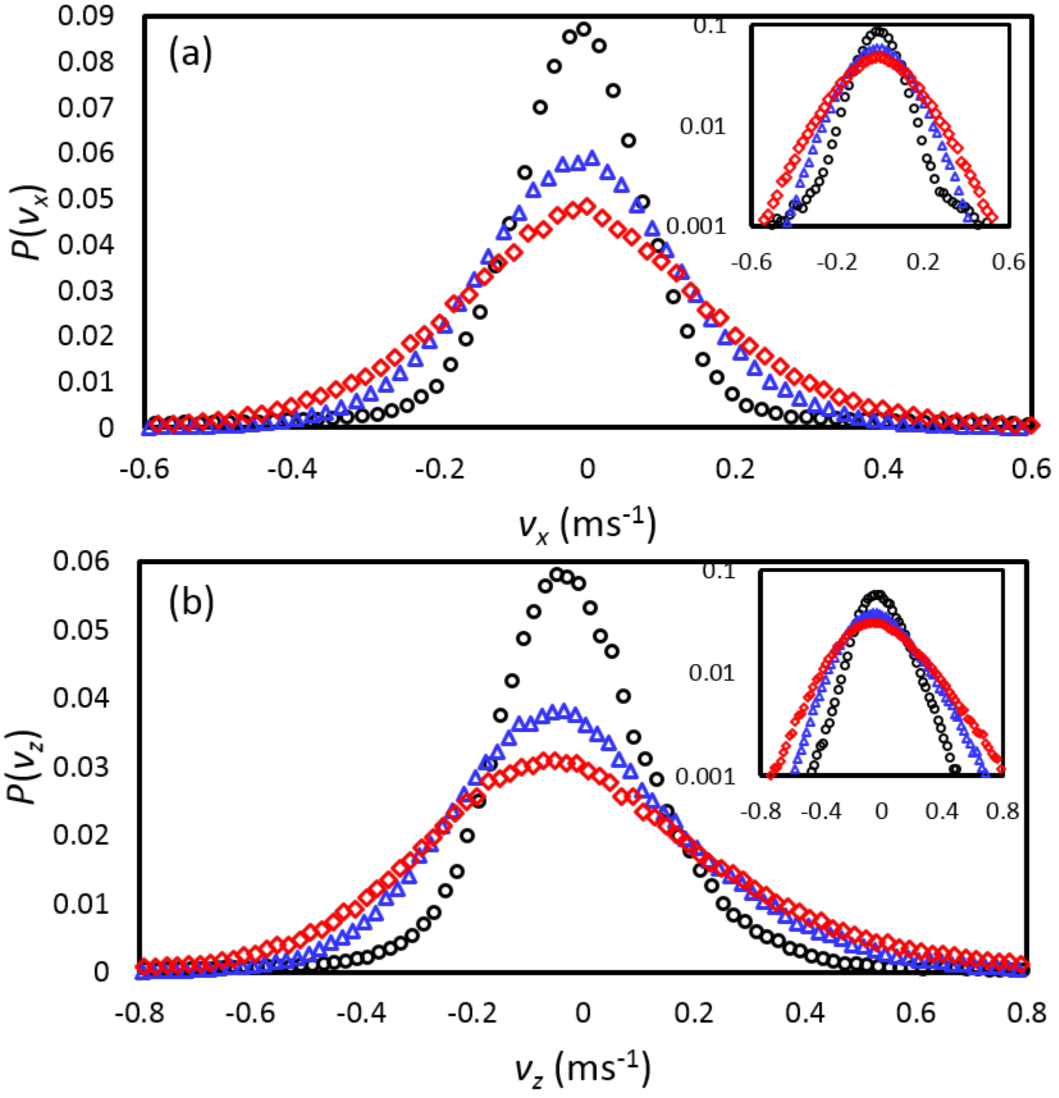

Figure 5.44: Velocity probability density functions for systems with moments of inertia $I = 7.2 \times 10^{-8}$ kgm^2 (black circles), $I = 9.6 \times 10^{-8}$ kgm^2 (blue triangles) and $I = 1.7 \times 10^{-7}$ kgm^2 (red diamonds). Data is shown for both horizontal (x) and vertical (z) velocity components. In all cases shown, the particle number N is equal to 100 and the peak driving velocity V is held constant at 0.68 ms^{-1}. Provided in the insets of each image are the same results plotted on a semilogarithmic scale. Image taken from reference [22].

space both smaller and larger than that discussed above. The observed invariance of the distributions produced in all cases strongly implies that our results are valid.

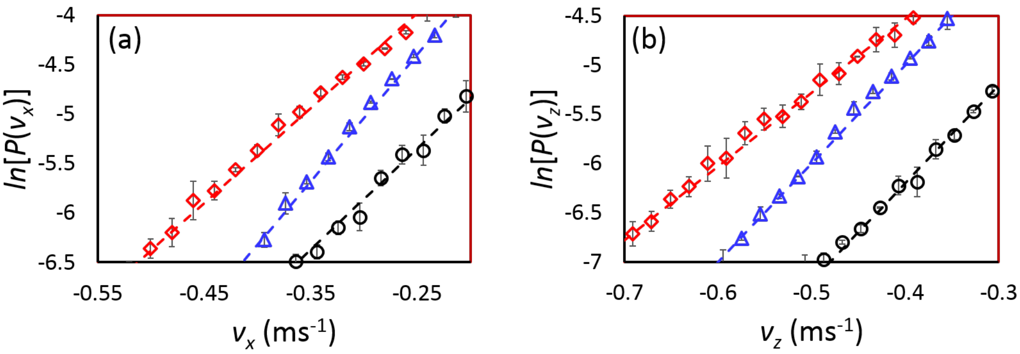

Figure 5.45: Log-linear plots of the high-velocity 'tails' corresponding to the velocity profiles shown in Figure 5.44 for (a) the horizontal and (b) the vertical components of particle motion. Linear least-squares fits to the data points shown are included as a guide to the eye. Image taken from reference [22].

Previous studies of systems comprising exclusively spherical particles suggest that the velocity distributions produced by gaseous, vertically vibrated granulates may be expected to follow a form ~ $\exp(-\beta|v|^{\alpha})$ [189–191], where α and β are constants, $\alpha = 2$ corresponding to a Gaussian distribution (as would be expected of a *molecular* gas [193]). Existing studies of elongated, non-spherical particles similar to those investigated here have also shown similar results [322]. The velocity profiles produced from our setup agree well with the expectations based on purely spherical systems, the distributions approximating a Gaussian for small $|v|$, deviating significantly at larger velocity values where we observe the presence of 'high energy tails', again in agreement with existing experimental [189, 323, 324], simulational [325, 326] and theoretical [327, 328] studies.

The high velocity tails observed in our experiment are all found to scale with an exponent $\alpha \approx 1$ as illustrated in Figure 5.45. This scaling differs from that typically anticipated for a system of spheres [190], but agrees closely with the findings of previous experimental investigations involving elongated particles [306]. This exponent is found to hold for all particle species studied, the linear relationship displayed in 5.45 breaking down only in the limit of small $P(v)$ where the inherently limited number of available data points results in a relative increase in the probability of large statistical fluctuations.

Additionally notable from Figure 5.44 is the fact that the velocity profiles corresponding to horizontal (x) motion are relatively narrow and possess increased peak heights at $v = 0$, indicative of the presence of *anisotropy* within our system. The anisotropic nature of vertically vibrated granular fluids is well known [1, 73, 329], arising due to the fact that, in such systems, energy is injected predominantly in the vertical (z) direction and transferred to the horizontal modes only with the aid of innately dissipative inter-particle collisions, resulting in comparatively greater vertical (as opposed to horizontal) velocities [73]. Our results suggest that the degree of anisotropy displayed by our systems may be dependent, to some degree, on the rotational inertia of the particles of which said systems are comprised, although further research is required in order to make any definitive, substantiated claims regarding this issue. As such, we will not continue further along this current line of discussion which, although potentially interesting, is somewhat external to the main aims of this current section.

By far the most striking, and novel, result observable from Figures 5.44 and 5.45 is that despite their similarity in almost all aspects – including mass, volume and elastic and frictional properties – the differing particle species display *markedly different dynamics*. The results shown here represent highly convincing evidence regarding the important rôle played by particles' rotational inertia, in agreement with the hypotheses drawn by Roskilly *et al.* [175] based on their simulational work. Specifically, our experimental results unambiguously demonstrate that, perhaps somewhat unexpectedly [307, 330], particles possessing greater rotational inertia exhibit, on average, higher *translational* velocities. It is possible that this increased average velocity and correspondingly, for the case of systems with zero mean velocity, such as those explored here, augmented granular temperature may explain, at least in part, the r_g-induced segregation observed in previous studies [21, 175]: as noted on numerous occassions throughout this thesis, particles possessing higher granular temperatures, T, will tend to migrate toward the upper regions of a given system, with the inverse being true for relatively 'cool', low-T particles. As such, in binary granulates wherein particles differ significantly only in their moments of inertia, it seems eminently reasonable that a species possessing a greater I value will segregate upwards.

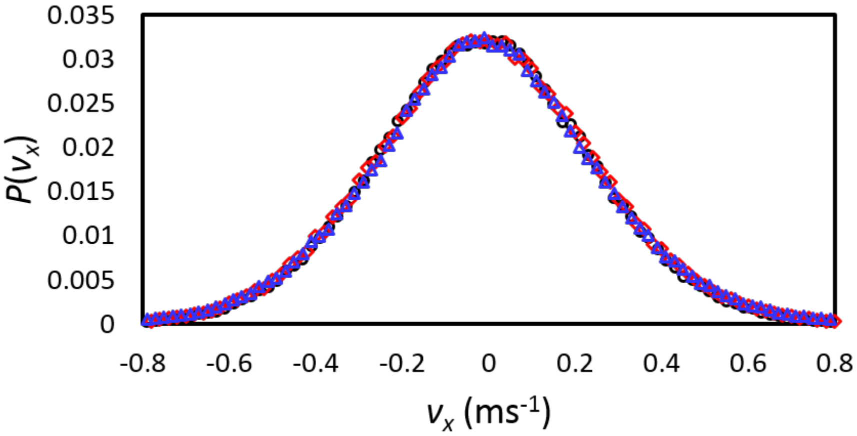

Figure 5.46: Velocity probability density functions for a series of single particle systems (N = 1) driven with an identical peak base velocity (V = 0.68 ms^{-1}) to the multi-particle systems depected in Figure 5.44. As with this previous image, data is shown for particles possessing moments of inertia $I = 7.2 \times 10^{-8}$ kgm^2 (black circles), $I = 9.6 \times 10^{-8}$ kgm^2 (blue triangles) and $I = 1.7 \times 10^{-7}$ kgm^2 (red diamonds). Unlike the corresponding image for the N = 100 case, however, the various velocity profiles for the single-particle case collapse almost perfectly onto a single curve; the reasons for the striking disparity between these two Figures is discussed at length in the main text. Image taken from reference [22].

Interestingly, despite the marked differences in the distribution of velocities for differing particle species in the monodisperse granulates discussed above, an entirely different situation is observed for the case of a single particle particle bouncing on a plate – even when all other parameters (most notably the driving frequency and amplitude applied) are held constant. For the single-particle case, velocity profiles for particles with differing

I-values are virtually indistinguishable, as is immediately obvious from the distributions provided in Figure 5.46.

Having summarised our major results, there arise two major questions: why does a vibrofluidised granular gas comprising particles with relatively large rotational inertia demonstrate higher translational velocities than an equivalent system of particles with comparatively low moments of inertia, and why is the same not true for the case of a equivalent single-particle system?

An answer to both of the above questions can, perhaps, be proffered through consideration of a single, perfectly elastic particle interacting with a similarly elastic, infinitely massive body undergoing vibratory motion. As may be theoretically expected, and has indeed been directly demonstrated in our own work [17], in a collision involving a single particle and the oscillating base-plate of our experimental system, the latter object may be treated as possessing an effectively *infinite mass* (as feedback from the accelerometer used to control the oscillatory motion will compensate for any momentum which would ordinarily be transferred to the plate). If we consider the extremely simple case of our single, elastic particle moving with velocity v in a direction normal to the surface of a stationary, infinite mass for which $\varepsilon = 1$ also, a collision between the two objects will, clearly, result in the simple reversal of the particle's velocity, irrespective of its mass – i.e. $\forall m : |v_{initial}| = |v_{final}|$. Clearly, then, a more massive particle travelling with the same initial velocity will possess a greater kinetic energy upon rebounding than a comparatively light particle. Let us now consider the same problem from the frame of reference of the colliding particle. In this inertial frame, we see a stationary particle being approached by, and colliding with our infinite mass – the analogue of the vibrating wall of our 'real' experimental system. From this viewpoint, it is apparent that if we consider two particles of masses m_1 and m_2 ($m_1 \neq m_2$) which are struck identically by such an object, both particles will receive an equal increase in velocity, but the heavier of the two will carry a higher translational kinetic energy. Following a similar set of arguments, one may similarly expect, for a pair of particles with rotational inertia I_1 and I_2 ($I_1 \neq I_2$) which are subject to identical collisions with an infinite mass, that the particle possessing the higher *moment of inertia* will receive a greater *rotational kinetic energy.*

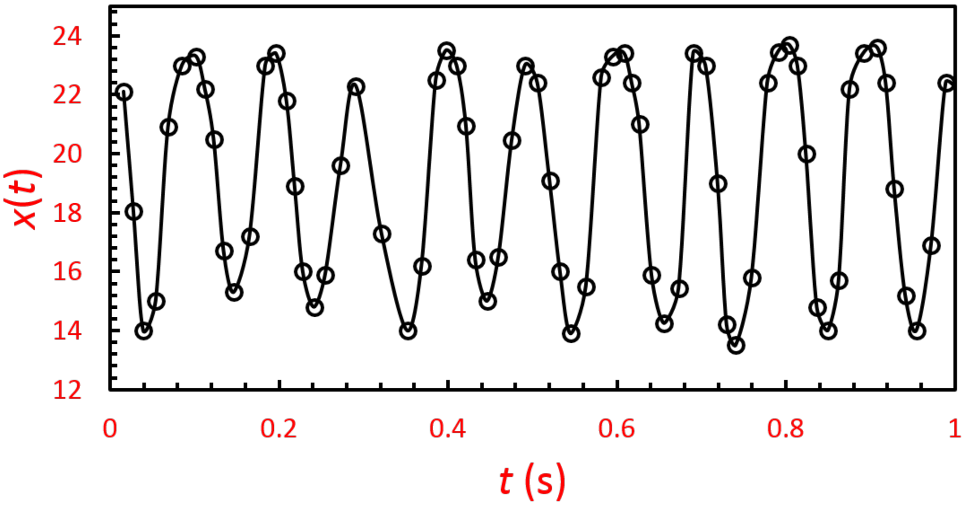

Figure 5.47: Experimentally obtained x-tracjectory of a single, asymmetrically irradiated particle undergoing free flight in a direction directly parallel to that of gravity.

If a particle undergoes numerous, repeated collisions with the infinitely massive, moving wall which is our vibrating base-plate, it is expected that all impact angles between the elongated particle and the base will be explored [331] and that, as such, the *average* energy stored in a given particle's rotational modes should increase proportionally with I. Although this assumption is based on a somewhat idealised scenario, In order to determine the average rotation rates, a single particle of each species is irradiated in such a manner that only one end of the particle becomes active. As such, the particle's rotational motion can be observed as a sinusoid superimposed on the position-time plots of the particle's motion in each spatial direction. By ensuring that the particles follow simple, relatively long parabolic trajectories (i.e. by using single-particle systems and strong vibrational energy inputs), a particle's rotational motion can be distinguished from its translational motion during periods of free flight. As an example, Fig. 5.47 shows the x-component of particle motion for a particle following a trajectory directly perpendicular to the system's base. By determining the period of the sinusoidal oscillation about the particle's known mean trajectory, it is easy to to extract an average rotation rate for this particular period of free flight. By averaging the rotation rates acquired over a large number of such flights, the mean rotation rate for each species can be determined. Our results confirm that, for single-particle systems, the rotation rate of all particles used remains approximately constant, irrespective of the rotational inertiæ possessed by the various species tested, thus providing relatively strong support for our hypothesis. It should be noted, however, that particles whose geometries differ in manners other than their rotational inertia – e.g. spheres, which also differ in their elongation – and hence interact differently with the energising base, will not necessarily possess the same rotation rate as the specific 'class' of particle used here.

In other words since rotational energy is defined as $E^{\circ} \equiv I\omega^2$ and, from the above discussion, $\omega \sim$ const., we may presume that, if all other system parameters remain invariant, the rotational kinetic energy imparted to a granular system will scale approximately linearly with the rotational inertia possessed by its particulate constituents.

Now that we have established a possible manner in which our higher-r_g particles may obtain a higher average *rotational* kinetic energy, E°, we must now attempt to explain how this may result in an increased *translational kinetic energy*, as observed in our experiments. In fact, there is a fairly simple solution to this problem; it has been demonstrated [223] that, under certain circumstances, collisions between particles may exhibit restitution coefficients with values greater than unity, i.e. particles experience a net *gain* in kinetic energy as motion is conveyed from the rotational to the translational modes. Clearly, particles possessing greater moments of inertia and hence, as we have recently established, greater E° values, will in effect possess a greater 'reservoir' of kinetic energy to draw upon, which would clearly be expected to result in a higher average translational energy for monodisperse systems composed of such particles.

In fact, our results strongly suggest that for a fixed particle number, N, and driving strength, V, there exists a *linear relationship* between the numerical value of the moment of inertia, I, possessed by particles forming a monodisperse bed and $E^{\dagger}$, the sum of the mean translational kinetic and gravitational potential energies possessed by the system. Evidence of this apparent relationship may be seen in Figure 5.48 although, due to the limited number of data points available, further research is required before we can definitively confirm the direct proportionality seemingly exhibited.

Having provided a cogent explanation of the mechanism by which monodisperse, multi-particle granulates comprising particles with large moments of inertia, I, obtain higher translational velocities than equivalent, lower-I systems, it remains only to explain why the same is not true of equivalent single-particle systems. In short, the lack of variation in linear velocity for different particle species stems from the absence of particle-particle interactions in the single grain case – without such interactions, the greater rotational energy with which higher-I particles are endowed cannot be converted to translational velocity, resulting in the near-identical velocity distributions seen in Figure 5.46. To address the question in greater detail, however, we must consider the nature of the energy flow within the two contrasting systems. In both situations, particle-base collisions may act to either provide energy to or remove energy from a given grain, i.e. either increase or decrease rotational velocity. *However*, in the muti-particle case it has been shown [332] that inter-particle collisions act to remove rotational energy both through dissipation and, importantly, through conversion to the translational modes. In fact, such collisions are thought to remove a *significant proportion* of particles' rotational motion[5]. This being the case, when any given member of a multi-particle bed recollides

---

[5] Unfortunately, this result cannot be reliably validated for our current system due to the fact that it is not possible to quantify rotational motion to an acceptable degree of accuracy for the multiple-particle systems discussed here, due to the increased presence of particle collisions as compared to the single-particle case.

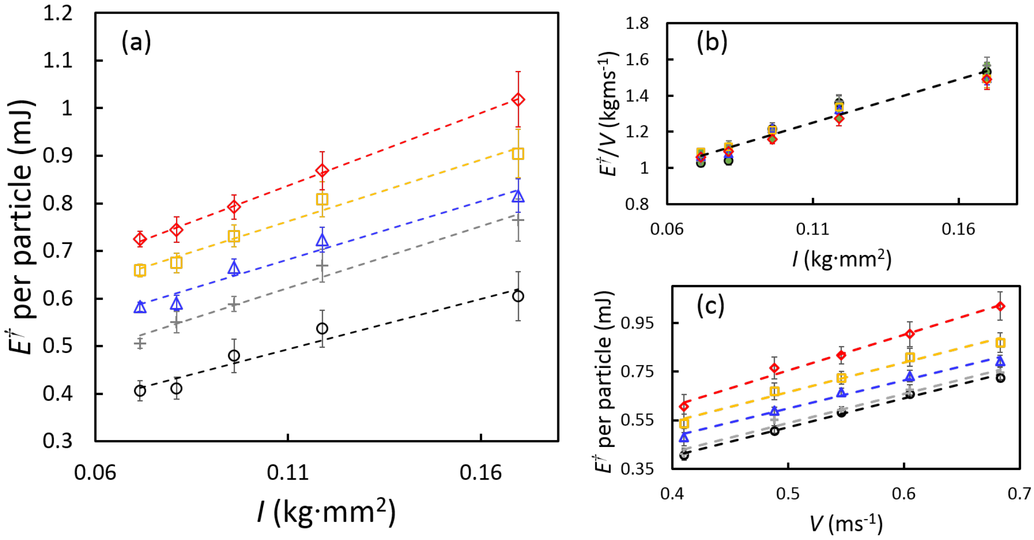

Figure 5.48: (a) $E^\dagger$, the sum of the time-averaged translational kinetic energy, $\bar{E}$, and gravitational potential energy, E_P, possessed by a granular bed plotted as a function of the moment of inertia, I, of the individual particles comprising each system. Data is shown for beds excited with peak driving velocities $V = 0.41$ ms^{-1} (black circles), $V = 0.49$ ms^{-1} (grey crosses), $V = 0.55$ ms^{-1} (blue triangles), $V = 0.61$ ms^{-1} (orange squares) and $V = 0.68$ ms^{-1} (red diamonds). In all cases, a fixed particle number $N = 100$ is used. Panel (b) shows the same data as presented in (a), this time normalised by the base velocity, V. Panel (c), meanwhile, shows $E^\dagger$ as a function of V, for particles with rotational inertiæ $I = 7.2 \times 10^{-8}$ kgm^2 (circles), $I = 8.1 \times 10^{-8}$ kgm^2 (crosses), $I = 9.6 \times 10^{-8}$ kgm^2 (triangles), $I = 1.2 \times 10^{-7}$ kgm^2 (squares) and $I = 1.7 \times 10^{-7}$ kgm^2 (diamonds). In all images shown, linear fits to the data points presented are included as a guide to the eye. Figure taken from reference [22].

with the vibrating base of the system, the base's motion is more likely to increase than to reduce the E° of said particle, resulting in a continual flux of energy from the oscillating base, through the rotational modes and eventually to the translational components of motion, the magnitude of this energy flux clearly being dependent upon I. Since our particles are all equally massive, such an energy flux will result in strongly divergent velocity distributions for systems comprising particles of differing rotational inertia, as clearly demonstrated in our Figure 5.45. The absence of such an energy flux in the single-particle case can therefore explain the lack of significant variation in the velocity profiles corresponding to these systems.

To summarize, in this section we have shown that particle geometry may exert a significant influence on the dynamical behaviours of both unary and binary granular systems. We have provided considerable support for the theories presented in previous studies which propose that particles' radii of gyration, r_g, play an important rôle in the behaviours of systems which are bidisperse-by-shape, presenting several mechanisms which may, at least partially, explain the segregation observed in such systems and the manner in which the strength of this segregation is found to vary with various system parameters.

6 Conclusions

In this thesis we have explored, in depth, two highly industrially relevant phenomena chosen from the plethora of fascinating behaviours exhibited by granular media – granular convection, and granular segregation.

We have shown how the presence of convection, and the strength of the related flow fields, can significantly impact the behaviours of granular systems in numerous manners, being capable, for instance, of altering the temperature and density of a granular bed, and the spatial distributions thereof, influencing the partition of energy between particles and – dependent on the circumstances – both promoting and preventing the separation of differing particle species. We have demonstrated that the strength of convective flow can be deliberately manipulated through the variation of simple, controllable parameters, and that this ability can be exploited in order to indirectly alter various other system properties.

We have proved that particles' material densities, elastic properties and geometries may all exert significant influence on the manner in which particulate systems comprising multiple constituents undergo separation or mixing. We have explored the manners in which the various segregative mechanisms corresponding to these particle properties interact, compete and cooperate, and the situations in which certain mechanisms may be expected to be dominant or, conversely, become entirely negligible. In particular, we have highlighted the strong impact of often overlooked properties such as the elasticity and precise geometry of particles. At present, the majority of simulational and theoretical frameworks concerning particulate media focus on purely spherical particles; it is hoped that our demonstration of the important rôle of particle geometry may encourage theorists to explore the considerable phase space external to the narrowly defined special case corresponding to systems comprising solely spherical constituents, thus eventually leading to a deeper, more general understanding of granular materials.

We have studied how the extent of segregation and the rate at which it is achieved may additionally be influenced by multiple system parameters external to the properties of the particles themselves; the relevant quantities include the strength with which the system is driven, the number of particles of which the bed is composed, the degree of polydispersity of the granulates explored, the size and geometry of the system and the strength (and indeed presence) of convection within the systems under investigation, amongst still other factors. Through this investigation, we have established the presence of hysteretic effects which may strongly influence a granular bed's dynamical and segregative behaviours, and demonstrated a means by which this hysteresis may be harnessed in order to optimise the separation of particle species and even facilitate flow in normally immobile systems. Such a finding is potentially of direct relevance to various industrial processes, and also of continued scirentific interest, as a full theoretical treatment of the phenomenon remains to be produced.

The work described within this thesis also raises several open questions, and hence provides considerable scope for future research; although there are many potential avenues arising from the studies presented here, we note here just a few carefully chosen ideas. Firstly, stemming from the work presented in section 4.1, it would be interesting to explore further the balancing of wall and particle dissipation in order to better understand the and even predict the material combinations for which zero convection may be achieved; the ability to deliberately suppress convection in an arbitrary system may be potentially beneficial, in particular since non-convective beds form a much simpler, and hence more easily studied, system. Secondly, following from our study of convective binary systems (section 4.2), the precise mechanisms underlying the relationship between convection and segregation remain to be confirmed. It would additionally be of interest to explain the apparent equilibration of particle temperatures for differing species in a well-mixed, convective granular bed (section 4.3). Finally, there remains significant scope for further research into the hysteretic nature of vibrofluidised beds, and in particular the numerous possible manners, of which we have thus far only explored a handful, in which this hysteresis may be exploited in order to control and favourably alter the states and dynamics of mono- and poly-disperse granulates.

The extensive range of differing phenomena and system parameters explored within these pages – which concern but a fraction of the manifold behaviours exhibited by granular media – may perhaps give some impression of the sheer scale of the task faced by researchers in the field of granular dynamics who wish, eventually, to provide a full understanding of these complex and multi-faceted systems. It is hoped that the new information provided by the work presented in this thesis may represent a small, incremental step toward this ultimate goal.

Appendices

Included as appendices to this thesis are the published research papers produced as part of the work discussed. The articles included are as follows:

1. Windows-Yule, C. R. K., and Parker, D. J. (2013). Boltzmann statistics in a three-dimensional vibrofluidized granular bed: Idealizing the experimental system. Physical Review E, 87(2), 022211.
2. Windows-Yule, C. R. K., Rivas, N., and Parker, D. J. (2013). Thermal Convection and Temperature Inhomogeneity in a Vibrofluidized Granular Bed: The Influence of Sidewall Dissipation. Physical review letters, 111(3), 038001.
3. Windows-Yule, C. R. K., and Parker, D. J. (2014). Energy non-equipartition in strongly convective granular systems. The European Physical Journal E, 37(3), 1-6.
4. Windows-Yule, C. R. K., and Parker, D. J. (2014). Self-diffusion, local clustering and global segregation in binary granular systems: The role of system geometry. Powder Technology, 261, 133-142.
5. Windows Yule, C. R. K., Weinhart, T., Parker, D. J., and Thornton, A. R. (2014). Effects of system packing on the segregation behaviours of granular systems. Physical review letters, 112.
6. Windows-Yule, C. R. K., Weinhart, T., Parker, D. J., and Thornton, A. R. (2014).

Influence of thermal convection on density segregation in a vibrated binary granular system. Physical Review E, 89(2), 022202.

7. Windows-Yule, C. R. K., and Parker, D. J. (2014). Center of mass scaling in three-dimensional binary granular systems. Physical Review E, 89(6), 062206.
8. Windows-Yule, C. R. K., Rivas, N., Parker, D. J., and Thornton, A. R. (2014). Low-frequency oscillations and convective phenomena in a density-inverted vibrofluidized granular system. Physical Review E, 90(6), 062205.
9. Windows-Yule, C. R. K., Rosato, A. D., Rivas, N., and Parker, D. J. (2014). Influence of initial conditions on granular dynamics near the jamming transition. New Journal of Physics, 16(6), 063016.
10. Windows-Yule, C. R. K., and Parker, D. J. (2014). Inelasticity-induced segregation: Why it matters, when it matters. EPL (Europhysics Letters), 106(6), 64003.
11. Windows-Yule, K., and Parker, D. (2015). Density-Driven Segregation in Binary and Ternary Granular Systems. KONA Powder and Particle Journal.
12. Windows-Yule, C. R. K., Maddox, B., and Parker, D. J. (2014). The role of rotational inertia in the dynamics of vibrofluidised granular gases. EPL (Europhysics Letters), 108(5), 58006.
13. Windows-Yule, C. R. K., Rosato, A. D., Thornton, A. R., and Parker, D. J. (2015). Resonance effects on the dynamics of dense granular beds: achieving optimal energy transfer in vibrated granular systems. New journal of physics, 17(2), 023015.
14. Windows-Yule, C. R. K., G. J. M. Douglas, and D. J. Parker (2015) Competition between geometrically induced and density-driven segregation mechanisms in vibrofluidized granular systems. Physical Review E 91(3), 032205.

15. Windows-Yule, C. R. K., Rosato, A. D., Parker, D. J., and Thornton, A. R. (2015). Maximizing energy transfer in vibrofluidized granular systems. Physical Review E, 91(5), 052203.

Bibliography

[1] CRK Windows-Yule and DJ Parker. Boltzmann statistics in a three-dimensional vibrofluidized granular bed: Idealizing the experimental system. *Physical Review E*, 87(2):022211, 2013.

[2] Kit Windows-Yule and David Parker. Density-driven segregation in binary and ternary granular systems. *KONA Powder and Particle Journal*, page (Advance Publication), 2015.

[3] Riina Tehver, Flavio Toigo, Joel Koplik, and Jayanth R Banavar. Thermal walls in computer simulations. *Physical Review E*, 57(1):R17, 1998.

[4] A Puglisi, V Loreto, U Marini Bettolo Marconi, and A Vulpiani. Kinetic approach to granular gases. *Physical Review E*, 59(5):5582, 1999.

[5] Rodrigo Soto. Granular systems on a vibrating wall: The kinetic boundary condition. *Physical Review E*, 69(6):061305, 2004.

[6] Evgeniy Khain, Baruch Meerson, and Pavel V Sasorov. Knudsen temperature jump and the navier-stokes hydrodynamics of granular gases driven by thermal walls. *Physical Review E*, 78(4):041303, 2008.

[7] CRK Windows-Yule, N Rivas, and DJ Parker. Thermal convection and temperature inhomogeneity in a vibrofluidized granular bed: The influence of sidewall dissipation. *Physical review letters*, 111(3):038001, 2013.

[8] CRK Windows-Yule, T Weinhart, DJ Parker, and A. R. Thornton. Influence of thermal convection on density segregation in a vibrated binary granular system. *Physical Review E*, 89(2):022202, 2014.

[9] CRK Windows-Yule and DJ Parker. Energy non-equipartition in strongly convective granular systems. *The European Physical Journal E*, 37(3):1–6, 2014.

[10] Klebert Feitosa and Narayanan Menon. Breakdown of energy equipartition in a 2d binary vibrated granular gas. *Physical review letters*, 88(19):198301, 2002.

[11] TW Martin, JM Huntley, and RD Wildman. Hydrodynamic model for a vibrofluidized granular bed. *Journal of Fluid Mechanics*, 535:325–345, 2005.

[12] I Goldhirsch, SH Noskowicz, and O Bar-Lev. Theory of granular gases: some recent results and some open problems. *Journal of Physics: Condensed Matter*, 17(24):S2591, 2005.

[13] CRK Windows-Yule, T Weinhart, DJ Parker, and AR Thornton. Effects of packing density on the segregative behaviors of granular systems. *Physical review letters*, 112(9):098001, 2014.

[14] C. R. K. Windows-Yule, A. D. Rosato, D. J. Parker, and A. R. Thornton. *Maximising Energy Tranfer in Vibrofluidised Granular Systems.* To be published.

[15] CRK Windows-Yule and DJ Parker. Self-diffusion, local clustering and global segregation in binary granular systems: The role of system geometry. *Powder Technology*, 261:133–142, 2014.

[16] CRK Windows-Yule, AD Rosato, N Rivas, and DJ Parker. Influence of initial conditions on granular dynamics near the jamming transition. *New Journal of Physics*, 16(6):063016, 2014.

[17] CRK Windows-Yule and DJ Parker. Center of mass scaling in three-dimensional binary granular systems. *Physical Review E*, 89(6):062206, 2014.

[18] CRK Windows-Yule and DJ Parker. Inelasticity-induced segregation: Why it matters, when it matters. *EPL (Europhysics Letters)*, 106(6):64003, 2014.

[19] R Brito, H Enríquez, S Godoy, and R Soto. Segregation induced by inelasticity in a vibrofluidized granular mixture. *Physical Review E*, 77(6):061301, 2008.

[20] Ricardo Brito and Rodrigo Soto. Competition of brazil nut effect, buoyancy, and inelasticity induced segregation in a granular mixture. *The European Physical Journal-Special Topics*, 179(1):207–219, 2009.

[21] C. R. K. Windows-Yule and D. J. Parker. *Granular Segregation in Vibrofluidised Systems with Non-Spherical Particles: Does the Sphere Approximation Roll?* To be published.

[22] CRK Windows-Yule, B Maddox, and DJ Parker. The role of rotational inertia in the dynamics of vibrofluidised granular gases. *EPL (Europhysics Letters)*, 108(5):58006, 2014.

[23] Nicolas Abatzoglou and Jean-Sébastien Simard. Prediction of segregation tendency occurrence in dry particulate pharmaceutical mixtures: Development of a mathematical tool adapted for granular systems application. *Pharmaceutical development and technology*, 10(1):59–70, 2005.

[24] Paul W Cleary and Mark L Sawley. Three-dimensional modelling of industrial granular flows. In *Second international conference on CFD in the minerals and process industries*, pages 95–100. CSIRO, 1999.

[25] JMNT Gray, M Wieland, and K Hutter. Gravity-driven free surface flow of granular avalanches over complex basal topography. *Proceedings of the Royal*

Society of London. Series A: Mathematical, Physical and Engineering Sciences, 455(1985):1841–1874, 1999.

[26] Troy Shinbrot, Nam H Kim, and N Nirmal Thyagu. Electrostatic precursors to granular slip events. *Proceedings of the National Academy of Sciences*, 109(27):10806–10810, 2012.

[27] JR Leeman, MM Scuderi, C Marone, DM Saffer, and T Shinbrot. On the origin and evolution of electrical signals during frictional stick slip in sheared granular material. *Journal of Geophysical Research: Solid Earth*, 2014.

[28] Mei-Lin Tsai, Chin-Fung Li, and Cheng-Yi Lii. Effects of granular structures on the pasting behaviors of starches 1. *Cereal Chemistry*, 74(6):750–757, 1997.

[29] Frederic Cointault, Philippe Sarrazin, and Michel Paindavoine. Measurement of the motion of fertilizer particles leaving a centrifugal spreader using a fast imaging system. *Precision Agriculture*, 4(3):279–295, 2003.

[30] Hideaki Miyamoto, Hajime Yano, Daniel J Scheeres, Shinsuke Abe, Olivier Barnouin-Jha, Andrew F Cheng, Hirohide Demura, Robert W Gaskell, Naru Hirata, Masateru Ishiguro, et al. Regolith migration and sorting on asteroid itokawa. *Science*, 316(5827):1011–1014, 2007.

[31] Richard G Holdich. *Fundamentals of particle technology.* Midland Information Technology and Publishing, 2002.

[32] Keiko M Aoki, Tetsuo Akiyama, Yoji Maki, and Tatsuyuki Watanabe. Convective roll patterns in vertically vibrated beds of granules. *Physical Review E*, 54(1):874, 1996.

[33] P Bergé and M Dubois. Rayleigh-bénard convection. *Contemporary Physics*, 25(6):535–582, 1984.

[34] Francisco Melo, Paul Umbanhowar, and Harry L Swinney. Transition to parametric wave patterns in a vertically oscillated granular layer. *Physical review letters*, 72(1):172, 1994.

[35] S Luding, E Clément, J Rajchenbach, and J Duran. Simulations of pattern formation in vibrated granular media. *EPL (Europhysics Letters)*, 36(4):247, 1996.

[36] MICHAEL Faraday. On the forms and states assumed by fluids in contact with vibrating elastic surfaces. *Philos. Trans. R. Soc. London*, 121(319):1831, 1831.

[37] JC Williams. The segregation of powders and granular materials. *Fuel Soc. J*, 14:29–34, 1963.

[38] Meheboob Alam and Stefan Luding. How good is the equipartition assumption for the transport properties of a granular mixture? *Granular Matter*, 4(3):139–142, 2002.

[39] Yunus A Cengel, Michael A Boles, and Mehmet Kanoğlu. *Thermodynamics: an engineering approach*, volume 5. McGraw-Hill New York, 2011.

[40] I Goldhirsch and G Zanetti. Clustering instability in dissipative gases. *Physical review letters*, 70(11):1619, 1993.

[41] I Goldhirsch, M-L Tan, and G Zanetti. A molecular dynamical study of granular fluids i: The unforced granular gas in two dimensions. *Journal of Scientific Computing*, 8(1):1–40, 1993.

[42] Sean McNamara and WR Young. Inelastic collapse in two dimensions. *Physical review E*, 50(1):R28, 1994.

[43] Sean McNamara and WR Young. Dynamics of a freely evolving, two-dimensional granular medium. *Physical Review E*, 53(5):5089, 1996.

[44] J Javier Brey, MJ Ruiz-Montero, and D Cubero. Origin of density clustering in a freely evolving granular gas. *Physical Review E*, 60(3):3150, 1999.

[45] Heinrich M. Jaeger, Sidney R. Nagel, and Robert P. Behringer. Granular solids, liquids, and gases. *Rev. Mod. Phys.*, 68:1259–1273, Oct 1996.

[46] S. Ogawa. Multitemperature theory of granular materials. In M. Satake S.C. Cowin, editor, *Proc. U. S.-Japan Symp. on Continuum Mechanics and Statistical Approaches in the Mechanics of Granular Materials*, pages 208–217. in Italian, 1978.

[47] Stuart B Savage. Gravity flow of cohesionless granular materials in chutes and channels. *Journal of Fluid Mechanics*, 92(01):53–96, 1979.

[48] RM Nedderman, U Tüzün, SB Savage, and GT Houlsby. The flow of granular materialsi: discharge rates from hoppers. *Chemical Engineering Science*, 37(11):1597–1609, 1982.

[49] William J Beck. Vibrating apparatus, June 24 1941. US Patent 2,246,497.

[50] JC Macrae, PC Finlayson, and WA Gray. Vibration packing of dry granular solids. *Nature*, 179:1365–1366, 1957.

[51] R Rutgers. Longitudinal mixing of granular material flowing through a rotating cylinder: Part i. descriptive and theoretical. *Chemical Engineering Science*, 20(12):1079–1087, 1965.

[52] R Rutgers. Longitudinal mixing of granular material flowing through a rotating cylinder: Part ii. experimental. *Chemical Engineering Science*, 20(12):1089–1100, 1965.

[53] S Luding, E Clément, A Blumen, J Rajchenbach, and J Duran. Studies of columns of beads under external vibrations. *Physical Review E*, 49(2):1634, 1994.

[54] Nicolás Mujica, Leonardo Caballero, and Francisco Melo. Collective motion and solid-liquid type transitions in vibrated granular layers. *Physica A: Statistical Mechanics and its Applications*, 263(1):362–368, 1999.

[55] E Clement and J Rajchenbach. Fluidization of a bidimensional powder. *EPL (Europhysics Letters)*, 16(2):133, 1991.

[56] K Helal, T Biben, and JP Hansen. Local fluctuations in a fluidized granular medium. *Physica A: Statistical Mechanics and its Applications*, 240(1):361–373, 1997.

[57] J Javier Brey, MJ Ruiz-Montero, and F Moreno. Hydrodynamics of an open vibrated granular system. *Physical Review E*, 63(6):061305, 2001.

[58] Rosa Ramırez and Rodrigo Soto. Temperature inversion in granular fluids under gravity. *Physica A: Statistical Mechanics and its Applications*, 322:73–80, 2003.

[59] RD Wildman, JM Huntley, and DJ Parker. Granular temperature profiles in three-dimensional vibrofluidized granular beds. *Physical Review E*, 63(6):061311, 2001.

[60] R Soto, Michel Mareschal, and D Risso. Departure from fourier's law for fluidized granular media. *Physical Review Letters*, 83(24):5003, 1999.

[61] S Luding, HJ Herrmann, and A Blumen. Simulations of two-dimensional arrays of beads under external vibrations: Scaling behavior. *Physical Review E*, 50(4):3100, 1994.

[62] Stephen Warr, Jonathan M Huntley, and George TH Jacques. Fluidization of a two-dimensional granular system: Experimental study and scaling behavior. *Physical Review E*, 52(5):5583, 1995.

[63] E Falcon, S Fauve, and C Laroche. Experimental determination of a state equation

for dissipative granular gases. *Journal de Chimie Physique et de Physico-Chimie Biologique*, 96(6):1111–1116, 1999.

[64] Rosa Ramírez, Dino Risso, and Patricio Cordero. Thermal convection in fluidized granular systems. *Physical review letters*, 85(6):1230, 2000.

[65] STEFAN Luding, Oliver Strauss, and SEAN McNamara. Segregation of polydisperse granular media in the presence of a temperature gradient. In *IUTAM Symposium on Segregation in Granular Flows*, pages 297–303. Springer, 2000.

[66] Vicente Garzó. Segregation in granular binary mixtures: Thermal diffusion. *EPL (Europhysics Letters)*, 75(4):521, 2006.

[67] JS Olafsen and JS Urbach. Clustering, order, and collapse in a driven granular monolayer. *Physical review letters*, 81(20):4369, 1998.

[68] Aaron S Keys, Adam R Abate, Sharon C Glotzer, and Douglas J Durian. Measurement of growing dynamical length scales and prediction of the jamming transition in a granular material. *Nature physics*, 3(4):260–264, 2007.

[69] PK Haff. Grain flow as a fluid-mechanical phenomenon. *Journal of Fluid Mechanics*, 134:401–430, 1983.

[70] A Kudrolli and J Henry. Non-gaussian velocity distributions in excited granular matter in the absence of clustering. *Physical Review E*, 62(2):R1489, 2000.

[71] Alexis Prevost, David A Egolf, and Jeffrey S Urbach. Forcing and velocity correlations in a vibrated granular monolayer. *Physical review letters*, 89(8):084301, 2002.

[72] GW Baxter and JS Olafsen. Experimental evidence for molecular chaos in granular gases. *Physical review letters*, 99(2):028001, 2007.

[73] Devaraj van der Meer and Peter Reimann. Temperature anisotropy in a driven granular gas. *EPL (Europhysics Letters)*, 74(3):384, 2006.

[74] Michael Faraday. On a peculiar class of acoustical figures; and on certain forms assumed by groups of particles upon vibrating elastic surfaces. *Philosophical Transactions of the Royal Society of London*, pages 299–340, 1831.

[75] RD Wildman, JM Huntley, and DJ Parker. Convection in highly fluidized three-dimensional granular beds. *Physical review letters*, 86(15):3304, 2001.

[76] Nagendra Shishodia and Carl R Wassgren. Particle segregation in vibrofluidized beds due to buoyant forces. *Physical review letters*, 87(8):084302, 2001.

[77] Leonardo Trujillo, Meheboob Alam, and Hans J Herrmann. Segregation in a fluidized binary granular mixture: Competition between buoyancy and geometric forces. *EPL (Europhysics Letters)*, 64(2):190, 2003.

[78] Leonardo Trujillo and Hans J Herrmann. A note on the upward and downward intruder segregation in granular media. *Granular Matter*, 5(2):85–89, 2003.

[79] J Talbot and P Viot. Wall-enhanced convection in vibrofluidized granular systems. *Physical review letters*, 89(6):064301, 2002.

[80] RD Wildman, TW Martin, PE Krouskop, J Talbot, JM Huntley, and DJ Parker. Convection in vibrated annular granular beds. *Physical Review E*, 71(6):061301, 2005.

[81] Peter Eshuis, Ko Van Der Weele, Devaraj Van Der Meer, Robert Bos, and Detlef Lohse. Phase diagram of vertically shaken granular matter. *Physics of Fluids (1994-present)*, 19(12):123301, 2007.

[82] Phillip J Holmes. The dynamics of repeated impacts with a sinusoidally vibrating table. *Journal of Sound and Vibration*, 84(2):173–189, 1982.

[83] Anita Mehta and JM Luck. Novel temporal behavior of a nonlinear dynamical system: The completely inelastic bouncing ball. *Physical review letters*, 65(4):393, 1990.

[84]

[85] CR Wassgren, CE Brennen, and ML Hunt. Vertical vibration of a deep bed of granular material in a container. *Journal of applied mechanics*, 63(3):712–719, 1996.

[86] E Clément, S Luding, A Blumen, J Rajchenbach, and J Duran. Fluidization, condensation and clusterization of a vibrating column of beads. *International Journal of Modern Physics B*, 7(09n10):1807–1827, 1993.

[87] S Douady, S Fauve, and C Laroche. Subharmonic instabilities and defects in a granular layer under vertical vibrations. *EPL (Europhysics Letters)*, 8(7):621, 1989.

[88] Akiko Ugawa and Osamu Sano. Undulations of a thin granular layer induced by vertical vibration. *Journal of the Physical Society of Japan*, 72(6):1390–1395, 2003.

[89] Osamu Sano. Dilatancy, buckling, and undulations on a vertically vibrating granular layer. *Physical Review E*, 72(5):051302, 2005.

[90] Peter Eshuis, Ko van der Weele, Devaraj van der Meer, and Detlef Lohse. Granular leidenfrost effect: Experiment and theory of floating particle clusters. *Physical review letters*, 95(25):258001, 2005.

[91] Johann Gottlob Leidenfrost. *De aquae communis nonnullis qualitatibus tractatus.* [Typis Joan. Sebast. Straube, Acad. typogr.] Impensis Hermanni Ovenni, Univers. bibliopolæ, 1756.

[92] Peter Eshuis, Devaraj van der Meer, Meheboob Alam, Henk Jan van Gerner, Ko van der Weele, and Detlef Lohse. Onset of convection in strongly shaken granular matter. *Physical review letters*, 104(3):038001, 2010.

[93] Harish Viswanathan, Nadeem A Sheikh, Ricky D Wildman, and Jonathan M Huntley. Convection in three-dimensional vibrofluidized granular beds. *Journal of Fluid Mechanics*, 682:185–212, 2011.

[94] C Laroche, S Douady, and S Fauve. Convective flow of granular masses under vertical vibrations. *Journal de Physique*, 50(7):699–706, 1989.

[95] P Evesque and J Rajchenbach. Instability in a sand heap. *Physical review letters*, 62(1):44, 1989.

[96] JAC Gallas, HJ Herrmann, and S Sokołowski. Convection cells in vibrating granular media. *Physical review letters*, 69(9):1371, 1992.

[97] EE Ehrichs, HM Jaeger, Greg S Karczmar, James B Knight, Vadim Yu Kuperman, and Sidney R Nagel. Granular convection observed by magnetic resonance imaging. *Science*, 267(5204):1632–1634, 1995.

[98] James B Knight, EE Ehrichs, Vadim Yu Kuperman, Janna K Flint, Heinrich M Jaeger, and Sidney R Nagel. Experimental study of granular convection. *Physical Review E*, 54(5):5726, 1996.

[99] James B Knight. External boundaries and internal shear bands in granular convection. *Physical Review E*, 55(5):6016, 1997.

[100] SS Hsiau and CH Chen. Granular convection cells in a vertical shaker. *Powder Technology*, 111(3):210–217, 2000.

[101] Dino Risso, Rodrigo Soto, Sergio Godoy, and Patricio Cordero. Friction and con-

vection in a vertically vibrated granular system. *Physical Review E*, 72(1):011305, 2005.

[102] Guy Metcalfe and Mark Shattuck. Pattern formation during mixing and segregation of flowing granular materials. *Physica A: Statistical Mechanics and its Applications*, 233(3):709–717, 1996.

[103] Fernando J Muzzio, Troy Shinbrot, and Benjamin J Glasser. Powder technology in the pharmaceutical industry: the need to catch up fast. *Powder technology*, 124(1):1–7, 2002.

[104] Nusruth Mohabuth, Philip Hall, and Nicholas Miles. Investigating the use of vertical vibration to recover metal from electrical and electronic waste. *Minerals engineering*, 20(9):926–932, 2007.

[105] C Zeilstra, MA Van Der Hoef, and JAM Kuipers. Simulation of density segregation in vibrated beds. *Physical Review E*, 77(3):031309, 2008.

[106] S Das Gupta, DV Khakhar, and SK Bhatia. Axial segregation of particles in a horizontal rotating cylinder. *Chemical engineering science*, 46(5):1513–1517, 1991.

[107] SB Savage and CKK Lun. Particle size segregation in inclined chute flow of dry cohesionless granular solids. *Journal of Fluid Mechanics*, 189:311–335, 1988.

[108] P Artega and U Tüzün. Flow of binary mixtures of equal-density granules in hopperssize segregation, flowing density and discharge rates. *Chemical Engineering Science*, 45(1):205–223, 1990.

[109] Khan Ahmad and IJ Smalley. Observation of particle segregation in vibrated granular systems. *Powder Technology*, 8(1):69–75, 1973.

[110] Anthony Rosato, Katherine J Strandburg, Friedrich Prinz, and Robert H Swend-

sen. Why the brazil nuts are on top: Size segregation of particulate matter by shaking. *Physical Review Letters*, 58(10):1038, 1987.

[111] James W Vallance and Stuart B Savage. Particle segregation in granular flows down chutes. In *IUTAM Symposium on Segregation in Granular flows*, pages 31–51. Springer, 2000.

[112] SC Yang. Density effect on mixing and segregation processes in a vibrated binary granular mixture. *Powder Technology*, 164(2):65–74, 2006.

[113] D Serero, I Goldhirsch, SH Noskowicz, and M-L Tan. Hydrodynamics of granular gases and granular gas mixtures. *Journal of Fluid Mechanics*, 554:237–258, 2006.

[114] Tamás Börzsönyi and Ralf Stannarius. Granular materials composed of shape-anisotropic grains. *Soft Matter*, 9(31):7401–7418, 2013.

[115] RL Brown. The fundamental principles of segregation. *The Institute of Fuel*, 13:15–19, 1939.

[116] NI Fattuhi. The influence of high frequency vibration on the compaction and segregation of concrete materials. *M. Sc. Diss. Univ. of Leeds*, 1971.

[117] J_ C Williams. The segregation of particulate materials. a review. *Powder technology*, 15(2):245–251, 1976.

[118] A Rosato, F Prinz, KJ Standburg, and R Swendsen. Monte carlo simulation of particulate matter segregation. *Powder Technology*, 49(1):59–69, 1986.

[119] James B Knight, HM Jaeger, and Sidney R Nagel. Vibration-induced size separation in granular media: the convection connection. *Physical review letters*, 70(24):3728, 1993.

[120] Yidan Lan and Anthony D Rosato. Convection related phenomena in granular dynamics simulations of vibrated beds. *Physics of Fluids (1994-present)*, 9(12):3615–3624, 1997.

[121] D Brone and FJ Muzzio. Size segregation in vibrated granular systems: A reversible process. *Physical Review E*, 56(1):1059, 1997.

[122] J Duran, J Rajchenbach, and E Clement. Arching effect model for particle size segregation. *Physical review letters*, 70(16):2431, 1993.

[123] Loic Vanel, Anthony D Rosato, and Rajesh N Dave. Rise-time regimes of a large sphere in vibrated bulk solids. *Physical review letters*, 78(7):1255, 1997.

[124] Daniel C Hong, Paul V Quinn, and Stefan Luding. Reverse brazil nut problem: competition between percolation and condensation. *Physical Review Letters*, 86(15):3423, 2001.

[125] Daniel C Hong. Condensation of hard spheres under gravity. *Physica A: Statistical Mechanics and its Applications*, 271(1):192–199, 1999.

[126] Paul V Quinn and Daniel C Hong. Liquid-solid transition of hard spheres under gravity. *Physical Review E*, 62(6):8295, 2000.

[127] Duncan A Sanders, Michael R Swift, RM Bowley, and PJ King. Are brazil nuts attractive? *Physical review letters*, 93(20):208002, 2004.

[128] DA Sanders, MR Swift, RM Bowley, and PJ King. The attraction of brazil nuts. *EPL (Europhysics Letters)*, 73(3):349, 2006.

[129] DA Sanders, Michael R Swift, RM Bowley, and PJ King. Influence of vibrational wave form on intruder clustering. *Applied physics letters*, 88(26):264106, 2006.

[130] LT Lui, Michael R Swift, RM Bowley, and PJ King. Intruder clustering in three-dimensional granular beds. *Physical Review E*, 75(5):051303, 2007.

[131] S.S. Hsiau and M.L. Hunt. Granular thermal diffusion in flows of binary-sized mixtures. *Acta Mechanica*, 114(1-4):121–137, 1996.

[132] RD Wildman and DJ Parker. Coexistence of two granular temperatures in binary vibrofluidized beds. *Physical review letters*, 88(6):064301, 2002.

[133] Vicente Garzó and James W Dufty. Hydrodynamics for a granular binary mixture at low density. *Physics of Fluids (1994-present)*, 14(4):1476–1490, 2002.

[134] JE Galvin, SR Dahl, and CM Hrenya. On the role of non-equipartition in the dynamics of rapidly flowing granular mixtures. *Journal of Fluid Mechanics*, 528:207–232, 2005.

[135] Vicente Garzó. Segregation in granular binary mixtures: Thermal diffusion. *EPL (Europhysics Letters)*, 75(4):521, 2006.

[136] J Javier Brey, MJ Ruiz-Montero, and F Moreno. Energy partition and segregation for an intruder in a vibrated granular system under gravity. *Physical review letters*, 95(9):098001, 2005.

[137] Anthony D Rosato, Denis L Blackmore, Ninghua Zhang, and Yidan Lan. A perspective on vibration-induced size segregation of granular materials. *Chemical Engineering Science*, 57(2):265–275, 2002.

[138] DA Huerta and JC Ruiz-Suárez. Vibration-induced granular segregation: a phenomenon driven by three mechanisms. *Physical Review Letters*, 92(11):114301, 2004.

[139] Matthias Schröter, Stephan Ulrich, Jennifer Kreft, Jack B Swift, and Harry L Swinney. Mechanisms in the size segregation of a binary granular mixture. *Physical Review E*, 74(1):011307, 2006.

[140] Troy Shinbrot and Fernando J Muzzio. Reverse buoyancy in shaken granular beds. *Physical Review Letters*, 81(20):4365, 1998.

[141] Troy Shinbrot. Granular materials: The brazil nut effectin reverse. *Nature*, 429(6990):352–353, 2004.

[142] APJ Breu, H-M Ensner, Ch A Kruelle, and I Rehberg. Reversing the brazil-nut effect: competition between percolation and condensation. *Physical review letters*, 90(1):014302, 2003.

[143] Joseph A Both and Daniel C Hong. Variational approach to hard sphere segregation under gravity. *Physical review letters*, 88(12):124301, 2002.

[144] Hong-qiang Wang, Guo-jun Jin, and Yu-qiang Ma. Simulation study on kinetic temperatures of vibrated binary granular mixtures. *Physical Review E*, 68(3):031301, 2003.

[145] Vicente Garzó. Brazil-nut effect versus reverse brazil-nut effect in a moderately dense granular fluid. *Physical Review E*, 78(2):020301, 2008.

[146] DA Huerta, Victor Sosa, MC Vargas, and JC Ruiz-Suárez. Archimedes principle in fluidized granular systems. *Physical Review E*, 72(3):031307, 2005.

[147] Leonardo Trujillo, Meheboob Alam, and Hans J Herrmann. Segregation in a fluidized binary granular mixture: Competition between buoyancy and geometric forces. *EPL (Europhysics Letters)*, 64(2):190, 2003.

[148] Q. Shi, G. Sun, M. Hou, and K. Lu. Density-driven segregation in vertically vibrated binary granular mixtures. *Phys. Rev. E*, 75:061302, Jun 2007.

[149] CH Tai, SS Hsiau, and CA Kruelle. Density segregation in a vertically vibrated granular bed. *Powder Technology*, 204(2):255–262, 2010.

[150] N Burtally, PJ King, and Michael R Swift. Spontaneous air-driven separation in vertically vibrated fine granular mixtures. *Science*, 295(5561):1877–1879, 2002.

[151] N Burtally, PJ King, Michael R Swift, and M Leaper. Dynamical behaviour of fine granular glass/bronze mixtures under vertical vibration. *Granular Matter*, 5(2):57–66, 2003.

[152] C Zeilstra, MA van der Hoef, and JAM Kuipers. Simulation study of air-induced segregation of equal-sized bronze and glass particles. *Physical Review E*, 74(1):010302, 2006.

[153] Eldin Wee Chuan Lim. Density segregation in vibrated granular beds with bumpy surfaces. *AIChE journal*, 56(10):2588–2597, 2010.

[154] CC Liao, ML Hunt, SS Hsiau, and SH Lu. Investigation of the effect of a bumpy base on granular segregation and transport properties under vertical vibration. *Physics of Fluids (1994-present)*, 26(7):073302, 2014.

[155] Nicolás Rivas, Suomi Ponce, Basile Gallet, Dino Risso, Rodrigo Soto, Patricio Cordero, and Nicolás Mujica. Sudden chain energy transfer events in vibrated granular media. *Physical review letters*, 106(8):088001, 2011.

[156] Nicolás Rivas, Patricio Cordero, Dino Risso, and Rodrigo Soto. Segregation in quasi-two-dimensional granular systems. *New Journal of Physics*, 13(5):055018, 2011.

[157] N Rivas, D Risso, R Soto, P Cordero, Pedro L Garrido, Joaqui´ n Marro, and F de los Santos. Energy bursts in vibrated shallow granular systems. In *AIP Conference Proceedings-American Institute of Physics*, volume 1332, page 184, 2011.

[158] Robert V Whitman. Session 3 effects of viscosity and inelasticity upon stress waves

through confined soil. *Shock, Vibration and Associated Environments: Papers*, (32), 1963.

[159] LT Lui, Michael R Swift, RM Bowley, and PJ King. Interaction between intruders in vibrated granular beds. *Physical Review E*, 77(2):020301, 2008.

[160] Jia Yan, Yang Xian-Qing, Deng Min, Guo Hai-Ping, and Ye Jian-Lan. Relative energy dissipation-induced effective attraction in granular mixture. *Chinese Physics B*, 19(12):128202, 2010.

[161] D Serero, SH Noskowicz, and I Goldhirsch. Theory of dilute binary granular gas mixtures. *Mathematical Modelling of Natural Phenomena*, 6(01):17–47, 2011.

[162] D SERERO, N GUNKELMANN, and T POSCHEL. Hydrodynamics of binary mixtures of granular gases with stochastic coefficient of restitution.

[163] George Hoffmeister, SC Watkins, and Julius Silverberg. Fertilizer consistency, bulk blending of fertilizer material: Effect of size, shape, and density on segregation. *Journal of Agricultural and Food Chemistry*, 12(1):64–69, 1964.

[164] Emilien Azéma, Farhang Radjai, Robert Peyroux, and Gilles Saussine. Force transmission in a packing of pentagonal particles. *Physical Review E*, 76(1):011301, 2007.

[165] Emilien Azéma and Farhang Radjaï. Stress-strain behavior and geometrical properties of packings of elongated particles. *Physical Review E*, 81(5):051304, 2010.

[166] Charlles RA Abreu, Frederico W Tavares, and Marcelo Castier. Influence of particle shape on the packing and on the segregation of spherocylinders via monte carlo simulations. *Powder Technology*, 134(1):167–180, 2003.

[167] D de Las Heras, Yuri Martínez-Ratón, and Enrique Velasco. Demixing and

orientational ordering in mixtures of rectangular particles. *Physical Review E*, 76(3):031704, 2007.

[168] Baptiste Saint-Cyr, J-Y Delenne, Charles Voivret, Farhang Radjai, and Philippe Sornay. Rheology of granular materials composed of nonconvex particles. *Physical Review E*, 84(4):041302, 2011.

[169] Masami Furuuchi and Keishi Gotoh. Shape separation of particles. *Powder technology*, 73(1):1–9, 1992.

[170] Keirnan R LaMarche, Matthew J Metzger, Benjamin J Glasser, and Troy Shinbrot. Shape-mediated ordering in granular blends. *Physical Review E*, 81(5):052301, 2010.

[171] Sho Asakura and Fumio Oosawa. On interaction between two bodies immersed in a solution of macromolecules. *The Journal of chemical physics*, 22(7):1255–1256, 1954.

[172] FM Van der Kooij, M Vogel, and HNW Lekkerkerker. Phase behavior of a mixture of platelike colloids and nonadsorbing polymer. *Physical Review E*, 62(4):5397, 2000.

[173] X Jia, R Caulkin, RA Williams, ZY Zhou, and AB Yu. The role of geometric constraints in random packing of non-spherical particles. *EPL (Europhysics Letters)*, 92(6):68005, 2010.

[174] R Caulkin, X Jia, M Fairweather, and RA Williams. Geometric aspects of particle segregation. *Physical Review E*, 81(5):051302, 2010.

[175] Stephen J Roskilly, Elizabeth A Colbourn, Oludolapo Alli, Daryl Williams, Kirsty A Paul, Eloise H Welfare, and Paul A Trusty. Investigating the effect of shape on particle segregation using a monte carlo simulation. *Powder Technology*, 203(2):211–222, 2010.

[176] Z Yang, DJ Parker, PJ Fryer, S Bakalis, and X Fan. Multiple-particle trackingan improvement for positron particle tracking. *Nuclear Instruments and Methods in Physics Research Section A: Accelerators, Spectrometers, Detectors and Associated Equipment*, 564(1):332–338, 2006.

[177] Z Yang, PJ Fryer, S Bakalis, X Fan, DJ Parker, and JPK Seville. An improved algorithm for tracking multiple, freely moving particles in a positron emission particle tracking system. *Nuclear Instruments and Methods in Physics Research Section A: Accelerators, Spectrometers, Detectors and Associated Equipment*, 577(3):585–594, 2007.

[178] Z Yang, X Fan, PJ Fryer, DJ Parker, and S Bakalis. Improved multiple-particle tracking for studying flows in multiphase systems. *AIChE journal*, 53(8):1941–1951, 2007.

[179] Z Yang, X Fan, S Bakalis, DJ Parker, and PJ Fryer. A method for characterising solids translational and rotational motions using multiple-positron emission particle tracking (multiple-pept). *International Journal of Multiphase Flow*, 34(12):1152–1160, 2008.

[180] X Fan, DJ Parker, and MD Smith. Labelling a single particle for positron emission particle tracking using direct activation and ion-exchange techniques. *Nuclear Instruments and Methods in Physics Research Section A: Accelerators, Spectrometers, Detectors and Associated Equipment*, 562(1):345–350, 2006.

[181] X Fan, DJ Parker, and MD Smith. Enhancing¡ sup¿ 18¡/sup¿ f uptake in a single particle for positron emission particle tracking through modification of solid surface chemistry. *Nuclear Instruments and Methods in Physics Research Section A: Accelerators, Spectrometers, Detectors and Associated Equipment*, 558(2):542–546, 2006.

[182] David J Parker and Xianfeng Fan. Positron emission particle trackingapplication and labelling techniques. *Particuology*, 6(1):16–23, 2008.

[183] DJ Parker, RN Forster, P Fowles, and PS Takhar. Positron emission particle tracking using the new birmingham positron camera. *Nuclear Instruments and Methods in Physics Research Section A: Accelerators, Spectrometers, Detectors and Associated Equipment*, 477(1):540–545, 2002.

[184] University of Birmingham Nuclear Physics Research Group. Positron imaging centre – positron emission particle tracking. http://www.np.ph.bham.ac.uk/pic/pept, July 2012.

[185] DJ Parker, CJ Broadbent, P Fowles, MR Hawkesworth, and P McNeil. Positron emission particle tracking-a technique for studying flow within engineering equipment. *Nuclear Instruments and Methods in Physics Research Section A: Accelerators, Spectrometers, Detectors and Associated Equipment*, 326(3):592–607, 1993.

[186] RD Wildman, JM Huntley, J-P Hansen, DJ Parker, and DA Allen. Single-particle motion in three-dimensional vibrofluidized granular beds. *Physical Review E*, 62(3):3826, 2000.

[187] Stephen Warr, George TH Jacques, and Jonathan M Huntley. Tracking the translational and rotational motion of granular particles: use of high-speed photography and image processing. *Powder Technology*, 81(1):41–56, 1994.

[188] S Warr and J-P Hansen. Relaxation of local density fluctuations in a fluidized granular medium. *EPL (Europhysics Letters)*, 36(8):589, 1996.

[189] JS Olafsen and Jeffery S Urbach. Velocity distributions and density fluctuations in a granular gas. *Physical Review E*, 60(3):R2468, 1999.

[190] Florence Rouyer and Narayanan Menon. Velocity fluctuations in a homogeneous 2d granular gas in steady state. *Physical review letters*, 85(17):3676, 2000.

[191] A Kudrolli and J Henry. Non-gaussian velocity distributions in excited granular matter in the absence of clustering. *Physical Review E*, 62(2):R1489, 2000.

[192] Alexis Prevost, David A Egolf, and Jeffrey S Urbach. Forcing and velocity correlations in a vibrated granular monolayer. *Physical review letters*, 89(8):084301, 2002.

[193] GW Baxter and JS Olafsen. Kinetics: Gaussian statistics in granular gases. *Nature*, 425(6959):680–680, 2003.

[194] J Javier Brey and MJ Ruiz-Montero. Velocity distribution of fluidized granular gases in the presence of gravity. *Physical Review E*, 67(2):021307, 2003.

[195] K Combs, JS Olafsen, A Burdeau, and P Viot. Thermostatistics of a single particle on a granular dimer lattice: Influence of defects. *Physical Review E*, 78(4):042301, 2008.

[196] Alexis Burdeau and Pascal Viot. Quasi-gaussian velocity distribution of a vibrated granular bilayer system. *Physical Review E*, 79(6):061306, 2009.

[197] RD Wildman and JM Huntley. Novel method for measurement of granular temperature distributions in two-dimensional vibro-fluidised beds. *Powder technology*, 113(1):14–22, 2000.

[198] DV Khakhar, JJ McCarthy, Troy Shinbrot, and JM Ottino. Transverse flow and mixing of granular materials in a rotating cylinder. *Physics of Fluids (1994-present)*, 9(1):31–43, 1997.

[199] Shu-San Hsiau and Shie-Chen Yang. Numerical simulation of self-diffusion and mixing in a vibrated granular bed with the cohesive effect of liquid bridges. *Chemical engineering science*, 58(2):339–351, 2003.

[200] Thomas W Leadbeater, David J Parker, and Joseph Gargiuli. Positron imaging systems for studying particulate, granular and multiphase flows. *Particuology*, 10(2):146–153, 2012.

[201] Peter A Cundall and Otto DL Strack. A discrete numerical model for granular assemblies. *Geotechnique*, 29(1):47–65, 1979.

[202] Peter A Cundall. Formulation of a three-dimensional distinct element modelpart i. a scheme to detect and represent contacts in a system composed of many polyhedral blocks. In *International Journal of Rock Mechanics and Mining Sciences & Geomechanics Abstracts*, volume 25, pages 107–116. Elsevier, 1988.

[203] R Hart, PA Cundall, and J Lemos. Formulation of a three-dimensional distinct element modelpart ii. mechanical calculations for motion and interaction of a system composed of many polyhedral blocks. In *International Journal of Rock Mechanics and Mining Sciences & Geomechanics Abstracts*, volume 25, pages 117–125. Elsevier, 1988.

[204] Mercurydpm.org.

[205] Anthony R. Thornton, Thomas Weinhart, Stefan Luding, and Onno Bokhove. Modeling of particle size segregation: Calibration using the discrete particle method. *International Journal of Modern Physics C*, 23(08), 2012.

[206] A. R. Thornton, T Weinhart, V Ogarko, and S Luding. Multi-scale modeling of multi-component granular materials. journal computer methods in materials science. *Computer Methods in Materials Science*, 13(2):1–16, 2013.

[207] A. R. Thornton, D. Krijgsman, A. te Voortwis, V. Ogarko, S. Luding, R. Fransen, S. Gonzalez, O. Bokhove, O. Imole, and T. Weinhart. *DEM 6: Proceedings of the 6th International Conference on Discrete Element Methods and Related Techniques*, page 393, 2013.

[208] Stefan Luding. Cohesive, frictional powders: contact models for tension. *Granular matter*, 10(4):235–246, 2008.

[209] Vitaliy Ogarko and Stefan Luding. A fast multilevel algorithm for contact detection of arbitrarily polydisperse objects. *Computer physics communications*, 183(4):931–936, 2012.

[210] Thomas Weinhart, Remco Hartkamp, Anthony R Thornton, and Stefan Luding. Coarse-grained local and objective continuum description of three-dimensional granular flows down an inclined surface. *Physics of Fluids (1994-present)*, 25(7):070605, 2013.

[211] Thomas Weinhart, Anthony R Thornton, Stefan Luding, and Onno Bokhove. From discrete particles to continuum fields near a boundary. *Granular Matter*, 14(2):289–294, 2012.

[212] Anthony R Thornton, Thomas Weinhart, Stefan Luding, and Onno Bokhove. Frictional dependence of shallow-granular flows from discrete particle simulations. 2012.

[213] Thomas Weinhart, Anthony R Thornton, Stefan Luding, and Onno Bokhove. Closure relations for shallow granular flows from particle simulations. *Granular matter*, 14(4):531–552, 2012.

[214] S González, CRK Windows-Yule, S Luding, DJ Parker, and AR Thornton. Shaping segregation: Convexity vs. concavity. *arXiv preprint arXiv:1410.6286*, 2014.

[215] Stefan Luding. Introduction to discrete element methods: basic of contact force models and how to perform the micro-macro transition to continuum theory. *European Journal of Environmental and Civil Engineering*, 12(7-8):785–826, 2008.

[216] Leonardo E Silbert, Deniz Ertaş, Gary S Grest, Thomas C Halsey, Dov Levine,

and Steven J Plimpton. Granular flow down an inclined plane: Bagnold scaling and rheology. *Physical Review E*, 64(5):051302, 2001.

[217] Mike P Allen, Dominic J Tildesley, et al. Computer simulation of liquids. 1987.

[218] William H Press, Saul A Teukolsky, William T Vetterling, and Brian P Flannery. Numerical recipes: The art of scientific computing (cambridge, 1992.

[219] Stefan Luding, E Clément, A Blumen, J Rajchenbach, and J Duran. Anomalous energy dissipation in molecular-dynamics simulations of grains: The detachment-effect. *Physical Review E*, 50(5):4113, 1994.

[220] JPA Tillett. A study of the impact of spheres on plates. *Proceedings of the Physical Society. Section B*, 67(9):677, 1954.

[221] Rosa Ramírez, Thorsten Pöschel, Nikolai V Brilliantov, and Thomas Schwager. Coefficient of restitution of colliding viscoelastic spheres. *Physical review E*, 60(4):4465, 1999.

[222] Stephan Ulrich, Matthias Schröter, and Harry L Swinney. Influence of friction on granular segregation. *Physical Review E*, 76(4):042301, 2007.

[223] Daniel L Blair and A Kudrolli. Collision statistics of driven granular materials. *Physical Review E*, 67(4):041301, 2003.

[224] P Sunthar and V Kumaran. Characterization of the stationary states of a dilute vibrofluidized granular bed. *Physical Review E*, 64(4):041303_1–041303_12, 2001.

[225] M. Y. Louge. http://grainflowresearch.mae.cornell.edu /impact/data/Impact

[226] RD Wildman, JT Jenkins, PE Krouskop, and J Talbot. A comparison of the predictions of a simple kinetic theory with experimental and numerical results for a vibrated granular bed consisting of nearly elastic particles of two sizes. *Physics of Fluids (1994-present)*, 18(7):073301, 2006.

[227] Isaac Goldhirsch. Introduction to granular temperature. *Powder Technology*, 182(2):130–136, 2008.

[228] D Paolotti, C Cattuto, U Marini Bettolo Marconi, and A Puglisi. Dynamical properties of vibrfluidized granular mixtures. *Granular Matter*, 5(2):75–83, 2003.

[229] Thomas Schwager and Thorsten Pöschel. Coefficient of normal restitution of viscous particles and cooling rate of granular gases. *Physical review E*, 57(1):650, 1998.

[230] Nikolai V Brilliantov and Thorsten Pöschel. Granular gases with impact-velocity-dependent restitution coefficient. In *Granular Gases*, pages 100–124. Springer, 2001.

[231] JS Van Zon, J Kreft, Daniel I Goldman, D Miracle, JB Swift, and Harry L Swinney. Crucial role of sidewalls in velocity distributions in quasi-two-dimensional granular gases. *Physical Review E*, 70(4):040301, 2004.

[232] R Sondergaard, K Chaney, and CE Brennen. Measurements of solid spheres bouncing off flat plates. *Journal of Applied Mechanics*, 112(3):694–699, 1990.

[233] O Zik and J Stavans. Self-diffusion in granular flows. *EPL (Europhysics Letters)*, 16(3):255, 1991.

[234] GC Barker and Anita Mehta. Transient phenomena, self-diffusion, and orientational effects in vibrated powders. *Physical Review E*, 47(1):184, 1993.

[235] Maher Moakher, Troy Shinbrot, and Fernando J Muzzio. Experimentally validated computations of flow, mixing and segregation of non-cohesive grains in 3d tumbling blenders. *Powder Technology*, 109(1):58–71, 2000.

[236] Li-Shin Lu and Shu-San Hsiau. Mixing in vibrated granular beds with the effect of electrostatic force. *Powder technology*, 160(3):170–179, 2005.

[237] Li-Shin Lu and Shu-San Hsiau. Mixing in a vibrated granular bed: Diffusive and convective effects. *Powder technology*, 184(1):31–43, 2008.

[238] JT Jenkins and E Askari. Boundary conditions for rapid granular flows: phase interfaces. *Journal of Fluid Mechanics*, 223:497–508, 1991.

[239] A Puglisi, V Loreto, U Marini Bettolo Marconi, A Petri, and A Vulpiani. Clustering and non-gaussian behavior in granular matter. *Physical review letters*, 81(18):3848, 1998.

[240] C Bizon, MD Shattuck, John R De Bruyn, JB Swift, WD McCormick, and Harry L Swinney. Convection and diffusion in patterns in oscillated granular media. *Journal of statistical physics*, 93(3-4):449–465, 1998.

[241] Alain Barrat and Emmanuel Trizac. Lack of energy equipartition in homogeneous heated binary granular mixtures. *Granular Matter*, 4(2):57–63, 2002.

[242] Alain Barrat and Emmanuel Trizac. Molecular dynamics simulations of vibrated granular gases. *Physical Review E*, 66(5):051303, 2002.

[243] Vicente Garzó and James Dufty. Homogeneous cooling state for a granular mixture. *Physical Review E*, 60(5):5706, 1999.

[244] Shu-San Hsiau, Chun-Chung Liao, Po-Yen Sheng, and Shih-Chang Tai. Experimental study on the influence of bed height on convection cell formation. *Experiments in fluids*, 51(3):795–800, 2011.

[245] Herbert B Callen and HL Scott. Thermodynamics and an introduction to thermostatistics. *American Journal of Physics*, 66(2):164–167, 1998.

[246] STEFAN Luding, Oliver Strauss, and SEAN McNamara. Segregation of polydisperse granular media in the presence of a temperature gradient. In *IUTAM Symposium on Segregation in Granular Flows*, pages 297–303. Springer, 2000.

[247] GC Barker and Anita Mehta. Vibrated powders: structure, correlations, and dynamics. *Physical Review A*, 45(6):3435, 1992.

[248] Eric Clément. Granular packing under vibration. In *Physics of dry granular media*, pages 585–600. Springer, 1998.

[249] P Evesque, E Szmatula, and J-P Denis. Surface fluidization of a sand pile. *EPL (Europhysics Letters)*, 12(7):623, 1990.

[250] E Falcon, S Fauve, and C Laroche. Cluster formation, pressure and density measurements in a granular medium fluidized by vibrations. *The European Physical Journal B-Condensed Matter and Complex Systems*, 9(2):183–186, 1999.

[251] Sung Joon Moon, MD Shattuck, C Bizon, Daniel I Goldman, JB Swift, and Harry L Swinney. Phase bubbles and spatiotemporal chaos in granular patterns. *Physical Review E*, 65(1):011301, 2001.

[252] A Lorenz, C Tuozzolo, and MY Louge. Measurements of impact properties of small, nearly spherical particles. *Experimental Mechanics*, 37(3):292–298, 1997.

[253] Frédéric Restagno, Cécile Ursini, Hervé Gayvallet, and Élisabeth Charlaix. Aging in humid granular media. *Physical review E*, 66(2):021304, 2002.

[254] Gerard V Middleton and Monty A Hampton. Part i. sediment gravity flows: mechanics of flow and deposition. 1973.

[255] GD Scott and DM Kilgour. The density of random close packing of spheres. *Journal of Physics D: Applied Physics*, 2(6):863, 1969.

[256] James G Berryman. Random close packing of hard spheres and disks. *Physical Review A*, 27(2):1053, 1983.

[257] George Y Onoda and Eric G Liniger. Random loose packings of uniform spheres and the dilatancy onset. *Physical Review Letters*, 64(22):2727, 1990.

[258] DV Khakhar, JJ McCarthy, and JM Ottino. Radial segregation of granular mixtures in rotating cylinders. *Physics of Fluids (1994-present)*, 9(12):3600–3614, 1997.

[259] S Miller and S Luding. Cluster growth in two-and three-dimensional granular gases. *Physical Review E*, 69(3):031305, 2004.

[260] Daniel L Blair and A Kudrolli. Clustering transitions in vibrofluidized magnetized granular materials. *Physical Review E*, 67(2):021302, 2003.

[261] Vicente Garzó. Thermal diffusion segregation in granular binary mixtures described by the enskog equation. *New Journal of Physics*, 13(5):055020, 2011.

[262] JR Melrose and RC Ball. The pathological behaviour of sheared hard spheres with hydrodynamic interactions. *EPL (Europhysics Letters)*, 32(6):535, 1995.

[263] RC Ball and JR Melrose. Lubrication breakdown in hydrodynamic simulations of concentrated colloids. *Advances in colloid and interface science*, 59:19–30, 1995.

[264] RS Farr, John R Melrose, and RC Ball. Kinetic theory of jamming in hard-sphere startup flows. *Physical Review E*, 55(6):7203, 1997.

[265] ME Cates, JP Wittmer, J-P Bouchaud, and Ph Claudin. Jamming, force chains, and fragile matter. *Physical review letters*, 81(9):1841, 1998.

[266] Anthony D Rosato and Doris Yacoub. Microstructure evolution in compacted granular beds. *Powder Technology*, 109(1):255–261, 2000.

[267] CR Wassgren, ML Hunt, and CE Brennen. Vertical side wall convection in deep beds of granular material subjected to vertical, sinusoidal oscillations. In *5th World Congress of Chemical Engineering, San Diego, CA, USA*, pages 355–360, 1996.

[268] Marc Bourzutschky and Jonathan Miller. granular convection in a vibrated fluid. *Physical review letters*, 74(12):2216, 1995.

[269] Elizabeth L Grossman. Effects of container geometry on granular convection. *Physical Review E*, 56(3):3290, 1997.

[270] A Prados, J Javier Brey, and B Sánchez-Rey. Hysteresis in vibrated granular media. *Physica A: Statistical Mechanics and its Applications*, 284(1):277–298, 2000.

[271] Giridhar Madras and Benjamin J McCoy. Reversible crystal growth–dissolution and aggregation–breakage: numerical and moment solutions for population balance equations. *Powder technology*, 143:297–307, 2004.

[272] S Dippel and S Luding. Simulation on size segregation: Geometrical effects in the absence of convection. *Journal de Physique I*, 5(12):1527–1537, 1995.

[273] S Luding and HJ Herrmann. Cluster-growth in freely cooling granular media. *Chaos: An Interdisciplinary Journal of Nonlinear Science*, 9(3):673–681, 1999.

[274] Konstantin L Gavrilov. Cluster model for compaction of vibrated granular materials. *Physical Review E*, 58(2):2107, 1998.

[275] Geoffroy Lumay and Nicolas Vandewalle. Experimental study of granular compaction dynamics at different scales: grain mobility, hexagonal domains, and packing fraction. *Physical review letters*, 95(2):028002, 2005.

[276] Charles S Campbell. Self-diffusion in granular shear flows. *Journal of Fluid Mechanics*, 348:85–101, 1997.

[277] Adam Ross Abate and Douglas J Durian. Approach to jamming in an air-fluidized granular bed. *Physical Review E*, 74(3):031308, 2006.

[278] RD Wildman, JM Huntley, and J-P Hansen. Self-diffusion of grains in a two-dimensional vibrofluidized bed. *Physical Review E*, 60(6):7066, 1999.

[279] Andrea J Liu and Sidney R Nagel. *Jamming and rheology: constrained dynamics on microscopic and macroscopic scales.* CRC Press, 2001.

[280] Aaron S Keys, Adam R Abate, Sharon C Glotzer, and Douglas J Durian. Measurement of growing dynamical length scales and prediction of the jamming transition in a granular material. *Nature physics*, 3(4):260–264, 2007.

[281] Pedro M Reis, Rohit A Ingale, and Mark D Shattuck. Caging dynamics in a granular fluid. *Physical review letters*, 98(18):188301, 2007.

[282] Olivier Pouliquen, M Belzons, and M Nicolas. Fluctuating particle motion during shear induced granular compaction. *Physical review letters*, 91(1):014301, 2003.

[283] Jaehyuk Choi, Arshad Kudrolli, Rodolfo R Rosales, and Martin Z Bazant. Diffusion and mixing in gravity-driven dense granular flows. *Physical review letters*, 92(17):174301, 2004.

[284] Mauro Sellitto and Jeferson J Arenzon. Free-volume kinetic models of granular matter. *Physical Review E*, 62(6):7793, 2000.

[285] G Marty and Olivier Dauchot. Subdiffusion and cage effect in a sheared granular material. *Physical review letters*, 94(1):015701, 2005.

[286] Andrea J Liu and Sidney R Nagel. Nonlinear dynamics: Jamming is not just cool any more. *Nature*, 396(6706):21–22, 1998.

[287] HP Zhang and HA Makse. Jamming transition in emulsions and granular materials. *Physical Review E*, 72(1):011301, 2005.

[288] Corey S O'Hern, Stephen A Langer, Andrea J Liu, and Sidney R Nagel. Random packings of frictionless particles. *Physical Review Letters*, 88(7):075507, 2002.

[289] Edmund R Nowak, James B Knight, Eli Ben-Naim, Heinrich M Jaeger, and Sidney R Nagel. Density fluctuations in vibrated granular materials. *Physical Review E*, 57(2):1971, 1998.

[290] Mario Nicodemi, Antonio Coniglio, and Hans J Herrmann. Frustration and slow dynamics of granular packings. *Physical Review E*, 55(4):3962, 1997.

[291] Keiji Watanabe and Hajime Tanaka. Direct observation of medium-range crystalline order in granular liquids near the glass transition. *Physical review letters*, 100(15):158002, 2008.

[292] Takeshi Kawasaki, Takeaki Araki, and Hajime Tanaka. Correlation between dynamic heterogeneity and medium-range order in two-dimensional glass-forming liquids. *Physical review letters*, 99(21):215701, 2007.

[293] Hajime Tanaka, Takeshi Kawasaki, Hiroshi Shintani, and Keiji Watanabe. Critical-like behaviour of glass-forming liquids. *Nature Materials*, 9(4):324–331, 2010.

[294] Andreea Panaitescu and Arshad Kudrolli. Spatial distribution functions of random packed granular spheres obtained by direct particle imaging. *Physical Review E*, 81(6):060301, 2010.

[295] Pedro M Reis, G Ehrhardt, A Stephenson, and T Mullin. Gases, liquids and crystals in granular segregation. *EPL (Europhysics Letters)*, 66(3):357, 2004.

[296] J Blouwolff and S Fraden. The coordination number of granular cylinders. *EPL (Europhysics Letters)*, 76(6):1095, 2006.

[297] Leonardo E Silbert, Deniz Ertaş, Gary S Grest, Thomas C Halsey, and Dov Levine. Geometry of frictionless and frictional sphere packings. *Physical Review E*, 65(3):031304, 2002.

[298] Leonardo E Silbert, Gary S Grest, and James W Landry. Statistics of the contact network in frictional and frictionless granular packings. *Physical Review E*, 66(6):061303, 2002.

[299] J Wadsworth. Experimental examination of local processes in packed beds of homogeneous spheres, national research council of canada. *Mech. Eng. Report MT-41*, 1960.

[300] RK McGeary. Mechanical packing of spherical particles. *Journal of the American Ceramic Society*, 44(10):513–522, 1961.

[301] Reviel Netz et al. *The Works of Archimedes: The two books On the sphere and the cylinder*, volume 1. Cambridge University Press, 2004.

[302] Harish Viswanathan, RD Wildman, JM Huntley, and TW Martin. Comparison of kinetic theory predictions with experimental results for a vibrated three-dimensional granular bed. *Physics of Fluids (1994-present)*, 18(11):113302, 2006.

[303] RH Boyd, RR Chance, and G Ver Strate. Effective dimensions of oligomers in size exclusion chromatography. a molecular dynamics simulation study. *Macromolecules*, 29(4):1182–1190, 1996.

[304] Paul C Hiemenz and Raj Rajagopalan. *Principles of Colloid and Surface Chemistry, revised and expanded*, volume 14. CRC Press, 1997.

[305] Ritu Verma, JC Crocker, TC Lubensky, and AG Yodh. Entropic colloidal interactions in concentrated dna solutions. *Physical review letters*, 81(18):4004, 1998.

[306] K Harth, U Kornek, T Trittel, U Strachauer, S Höme, K Will, and R Stannarius. Granular gases of rod-shaped grains in microgravity. *Physical Review Letters*, 110(14):144102, 2013.

[307] Sean McNamara and Stefan Luding. Energy flows in vibrated granular media. *Physical Review E*, 58(1):813, 1998.

[308] V Kumaran. Temperature of a granular material fluidized by external vibrations. *Physical Review E*, 57(5):5660, 1998.

[309] Joshua A Dijksman and Martin van Hecke. The role of tap duration for the steady-state density of vibrated granular media. *EPL (Europhysics Letters)*, 88(4):44001, 2009.

[310] P Pierański. Jumping particle model. period doubling cascade in an experimental system. *Journal de Physique*, 44(5):573–578, 1983.

[311] NB Tufillaro, TM Mello, YM Choi, and AM Albano. Period doubling boundaries of a bouncing ball. *Journal de Physique*, 47(9):1477–1482, 1986.

[312] S Douady, S Fauve, and C Laroche. Subharmonic instabilities and defects in a granular layer under vertical vibrations. *EPL (Europhysics Letters)*, 8(7):621, 1989.

[313] Anita Mehta and JM Luck. Novel temporal behavior of a nonlinear dynamical system: The completely inelastic bouncing ball. *Physical review letters*, 65(4):393, 1990.

[314] Francisco Melo, Paul B Umbanhowar, and Harry L Swinney. Hexagons, kinks, and disorder in oscillated granular layers. *Physical review letters*, 75(21):3838, 1995.

[315] E Van Doorn and RP Behringer. Dilation of a vibrated granular layer. *EPL (Europhysics Letters)*, 40(4):387, 1997.

[316] JM Pastor, Diego Maza, Iker Zuriguel, A Garcimartin, and J-F Boudet. Time resolved particle dynamics in granular convection. *Physica D: Nonlinear Phenomena*, 232(2):128–135, 2007.

[317] Martín Sánchez, Gustavo Rosenthal, and Luis A Pugnaloni. Universal response of optimal granular damping devices. *Journal of Sound and Vibration*, 331(20):4389–4394, 2012.

[318] Martín Sánchez and C Manuel Carlevaro. Nonlinear dynamic analysis of an optimal particle damper. *Journal of Sound and Vibration*, 332(8):2070–2080, 2013.

[319] Rosa Ramırez and Rodrigo Soto. Temperature inversion in granular fluids under gravity. *Physica A: Statistical Mechanics and its Applications*, 322:73–80, 2003.

[320] HS Wright, Michael R Swift, and PJ King. Stochastic dynamics of a rod bouncing upon a vibrating surface. *Physical Review E*, 74(6):061309, 2006.

[321] Changxing Li, Zongyan Zhou, Ruiping Zou, David Pinson, and Aibing Yu. Segregation of binary mixtures of spheres and ellipsoids. In *POWDERS AND GRAINS 2013: Proceedings of the 7th International Conference on Micromechanics of Granular Media*, volume 1542, pages 767–770. AIP Publishing, 2013.

[322] Ricky D Wildman, J Beecham, and TL Freeman. Granular dynamics of a vibrated bed of dumbbells. *The European Physical Journal-Special Topics*, 179(1):5–17, 2009.

[323] W Losert, DGW Cooper, J Delour, A Kudrolli, and JP Gollub. Velocity statistics in excited granular media. *Chaos: An Interdisciplinary Journal of Nonlinear Science*, 9(3):682–690, 1999.

[324] Alain Barrat, Emmanuel Trizac, and Matthieu H Ernst. Granular gases: dynamics and collective effects. *Journal of Physics: Condensed Matter*, 17(24):S2429, 2005.

[325] TPC Van Noije and MH Ernst. Velocity distributions in homogeneous granular fluids: the free and the heated case. *Granular Matter*, 1(2):57–64, 1998.

[326] José Maria Montanero and Andrés Santos. Computer simulation of uniformly heated granular fluids. *Granular Matter*, 2(2):53–64, 2000.

[327] J Javier Brey, D Cubero, and MJ Ruiz-Montero. High energy tail in the velocity distribution of a granular gas. *Physical Review E*, 59(1):1256, 1999.

[328] MH Ernst and R Brito. High-energy tails for inelastic maxwell models. *EPL (Europhysics Letters)*, 58(2):182, 2002.

[329] Peter E Krouskop and Julian Talbot. Anisotropic energy distribution in three-dimensional vibrofluidized granular systems. *Physical Review E*, 69(6):061308, 2004.

[330] S Luding. Granular materials under vibration: Simulations of rotating spheres. *Physical Review E*, 52(4):4442, 1995.

[331] Giulio Costantini, Umberto Marini Bettolo Marconi, Galina Kalibaeva, and Giovanni Ciccotti. The inelastic hard dimer gas: A nonspherical model for granular matter. *The Journal of chemical physics*, 122(16):164505, 2005.

[332] Dmitri Volfson, Arshad Kudrolli, and Lev S Tsimring. Anisotropy-driven dynamics in vibrated granular rods. *Physical Review E*, 70(5):051312, 2004.